

**SYNTHESIS, CHARACTERIZATION AND SINGLE
CRYSTAL XRD, COMPUTATIONAL AND BIOLOGICAL
STUDIES OF SOME CHROMANONE AND IMIDAZOLE-
BASED AZOMETHINE LIGANDS AND THEIR BIVALENT
METAL COMPLEXES**

A THESIS SUBMITTED TO THE
NATIONAL INSTITUTE OF TECHNOLOGY WARANGAL
FOR THE DEGREE OF
DOCTOR OF PHILOSOPHY
IN
CHEMISTRY
BY

AJMEERA RAMESH
(Roll No. 716062)



under the guidance of
Prof. A. Ramachandraiah
Professor (HAG) of Chemistry (Retd)

DEPARTMENT OF CHEMISTRY
NATIONAL INSTITUTE OF TECHNOLOGY WARANGAL
HANUMAKONDA, 506 004, TELANGANA, INDIA

October, 2022

CERTIFICATE

This is to certify that the thesis entitled "**SYNTHESIS, CHARACTERIZATION AND SINGLE CRYSTAL XRD, COMPUTATIONAL AND BIOLOGICAL STUDIES OF SOME CHROMANONE AND IMIDAZOLE-BASED AZOMETHINE LIGANDS AND THEIR BIVALENT METAL COMPLEXES**", is the record of the bona fide original work carried out in the Department of Chemistry, National Institute of Technology Warangal by **AJMEERA RAMESH (Regd. No. 716062)** under my supervision and the same has not been submitted anywhere for the award of any degree or diploma.



Prof. A. RAMACHANDRAIAH
(Research Supervisor)
Professor (HAG) of Chemistry (Retd, 2021)
Department of Chemistry
National Institute of Technology Warangal
Hanumakonda, 506 004, Telangana, India

STATEMENT

I hereby declare that the subject matter, embodied in this thesis, entitled, “**SYNTHESIS, CHARACTERIZATION AND SINGLE CRYSTAL XRD, COMPUTATIONAL AND BIOLOGICAL STUDIES OF SOME CHROMANONE AND IMIDAZOLE-BASED AZOMETHINE LIGANDS AND THEIR BIVALENT METAL COMPLEXES**”, is an outcome of the investigations and research work carried out by me in the Department of Chemistry, National Institute of Technology Warangal, under the guidance of Prof. A. Ramachandraiah, Professor (HAG) of Chemistry, and the same has not been submitted elsewhere either in part or in full for any degree or diploma.



AJMEERA RAMESH
Author of the Thesis

ACKNOWLEDGMENTS

The work presented in this thesis would not have been possible without the cooperation and close association with many people. I take this opportunity to extend my heartfelt gratitude and appreciation to all those who made this Ph.D. thesis work possible.

Firstly, it gives me an immense pleasure and delight to express my deep sense of profound gratitude to my research supervisor, **Prof. A. Ramachandraiah (HAG)**, Department of Chemistry, National Institute of Technology Warangal for his inspiring and valuable guidance. His encouragement and co-operation have helped me in attaining my goal. It would have been impossible to achieve this goal without his support and valuable advice. I consider myself fortunate that he has given me a decisive acceleration to my career. I will be very thankful to him throughout my life.

I am greatly indebted to Prof. **N. V. Ramana Rao**, Director, National Institute of Technology Warangal for providing me an opportunity to work first as an institute Full-Time Research Fellow under the UGC's Rajiv Gandhi National Fellowship and then as the Part-Time PhD Scholar. I am also thankful to him for allowing me to use the Institute's infrastructure and other facilities. I would express my gratefulness to **Prof. G. R. C. Reddy**, the former Director, National Institute of Technology Warangal for his generous support. It is my pleasant duty to express my deep sense of gratitude to **Prof. D. Kashinath**, Head, Department of Chemistry and to the former Heads, viz., **Prof. Vishnu Shanker**, **Prof. P. V. Srilakshmi**, **Prof. K. V. Gobi** and **Prof. V. Rajeswar Rao**, for their valuable suggestions, timely help and support.

I express my sincere thanks to the **Doctoral Scrutiny Committee (DSC)** Members, **Prof. K. Laxma Reddy** and **Dr. B. Srinivas**, Department of Chemistry and **Prof. Shirish H Sonawane**, Department of Chemical Engineering for their constant encouragement and constructive suggestions during my research work and the DSC Proceedings. My special thanks are to **Dr. B. Srinivas** and **Dr. Ravinder Pawar**, Department of Chemistry, National Institute of Technology Warangal for their help in the SC-XRD data interpretation and the DFT/B3LYP calculations, respectively.

I take this opportunity to thank **Prof. Venkatathri Narayanan**, **Dr. Raghu Chitta**, **Dr. K. Hari Prasad**, **Dr. S. Nagarajan**, **Dr. M. Raghudas**, **Dr. Ch. Jugun Prakash**, **Dr. Mukul Pradhan**, **Dr. Rajeshkhanna Gaddam**, **Dr. V. Rajeshkumar** and other faculty members of the Department of Chemistry for their suggestions and encouragement.

I also acknowledge with thanks the cooperation from **Dr. Podeti Srinivas**, and **Mr. P. Dayaker**, Department of Biotechnology, Kakatiya University, Warangal, for recording the biological activities of the compounds that I have synthesized and studied.

I fondly remember the time I spent with and acknowledge with thanks the cooperation from my research colleagues, **Dr. G. Srinivasa Rao**, **Dr. Ms. N. Manjula Reddy**, **Mr. T. Dhananjay Rao**, and **Ms. B. Divya**. I am also thankful to **Dr. A. Bhargava Sai**, **Mr. K. Vijendar Reddy** and **Mr. B. Prashanth**, for their support, encouragement and creating a pleasant atmosphere in the lab during my Ph.D. work.

It gives me a great pleasure to muse my campus life with my research colleagues in the Department, **A. Naveen Kumar, P. Venkatesham, Dr. T. Sanjeeva, Dr. M. Venkanna, Dr. P. Babji, Dr. J. Parameswara Chary, Dr. B. Paplal, Dr. G. Ramesh, Dr. K. Vimal Kumar, Ms. P. Soumya, Ms. Pooja, Dr. Ch. Suman, Dr. V. Sunil Kumar, Dr. Ms. K. Sujatha, Dr. M. Srikanth, Dr. G. Ambedkar, , N. Satyanarayana, Ms. R. Hithavani, Dr. K. Sathish, Dr. K. Shekar, Ch. Raju, Dr. S. Suresh, R. Venkatesh, B. Anjaiah, K. Madhu, V Rukya Naik, G. Sripal reddy, G. Srinath, K. Sampath, G. Sivaparwathi, M. Shreesha, S. Akanksha, T. Shirisha, R. Vara Prasad, R. Arun, Ms. J. Swathi, B. Srikanth, Anindya Roy, Ms. Khushboo Agarwala, Ms. Tohira Banoo, Ms. M. Sasi Sree, Akash Kumar, Avinash Sharma, B. Apurba, M. Subir, M. Faizan, M. Arokiaraj, M. Vijay, Aarti Gautam, B. Srikanth, Ch. Vijay Kumar and Dr. G. Rama Rao** and other research scholars in the Institute for their good company and nice atmosphere in and outside the laboratory and their encouragement and help during my research period.

I would like to convey my heartfelt thanks to all the **faculty members** of the Department Biotechnology for their great support and encouragement while I was on one hand an employee of the Department of Biotechnology but a Part-Time PhD Scholar of the Department of Chemistry, on the other.

It would be discourteous on my part if I do not acknowledge the affection and sacrifices from my family. My heartfelt reverence goes to my beloved father, **Sri Mangthu** and my late mother, **Ambali** and step-mother, **Neela** for their moral support and inspiration to never to give up. I would value the care, love and concern from my siblings **Mr. Suresh, Mr. Naresh and Ms. Mounika**.

My special thanks are due to **Dr. V. Prabavathi**, MBBS, DGO, Bharathi Nursing Home for her medical care during my wife's pregnancy.

My heartfelt thanks are to my beloved wife, **Ms. A. Srilatha** and affectionate love to my two sons, **Chi. A. Neethan** and **Chi. A. Sreehan** for their understanding, patience, perseverance, and encouragement all these years.

Finally, I thank one and all of those who have helped me in various capacities, ways and means all through my research work at the Department of Chemistry and job at the Department of Biotechnology

AJMEERA RAMESH

CONTENTS

CERTIFICATE	(i)
STATEMENT	(ii)
ACKNOWLEDGEMENTS	(iii)

CHAPTER-I	INTRODUCTION	Page No
1.1	General Introduction of Schiff Bases and Their Metal Coordination	3
1.2	General Introduction to Chromones	7
1.3	Introduction to 3-formyl-6-methylchromone Schiff bases	9
1.4	General Introduction to 2-butyl-4-chloro-5-formylimadazole (BCFI) Schiff Bases	10
1.5	Schiff Base Metal Complexes	13
1.6	General Introduction to Thiosemicarbazide	13
1.7	Literature Survey on 2-butyl-4-chloro-1H-imidazole-5-carbaldehyde Schiff Base Metal Complexes	14
1.8	Literature Survey on 3-Formylchromone Substituted Schiff Base Metal Complexes	15
1.9	Computational Chemistry and Molecular Modelling Studies	17
1.10	Scope for the Present Work	30
1.11	Objectives of the Present Work	31
	References	33
CHAPTER-II	MATERIALS AND METHODS	
PART A	MATERIALS	
2A.1	Materials and Chemicals Used in the Present Study	42
2A.2	Preparation of the Ligands	42
2A.3	Preparation of Divalent Metal Complexes	44
PART B	METHODS	
2B.1	The Buffers	47
2B.2	Sampling Methods and Instrumental Operations	48
2B.3	X-Ray Crystallographic Studies	49
2B.4	Molecular Modelling	51
2B.5	Hirshfeld Surface Analysis	55
2B.6	Biological Screening Methods	56
2B.7	Molecular Protein Docking Interactions	56
	References	58

CHAPTER-III	SYNTHESIS AND SPECTRAL, SINGLE CRYSTAL XRD, DFT-COMPUTATIONAL AND BIOLOGICAL ACTIVITY STUDIES OF A NEW SCHIFF BASE OF 4-AMINOANTIPYRINE AND INVESTIGATIONS OF ITS Co(II), Ni(II), Cu(II) AND Zn(II) COMPLEXES	
PART A	SPECTRAL, PHYSICOCHEMICAL AND COORDINATION CHEMISTRY STUDIES OF 4AAP-BCFI	
3A.1	Physical and Elemental Analysis	62
3A.2	Mass Spectral Analysis	63
3A.3	FT-IR Spectral Studies	65
3A.4	Electronic Spectral Studies	66
3A.5	^1H and ^{13}C -NMR Spectral Studies	67
3A.6	Electron Spin Resonance ESR Spectral Study of $[\text{Cu}(4\text{AAP-BCFI})_2(\text{H}_2\text{O})_2]^{2+}$	69
3A.7	Spectrophotometric Titration of 4AAP-BCFI (Job's Monovariation Method)	70
3A.8	Thermal Analysis	70
PART B	SINGLE CRYSTAL X-RAY CRYSTALLOGRAPHIC STUDIES AND DFT/B3LYP CALCULATIONS OF 4AAP-BCFI AND ITS METAL COMPLEXES: CORRELATION OF EMPERICAL AND MODELLED DATA	
3B.1	X-Ray Crystal Structure Analysis of 4AAP-BCFI	72
3B.2	Computational Studies	76
3B.3	Hirshfeld Surface Calculations	84
3B.4	Comparative Molecular Modelling Studies of $[\text{M}(4\text{AAP BCFI})_2(\text{H}_2\text{O})_2]$ in the Light of XRD Studies of 4AAP-BCFI	85
3B.5	Stability Analysis	86
PART C	BIOLOGICAL ACTIVITY AND MOLECULAR DOCKING STUDIES OF 4AAP-BCFI AND ITS METAL COMPLEXES	
3C.1	<i>In vitro</i> Antimicrobial Activity	88
3C.2	<i>In vitro</i> Antioxidant Property	88
3C.3	Molecular Docking Studies	89
3C.4	<i>In-silico</i> Drug Likeness Property of 4AAP-BCFI	94
	References	96
CHAPTER-IV	SYNTHESIS, CHARACTERIZATION, CRYSTAL STRUCTURE DETERMINATION, COMPUTATIONAL MODELLING AND BIOLOGICAL STUDIES OF A NEW (2-HYDROXY-5-METHYLPHENYL)(1H-PYRAZOL-4-YL)METHANONE AND ITS Zn(II) AND Cu(II), Ni(II), Co(II) COMPLEXES	
PART A	SPECTRAL CHARACTERIZATION, (2-HYDROXY-5-METHYLPHENYL)(1H-PYRAZOL-4-YL)METHANONE (HMPM) AND ITS Zn(II), Cu(II), Ni(II) AND Co(II) COMPLEXES	
4A.1	Physical and Elemental Analysis	98
4A.2	FT-IR Spectral Studies	99

4A.3	Electronic Spectral Studies	99
4A.4	^1H and ^{13}C -NMR Spectral Studies	101
4A.5	Deprotonation Equilibria for HMPM and $[\text{Zn}(\text{HMPM})_4\text{Cl}_2]$	101
4A.6	Fluorescence Spectra	105
4A.7	Electron Spin Resonance Spectroscopic Studies of $\text{Cu}(\text{HMPM})_4\text{Cl}_2$ Complex	106
PART B	MOLECULAR STRUCTURE DETERMINATION BY SINGLE CRYSTAL X-RAY DIFFRACTION AND HIRSHFELD SURFACE ANALYSIS OF $[\text{Zn}(\text{HMPM})_4\text{Cl}_2]$ AND MOLECULAR MODELLING OF $[\text{M}(\text{HMPM})_4\text{Cl}_2]$ COMPLEXES	
4B.1	Crystal Structure Analysis of $[\text{Zn}(\text{HMPM})_4\text{Cl}_2]$	108
4B.2	Computational Modelling Studies on $[\text{Zn}(\text{HMPM})_4\text{Cl}_2]$ and HMPM by Extended Tight Binding (xTB)	110
4B.3	Molecular Electrostatic Potential (MESP) of HMPM and $[\text{Zn}(\text{HMPM})_4\text{Cl}_2]$	117
4B.4	Frontier Orbitals of HMPM and $[\text{Zn}(\text{HMPM})_4\text{Cl}_2]$	125
4B.5	Hirshfeld Surface Analysis	127
PART C	BIOLOGICAL ACTIVITY STUDIES OF HMPM AND $[\text{M}(\text{HMPM})_4\text{Cl}_2]$ COMPLEXES	
4C.1	Biological Studies	131
4C.2	Molecular Docking Analysis	134
	References	141
CHAPTER-V	SPECTRAL AND BIOLOGICAL STUDIES OF A NOVEL SERIES OF CHROMANONES AND THEIR METAL COMPLEXES AND CORRELATION OF THEIR COMPUTATIONAL STUDIES WITH THE SINGLE CRYSTAL XRD MOLECULAR STRUCTURE OF ONE CHROMANONE OF THE SERIES	
PART A	SPECTRAL, COORDINATION CHEMISTRY STUDIES OF TATMC AND 3FMC-2AB-R	
	Section-A1	
5A.1	Studies of TATMC and Its Metal Complexes	143
5A.2	ESI-Mass Spectrum of TATMC	144
5A.3	NMR Spectral Studies of TATMC	144
5A.4	FTIR Spectral Studies of TATMC and Its Metal Complexes	145
5A.5	Electronic Spectral Analysis of TATMC and Its Metal Complexes	147
5A.6	Fluorescence Spectral Studies of TATMC and Its Complexes	149
5A.7	ESR Spectral Study of $[\text{Cu}(\text{TATMC})_2\text{Cl}_2]$	149
5A.8	Spectrophotometric Titration of TATMC (Job's Monovariation Method)	150
5A.9	SEM-EDX Morphological Study of TATMC and Its Complexes	150
5A.10	Proposed Structures of TATMC and Its Complexes	152
	Section-A2	
5A.1	Physical Characteristics of Chromanones 3FMC-2AB-R	153

5A.2	Infrared Spectral Analysis of 3FMC-2AB-R (3a-e)	154
5A.3	ESI-Mass Spectral Study of 3FMC-2AB-R	156
5A.4	Absorption Spectral Studies of 3FMC-2AB-R	158
5A.5	Fluorescence Spectral Analysis of Chromanones 3FMC-2AB-R	158
5A.6	NMR Spectral Data Analysis of 3FMC-2AB-R (3a-e)	159
PART B	SINGLE CRYSTAL XRD AND COMPUTATIONAL STUDIES OF TATMC AND 3FMC-2AB-R AND CORRELATION OF THE EMPERICAL AND MODELLED DATA	
	Section-B1	
5B.1	Crystal Structure Analysis of TATMC	166
5B.2	Hirshfeld Surface Analysis	168
5B.3	Molecular Electrostatic Potential	170
5B.4	Molecular Modelling Studies of TATMC and M(TATMC)₂ Complexes	171
5B.5	Molecular Orbital Properties	173
5B.6	Molecular Modelled Data and Geometry of the Complexes	176
	Section-B2	
5B.1	Molecular Modelling Studies of Chromanone 3FMC-2AB-R	180
5B.2	Density Functional Theory Calculations	180
5B.3	HOMO-LUMO Analysis	181
5B.4	Conformational Analysis and Consideration of Tautomerism in 3FMC-2AB-R	183
PART C	BIOLOGICAL AND MOLECULAR DOCKING STUDIES OF TATMC AND ITS COMPLEXES AND CHROMANONES 3FMC-2AB-R	
	Section-C1	
5C.1	Biological Activity for TATMC and [M(TATMC)₂X₂]	193
5C.2	Docking Studies of TATMC and Its Complexes	195
5C.3	<i>In-silico</i> Prediction of Drug Likeness and ADME Properties of TATMC	197
	Section-C2	
5C.1	Biological Studies of 3FMC-2AB-R	199
5C.2	Molecular Docking Studies of 3FMC-2AB-R	202
5C.3	<i>In-silico</i> Drug-Likeness Analysis of 3FMC-2AB-R	203
	References	205
	SUMMARY AND CONCLUSION	207
	PUBLICATIONS FROM THE WORK PRESENTED IN THIS THESIS	210
	CONFERENCES AND WORKSHOPS ATTENDED	210
	BIO-DATA	212

CHAPTER – I

INTRODUCTION

CHAPTER-I

INTRODUCTION

Chemistry is honoured as the Central Science. It is Chemistry which absorbs any new development in science and technology as the quickest customer. As new approaches surface, Chemistry acquires new and novel prescripts, X, like, Organometallic, Medicinal, Nuclear, Food, Supramolecular, Combinatorial, Computational, Astro/Cosmo, Geo, Green, Atmospheric, Phyto, etc among many others to be phrased as X Chemistry. Now there is 'Click Chemistry' for which the 2022 Nobel Prize was declared. Chemical sciences conventionally investigate the interrelationship between macroscopic properties as an outcome of the molecular structures. It is finally by the fact how the atoms stay in space by chemical connectivity with other atoms that enables the materials acquire certain special properties. Only structural sets of bond lengths, bond angles, and dihedral angles distinguish one isomer from another in terms of spatial characteristics. Single crystal X-ray diffraction (XRD) studies let us "see" molecules' invisible atoms, which can be magnified virtually on a screen or piece of paper. Computational chemistry, on the other hand, has been built on the virtual fields of quantum mechanics. The most advanced theoretical development of quantum mechanics, with the latest developments in the computer technology, have enabled chemists to visualize and model known and unknown compounds and to evaluate their physicochemical properties without even truly characterizing them experimentally either by wet or instrumental methods of chemical analysis. The power of computational chemistry [1] has been serving as a remarkable modern application for chemists to first predict the structural properties of the materials by computational modeling techniques before using chemicals and reagents to really synthesizing them for applications in industry and health sectors [2] by molecular docking studies [3].

In juxtaposition with structures obtained from molecular structures obtained from single crystal XRD methods experimentally, a great deal of research is going on in the world these days to understand the reliability and authenticity of the modelled structural properties by computational chemical methods [4,5] though the levels of sophistication varies with versions of computational chemistry software. As to how much quantum mechanical rigour is used in the development of the software is the factor that would decide the degree of agreement between the real and modelled properties of molecules. Old software such as PH4, PC MODEL, ACD Labs, etc. were very primitive molecular modelling software which provide only very rudimentary spatial structure of the molecules. Software such as Chem 3D, marketed by Perkin Elmer, AM1 promoted by WinMOPAC, Gaussian, generated by Sun, Sybil from Certara, DFT based software from VASP,

ABINIT, CASTEP, CP2K etc. from other commercial outlets with varied levels of reliability of agreement of the modelled properties with the experimental ones, are presently used by various research groups [6-8]. A few representative examples of computational chemistry software currently in use and application are provided in **Table 1.2**.

Our major objective is to consider preparation of some novel organic compounds with a manageable middle-level formula weight of 300 to 500 daltons emerging from about 30 non-metallic atoms, then to generate their single crystals and to obtain their molecular structure by single crystal XRD methods before or after computational modeling and correlating the degree of agreement of the structural data. The synthesized compounds and their coordinated metal complexes were subsequently characterized by a variety of spectroscopic, electrochemical, and other experimental techniques in order to correlate them with the XRD structures, the attributes derived from molecular modeling, and the orbital energies and morphologies. Conformational analysis by both single bond dihedral torsion and double dihedral torsion was also considered to establish the most stable single molecules by global minimum energy values. The compounds would be also studied for their biological applications and molecular docking studies.

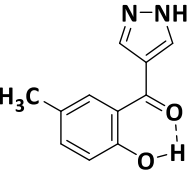
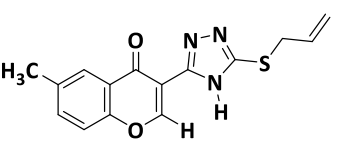
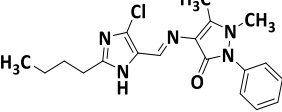
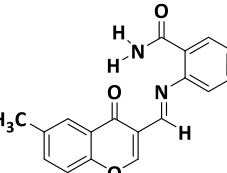
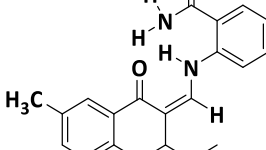
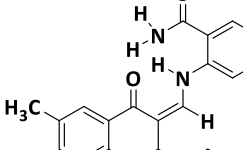
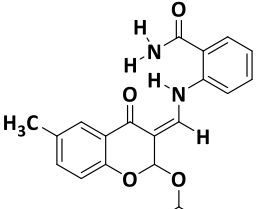
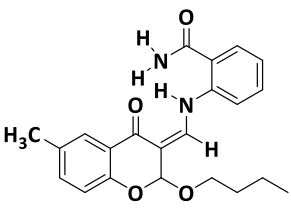
The benefits of this approach is that in case the XRD and modelled data are in good agreement and the compounds are proven to be potential ligands for metal-coordination, the complexes would also be attempted for XRD studies and molecular modelling. If we would be unable to develop single crystals, suitable enough for the XRD, for the complexes or ligands, such molecules would be modelled and their structural properties would be estimated based on the XRD properties of their structural analogues.

We have identified inadequacy of cases to infer the great deal of applications of computational methods to successfully arrive at the structures and properties of molecules as vindicated by experimental XRD results. In order to extend the power of computational chemistry in predicting the structure and properties of various classes of azomethine compounds, we chose to study the class of not-yet-reported chromanone and imidazole compounds some of which serve as either monodentate or bidentate ligands for metal coordination through nitrogen/ oxygen functionality present exocyclic or endocyclic by heterocyclic.

We have synthesized and studied a few nitrogenous organic compounds as representatives for computational modeling and to correlate the computational data with molecular structural data obtained through single crystal XRD empirical studies. Some of these compounds have been used for metal coordination. The operational and reliability features of some of the computational tools

available in the market and in open access and used in the current chemical research are described, in detail [9]. The following are the compounds chosen and studied in detail.

Table 1.1 Structures of the compounds investigated

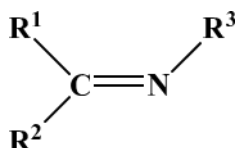
Nature/Type	Nitrogen-Endocyclic	Nitrogen-Exocyclic
Ligand Type	 HMPM  TATMC	 4AAP-BCFI  3FMC-2AB-H  3FMC-2AB-OMe  3FMC-2AB-OEt  3FMC-2AB-O(iPr)  3FMC-2AB-O(n-But)
Complex Type	$[\mathbf{M}(\mathbf{HMPM})_4\mathbf{Cl}_2]$ $[\mathbf{M}(\mathbf{TATMC})_2\mathbf{Cl}_2]$	$[\mathbf{M}(\mathbf{4AAP-BCFI})_2(\mathbf{H}_2\mathbf{O})_2]$

The state of the art of nitrogenous and thio-organic compounds is briefly outlined hereunder:

1.1 General Introduction of Schiff Bases and Their Metal Coordination

Hugo Schiff discovered the condensing of carbonyl compounds with primary amines in 1864 and the product is now known as a Schiff base compounds. Schiff bases **Figure (1.1)** holding different electron donating or electron withdrawing groups (R₁, R₂ and R₃) on the molecular skeleton exhibit vividity in their chemical, electronic, electrochemical and structural manifestations.

Schiff bases have been playing an influential role in coordination chemistry as ligands, which have the capability to form stable metal complexes with different metals in various oxidation states. Schiff base ligands are very popular because they are easy to make and don't cost much. Schiff bases are the compounds containing imine ($>\text{C}=\text{N}-$) or azomethine ($-\text{CH}=\text{N}-$) functional group. The azomethine group is specifically suitable for binding to metal ions *via* the N and O atom lone pair. The investigation of crystal packing and intermolecular interactions in the solid state of different azomethine can provide useful information for the design and production of novel device materials [10-14]. Schiff base molecules having labile protons adjacent to the pyrazole moiety such as p-cresol exhibit electronic spectral changes associated with deprotonation. The Schiff base can be represented by the general structure shown in **Figure 1.1**.



R¹, R² and / or R³ = alkyl or aryl

Figure 1.1 General structure of a Schiff base

Schiff bases containing different donor atoms are widely reported in literature as excellent chelating agents due to the presence of the lone pair of electrons in sp^2 hybridized orbital of their nitrogen atom [4] besides other donor atoms. Depending on the number of donor atoms in the Schiff base, they are monodentate (1), bidentate (2), tridentate (3), tetridentate (4) or polydentate (5) ligands (**Figure 1.2**). The donor atoms bind with transition metal ions and form more stable complexes. Nitrogen offers varied oxidations states, Lewis base character and multiple valences and a variety of electronic transitions, namely, $\sigma \rightarrow \sigma^*$, $\text{n} \rightarrow \sigma^*$, $\pi \rightarrow \pi^*$ and $\text{n} \rightarrow \pi^*$. Coplanarity of the orbital containing the lone pair electrons of nitrogen to the $-\text{C}=\text{N}-$ bond and nuclear spin $I=1$ of N give a great scope to influence the EPR and magnetic studies of the complexes.

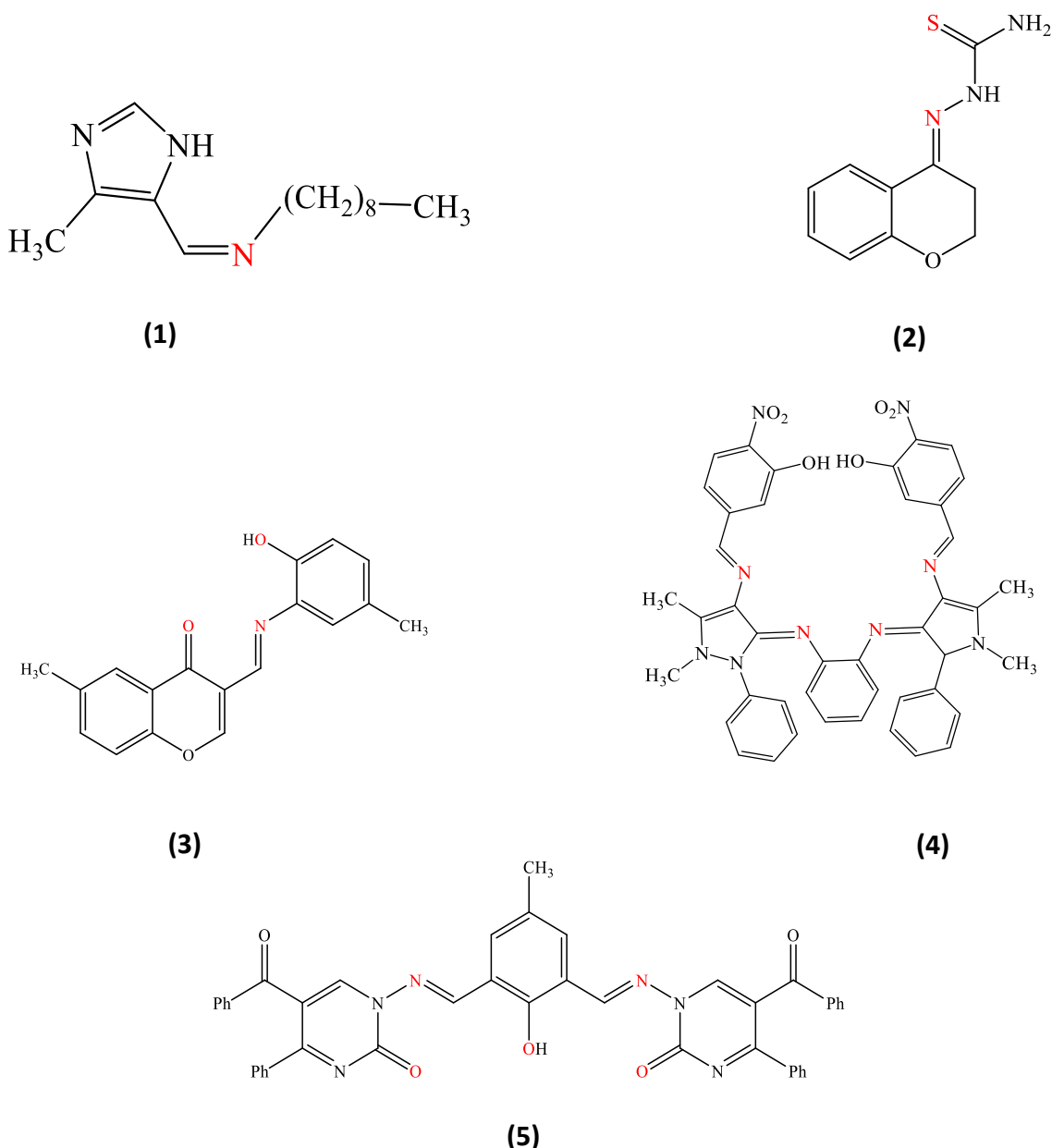


Figure 1.2 Schiff bases with different number of donor atoms

The Schiff base is an important part of figuring out how inorganic chemistry works, especially because of how it affected the growth of coordination chemistry. Schiff bases are a significant group of ligands because of their selectivity, synthetic flexibility and sensitivity to the central metal atom. Schiff bases are used as intermediates in organic synthesis, catalysts, pigments and dyes, and as polymer stabilizers [15-21]. Schiff bases have earned utmost significance in medicinal and pharmaceutical areas because of their biological activities like antimicrobial [22],

analgesic [23], anti-inflammatory [24], antitubercular [25], anticonvulsant [26], anthelmintic [27], antioxidant [28] and anticancer [29] are shown in **Figure 1.3**.

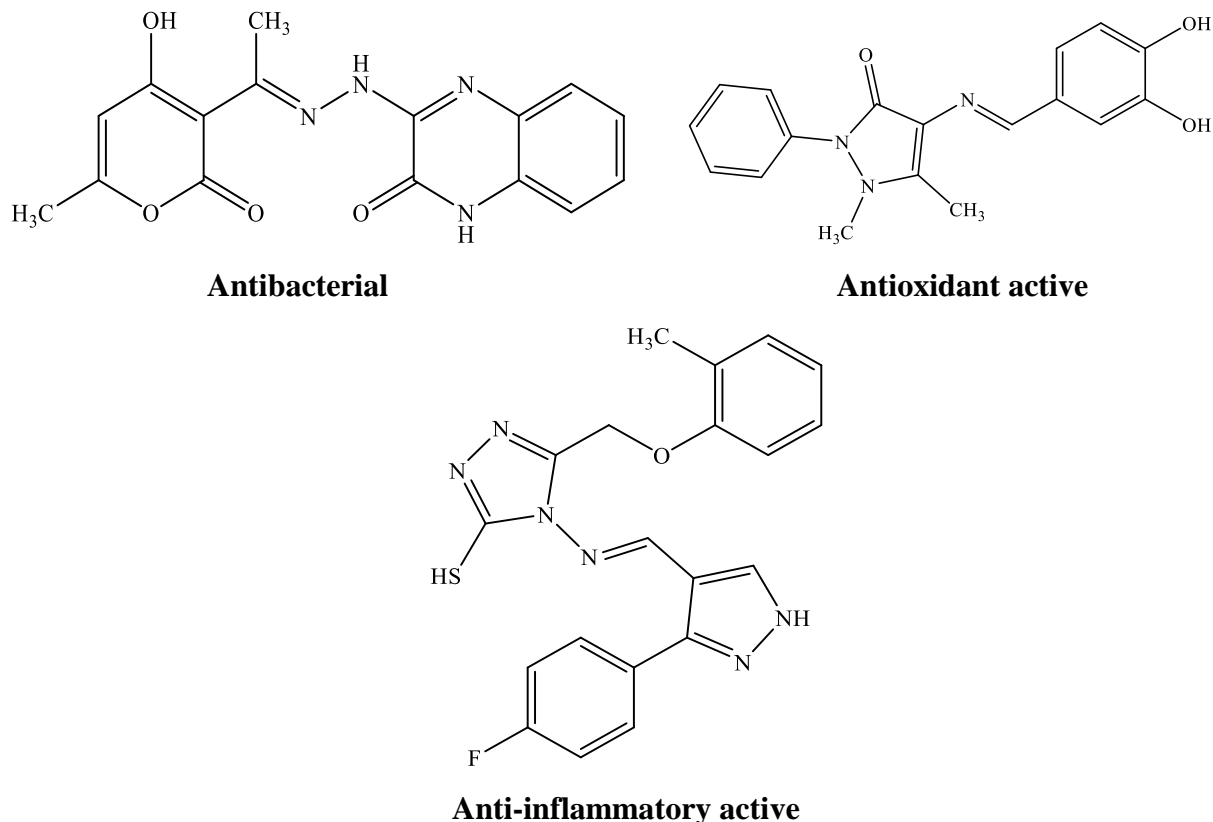


Figure 1.3 Examples for biologically active Schiff bases

Amines have a unique niche in organic chemistry. These are found in amino acids, peptides, proteins (enzymes and glycoproteins), lactams, porphyrins, chlorophyll, nucleosides, nucleotides, DNA, RNA, alkaloids, and many other naturally occurring, biologically significant compounds. They are also present in a lot of the synthetic substances that are used to make medications for commercial applications. Amines are not only crucial building components in many common polymers, such as nylons and polyamides, but also are used as bases in many synthetic transformations. They also serve as key intermediates in organic synthesis, especially to be adducted as Schiff bases, in which they convert carbonyl groups ($-\text{C}=\text{O}$) into azomethine ($-\text{C}=\text{N}$) moieties. Schiff bases, or azomethine compounds have become as unique class of compounds by themselves to possess a host of biological application and in coordination chemistry as potential ligands. Compounds with proven biological applications, possessing an azomethine group ($\text{R}_1\text{R}_2\text{C}=\text{NR}_3$) are presented in **Figure 1.3**.

Due to the diversity of Schiff base ligands and their metal complexes, as well as their analytical, commercial, and biological uses, it is particularly attractive to conduct additional studies in this field. In the present experiment, Schiff bases were synthesized using 3-formyl-6-methylchromone and 2-butyl-4-chloro-1H-imidazole-5-carbaldehyde. Below is a quick explanation of several types of compounds.

1.2 General Introduction to Chromones

Chromone is a substituted keto group linked to the pyrin ring of a benzopyran derivative.

Figure 1.4 depicts the chromone structure.

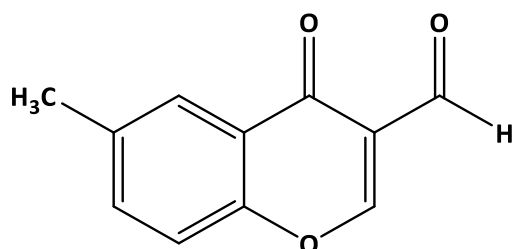


Figure 1.4 Structure of the chromone

Chromone chemistry has been widely explored and extensively studied over the last few decades. Chromone is the structural framework of various bioactive chemicals with both natural and synthetic origins, and it has a high medicinal value and low toxicity. [30]. Khellin is an example of a natural origin chromone derivative, extracted from the seeds of the plant *Ammi visnaga*, and it was the first chromone in clinical practice which was used for the treatment of vitiligo, a pigmentation disorder. Flavoxate was used as smooth muscle relaxant to treat urge incontinence molecular structures are shown in **Figure 1.5** [31].

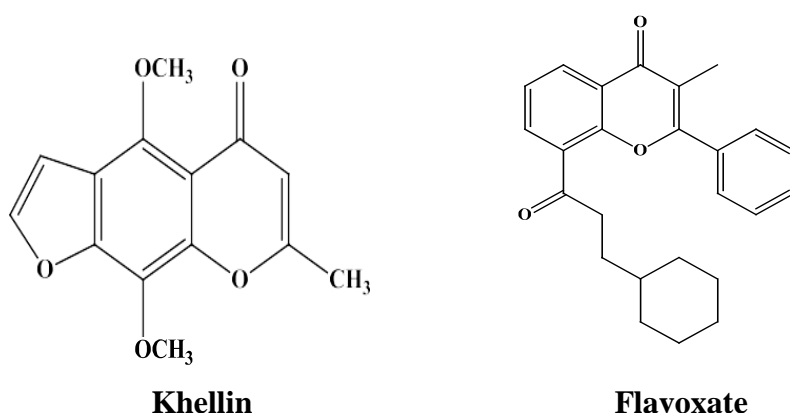
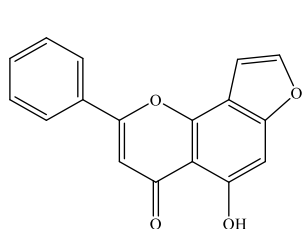
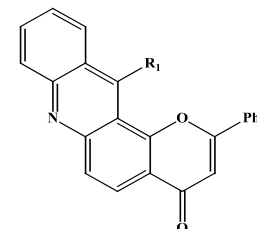


Figure 1.5 Examples of pharmaceutically important natural origin chromone-based compounds

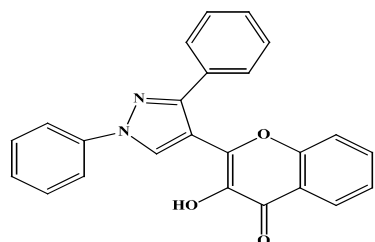
Chromones are a group of naturally existing oxygen containing heterocyclic compounds; these compounds contain γ -pyrone ring which combines with benzene ring at the 5th and 6th - position. Chromones and their derivatives are generally distributed in nature and they occur as a pigment in plant leaves and flowers. Chromone compounds are minor constituents of the human diet and have been reported to exhibit a wide range of biological activities like antimicrobial, antiviral, antioxidant, antitumor, anti-HIV, anti-inflammatory and ant allergic activities are shown in **Figure 1.6** [32]



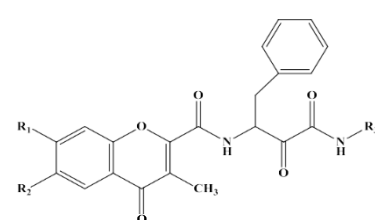
Antibacterial active



Anticancer active



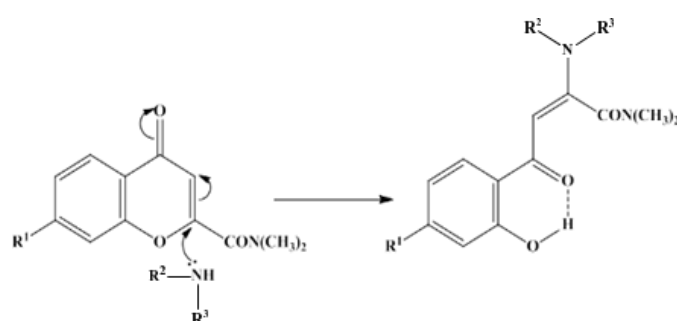
Antifungal active



Antioxidant active

Figure 1.6 Examples for biologically active chromone derived compounds

D.N. Davidson *et al.* have reported the susceptibility of chromone derivatives to ring-opening *via* nucleophilic attack at C₂ which has been illustrated by the amine-mediated ring-opening of substituted chromone-2-carboxamides are shown in **Figure 1.7** [33].

**Figure 1.7** Nucleophilic attack at C₂ position for ring opening in chromone derivatives

1.3 Introduction to 3-formyl-6-methylchromone Schiff bases

An electron-withdrawing group at 5th position of the chromone moiety changes the reactivity of the pyrone ring with respect to nucleophilic agents and gives a wide range of synthetic possibilities of 3-substituted chromones [34]. The chemistry of 3-substituted chromones, mainly 3-formyl-6-methylchromone have gained a lot of interest due to the ease of preparation and applications in different fields. The structure of 3-formyl-6-methylchromone is shown in **Figure 1.8**.

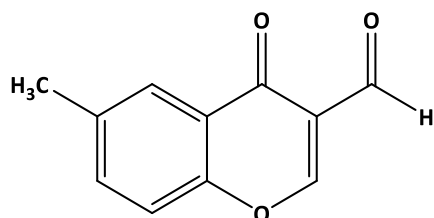


Figure 1.8 Structure of 3-formyl-6-methylchromone

3-formyl-6-methylchromone was developed by Vilsmeier-Haack method and it is synthesized from 2-hydroxyacetophenones, DMF and POCl_3 reagents are shown in **Figure 1.9** [35].

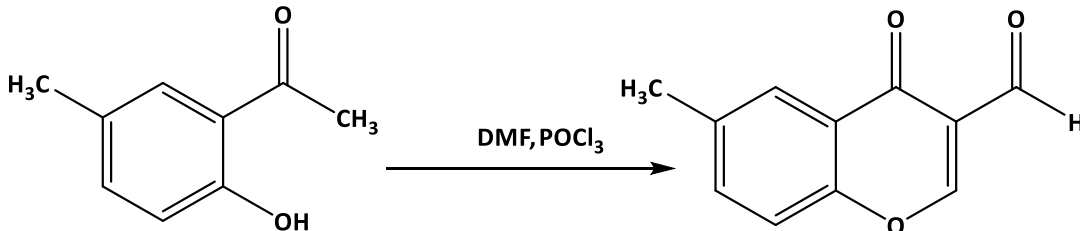


Figure 1.9 Vilsmeier-Haack synthesis of 3-formyl-6-methylchromone

3-formyl-6-methylchromone possesses three electronic centers from a synthetic perspective: an unsaturated keto function, a highly active electrophilic center at C2, and a conjugated second carbonyl group at C3. Synthesis of formylchromone Schiff base ligands and their coordination complexes reveals increased biological activity, including antibacterial, antiviral, anticancer, antioxidant, DNA binding and DNA cleavage, etc. [36, 37]. In contrast, Bharath et al. and Ishar et al. demonstrated that formyl chromone derivatives work as powerful anticancer agents towards human colon cancer and topoisomerase inhibitor [38 (a, b)]. In addition to being used as catalysts, analytical reagents, and NLO materials, etc., [39 (a, b)], these derivatives have a wide range of other applications. In recent years, it has become a new focus of study for inorganic chemists. However, research on the metal complexes of 3-formylchromone Schiff bases is limited. [40 (a-d)].

A number of studies on 3-formyl-6-methylchromone compounds have confirmed their antitumor, anti-thymidine phosphorylase, antimicrobial, antiviral, antioxidant, and insecticidal activities shown in **Figure 1.10**.

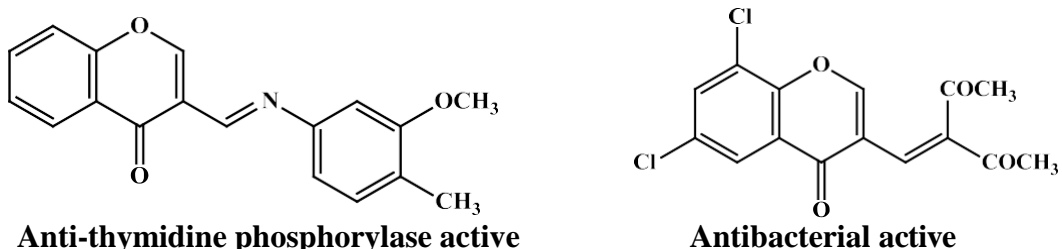


Figure 1.10 Biologically active 3-formylchromones

The reaction of 3-formyl-6-methylchromone with primary aromatic amines leads to various products depending on the nature of the amine and/or experimental conditions (**Scheme 1.1**).

A. Dziewulska-Kułaczkowska *et al.* reported the reactions between 3-formylchromone with aniline or 6-amino-1,4-benzodioxane. 4-Chromanones are formed by the opening of the pyrone ring where an addition of $-OCH_3$ group at C_2 occurs. Chromanones can be synthesized this way from chromones [41].

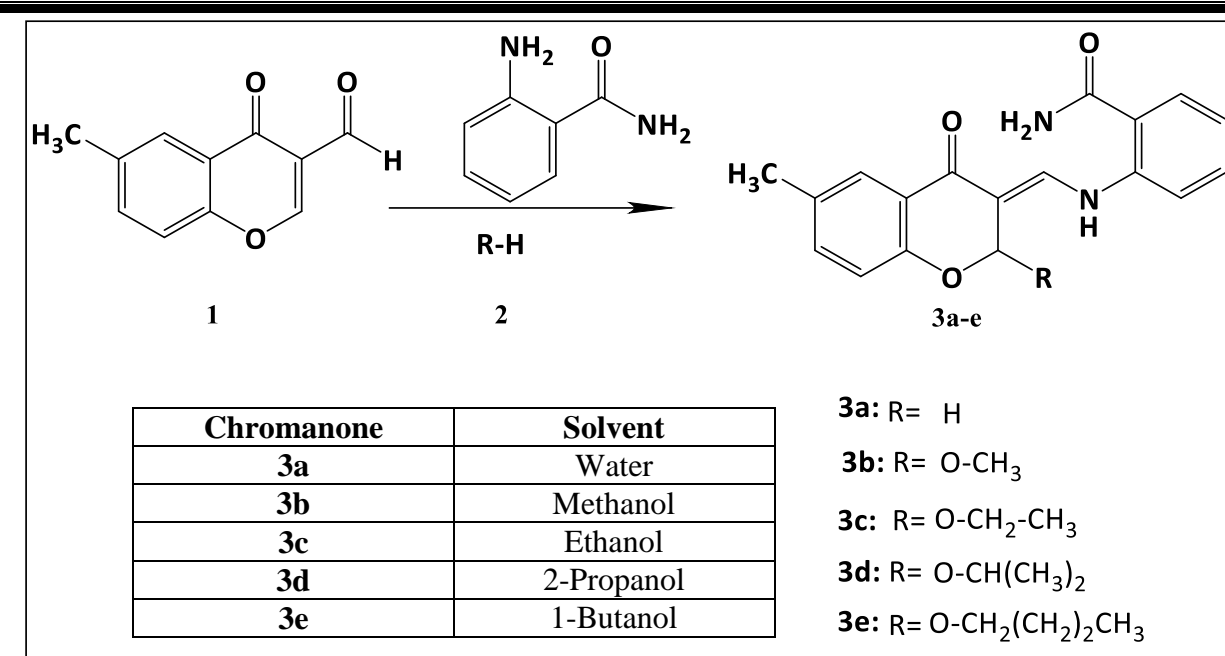
Mayuri B *et al.* reported the reactions between 3-formylchromone with O-aniline are formed by the opening of the pyrone ring where an addition of $-OCH_3$ group at C_2 occurs [42].

S. V. Ryabukhin *et al.* reported the reactions of 3-formylchromone with electron rich anilines in the presence of TMSCl. There is a ring cleavage and a new ring formation takes place in the reactions to get the corresponding quinolines in good yields [43].

A few of the above ligands and complexes have been structurally investigated by both experimentally and by computational molecular modeling followed by correlating the structural data.

1.4 General Introduction to 2-butyl-4-chloro-5-formylimadazole (BCFI) Schiff Bases

Imidazole is a five-membered heterocyclic molecule with two non-adjacent nitrogen atoms that is present in several biological molecules, natural substances, and manufactured organic chemicals. The extensive pharmaceutical applications of Schiff base complexes based on imidazole have inspired researchers to concentrate on their unique chemotherapeutic utility as anticancer, antibacterial, antioxidant, antiviral, antileishmanial, etc. agents [44-45]. With the aid of weak interactions, a multitude of medications contain imidazole compounds.



Scheme 1.1 Synthesis of various Schiff bases from 3-formyl-6-methylchromone in different solvents

The planar ring structure of imidazole is connected with electron-rich nitrogen donors, which increases their affinity for binding with many bio receptors and enzymes. The pharmacokinetic features of the pilot molecules are utilized as a solution for water solubility, bioavailability, and toxicity parameters because it is a polar molecule. Any chemical compound containing imidazole derivatives would certainly have therapeutic significance.

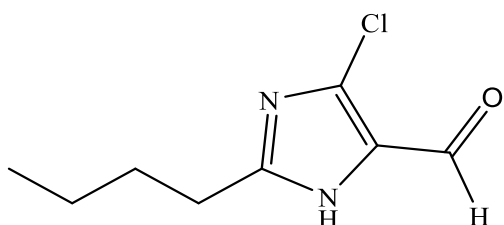


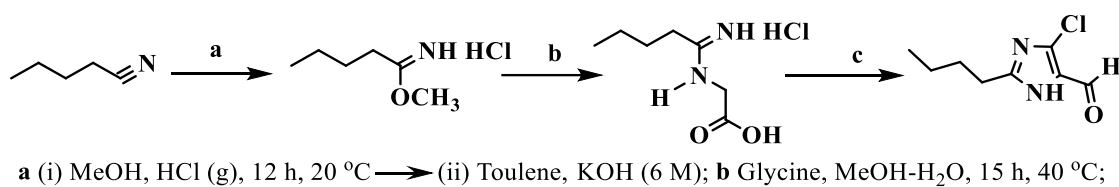
Figure 1.11 Structure of 2-butyl-4-chloro-5-formylimidazole (**BCFI**)

1.4.1 Synthesis of 2-butyl-4-chloro-1H-imidazole-5-carbaldehyde building block

By passing HCl gas through a solution of pentanonitrile and MeOH at -15 to 0 °C and stirring at 20 °C for 12 hours, pentanimidate hydrochloride can be prepared and neutralized using an aqueous KOH solution. The toluene solution of the free base was directly added to the glycine suspension in MeOH-H₂O without further treatment. After 15 hours of stirring at room temperature, the crude reaction mixtures were exposed to the modified Vilsmeier Reaction in the presence of POCl₃ at -5 °C., followed by the addition of DMF at 100 °C for 3 hours [46]. The toluene extract containing the

desired product was treated with 10% aqueous KOH and the aqueous portion was carefully acidified with acetic acid to obtain the precipitate that was recrystallized in the toluene-cyclohexane solvent mixture, yielding a pale yellow solid of 2-butyl-4-chloro-1-imidazole-5-carbaldehyde (**Scheme 1.2**).

This was confirmed from $^1\text{H-NMR}$ spectrum by the appearance of -NH proton at δ 11.83 as broad singlet, CHO proton at δ 9.59 as singlet, at δ 2.81 as triplet ($J = 7.5$ Hz, 2H), CH₃ protons at δ 0.95 as triplet ($J = 7.5$ Hz, 3H). Formation of the ligand is also evident from $^{13}\text{C-NMR}$ spectrum by the appearance of aldehyde carbon at δ 177.6, aromatic carbons of imidazole ring appeared at δ 154.9, 142.0, 125.7, 124.1, butyl chain carbons appeared at δ 29.7, 28.5, 22.1, 13.5 ppm respectively. Its IR spectrum exhibited strong absorption band at 1671 cm^{-1} for aldehydic functional group. In ESI-MS spectrum of peak at m/z 209 $[\text{M}+\text{Na}]^+$ confirmed the structure 14 as 2-butyl-4-chloro-1H-imidazole-5-carbaldehyde.



Scheme

1.2 Stepwise synthesis of 2-butyl-4-chloro-1H-imidazole-5-carbaldehyde

Aabaka Sreenath Reddy *et al.* reported the synthesis and antimicrobial activity of 2-butyl-4-chloro-1H-imidazole-5-carbaldehyde derived Schiff bases [47].

Aabaka Sreenath Reddy *et al.* reported the synthesis and anticancer and antioxidant activity of 2-butyl-4-chloro-1H-imidazole-5-carbaldehyde derived Schiff bases [48].

Furthermore, the process of chelation/coordination plays a significant role in the biological system. Many literature studies revealed that the biological activity of various compounds used as drugs is enhanced by chelation with the metal ions shown in **Figure 1.12**.

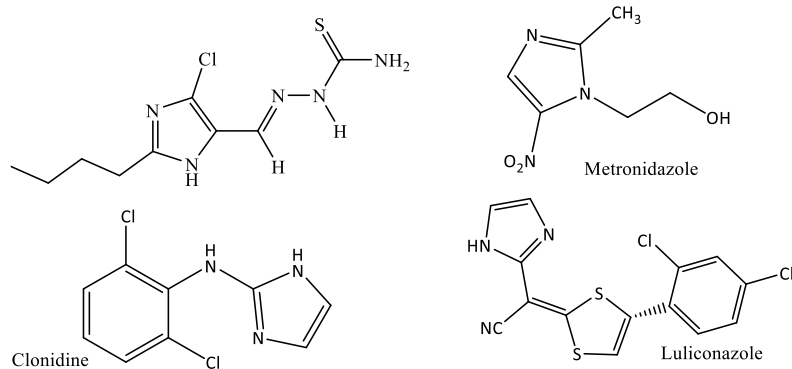


Figure 1.12 Examples of imidazole containing bioactive molecules

1.5 Schiff Base Metal Complexes

Due to their structure, chemical properties, and many biological activities, Schiff base transition metal complexes are of special interest to inorganic chemists. Since 1840, Schiff base transition metal complexes have been known. Under optimal experimental conditions, these complexes are primarily synthesized by treating transition metal salts with Schiff bases. In recent years, the significance of metal-based pharmaceuticals has increased in the domains of medicine, catalysis, and non-linear optical devices (**Figure 1.13**).

Numerous studies have been done on the chemistry of Schiff base metal complexes with nitrogen donors. This could be due to how stable they are and how useful they are in a variety of fields, including electrochemistry, catalysis, oxidation, and biological activity [49, 50].

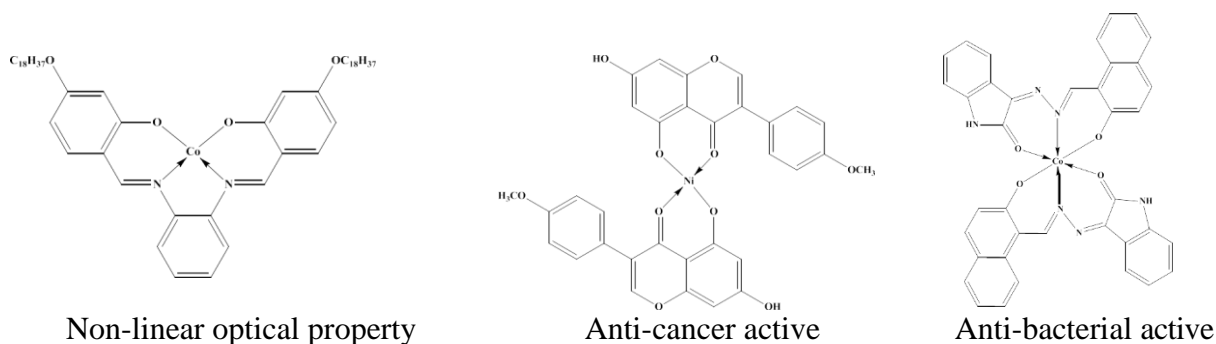


Figure 1.13 Examples of multidentate Schiff base complexes

1.6. General Introduction to Thiosemicarbazide

Good number of thiosemicarbazones/substituted thiosemicarbazones ligands have been synthesized by condensation of aliphatic, aromatic or heterocyclic aldehyde or ketones with thiosemicarbazides/substituted thiosemicarbazides under ambient conditions [51, 52].

Thiosemicarbazones an important class of N, S donor ligand shown in **Figure 1.14**. They generally binds to the metals through N¹, S or N² donor atoms forming four or five membered rings respectively.

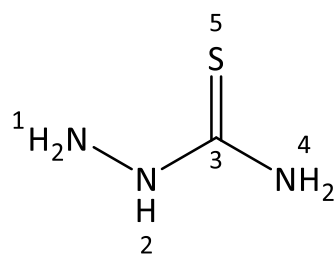


Figure 1.14 Structure of thiosemicarbazide

Research on coordination chemistry, analytical applications and biological activities of thiosemicarbazones and their metal complexes have become a subject of immense interest for coordination chemists [53].

Depending on the N(4) substituent in the aldehyde or ketone employed to condense with thiosemicarbazide, the reactivity of thiosemicarbazones varies [54]. Chelating capacity with transition metal ions is associated to the metabolic activities of thiosemicarbazones. Conforming to the biological features of thiosemicarbazones and their metal complexes, biologically active thiosemicarbazones are planar and include a pyridine ring or its derivatives, resulting in N, N, and S tridentate systems [55]. Changing the point of attachment of the thiosemicarbazone chain from the 2-position in the pyridine ring to the 3- or 4-position causes a decrease in activity in the some cases, presumably due to a decrease in coordination ability, whereas the presence of a bulky group at the terminal nitrogen significantly boosts activity. Thus, an additional possible bonding site and the presence of bulky groups at the N (4) position of the thiosemicarbazone moiety significantly increase biological activity [56]. Therefore, it is essential to characterize the structure of the complex in order to understand its behavior and function in the body.

In some cases, thiosemicarbazides leads to form cyclized structure of membered on heating with KOH solution examples are,

Nazar Trotsko *et al* [57] reported the cyclizationc compounds with (5-arylidene-2,4-dioxothiazolidin-3-yl)acetyl chlorides.

Sharad N. Shelke *et al.* reported the cyclized compounds with hydrazones with various substituted 3-formylchromone.

Joshi, N.S et al. reported the cyclized compounds with hydrazones with various substituted 3-formylchromone.

1.7 Literature Survey on 2-butyl-4-chloro-1H-imidazole-5-carbaldehyde Schiff Base Metal Complexes

The condensation reactions of 2-butyl-4-chloro-1H-imidazole-5-carbaldehyde with thiosemicarbazide of (E)-2-((2-butyl-4-chloro-1H-imidazole-5-yl)methylene)-nmethylhydrazinecarbothioamide ($C_{10}H_{16}N_5ClS$) complexes were reported by Sreenath Reddy A *et al.* The results of molecular docking also supplied important information for the future development of more effective inhibitors [58] and these chemicals have demonstrated promising antitumor action.

Sreenath Reddy A *et al.* described the synthesis, spectroscopic characterization, and biological applications of Cu(II) and Ni(II) complexes containing 2-butyl-4-chloro-5-

formylimidazole thiosemicarbazone, with equivalent antimicrobial efficacy against gram-negative and gram-positive bacteria. The Cu(II)-L combination exhibited an inhibitory concentration 50 of 80 $\mu\text{g}/\text{ml}$, whereas the Ni(II)-L complex exhibited an inhibitory concentration 50 of 100 $\mu\text{g}/\text{ml}$ [59].

Sreenath Reddy A *et al.* reported the synthesis, spectroscopic characterization and antibacterial activity tests of 2-Butyl-4-chloro-5-formylimidazole thiosemicarbazone and its manganese (II) complex [60]. Both gram-negative and gram-positive bacteria exhibited comparable antimicrobial activity.

1.8 Literature Survey on 3-Formylchromone Substituted Schiff Base Metal Complexes

J. Quiroga *et al.* reported the synthesis of novel pyrido[2,3-d]pyrimidines from the reaction of 3-formylchromone and 6-aminopyrimidines employing microwave irradiation. [61].

Condensation reactions of 3-formylchromone with 1-(2,4-difluorophenyl-2-[1,2,4] triazol-4-yl) ethanone, benzo[d] isoxazol-3-yl-acetic acid, and N-methylpiperazine were reported by V.B. Halnor *et al.* The compounds were tested for antimicrobial activity against *E. coli* (gram-negative bacteria), *S. albus* (gram-positive bacteria) and *A. niger* (fungi) [62].

M.P.S. Ishar *et al.* reported the synthesis of 2-substituted-6-chloro-3-formylchromones and 2,7-disubstituted-6-fluoro-3-formylchromones, which exhibited promising anticancer activity [63].

V. Barve *et al.* reported the synthesis of 3-formylchromone Schiff base derivatives and their copper complexes. The synthesized compounds were characterized and studied for their anticancer activity. The IC_{50} values of the complexes were far less than the ligands [64].

M. Kalanithi *et al.* reported the synthesis of metal complexes with the ligand derived from 3-formylchromone with 2-aminothiazole. The ligand and its metal complexes were characterized by different analytical tools. The antimicrobial activity against the species *A. niger*, *S. aureus*, *C. albicans*, *P. aeruginosa*, *E. coli* and *B. subtilis*, was tested and compared with the ligand activity. The metal complexes showed more activity due to the chelation process [65].

M. Al-Rashida *et al.* prepared chromone containing sulfonamide enamines from 3-formylchromone, 6-bromo-3-formylchromone, 6-ethyl-3-formylchromone, 6-fluoro-3-formylchromone and 6, 8-dibromo-3-formylchromone with 3 and 4-aminobenzene sulfonanmides. All compounds exhibited excellent carbonic anhydrase (CA) inhibition activity [66].

The synthesis and characterization of Cu(II) and Zn(II) complexes with the new Schiff base ligand derived from 2-amino-3-formylchromone with (*R*)-2-amino-2-phenylethanol have been reported by F. Arjmand *et al.* The DNA binding results showed that both the metal complexes bind to CT-DNA by electrostatic groove binding mechanism. The Cu(II) complex shown efficient cleavage activity of plasmid pBR322 DNA [67].

The synthesis and characterization of transition metal(II) complexes with 3-(anilinomethylene)-2-methoxychroman-4-one were reported by A. Dziewulska- Kułaczkowska *et al.* at room temperature, the complexes are stable and have electrolyte and non-electrolyte nature [68].

C. Anitha *et al.* described the preparation and characterization of VO(II), Co(II), Ni(II), Cu(II), and Zn(II) Schiff base complexes prepared from 5-(4-chloro-phenylazo)-2-hydroxybenzaldehyde, 3-formylchromone, and p-phenylenediamine. In terms of antibacterial activity, Cu(II) and Zn(II) complexes were more effective. The synthesized compounds exhibited enhanced luminescence [69].

The synthesis of silver (I) complexes with 3-formyl-6-methylchromone-phenyl hydrazone and 3-formyl-6-methylchromone-*p*-chlorophenyl hydrazone was reported by L.V. Tamayo *et al.* The antimicrobial and cytotoxic effects of chromone derivatives increased with coordination to silver (I) [70].

R. Kumar *et al.* reported the synthesis of chromone-3-acrylic acid and its derivatives, namely 6-hydroxy chromone-3-acrylic acid and 7-methoxy chromone-3-acrylic acid and tested them for the first time as corrosion inhibitors for the control of corrosion of low-alloy steel corrosion in 1 M H₂SO₄ and found that they were highly effective [71].

J.E. Philip *et al.* observed that the interactions of chromone hydrazones with acetate salts of transition metals such as Cu(II), Ni(II), and Zn(II) produced mononuclear metal complexes.

Antidiabetic activity, i.e., enzyme inhibition of α -amylase and α -glucosidase, CT-DNA contact, and molecular docking, were investigated in the biological research [72]. P.M. Kasapidou *et al.* reported the 3-component reaction of 3-formylchromones with arylhydrazines and acetylenedicarboxylates [73].

G. Singh *et al.* synthesized the hydrazones through a green route which provides easy access to the hybrid class of compounds with the combination of 3-formylchromone derivatives. The newly synthesized compounds showed significant antimicrobial activities [74].

E. Sneha Jose and colleagues discovered an unique family of mononuclear 2-methoxy-4-chromanones ligated to Cu(II), Zn (II), and Ni(II) complexes. The compounds were shown to be weak α -amylase inhibitors and potent α -glucosidase inhibitors, similar to the majority of diabetes medications [75]. Water-soluble Cu(II) complexes of 7-hydroxy-4-oxo-4H-chromene-3-carbaldehyde-4(N)-substituted semicarbazones were reported by G. Kalaiarasi *et al.* In vitro biological studies demonstrated their potential DNA/protein binding, microbial growth inhibition, and effect on cancer cells [76].

The aforementioned literature review is focused on the synthesis, characterization, structural investigations, and biological activities of 2-butyl-4-chloro-1H-imidazole-5-carbaldehyde and 3-formylchromone substituted Schiff bases and their metal (II) complexes, with specific reference to the types of compounds discussed in the thesis.

1.9. Computational Chemistry and Molecular Modelling Studies

Computational Chemistry is the new branch of theoretical chemistry when virtual chemical materials are mathematically treated with the rules of quantum mechanics. It employs computers to generate data such as structural features or simulated experimental results. Computational chemistry is the application of chemical, mathematical, and computing expertise to the resolution of interesting chemical problems. Even though only a few aspects of chemistry can be computed precisely, nearly every aspect has been described qualitatively or in a manner that is close to quantitative.

The basis of molecular modeling is to model and investigate the behavior of molecules, from small chemical systems to huge biological molecules and material assemblies. Crystal engineering and applications require a comprehensive understanding of the structure, stability, and response characteristics of molecular crystals at certain pressures and temperatures. Computational chemistry has proven to be a beneficial tool for researching compounds that are either difficult to get or incredibly expensive. It also helps chemists make predictions before they do real experiments, which makes it easier for them to make observations. Computer software can calculate a variety of molecular unit properties. Molecular Modeling and Computational Chemistry have applications in drug design, computational biology and materials research. E bejer *et al.* report the molecular simulation approaches need more processing power and software [77]. Classical mechanistic force-field techniques have dominated crystal structure prediction and modeling of molecular crystals for a very long period. In light of expanding processing capability and the development of increasingly advanced quantum-mechanical approximations, first-principles techniques based on density functional theory are now applied to molecular crystals with real-world relevance. Optimization of geometry is the most essential of these calculations.

Observing the molecular potential energy surface and achieving equilibrium between the molecule and the generated energy is the process of geometry optimization. The surface of potential energy represents the link between bond distance and energy associated with nuclear locations. When a global minimum is found, indicating the structure with the lowest Eigen energy, the structure is said to be optimized. The gradient, or first derivative of the potential energy surface, assists the program in locating the global minimum by describing the slope and indicating the direction in which the energy decreases most rapidly relative to the initial input. When convergence requirements are satisfied, the optimization procedure is concluded. Using an optimal geometry,

bond energies, bond lengths, bond angles, and dihedral angles all could be determined. In order to accurately compute any other parameter, geometry optimization must be performed to a basis level equal to or greater than the parameter to be calculated. After adjusting the shape, each structural unit is subjected to a vibrational frequency computation. The motion directions, amplitudes, and modes of vibration of nuclei at their ground and excited states are calculated.

The computational chemistry has reached such an advanced stage that contemporary chemist can predict their macroscopic properties based on quantum mechanical molecular modelling without having to synthesize the compounds and characterize and can visualize the molecular spatial geometry (with all the structural parameters viz., bond lengths, bond angles and dihedral angles). The following are the steps trekked in molecular modeling by Computational Chemical Methods (**Figure 1.15**).

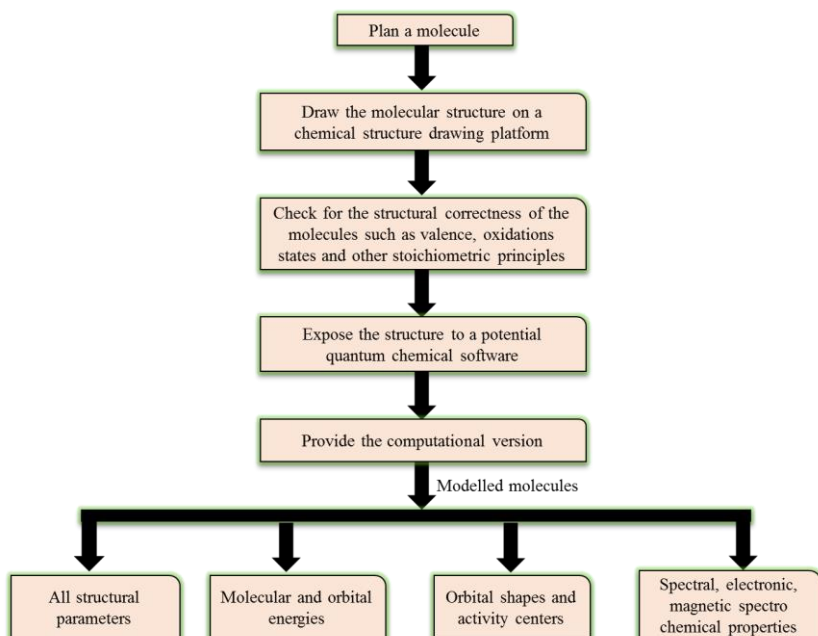


Figure 1.15 A Schematic of the *ab initio* sequence of molecular modelling

A variety of skeletal structural drawing software are available both in open access and proprietary domains for molecular structure drawing, quantum mechanical studies and for molecular modelling and molecular docking, inter molecular interactions and bio-molecular docking.

A few chemical software to work on modeling are presented in **Table 1.2**

The various versions of molecular modelling software employ a blend of classical mechanics and quantum mechanics to varied degrees of advancement and sophistication.

Table 1.2 A few examples for molecular modelling software

S.No	Application	Proprietary:	Free Software:
(a)	Structural Drawing	ACD/ChemSketch, BIOVIA Draw, ChemDraw, ChemWindow, Marvin Sketch, etc.	BKChem, JChemPaint, Molsketch, XDrawChem etc.
(b)	Quantum Mechanical Molecular Modelling	CPMD, CHEMKIN, Discovery Studio, Desmond, Glide, Gaussian, MOPAC, Spartan, GAMESS, Q-Chem, Chem3D, AMBER, MODELLER, UCSF Chimera etc.	BigDFT, CONQUEST, MPQC, ORCA, Quantum ESPRESSO, GROMACS, OpenMM, CP2K, AutoDock, AutoDock Vina, Avogadro, Jmol, Cantera, Chemistry Development kit, RasMol, Open Babel etc.
(c)	Molecular Docking	Glide, LeDock, MOE etc.	AutoDock, AutoDockVina, FlexAID, rDock etc.

Whereas medium range and low-cost software utilized Hartree-Fock method based on self-consistent theory (SCF) on many body systems advance theories such as Density Functional Theory (DFT), Time-dependent Density Functional Theory (TD-DFT), use frontier molecular orbital functional and inter electronic interactions wherein electron cloud of the whole molecule is taken as localized density variation on the basis of Thomas-Fermi model developed by Walter Kohn (1998, Nobel prize) and Lu Jeu Sham.

Irrespective of the modernity, any of the above molecular modelling software uses Born-Oppenheimer approximation, which treats the positively charged nuclei of the molecules or clusters as fixed in space which generate a static external potential (\hat{V}) over the moving electrons. Then a time independent function describing stationary electronic state $\Psi(r_1, r_2, \dots, r_N)$ is generated followed by its Hamiltonian operation through Schrodinger equation,

$$\hat{H}\Psi = [\hat{T} + \hat{V} + \hat{U}] \Psi = \left[\sum_{i=1}^N \left(-\frac{\hbar^2}{2m_i} \nabla_i^2 \right) + \sum_{i=1}^N V(r_i) + \sum_{i < j}^N U(r_i, r_j) \right] \Psi = E\Psi \quad (1.1)$$

where,

\hat{H} = Hamiltonian operator for the wave function (Ψ) of the N electron system, \hat{T} is the total kinetic energy of all the electrons.

\hat{V} is the inter electronic interactions energy

\hbar = Plank constant

m_i = mass of the i^{th} electron

∇_i^2 = Laplacian operator

E = Total energy of the system (sum of potential and kinetic energies)

Here r_i is the radial distance of the i^{th} electron from the origin of the Cartesian coordinate system while medium range molecular modelling software use the simplest Hartree-Fock methods,

use Kohn-Sham equations on normalized wave functions (Ψ) along with the electron density functional, $n_i(r_i)$ given by (for arbitrary first electron)

$$n_1(r_1) = N \int d^3 r_2 \dots, \int d^3 r_N \Psi^*(r_1, r_2, \dots, r_N) \Psi(r_1, r_2, \dots, r_N) \quad (1.2)$$

With certain local density approximations, (LDA)

$$E_{XCi}^{LDA} [n_i] = \int \epsilon_{XCi}(n_i) n_i(r_i) d^3 r_i \quad (1.3)$$

And local spin density approximations [LSDA]

$$E_{XCi}^{LSDA} [n_{i\uparrow}, n_{j\downarrow}] = \int \epsilon_{XCi}(n_{i\uparrow}, n_{j\downarrow}) n_i(r_i) d^3 r_i \quad (1.4)$$

where

ϵ_{XCi} = is the sum of the inter electronic exchange part (ϵ_{Xi}) and correlation part (ϵ_{Ci})

Along with generalized gradient approximations (GGA)

$$E_{XCi}^{GGA} [n_{i\uparrow}, n_{j\downarrow}] = \int \epsilon_{XCi}(n_{i\uparrow}, n_{j\downarrow}, \nabla n_{i\uparrow}, \nabla n_{j\downarrow}) n_i(r_i) d^3 r_i \quad (1.5)$$

And Thomas-Fermi model, Hohenberg-Kohn theorem have developed an equation for the lowest Eigen value (global minimum) of the n electron system has given below

$$E_{(V,N)}[n] = F[n] + \int V(r_i) n_i(r_i) d^3 r_i \quad (1.6)$$

In molecular modeling, one generates a 3-D structure of the most stable molecule (with the least possible eigen value) by exposing the molecule to a quantum mechanical machinery as mentioned above.

Occasionally, some of the properties of the compounds (molecules) depend simultaneously on more than one independent variable. Though there are a variety of graphical software are available to generate plot of the functions like, $y = f(x)$ where y is the domain of the dependent variable (property) and the x is that of the independent. In order to picture plots of the kind, $z = f(x, y)$ where z is the domain of the data of the dependent variable (property) and x and y are those of the dependent ones, one may have to depend on some special software. One may be interested in the conformational analysis of the molecule over an important single bond or over a pair of bonds. Plots of molecular energy as a function of torsional angle over a bond can be obtained by incremental twisting of the molecular segments connected by the bond and by obtaining the respective eigen value at each of the twists. A 2-D plot can, then, be obtained for the conformational energy diagram. However, if two major molecular moieties are linked at 1,3 carbons, the conformational energy diagram may have to be obtained as the plot of eigen value vs the angle of torsion over 1-2 carbon bond and also as a simultaneous function of the torsional angle over the 2-3 carbon atoms. In such cases, a 3-D plotting is necessary. There are commercial and open access software which generate

data-set of z domain, as a simultaneous function of x-data-set and y-data-set, in case one has experimental data of the z as independently function of x and y variables. This process is called, Gridding. The grid files can be transformed in to 3-dimensional images in various formats, mostly as wire-frame diagrams or surfaces. Commercial software such as GoldenSoft's Surfer and Grapher can execute such operations. A few routinely used chemistry software, available both in open access and commercial markets for molecular modelling are presented in **Table 1.3**.

Structural data arrived at from single crystal X-Ray diffractometric studies and those from molecular modeling on DFT theoretical platforms have been compared and were proven to be indications amazing success for the modeling methods. Examples of Schiff bases and their complex are presented in **Table 1.5** through **Table 1.9** along with their molecular structural data obtained experimentally (by single crystal diffractometry) and computational methods evaluated by DFT/B3LYP [78-82]. The molecular structures of the compounds mentioned in these Tables are presented in **Table 1.4**.

3-dimensional images (and molecular structures) cannot be placed on a 2-dimensional stationery or monitor screens. The major population of quinolinone and imidazolyl heterocycles are three dimensional. To virtually visualize the 3-dimensional perceptions, a few optical gadgets have been developed on the human eye's optical illusion. Two of the most popular methods are (i) Stereography and (ii) Anaglyphy. In Stereography, the left-eye view and the right-eye view of the true 3-D picture in 2-D format are placed side by side at a distance of about 5 cms (typical human eye separation distance and each figure is viewed separately by the respective eye by a gadget called, stereograph (shown in **Figure 1.16**) [81] and the brain synthesizes the 3-D perception.

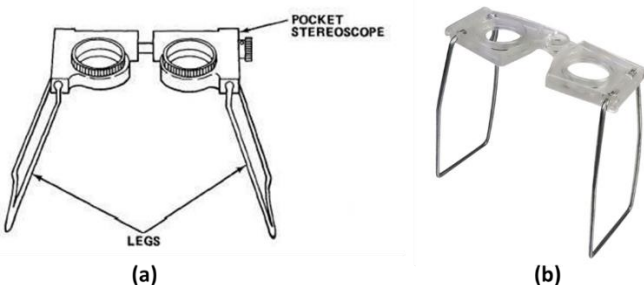


Figure 1.16 (a) Fabricated and **(b)** commercial low-cost stereographs

Table 1.3 Some popular molecular modelling software

Program	Organization	Function
ChemDoodle	iChemLabs	Producing chemical 3D structures, graphics, animations, molecular masses, and elemental analysis calculations. The optimizations were performed using a MMFF94 force field with a conjugate gradient search direction and Newton line search to convergence. It comes with a visualization tool called ChemDoodle 3D that transforms the 2D chemical structures into unique 3D models.
Hypercube	HyperChem Site Licenses	With single point, geometry optimization, or transition state search computations, use HyperChem to examine the potential energy surfaces of quantum or classical models. Include the effects of thermal mobility in simulations using Metropolis Monte Carlo, Langevin dynamics, or molecular dynamics. It is possible to incorporate user-defined structural restrictions.
Avogadro	Avogadro Chemistry. Powered by Jekyll & Minimal Mistakes.	Avogadro is a program that creates various computational chemistry packages and facilitates the import of chemical data. It is utilized by beginning and experienced chemists alike in a variety of scientific disciplines, including computational chemistry, molecular modeling, bioinformatics, and materials science. This software's powerful features for molecular editing and flexible, high-quality rendering are some of its main benefits.
ChemAxon	ChemAxon	Tools for drug research, chemical database searching, and management are all included in the Chemaxon Products line. For academic use, products come with free licenses. The desktop applications from Chemaxon include JChem for Excel, which combines the structure handling capabilities of JChem and Marvin within a Microsoft Excel environment; Instant JChem, a desktop application for end-user scientists; and Marvin, free chemistry software for drawing and visualizing chemical structures. The program can be used to forecast logP values and pKa values. Using Markush structures from the Thomson Reuters Derwent World Patents Index (DWPIISM) database, the business built Markush structure storage and search capabilities (without enumeration). Many Pearson MasteringChemistry courses use Chemaxon's JChem, MarvinSketch, and MarvinView as its chemistry tools.

BIOVIA Draw		An application for drawing molecules called BIOVIA Draw is primarily intended for chemists and other professional members of the chemical industry. It provides them with an entire range of tools for designing and manipulating intricate molecules, chemical processes, and biological sequences. It has an easy-to-use interface that makes it possible to look at, share, and keep scientific knowledge.
MolView	MolView AGPL Free Software	The chemistry modeling program MolView has a very unique interface compared to the other programs described before. Its primary distinction is that it is a free, accessible web application. In comparison to the other packages described above, MolView has a very distinct interface and is a modeling tool for chemistry. The key distinction between a molecular editor and a viewer for 3D models is that both are available in this open-source web application. We may upload molecules from significant databases, including PubChem, the RCSB Protein Data Bank, and the Crystallography Open Database as a user. In addition to establishing structural formulas, MolView also allows for the depiction of chains, modeling and simulation of protein assembly, and protein display. Additionally, you can export several types of data in the JCAMP file format or the PNG format (as a snapshot from the interactive spectrum) (JCAMP-DX file of the current spectrum).
ACD/ChemSketch	ACD/Labs	It is available as free and commercial. However, it is a rather complete piece of software that either high school pupils or university chemistry students can use for educational purposes. You may create Markush structures, polymer structures, organometallic structures, and organic chemical structures using this software. Calculations for molecular weight, density, molar refractivity, etc. can be made. It can provide 3D structures.

ChemDraw Professional	PerkinElmer	Single drawing solution that is reliable for handling and representing organic, organometallic, polymeric, and biopolymer materials (including amino acids, peptides, DNA, and RNA sequences) as well as working with sophisticated stereochemistry. Chemists can draw and submit chemical compound and reaction searches automatically to SciFinder using ChemDraw Professional instead of spending time laboriously cutting and pasting. Using a wide variety of biological templates and drawing tools to produce dynamic drawings of cells and metabolic pathways, incorporating live chemical items when necessary, scientists can rapidly, effectively, and precisely communicate findings and ideas. ChemDraw Professional helps scientists forecast characteristics, create spectra, create accurate IUPAC names, and determine reaction stoichiometry while speeding up the process and improving data quality. It offers molecular mechanics, molecular dynamics calculations, and 3D structures.
Gaussian	Gaussian, INC	Chemists, chemical engineers, biochemists, physicists, and other scientists utilize the computer application Gaussian. To anticipate energies, chemical structures, spectroscopic data (NMR, IR, UV, etc.), and much more complex calculations, it makes use of the fundamental laws of quantum mechanics. You can simulate molecular systems of increasing scale with more precision and under a wider range of real-world situations, leading to the advanced capabilities and performance improvements offered by Gaussian09. One of these features is the ability to model the reaction of very large systems using ONIOM. Examine the gas phase's and the solution's excited states. Forecasts for future spectra performance enhancements, user-friendly features, and new and improved methods IR and Raman, NMR, UV/Visible, Vibrational Circular Dichroism (VCD), Raman Optical Activity (ROA), Electronic Circular Dichroism (ECD), Optical Rotary Dispersion (ORD), Hyperfine Spectra (Microwave Spectroscopy), Franck-Condon, Herzberg-Teller, and Franck-Condon/Herzberg-Teller analyses are just a few of the spectra that Gaussian09 gives you a choice of very accurate energy methods for estimating thermochemical quantities, photochemistry and other excited state processes, and solvent effects when we are optimizing structures and making predictions about most molecular properties.

CrystalExplorer	School of Biomedical and Chemical Sciences, University of Western Australia, Nedlands 6009, Australia	Free software named CrystalExplorer (CE) is designed to examine crystal structures in the *.cif file format. For example, Hirshfeld surface analysis, intermolecular interactions, polymorphism, the impact of pressure and temperature on crystal structure, single-crystal to single-crystal interactions, void analysis, and structure-property relationships are all solid-state chemistry topics that can be studied using CE. CE's graphical interface for 3D crystal structure visualization has greatly improved.
Grapher	GOLDEN SOFTWARE, USA	Grapher is a graphing calculator that can produce both 2D graphs in the following coordinate systems: standard system, cylindrical system, and spherical system, as well as 3D graphs in the following coordinate systems: polar coordinates, linear-logarithmic, log-log, and polar log. It is one of the few high-end graphing apps that can export clear vector drawings for usage in printed documents with ease (although exporting 3D graphs to vector is not possible). Both 2D and 3D graph animation are supported, and a QuickTime file is produced.
Surfer		Microsoft Windows is required to operate Surfer, a full-featured 3D visualization, contouring, and surface modelling application by Golden Software. In addition to many other things, Surfer is widely used for terrain modelling, landscape visualization, surface analysis, contour mapping, 3D surface mapping, gridding, and volumetric.

All commercially available Molecular Modeling software apps generates a pair of single molecular structures that can be viewed by a stereograph. The single crystal X-Ray Diffractometer's microprocessors also are consisting of this provision. An example of stereographically generated molecular structure is shown in **Figure 1.17** [82]. This kind pictures can be virtually seen as 3-D objects by cross-view wherein the eyes focus deep down through the middle of the two structures as if ignored

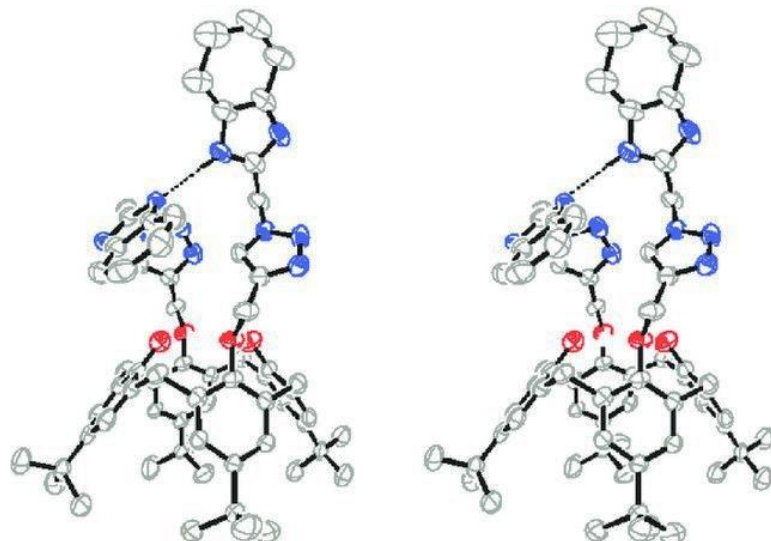


Figure 1.17 Discosoma coral chromophore shown in stereographic projection

In the Anaglyphy, the left and right eye views of the true 3-D picture (molecular structure) is split into 2 differently colored (usually cyan and blue) 2-D graphical pictures aligned slightly staggered as it would have been by the two eyes. An unusual goggle (spectacles) with left side cyan and right side blue is used to see the above mentioned anaglyph picture. The picture in cyan color is seen by left eye only and the blue one by the right eye only. Thereby the brain is able to synthesize the two different images into one 3-D picture.

The image of a typical anaglyph spectacles (goggle) is shown in **Figure 1.18**.



Figure 1.18 A typical anaglyph spectacle

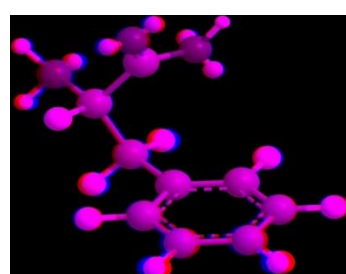


Figure 1.19 The anaglyph picture of phenylalanine

The anaglyph image of phenylalanine is shown in **Figure 1.19**

Table 1.4 Comparison of the structures evaluated experimentally by XRD and theoretically by modelling

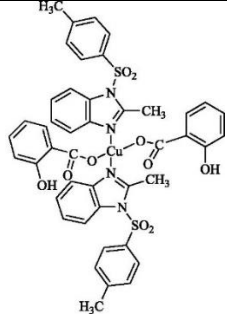
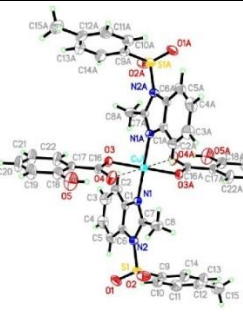
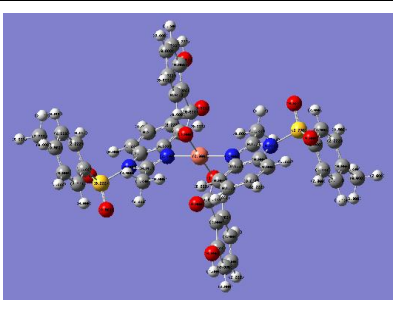
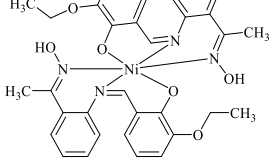
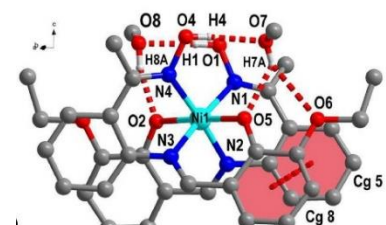
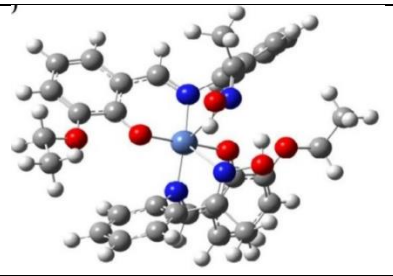
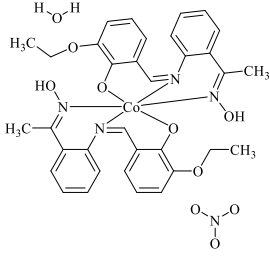
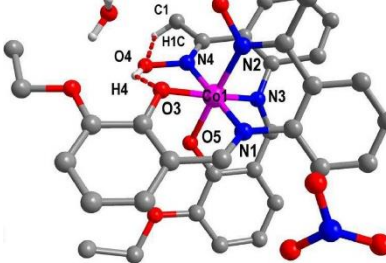
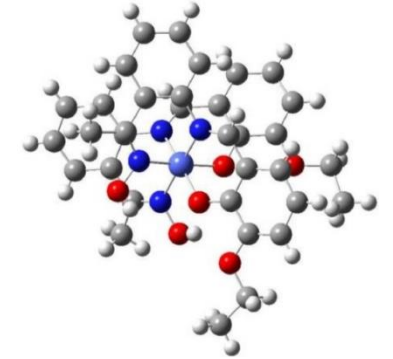
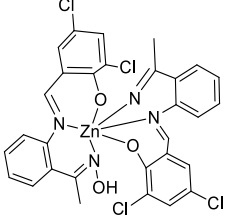
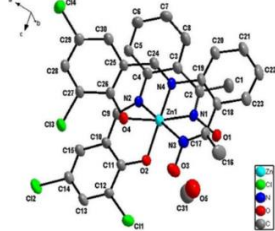
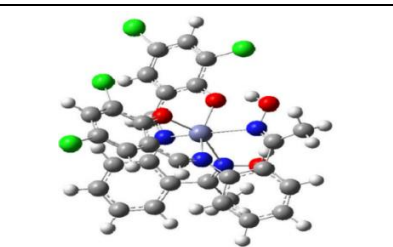
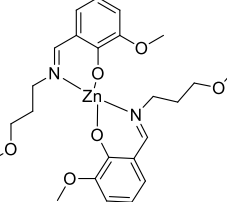
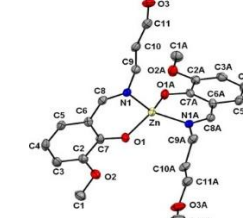
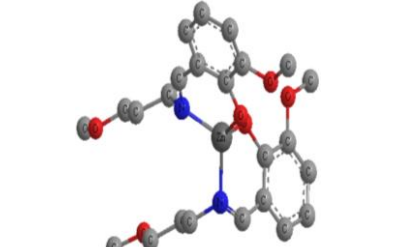
S. No	Structure	Molecular structure from XRD	Molecular structure from DFT
1.			
2.			
3.			
4.			
5.			

Table 1.5 Selected bond distances (Å) and bond angles (°) of **bis(2-hydroxylbenzoato- κ^2 O,O')bis(2-methyl-1-(toluene-4-sulfonyl)-1H-benzimidazole) copper(II) complex** (vide structure at S.No. 1, in Table 1.4) obtained experimentally by XRD and computationally DFT-modelling in correlation

Atomic string	XRD	DFT	XRD-DFT	Atomic string	XRD	DFT	XRD-DFT
BOND DISTANCES				BOND ANGLES			
Cu1–O3	1.955	1.961	-0.006	O3–Cu1–O3A	180.00	179.93	0.07
Cu1–N1	2.002	2.033	-0.031	O3–Cu1–N1A	91.19	90.45	0.74
Cu1–O4	2.574	2.470	0.104	O3A–Cu1–N1	91.18	90.50	0.68
				N1A–Cu1–N1	180	179.70	0.3
				O3–Cu1–N1A	88.82	89.59	-0.77
				O3A–Cu1–N1	91.18	90.50	0.68
				O4–Cu1–O4A	179.98	179.50	0.48
				O4–Cu1–O3A	123.99	121.09	2.9
				O3–Cu1–O4	56.01	58.94	-2.93
				O3–Cu1–N1A	91.19	90.45	0.74
				O3A–Cu1–N1	91.18	90.50	0.68
				O3–Cu1–N1	88.81	89.59	-0.78
				N1A–Cu1–N1	180	179.70	0.3

Table 1.6 Selected bond distances (Å) and bond angles (°) of **bis(E)-1-(2-((Z)-3-ethoxy-2-hydroxybenzylidene)amino)phenyl)ethan-1-one oxime Ni(II) complex** (vide structure at S.No. 2, in Table 1.4) obtained experimentally by XRD and computationally DFT-modelling in correlation

Atomic string	XRD	DFT	XRD-DFT	Atomic string	XRD	DFT	XRD-DFT
BOND DISTANCES				BOND ANGLES			
Ni(1)–O(2)	2.027	1.9713	0.0557	O(2)–Ni(1)–N(1)	90.06	90.0438	0.0162
Ni(1)–N(1)	2.103	2.1443	-0.0413	O(2)–Ni(1)–N(3)	92.76	88.1643	4.5957
Ni(1)–N(3)	2.034	1.9369	0.0971	O(5)–Ni(1)–O(2)	177.81	179.1133	-1.3033
Ni(1)–O(5)	2.026	1.9713	0.0547	O(5)–Ni(1)–N(2)	92.70	89.1689	3.5311
Ni(1)–N(2)	2.048	1.9369	0.1111	O(5)–Ni(1)–N(4)	90.70	90.0716	0.6284
Ni(1)–N(4)	2.105	2.1445	-0.0395	N(2)–Ni(1)–N(1)	82.27	79.3184	2.9516
				N(3)–Ni(1)–N(1)	176.1	173.5627	2.5373
				N(3)–Ni(1)–N(4)	82.41	78.2993	4.1107
				O(2)–Ni(1)–N(2)	85.71	88.7659	-3.0559
				O(2)–Ni(1)–N(4)	90.82	90.7156	0.1044
				O(5)–Ni(1)–N(1)	91.21	90.7397	0.4703
				O(5)–Ni(1)–N(3)	85.89	89.7789	-3.8889
				N(1)–Ni(1)–N(4)	100.27	97.3223	2.9477
				N(2)–Ni(1)–N(4)	175.73	171.5823	4.1477
				N(3)–Ni(1)–N(2)	95.23	97.1166	-1.8866
				C(15)–O(2)–Ni(1)	122.20	125.5735	-3.3735
				O(2)–Ni(1)–N(1)	90.06	90.0438	0.0162
				O(2)–Ni(1)–N(3)	92.76	88.1643	4.5957

O(3)–Ni(1)–N(1)	177.81	179.1133	-1.3033
O(5)–Ni(1)–N(2)	92.70	89.1689	3.5311
O(5)–Ni(1)–N(4)	90.70	90.0716	0.6284
N(2)–Ni(1)–N(1)	82.27	79.3184	2.9516

Table 1.7 Selected bond distances (Å) and bond angles (°) of **bis(E)-1-(2-((Z)-3-ethoxy-2-hydroxybenzylidene)amino)phenyl)ethan-1-one oxime Co(II) complex** (vide structure at **S. No. 3**, in **Table 1.4**) obtained experimentally by XRD and computationally DFT-modelling in correlation

Atomic string	XRD	DFT	XRD-DFT
Co(1)–O(3)	1.88	1.938	-0.055
Co(1)–N(3)	1.91	1.963	-0.053
Co(1)–N(1)	1.90	1.982	-0.081
Co(1)–O(5)	1.88	1.896	-0.015
Co(1)–N(4)	1.93	1.964	-0.027
Co(1)–N(2)	1.926	1.939	-0.013
O(3)–Co(1)–N(1)	91.23	91.207	0.023
O(3)–Co(1)–N(2)	91.36	91.753	-0.393
O(5)–Co(1)–N(3)	89.76	89.971	-0.211
N(1)–Co(1)–N(3)	96.35	97.805	-1.455
N(2)–Co(1)–N(4)	93.58	94.346	-0.766
C(26)–N(1)–Co(1)	123.8	122.807	0.993
O(3)–Co(1)–N(3)	171.97	169.583	2.387
O(5)–Co(1)–O(3)	87.51	87.195	0.315
O(5)–Co(1)–N(4)	90.51	93.260	-2.75
N(1)–Co(1)–N(4)	177.18	178.310	-1.13
C(32)–O(3)–Co(1)	122.20	121.990	0.21
C(25)–N(1)–Co(1)	116.00	116.856	-0.856

Table 1.8 Selected bond distances (Å) and bond angles (°) of **[Zn(L)₂]**, where **L = (E)-1-(2-Aminophenyl) ethanone oxime** (vide structure at **S. No. 4**, in **Table 1.4**) obtained experimentally by XRD and computationally DFT-modelling in correlation

Bond lengths				Bond angles			
Atomic String	XRD	DFT	XRD-DFT	Atomic String	XRD	DFT	XRD-DFT
Zn1-O2	1.999	2.039	-0.04	O2-Zn1-O4	87.6	90.35	-2.75
Zn1-N2	2.129	2.208	-0.079	O2-Zn1-N2	89.8	87.67	2.13
Zn1-N3	2.046	2.155	-0.109	O2-Zn1-N4	166.6	164.77	1.83
Zn1-O4	2.042	2.060	-0.018	O4-Zn1-N2	91.1	87.47	3.63
Zn1-N2	2.010	2.099	-0.089	O4-Zn1-N4	84.6	84.34	0.26
Zn1-N4	2.041	2.109	-0.068	N1-Zn1-N3	94.4	94.64	-0.24
				N2-Zn1-N3	172.9	169.51	3.39
				N3-Zn1-N4	83.1	80.65	2.45
				O2-Zn1-N1	97.5	100.3	-2.8

Table 1.9 Selected bond distances (Å) and bond angles (°) of $[\text{Zn}(\text{L})_2]$, where $\text{L} = (\text{E})\text{-2-methoxy-6-((3-methoxypropyl)imino) - -methylphenol}$ (vide structure at S. No. 5, in Table 1.4) obtained experimentally by XRD and computationally DFT-modelling in correlation

Bond lengths				Bond angles			
String	XRD	DFT	XRD-DFT	String	XRD	DFT	XRD-DFT
Zn-O1	1.937	1.953	-0.016	O1-Zn-N1	95.31	93.25	2.06
Zn-N1	2.001	2.086	-0.085	O1-Zn-O1A	110.93	131.80	-20.87
O1-C7	1.309	1.297	0.012	O1-Zn-N1A	116.84	109.1	7.74
O2-C1	1.421	1.413	0.008	N1-Zn-N1A	122.64	123.67	-1.03
O2-C2	1.362	1.363	-0.001				
O3-C11	1.424	1.413	0.011				
O3-C12	1.421	1.409	0.012				
N1-C8	1.293	1.301	-0.008				
N1-C9	1.455	1.466	-0.011				
C2-C7	1.423	1.443	-0.02				
C6-C8	1.434	1.438	-0.004				

The work presented in the thesis with reference to the above was carried out with respective the following scope and objectives for my investigations

1.10 Scope for the Present Work

- In the regime of Green Chemistry chemical research is applying due care to the chemicals used for synthesis and other purposes.
- Hostility towards chemicals is becoming a general opinion among people. Hence before attempting to synthesize new chemicals products for any specific applications erstwhile practice of trials and error cannot be contemporary method it is advised to first computationally modelled the desired product and its precursors for the synthetic relationship and only if the quantum chemistry is compatible one should actually proceed for synthesis.
- Computational modelling would also provide substantial support for the desired product's Quantitative Structure-Activity Relationships (QSARs).
- In order to make the above consideration reliable and authenticate, more number of compounds must be rallied into a data bank. Where their crystallographic structural data and their computationally modelled structural data are in good agreement towards this goal a great deal of research is presently ripe all over the world in synthesizing new molecules and studying their

structure and properties along with their computationally modelled structural and other properties.

- It is thereby advisable to consider molecules for the above purpose among those groups of compounds which have potential biological and medicinal applications. Schiff bases and chromanone compound with some heterocyclic linkages are best suited presence of azomethine moiety would also render these molecules as potential ligands to generate coordination compounds.

1.11 Objectives of the Present Work

- To synthesize a set of novel Schiff base and chromanone based heterocyclic compounds and along with their bivalent metal complexes.
- To develop single crystals for the ligand and complexes to arrive at their crystallographic properties and molecular structures.
- To characterize the ligands and complexes by various instrumental methods such as Mass, FT-IR, UV-Vis, ^1H , ^{13}C -NMR TGA-DTA, ESR and SEM-EDX to relate the experimental data with their XRD molecular structure.
- To model the synthesized compounds by computational chemical methods such as Chem draw pro, Grapher, Surper, Mercury, DFT-Gaussian, Crystal explorer, Schrodinger, AutoDockVina to evaluate their structural and quantum mechanical properties.
- To correlate the XRD experimental structural data with those of the computationally modelled data in order to arrive at the reliability of the modelling software for future applications.
- To explore the molecular docking capabilities of the ligands and complexes unto some selected proteins and enzymes to understand their possible biological applications.
- To investigate the pharmacological applications by bio assaying of the compounds synthesized.

To realize the above objectives with the scope mentioned, we have synthesized and investigated a few organic ligands with nitrogenous heterocyclic (imidazole, triazole or pyrazole rings) or oxygen heterocyclics (chromanone) extinctions over azomethine functionality and their possible transition metal complexes as shown in **Table 1.1**, as examples.

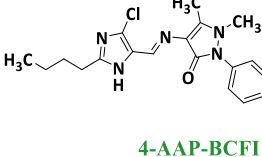
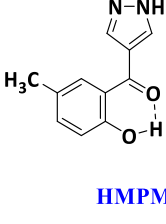
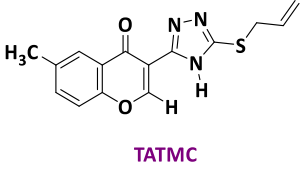
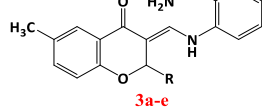
Single crystals suitable of these organic and coordination compounds could be isolated for X-Ray Diffractometry. Repeated attempts with changed conditions such as solvents, temperature and annealing, single crystals could not be obtained for the chromanone series of compounds suitable for XRD studies. Detailed physicochemical characterization with some modern analytical instruments has been carried out on all the ligands and the complexes synthesized. Molecular Modeling has also been done on all the synthesized compounds to a varied degree of sophistication and the structural

and spectroscopic data were correlated with those of experimental molecular structural data obtained from XRD studies and other investigations. Almost all the ligands and their complexes were studied for their biological applications and protein-docking studies.

The procedures of the synthesis of the chosen compounds and the details of the experimental methods used, are presented in **Chapter II** and the results of laboratory investigations, crystallographic studies, molecular modeling and docking and biological studies of these compounds, from the contents of the subsequent chapters. It has been planned to investigate the following imine bases derived from 2-butyl-4-chloro-1H-imidazole-5-carbaldehyde (**BCFI**) as well as 3-formyl-6-methylchromone (**3FMC**). Using the starting reactants and products investigated are under placed in **Table 1.10**.

The investigations of the compounds are presented in detail in this Thesis. The studies have been successfully published in some reputed journals [**83, 84**].

Table 1.10 Gallery of the ligands investigated along with their complexes

I.	(E)-4-(((2-butyl-4-chloro-1H-imidazol-5-yl)methylene)amino)-1,5-dimethyl-2-phenyl-1,2-dihydro-3H-pyrazol-3-one (4-AAP-BCFI)	 4-AAP-BCFI
II.	(2-hydroxy-5-methylphenyl)(1H-pyrazol-4-yl)methanone (HMPM)	 HMPM
III.	3-(5-(allylthio)-4H-1,2,4-triazol-3-yl)-6-methyl-4H-chromen-4-one (TATMC)	 TATMC
IV.	(E)-2-(((2-methoxy-6-methyl-4-oxochroman-3-ylidene)methyl)amino)benzamide (3FMC-2AB-R)	 3a-e 3a: R= H ; 3b: R= O-CH ₃ ; 3c: R= O-CH ₂ -CH ₃ ; 3d: R= O-CH(CH ₃) ₂ ; 3e: R= O-CH ₂ (CH ₂) ₂ CH ₃

References

[1] Wormer, P. E. S.; Avoird, A. van der. Forty Years of Ab Initio Calculations on Intermolecular Forces. In *Theory and Applications of Computational Chemistry*; Elsevier, 2005, 1047–1077. <https://doi.org/10.1016/B978-044451719-7/50080-9>.

[2] Gould, I. R. Computational Chemistry: Application to Biological Systems. *Molecular Simulation* **2001**, *26* (1), 73–83. <https://doi.org/10.1080/08927020108024201>.

[3] Stanzione, F.; Giangreco, I.; Cole, J. C. *Use of Molecular Docking Computational Tools in Drug Discovery*, 1st ed.; Elsevier B.V., 2021; Vol. 60. <https://doi.org/10.1016/bs.pmch.2021.01.004>.

[4] Kumar, R.; Obrai, S. Comparison of Computational Studies with the X-Ray Crystal Structure of Directly Synthesized Bis(D,L-Aminobutyric)Copper(II) Complex. *Journal of Structural Chemistry* **2014**, *55* (2), 241–247. <https://doi.org/10.1134/S0022476614020073>.

[5] Kumar, R.; Obrai, S. Comparison of Computational Studies with the X-Ray Crystal Structure of Directly Synthesized Bis(D,L-Aminobutyric)Copper(II) Complex. *Journal of Structural Chemistry* **2014**, *55* (2), 241–247. <https://doi.org/10.1134/S0022476614020073>.

[6] Abdul Jaleel, U. C.; Rakhila, M.; Parameswaran, G. Comparison between Investigational IR and Crystallographic Data with Computational Chemistry Tools as Validation of the Methods. *Advances in Physical Chemistry* **2010**, *2010*, 1–5. <https://doi.org/10.1155/2010/787813>.

[7] Gao, T.; Andino, J. M.; Alvarez-Idaboy, J. R. Computational and Experimental Study of the Interactions between Ionic Liquids and Volatile Organic Compounds. *Physical Chemistry Chemical Physics* **2010**, *12* (33), 9830. <https://doi.org/10.1039/c003386c>.

[8] Pöhls, J.-H.; Heyberger, M.; Mar, A. Comparison of Computational and Experimental Inorganic Crystal Structures. *Journal of Solid State Chemistry* **2020**, *290*, 121557. <https://doi.org/10.1016/j.jssc.2020.121557>.

[9] Pöhls, J.-H.; Heyberger, M.; Mar, A. Comparison of Computational and Experimental Inorganic Crystal Structures. *Journal of Solid State Chemistry* **2020**, *290*, 121557. <https://doi.org/10.1016/j.jssc.2020.121557>.

[10] Holman, K. T.; Pivovar, A. M.; Ward, M. D. Engineering Crystal Symmetry and Polar Order in Molecular Host Frameworks. *Science* (80). **2001**, *294* (5548), 1907–1911. <https://doi.org/10.1126/science.1064432>.

[11] Kudernac, T.; Sändig, N.; Fernández Landaluce, T.; van Wees, B. J.; Rudolf, P.; Katsonis, N.; Zerbetto, F.; Feringa, B. L. Intermolecular Repulsion through Interfacial Attraction: Toward Engineering of Polymorphs. *Journal of American Chemical Society* **2009**, *131* (43), 15655–15659. <https://doi.org/10.1021/ja901718q>.

[12] Fernández-G, J. M.; Del Rio-Portilla, F.; Quiroz-García, B.; Toscano, R. A.; Salcedo, R. The Structures of Some Ortho-Hydroxy Schiff Base Ligands. *Journal of Molecular Structure* **2001**. [https://doi.org/10.1016/S0022-2860\(00\)00915-7](https://doi.org/10.1016/S0022-2860(00)00915-7).

[13] Muthuraman, M.; Le Fur, Y.; Bagieu-Beucher, M.; Masse, R.; Nicoud, J. F.; George, S.; Nangia, A.; Desiraju, G. R. C-H···O and C-H···N Hydrogen Bond Networks in the Crystal Structures of Some 1,2-Dihydro-N-Aryl-4,6-Dimethylpyrimidin-2-Ones. *Journal of Solid State Chemistry* **2000**. <https://doi.org/10.1006/jssc.2000.8685>.

[14] Majid, S. A.; Mir, J. M.; Paul, S.; Akhter, M.; Paray, H.; Ayoub, R.; Shalla, A. H. Experimental and Molecular Topology-Based Biological Implications of Schiff Base Complexes: A Concise Review. *Reviews in Inorganic Chemistry* **2019**, 39 (2), 113–128. <https://doi.org/10.1515/revic-2018-0023>.

[15] (a) Fuchs, M.; Schmitz, S.; Schäfer, P. M.; Secker, T.; Metz, A.; Ksiazkiewicz, A. N.; Pich, A.; Kögerler, P.; Monakhov, K. Y.; Herres-Pawlis, S. Mononuclear Zinc(II) Schiff Base Complexes as Catalysts for the Ring-Opening Polymerization of Lactide. *European Polymer journal* **2020**, <https://doi.org/10.1016/j.eurpolymj.2019.109302>.

(b) Drozdzak, R.; Allaert, B.; Ledoux, N.; Dragutan, I.; Dragutan, V.; Verpoort, F. Ruthenium Complexes Bearing Bidentate Schiff Base Ligands as Efficient Catalysts for Organic and Polymer Syntheses. *Coordination Chemistry Reviews*. **2005**. <https://doi.org/10.1016/j.ccr.2005.05.003>.

[16] Nejati, K.; Rezvani, Z.; Massoumi, B. Syntheses and Investigation of Thermal Properties of Copper Complexes with Azo-Containing Schiff-Base Dyes. *Dyes and Pigments* **2007**, 75 (3), 653–657. <https://doi.org/10.1016/j.dyepig.2006.07.019>.

[17] (a) Gupta, K. C.; Sutar, A. K. Catalytic Activities of Schiff Base Transition Metal Complexes. *Coordination Chemistry Reviews* **2008**, 252 (12–14), 1420–1450. <https://doi.org/10.1016/j.ccr.2007.09.005>.

(b) Liu, X.; Manzur, C.; Novoa, N.; Celedón, S.; Carrillo, D.; Hamon, J. R. Multidentate Unsymmetrically-Substituted Schiff Bases and Their Metal Complexes: Synthesis, Functional Materials Properties, and Applications to Catalysis. *Coordination Chemistry Reviews* **2018**, 357, 144–172. <https://doi.org/10.1016/j.ccr.2017.11.030>.

(c) Gupta, K. C.; Sutar, A. K. Catalytic Activities of Schiff Base Transition Metal Complexes. *Coordination Chemistry Reviews* **2008**, 252 (12–14), 1420–1450. <https://doi.org/10.1016/j.ccr.2007.09.005>.

[18] Akelah, A.; Kenawy, E. R.; Sherrington, D. C. Agricultural Polymers with Herbicide/Fertilizer Function-III. Polyureas and Poly(Schiff Base)s Based Systems. *European Polymer Journal* **1993**, 29 (8), 1041–1045. <https://doi.org/10.1016/0014-305790306-Z>.

[19] Wahba, O. A. G.; Hassan, A. M.; Naser, A. M.; Hanafi, A. M. Preparation and Spectroscopic Studies of Some Copper and Nickel Schiff Base Complexes and Their Applications as Colouring Pigments in Protective Paints Industry. *Egyptian Journal of Chemistry* **2017**, 60 (1), 25–40. <https://doi.org/10.21608/ejchem.2017.517.1000>.

[20] Abu-Dief, A. M.; Mohamed, I. M. A. A Review on Versatile Applications of Transition Metal Complexes Incorporating Schiff Bases. *Beni-Suef University Journal of Basic and Applied Sciences* **2015**, 4 (2), 119–133. <https://doi.org/10.1016/j.bjbas.2015.05.004>.

[21] Uddin, M. N.; Ahmed, S. S.; Alam, S. M. R. REVIEW: Biomedical Applications of Schiff Base Metal Complexes. *Journal of Coordination Chemistry* **2020**, 73 (23), 3109–3149. <https://doi.org/10.1080/00958972.2020.1854745>.

[22] Da Silva, C. M.; Da Silva, D. L.; Modolo, L. V.; Alves, R. B.; De Resende, M. A.; Martins, C. V. B.; De Fátima, Â. Schiff Bases: A Short Review of Their Antimicrobial Activities. *Journal of Advanced Research* **2011**, 2(1), 1–8. <https://doi.org/10.1016/j.jare.2010.05.004>.

[23] Deivanayagam, P.; Bhoopathy, P.; Thanikaikarasan, S. Synthesis, Characterization, Antimicrobial, Analgesic and CNS Studies of Schiff Base Cu(II) Complex Derived from 4-Choro-o-Phenylene Diamine. *International Journal of Advanced Chemistry* **2014**, 2 (2), 166. <https://doi.org/10.14419/ijac.v2i2.3338>.

[24] (a) Azam, M.; Al-Resayes, S. I.; Trzesowska-Kruszynska, A.; Kruszynski, R.; Shakeel, F.; Soliman, S. M.; Alam, M.; Khan, M. R.; Wabaidur, S. M. Zn(II) Complex Derived from Bidentate Schiff Base Ligand: Synthesis, Characterization, DFT Studies and Evaluation of Anti-Inflammatory Activity. *Journal of Molecular Structure* **2020**, 1201, 127177. <https://doi.org/10.1016/j.molstruc.2019.127177>.
 (b) Ki, J.; Mukherjee, A.; Rangasamy, S.; Purushothaman, B.; Song, J. M. Insulin-Mimetic and Anti-Inflammatory Potential of a Vanadyl-Schiff Base Complex for Its Application against Diabetes. *RSC Advances* **2016**, 6(62), 57530–57539. <https://doi.org/10.1039/c6ra11111d>.

[25] Budhani, P.; Iqbal, S. A.; Bhattacharya, S. M. M.; Mitu, L. Synthesis, Characterization and Spectroscopic Studies of Pyrazinamide Metal Complexes. *Journal of Saudi Chemical Society* **2010**, 14 (3), 281–285. <https://doi.org/10.1016/j.jscs.2010.02.009>.

[26] Patole, J.; Shingnapurkar, D.; Padhye, S.; Ratledge, C. Schiff Base Conjugates of P-Aminosalicylic Acid as Antimycobacterial Agents. *Bioorganic Medicinal Chemistry Letters* **2006**, 16 (6), 1514–1517. <https://doi.org/10.1016/j.bmcl.2005.12.035>.

[27] Ren, S.; Wang, R.; Komatsu, K.; Bonaz-Krause, P.; Zyrianov, Y.; McKenna, C. E.; Csipke, C.; Tokes, Z. A.; Lien, E. J. Synthesis, Biological Evaluation, and Quantitative Structure–Activity Relationship Analysis of New Schiff Bases of Hydroxysemicarbazide as Potential Antitumor Agents. *Journal of Medicinal Chemistry* **2002**, (45), 410–419. <https://doi.org/10.1021/jm010252q>.

[28] Kumar, M.; Padmini, T.; Ponnuvel, K. Synthesis, Characterization and Antioxidant Activities of Schiff Bases Are of Cholesterol. *Journal of Saudi Chemical Society* **2017**, 21, S322–S328. <https://doi.org/10.1016/j.jscs.2014.03.006>.

[29] Malik, M. A.; Dar, O. A.; Gull, P.; Wani, M. Y.; Hashmi, A. A. Heterocyclic Schiff Base Transition Metal Complexes in Antimicrobial and Anticancer Chemotherapy. *Medicinal Communication* **2018**, 9 (3), 409–436. <https://doi.org/10.1039/c7md00526a>.

[30] (a) Sosnovskikh, V.Y.; Irgashev, R.A.; Levchenko, A.A. Uncatalyzed addition of indoles and N-methylpyrrole to 3-formylchromones: synthesis and some reactions of (chromon-3-yl)bis(indol-3-yl)methanes and E-2-hydroxy-3-(1-methylpyrrol-2-ylmethylene)chroman-4-ones. *Tetrahedron* **2008**, 28(64), 6607-6614. <https://doi.org/10.1016/j.tet.2008.05.032>; (b) Siddiqui, Z.N.; Farooq, F. A practical one pot synthesis of novel 2-hydroxy-4-chromanone derivatives from 3-formylchromone. *Journal of Chemical Sciences* **2012**, (124), 1097-1105. <https://doi.org/10.1007/s12039-012-0300-y>.

[31] Ellis, G. P. Chromone Carboxaldehydes. Chemistry of Heterocyclic Compounds 1977, (31), 921. <https://doi.org/10.1002/9780470187012.ch19>.

[32] Dziewulska-Kułaczkowska, A.; Mazur, L. Structural studies and characterization of 3-formylchromone and products of its reactions with chosen primary aromatic amines. *Journal of Molecular Structure* 2011, 2-3(985) 233-242. <https://doi.org/10.1016/j.molstruc.2010.10.049>.

[33] Davidson, D.N.; English, R.B.; Kaye, P.T. Chromone studies. Part 4. Structural analysis of chromone-derived 2-amino-3-(2-hydroxybenzoyl)acrylamides. *Journal of the Chemical Society Perkin Transactions* **1991**, 2, 1181-1185. <https://doi.org/10.1039/P29910001181>.

[34] Sosnovskikh, V.Y.; Irgashev, R.A.; Moshkin, V.S.; Kodess, M.I. Reaction of 3-(polyfluoroacyl)chromones with hydrazines: new regioselective synthesis of RF-containing pyrazoles. *Russ. Chem. Bull.* **2008**, (57), 2146. <https://doi.org/10.1007/s11172-008-0291-5>.

[35] Nohara, A.; Umetani, T.; Sanno, Y. Studies on antianaphylactic agents—I: A facile synthesis of 4-oxo-4H-1-benzopyran-3-carboxaldehydes by Vilsmeier reagents. *Journal of Tetrahedron* **1974**, 19(30), 3553-3561.

[36] El-Gammal, O.A.; El-Reash, G.A.; Ahmed, S.F. Structural, Spectral, Thermal And Biological Studies On 2-Oxo-N'-(4-Oxo-4H-Chromen-3-Yl)Methylene)-2-(Phenylamino)Acetohydrazide (H2L) And Its Metal Complexes. *Journal of Molecular Structure* **2012**, 1007, 1-10. <https://doi.org/10.1016/j.molstruc.2011.03.043>.

[37] Puccetti, L.; Fasolis, G.; Vullo, D.; Chohan, Z.H.; Scozzafava, A.; Supuran, C.T. Carbonic Anhydrase Inhibitors. Inhibition of Cytosolic/Tumor-Associated Carbonic Anhydrase Isozymes I, II, IX, And XII with Schiff's Bases Incorporating Chromone and Aromatic Sulfonamide Moieties, and Their Zinc Complexes. *Bioorganic Medicinal Chemistry Letters* **2005**, 12(15) 3096-3101. <https://doi.org/10.1016/j.bmcl.2005.04.055>.

38. (a) Baráth, Z.; Radics, R.; Spengler, G.; Ocovszki, I.; Kawase, M.; Motohashi, N.; Shirataki, Y.; Shah, A. Multidrug Resistance Reversal by 3-Formylchromones in Human Colon Cancer and Human mdr1 Gene-transfected Mouse Lymphoma Cells. *Journal of Molnár, In Vivo (Brooklyn)* **2006**, 20(5), (645-649; (b) Ishar, M.P.S.; Singh, G.; Singh, S.; Sreenivasan, K.K.; Singh, G. Design, Synthesis, and Evaluation Of Novel 6-Chloro-/Fluorochromone Derivatives As Potential Topoisomerase Inhibitor Anticancer Agents. *Bioorganic Medicinal Chemistry Letters* **2006**, 5(16), 1366-1370. <https://doi.org/10.1016/j.bmcl.2005.11.044>.

[39] (a) Hassan, A.M.A.; Hanafy, A.I.; Ali, M.M.; Salman, A.A.; El-shafay, Z.A. ; El- wahab, Z.H.A.; Salama, I.A. Synthesis, Characterization and Catalytic Activity of Chromone Derivative Schiff Base Complexes; Rapid Hydrolysis of Phosphodiester in An Aqueous Medium. *Journal of Basic Applied. Chemistry* **2012**, (2) 1-11; (b) Kalanithi, M.; Kodimunthiri, D.; Rajarajan, M.; Thamaraj, P. Synthesis, Characterization And Biological Activity of Some New VO(IV), Co(II), Ni(II), Cu(II) and Zn(II) Complexes of Chromone Based NNO Schiff Base Derived From 2-Aminothiazole. *Spectrochimica Acta - Part A Molecular and Biomolecular Spectroscopy* **2011**, 1(82), 290-298. <https://doi.org/10.1016/j.saa.2011.07.051>.

[40] (a) Kavitha, P.; Saritha, M.; Reddy, K.L. Synthesis, Structural Characterization, Fluorescence, Antimicrobial, Antioxidant and DNA Cleavage Studies of Cu(II) Complexes of Formyl Chromone Schiff Bases. *Spectrochimica Acta Part a Mol. Biomolecular Spectroscopy* **2013**, 102 159-168. <https://doi.org/10.1016/j.saa.2012.10.037>; (b) Kavitha, P.; Laxma Reddy, K. Synthesis, Spectral Characterisation, Morphology, Biological Activity and DNA Cleavage Studies of Metal Complexes with Chromone Schiff Base. *Arabian Journal Chemistry* **2016**, 4(9), 596-605. <https://doi.org/10.1016/j.arabjc.2012.09.001>; (c) Kavitha, P.; Laxma Reddy, K. Pd(II) Complexes Bearing Chromone Based Schiff Bases: Synthesis, Characterisation and

Biological Activity Studies. *Arabian Journal of Chemistry* **2016**, 5(9), 640-648. <https://doi.org/10.1016/j.arabjc.2013.06.018>; (d) Kavitha, P.; Rama Chary, M.; Singavarapu, B.V.V.A.; Laxma Reddy, K. Synthesis, Characterization, Biological Activity And DNA Cleavage Studies of Tridentate Schiff Bases and Their Co(II) Complexes. *Journal of Saudi Chemical Society* **2016**, 1(20), 69-80. <https://doi.org/10.1016/j.jschs.2013.03.005>.

[41] A. Dziewulska-Kułaczkowska, L. Mazur, Structural studies and characterization of 3-formylchromone and products of its reactions with chosen primary aromatic amines. *Journal of Molecular Structures* **2011**, 2-3(985), 233-242. <https://doi.org/10.1016/j.molstruc.2010.10.049>.

[42] Mayuri, B.; Kavitha, P.; Basavoju, S.; Bhargavi, G.; Reddy, K. L. Synthesis, Structural Characterisation and Biological Evolution of Chromanones. *Journal of Molecular Structures* **2017**, 1145, 1–9. <https://doi.org/10.1016/j.molstruc.2017.05.013>.

[43] Ryabukhin, S.; Plaskon, A.; Volochnyuk, D.; Tolmachev, A. Chlorotrimethylsilane-Mediated Synthesis of Functionalized 2-(2-Hydroxybenzoyl)Pyrido[1,2-a] Benzimidazoles. *Synthesis (Stuttg)* **2007**, (20), 3155–3162. <https://doi.org/10.1055/s-2007-990790>.

[44] Rani, N.; Sharma, A.; Singh, R. Imidazoles as Promising Scaffolds for Antibacterial Activity: A Review. *Mini-Reviews Medicinal Chemistry* **2013**, 13 (12), 1812–1835. <https://doi.org/10.2174/13895575113136660091>.

[45] Bhati, S.; Kumar, V.; Singh, S.; Singh, J. Synthesis, Characterization, Antimicrobial, Anti-Tubercular, Antioxidant Activities and Docking Simulations of Derivatives of 2-(Pyridin-3-Yl)-1Hbenzo[d] Imidazole and 1,3,4-Oxadiazole Analogy. *Letters in Drug Design and Discovery* **2020**, 17 (8), 1047–1059. <https://doi.org/10.2174/1570180816666191122105313>.

[46] Griffiths, G. J.; Hauck, M. B.; Imwinkelried, R.; Kohr, J.; Roten, C. A.; Stucky, G. C.; Gosteli, J. Novel Syntheses of 2-Butyl-5-Chloro-3 H -Imidazole-4-Carbaldehyde: A Key Intermediate for the Synthesis of the Angiotensin II Antagonist Losartan. *Journal of Organic Chemistry* **1999**, 64 (22), 8084–8089. <https://doi.org/10.1021/jo9824910>.

[47] Reddy, A. S.; Mao, J.; Krishna, L. S.; Badavath, V. N.; Maji, S. Synthesis, Spectral Investigation, Molecular Docking and Biological Evaluation of Cu(II), Ni(II) and Mn(II) Complexes of (E)-2-((2-Butyl-4-Chloro-1H-Imidazol-5-Yl)Methylene)-N-Methylhydrazinecarbothioamide (C10H16N5ClS) and Its DFT Studies. *Journal of Molecular Structure* **2019** (1196), 338-347. <https://doi.org/10.1016/j.molstruc.2019.06.085>.

[48] Aabaka, S. R.; Yaaratha, S.; Krishna, L. S.; Das, S. K.; Ammireddy, V. R. (E)-2-[(2-Butyl-4-Chloro-1 H -Imidazol-5-Yl)Methylidene]- N -Methylhydrazine-1-Carbothioamide Monohydrate. IUCrData 2016, 1 (9), x161514. <https://doi.org/10.1107/S2414314616015145>.

[49] Mendum, P.; Kumari, C. G.; Ragi, R. Synthesis, Characterization, DNA Binding, DNA Cleavage and Antimicrobial Studies of Schiff Base Ligand and Its Metal Complexes. *J. Fluoresc.* 2015. <https://doi.org/10.1007/s10895-015-1520-6>.

[50] Bheemarasetti, M.; Palakuri, K.; Raj, S.; Saudagar, P.; Gandamalla, D.; Yellu, N. R.; Kotha, L. R. Novel Schiff Base Metal Complexes: Synthesis, Characterization, DNA Binding, DNA Cleavage and Molecular Docking Studies. *Journal of Iranian Chemical Society* **2018**, 15 (6), 1377–1389. <https://doi.org/10.1007/s13738-018-1338-7>.

[51] Kalaiarasi, G.; Rajkumar, S. R. J.; Dharani, S.; Lynch, V. M.; Prabhakaran, R. Synthesis, Spectral Characterization and Biological Evaluation of Some Copper(II) Complexes

Containing 4-Oxo-4H-Chromene-3-Carbaldehyde-4(N)-Substituted Thiosemicarbazones. *Inorganica Chimica Acta* **2018**, (471), 759-776. <https://doi.org/10.1016/j.ica.2017.12.008>.

[52] Jayakumar, K.; Seena, E. B.; Kurup, M. R. P.; Kaya, S.; Serdaroglu, G.; Suresh, E.; Marzouki, R. Spectral, Thermal and DFT Studies of Novel Nickel(II) Complexes of 2-Benzoylpyridine-N4-Methyl-3- Thiosemicarbazone: Crystal Structure of a Square Planar Azido-Nickel(II) Complex. *Journal of Molecular Structure* **2022**, (1253), 132257. <https://doi.org/10.1016/j.molstruc.2021.132257>.

[53] Haribabu, J.; Srividya, S.; Mahendiran, D.; Gayathri, D.; Venkatramu, V.; Bhuvanesh, N.; Karvembu, R. Synthesis of Palladium (II) Complexes via Michael Addition: Antiproliferative Effects through ROS-Mediated Mitochondrial Apoptosis and Docking with SARS-CoV-2. *Inorganic Communications* **2020**, 59 (23), 17109–17122. <https://doi.org/10.1021/acs.inorgchem.0c02373>.

[54] Syamal, A.; Maurya, M. R. Synthesis and Characterization of New Dioxomolybdenum(VI) Complexes of ONS Donor Schiff Bases Derived from Thiosemicarbazide, S-Methyldithiocarbazate, S-Benzylidithiocarbazate and o-Hydroxy-Aromatic Aldehydes/Ketones. *Transition Metal Chemistry* **1986**, (11), 255-258. <https://doi.org/10.1007/BF00959926>.

[55] Paul, P.; Bhattacharya, S. Palladium Complexes of Pyrrole-2-Aldehyde Thiosemicarbazone: Synthesis, Structure and Spectral Properties. *Journal of Chemical Sciences* **2014**, (126), 1547-1555. <https://doi.org/10.1007/s12039-014-0699-4>.

[56] Jacob, J. M.; Kurup, M. R. P.; Nisha, K.; Serdaroglu, G.; Kaya, S. Mixed Ligand Copper(II) Chelates Derived from an O, N, S- Donor Tridentate Thiosemicarbazone: Synthesis, Spectral Aspects, FMO, and NBO Analysis. *Polyhedron* **2020**, 189, 114736. <https://doi.org/10.1016/j.poly.2020.114736>.

[57] Trotsko, N.; Dobosz, M.; Jagiełło-Wójtowicz, E. Cyclization of Thiosemicarbazide Derivatives of 5-Arylidene-2,4-Dioxothiazolidine-3-Acetic Acids to 1,3,4-Thiadiazoles and Their Pharmacological Properties. *Acta Poloniae Pharmaceutica*. 2007, 64 (3), 227–231.

[58] Reddy, A. S.; Mao, J.; Krishna, L. S.; Badavath, V. N.; Maji, S. Synthesis, Spectral Investigation, Molecular Docking and Biological Evaluation of Cu(II), Ni(II) and Mn(II) Complexes of (E)-2-((2-Butyl-4-Chloro-1H-Imidazol-5-Yl)Methylene)-N-Methylhydrazinecarbothioamide (C10H16N5ClS) and Its DFT Studies. *Journal of Molecular Structure*. 2019 (1196), 338-347. <https://doi.org/10.1016/j.molstruc.2019.06.085>.

[59] Reddy, A.; Krishna, L.; Rashmi, H.; Devi, P.; Sarala, Y.; Reddy, A. Synthesis, Spectroscopic Characterization and Biological Applications of Cu(II) and Ni(II) Complexes with 2-Butyl-4-Chloro-5-Formylimidazole Thiosemicarbazone. *Journal of Applied Pharmaceutical Sciences*. 2016, 107–112. <https://doi.org/10.7324/JAPS.2016.601015>.

[60] Sreenath Reddy, A.; Sivasankar Reddy, M.; Kotakadi, V. S.; Chalapathi, P. V.; Varada Reddy, A. Synthesis, Spectroscopic Characterization and Antimicrobial Activity Studies of 2-Butyl-4-Chloro-5-Formylimidazole Thiosemicarbazone and Its Manganese (II) Complex. *Journal of Applied Pharmaceutical Sciences*. 2014. <https://doi.org/10.7324/JAPS.2014.41217>.

[61] Mendum, P.; Kumari, C. G.; Ragi, R. Synthesis, Characterization, DNA Binding, DNA Cleavage and Antimicrobial Studies of Schiff Base Ligand and Its Metal Complexes. *Journal of Fluorescence* **2015**, (25) 369-378. <https://doi.org/10.1007/s10895-015-1520-6>.

[62] Sneha Jose, E.; Philip, J. E.; Shanty, A. A.; Kurup, M. R. P.; Mohanan, P. V. Novel Class of Mononuclear 2-Methoxy-4-Chromanones Ligated Cu (II), Zn (II), Ni (II) Complexes: Synthesis, Characterisation and Biological Studies. *Inorganica Chimica Acta* **2018**, (478), 155-165. <https://doi.org/10.1016/j.ica.2018.03.023>.

[63] Ishar, M.P.S.; Singh, G.; Singh, S.; Sreenivasan, K.K.; Singh, G. Design, synthesis, and evaluation of novel 6-chloro-/fluorochromone derivatives as potential topoisomerase inhibitor anticancer agents. *Bioorganic Medicinal Chemistry Letters* **2006**, 5(16), 1366-1370. <https://doi.org/10.1016/j.bmcl.2005.11.044>

[64] Barve, V.; Ahmed, F.; Adsule, S.; Banerjee, S.; Kulkarni, S.; Katiyar, P.; Anson, C. E.; Powell, A. K.; Padhye, S.; Sarkar, F. H. Synthesis, Molecular Characterization, and Biological Activity of Novel Synthetic Derivatives of Chromen-4-One in Human Cancer Cells. *Journal of Medicinal Chemistry* **2006**, 49 (13), 3800–3808. <https://doi.org/10.1021/jm051068y>.

[65] Kalanithi, M.; Kodimunthiri, D.; Rajarajan, M.; Tharmaraj, P. Synthesis, Characterization and Biological Activity of Some New VO(IV), Co(II), Ni(II), Cu(II) and Zn(II) Complexes of Chromone Based NNO Schiff Base Derived from 2-Aminothiazole. *Spectrochim. Acta Part A Mol. Biomol. Spectrosc.* **2011**, 82 (1), 290–298. <https://doi.org/10.1016/j.saa.2011.07.051>.

[66] Kalaiarasi, G.; Rajkumar, S. R. J.; Dharani, S.; Lynch, V. M.; Prabhakaran, R. Synthesis, Spectral Characterization and Biological Evaluation of Some Copper(II) Complexes Containing 4-Oxo-4H-Chromene-3-Carbaldehyde-4(N)-Substituted Thiosemicarbazones. *Inorganica Chimica Acta* **2018**, (471), 759-776. <https://doi.org/10.1016/j.ica.2017.12.008>.

[67] Arjmand, F.; Sayeed, F.; Muddassir, M. Synthesis of New Chiral Heterocyclic Schiff Base Modulated Cu(II)/Zn(II) Complexes: Their Comparative Binding Studies with CT-DNA, Mononucleotides and Cleavage Activity. *J. Photochem. Photobiol. B Biol.* **2011**, 103 (2), 166–179. <https://doi.org/10.1016/j.jphotobiol.2011.03.001>.

[68] Dziewulska-Kułaczkowska, A. Thermal and Spectral Studies of Mn(II), Co(II), Ni(II), Cu(II) and Zn(II) Complexes with 3-(Anilinomethylene)-2-Methoxychroman-4-One. *J. Therm. Anal. Calorim.* **2012**, 109 (1), 7–15. <https://doi.org/10.1007/s10973-011-1387-y>.

[69] Anitha, C.; Sheela, C. D.; Tharmaraj, P.; Johnson Raja, S. Synthesis and Characterization of VO(II), Co(II), Ni(II), Cu(II) and Zn(II) Complexes of Chromone Based Azo-Linked Schiff Base Ligand. *Spectro Chimica Acta - Part A: Molecular and Biomolecular Spectroscopy* **2012**, (98), 35–42. <https://doi.org/10.1016/j.saa.2012.08.022>.

[70] Gullino, M. L.; Tinivella, F.; Garibaldi, A.; Kemmitt, G. M.; Bacci, L.; Sheppard, B. Mancozeb: Past, Present, and Future. *Plant Disease* **2010**, 94 (9), 1076–1087. <https://doi.org/10.1094/PDIS-94-9-1076>.

[71] Kalaiarasi, G.; Rex Jeya Rajkumar, S.; Dharani, S.; Rath, N. P.; Prabhakaran, R. New Cationic and Neutral Copper(II) Complexes Containing 7-Hydroxy-4-Oxo-4[H]-Chromene Derived ONO Pincer Ligands: Synthesis, Characterization and in Vitro Biological Evaluations. *J. Photochemistry Photobiology B Biology* **2018**, 180, 77–88. <https://doi.org/10.1016/j.jphotobiol.2018.01.017>.

[72] Philip, J. E.; Shahid, M.; Prathapachandra Kurup, M. R.; Velayudhan, M. P. Metal Based Biologically Active Compounds: Design, Synthesis, DNA Binding and Antidiabetic Activity of 6-Methyl-3-Formyl Chromone Derived Hydrazones and Their Metal (II) Complexes. *J. Photochemistry Photobiology B. Biology* **2017**, (175), 178–191. <https://doi.org/10.1016/j.jphotobiol.2017.09.003>.

[73] Kasapidou, P.; Zarganes-Tzitzikas, T.; Tsoleridis, C.; Stephanidou-Stephanatou, J.; Neochoritis, C. Manipulating a Multicomponent Reaction: A Straightforward Approach to Chromenopyrazole Hybrid Scaffolds. *Synthesis (Stuttg)* **2017**, *49* (16), 3619–3632. <https://doi.org/10.1055/s-0036-1589013>.

[74] Singh, G.; Malhotra, R. Synthesis and Antimicrobial Activity of Thiosemicarbazide Induced Hydrazone of 4-Oxo-4H-Chromene-3-Carbaldehyde. In *AIP Conference Proceedings* **2017**, (1860), 020064. <https://doi.org/10.1063/1.4990363>.

[75] Al-Rashida, M.; Ashraf, M.; Hussain, B.; Nagra, S. A.; Abbas, G. Discovery of New Chromone Containing Sulfonamides as Potent Inhibitors of Bovine Cytosolic Carbonic Anhydrase. *Bioorganic Medicinal Chemistry* **2011**. <https://doi.org/10.1016/j.bmc.2011.04.040>.

[76] Korzhenko, K. S.; Osipov, D. V.; Osyanin, V. A.; Klimochkin, Y. N. Divergent Pathways for Reactions of 3-Formylchromone with Cyclic Secondary Amines in Alcoholic Media. *SynOpen* **2019**, *03* (04), 164–168. <https://doi.org/10.1055/s-0039-1690339>.

[77] Ebejer, J.-P.; Fulle, S.; Morris, G. M.; Finn, P. W. The Emerging Role of Cloud Computing in Molecular Modelling. *Journal of Molecular Graphics and Modelling* **2013**, *44*, 177–187. <https://doi.org/10.1016/j.jmgm.2013.06.002>.

[78] Chai, L. Q.; Zhang, J. Y.; Chen, L. C.; Li, Y. X.; Tang, L. J. Synthesis, Crystal Structure, Spectroscopic Properties and DFT Calculations of a New Schiff Base-Type Zinc(II) Complex. *Research on Chemical Intermediates* **2016**, *42* (4), 3473–3488. <https://doi.org/10.1007/s11164-015-2226-8>.

[79] Wang, Z. Conrad-Limpach Quinoline Synthesis. In *Comprehensive Organic Name Reactions and Reagents*; John Wiley & Sons, Inc.: Hoboken, NJ, USA, **2010**, 692–696. <https://doi.org/10.1002/9780470638859.conrr152>.

[80] Ghorai, P.; Saha, R.; Bhuiya, S.; Das, S.; Brandão, P.; Ghosh, D.; Bhaumik, T.; Bandyopadhyay, P.; Chattopadhyay, D.; Saha, A. Syntheses of Zn(II) and Cu(II) Schiff Base Complexes Using N,O Donor Schiff Base Ligand: Crystal Structure, DNA Binding, DNA Cleavage, Docking and DFT Study. *Polyhedron* **2018**, *141*, 153–163. <https://doi.org/10.1016/j.poly.2017.11.041>.

[81] Devi, S. Stereoscopic Vision, Stereoscope, Selection of Stereo Pair and Its Orientation. *International Journal of Science and Research (IJSR) ISSN (Online Impact Factor* **2012**, *3* (9), 2319–7064.

[82] Rakesh Kumar, P.; Vijaya Kumar, H.; Prasenjit, M.; Pulla Rao, Ch. Ratiometric fluorescence off-on-off sensor for Cu²⁺ in aqueous buffer by a lower rim triazole linked benzimidazole conjugate of calix[4]arene. *Dalton Transactions* **2012**, *(41)*, 10652. <https://doi.org/10.1039/c2dt30432e>.

[83] Ramesh, A.; Pawar, R.; Shyam, P.; Ramachandraiah, A. Synthesis, DFT Calculations and Biological Activity of a New Schiff Base of 4-Aminoantipyrine and Its Co(II), Ni(II), Cu(II) and Zn(II) Complexes and Crystal Structure of the Schiff Base. *Research on Chemical Intermediates* **2021**, *(47)*, 4673–4697. <https://doi.org/10.1007/s11164-021-04552-1>.

[84] Ramesh, A.; Srinivas, B.; Pawar, R.; Ramachandraiah, A. Synthesis, Characterization, Crystal Structure Determination, Computational Modelling and Biological Studies of a New Tetrakis-(2-Hydroxy-5-Methylphenyl)(1H-Pyrazol-4-Yl)Methanonezinc(II) Complex. *Journal of Molecular Structure* **2022**, *(1255)*, 132377. <https://doi.org/10.1016/j.molstruc.2022.132377>.

CHAPTER – II

MATERIALS AND METHODS

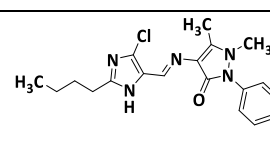
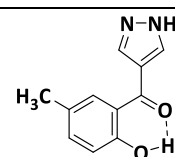
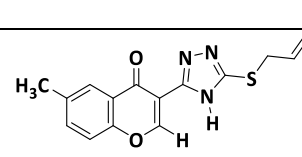
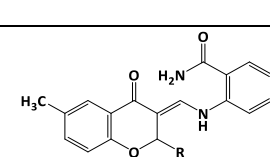
CHAPTER-II

MATERIALS AND METHODS

This Chapter, entitled, ‘**Materials and Methods**’, describes the experimental aspects such as the procedures of synthesis, purification and crystallization of the materials investigated, sampling techniques and methods of measurements involved in the instrumental analysis of the compounds, data management, computational procedures, details of biological assaying, etc., among others.

This Chapter is divided into two parts, **Part A**, **Part B**, out of which **Part A** deals with the synthesis, purification, crystallization of the chosen compounds and other wet methods of materials while **Part B** with the details of instrumental performed characterization of the compounds besides the computational chemistry procedures on the modelled compounds. **Part B** also introduces the principles, instrumentation and applications of some modern methods used during our studies.

Table 2.1 Compounds synthesized and investigated as ligands for complexation

V.	(E)-4-(((2-butyl-4-chloro-1H-imidazol-5-yl)methylene)amino)-1,5-dimethyl-2-phenyl-1,2-dihydro-3H-pyrazol-3-one (4-AAP-BCFI)	 4-AAP-BCFI
VI.	(2-hydroxy-5-methylphenyl)(1H-pyrazol-4-yl)methanone (HMPM)	 HMPM
VII.	3-(5-(allylthio)-4H-1,2,4-triazol-3-yl)-6-methyl-4H-chromen-4-one (TATMC)	 TATMC
VIII.	(E)-2-(((2-methoxy-6-methyl-4-oxochroman-3-ylidene)methyl)amino)benzamide (3FMC-2AB-R)	 3a-e $\begin{aligned} \mathbf{3a:} & R = H; \mathbf{3b:} R = O-CH_3; \\ \mathbf{3c:} & R = O-CH_2-CH_3; \mathbf{3d:} R = O-CH(CH_3)_2; \\ \mathbf{3e:} & R = O-CH_2(CH_2)_2CH_3 \end{aligned}$

PART-A

MATERIALS

2A.1 Materials and Chemicals Used in the present Study

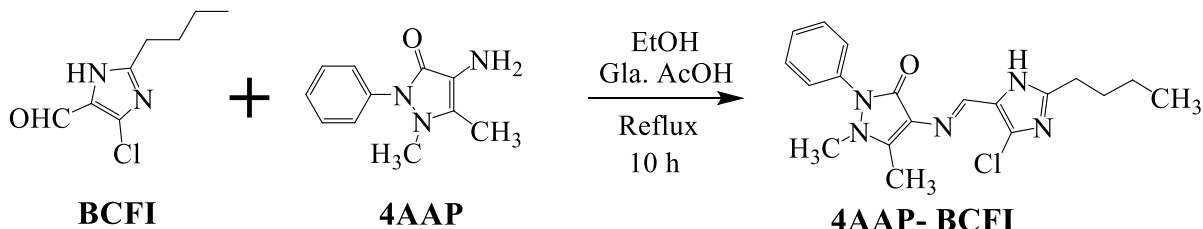
All reagents used were of analytical reagent grade and made of the commercially available one were purchased from MERCK, Sigma-Aldrich, SD Fine, Himedia, and other chemical industries. Dimethylformamide (DMF), phosphorous oxychloride, (2-hydroxy-5-methylphenyl) ethan-1-one, 4-aminoantipyrine, thiosemicarbazide, 3-formyl-6-methylchromone and 2-butyl-4-chloro-5-formylimadazole and the metal acetates and chlorides of Co(II), Ni(II), Cu(II) and Zn(II) used were of AR grade. The solvents such as methanol, ethanol, acetone, dimethylsulphoxide (DMSO) etc., used were of spectroscopic grade used without further purification.

2A.2. Preparation of the Ligands

The **4AAP-BCFI** ligand was prepared by condensation of 2-butyl-4-chloro-5-formylimadazole with 4-aminoantipyrine respectively.

2A.2.1 Preparation of (E)-4-((2-butyl-4-chloro-1H-imidazol-5-yl)methylene)amino)-1,5-dimethyl-2-phenyl-1,2-dihydro-3H-pyrazol-3-one (4AAP- BCFI)

To a 1g (5 mmole) of 4-aminoantipyrine (**4AAP**), dissolved in 20 ml of ethanol, was added 10ml of an ethanolic solution of 0.933g (5 mmole) of 2-butyl-4-chloro-5-formylimadazole (**BCFI**) in the presence of 2 drops of acetic acid while stirring. The mixture was refluxed for 10 hours before the contents of the flask were cooled to room temperature (**Scheme 2.1**) to obtain the yellow crystalline solid of **4AAP-BCFI** which was filtered, washed with ethanol and dried in air.

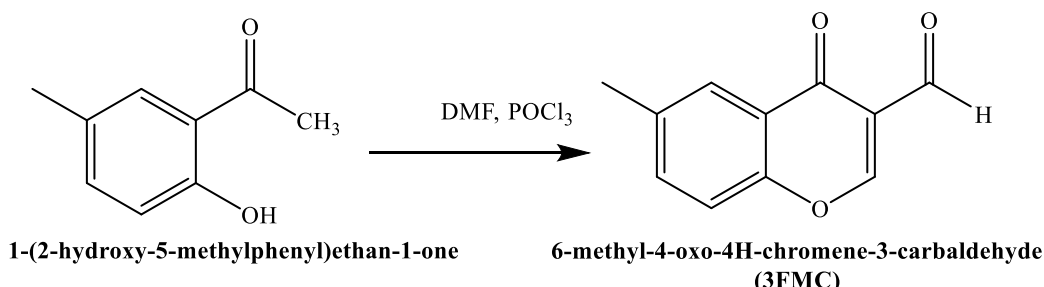


Scheme 2A.1 Schematic of the synthesis of **4-AAP-BCFI**

The **HMPM**, **TATMC** and **3FMC-2AB-R (3a-e)** ligands were prepared in two steps. In the first step 3-formyl-6-methylchromone was prepared by using Vilsmeier-Haack synthesis [1]. In the second step 3-formyl-6-methylchromone was condensed with thiosemicarbazide and 2-aminobenzamide, to get the corresponding ligands.

2A.2.2 Synthesis of 3-formyl-6-methylchromanone (3FMC)

3-formyl-6-methylchromanone was synthesized by adopting the literature method [1]. To 44 ml of dimethylformamide was added 20 ml of phosphorous oxychloride drop wise in ice cold condition and stirred the mixture for 30 min. After that, 12 ml of 2-hydroxyacetophenone was added drop wise. The reaction mixture was stirred for 2-3 h. The reaction mixture was kept to cool for overnight and then treated with ice cold water to give yellow colour solid. Upon recrystallization in ethanol light yellow colour crystalline solid was separated. The product was then dried and used. Yield: 82%, M.P: 142 °C.

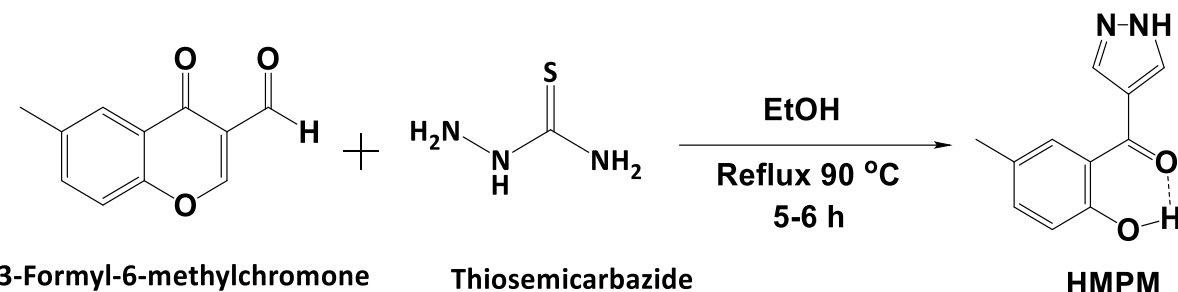


Scheme 2A.2 Synthesis of 3-formyl-6-methylchromone **3FMC**

2A.2.3 Preparation of (2-hydroxy-5-methylphenyl)(1*H*-pyrazol-4-yl)methanone (HMPM)

A low yield (47%) method for the synthesis of **HMPM** was reported elsewhere [2] by condensing 6-methyl-4-oxo-4H-chromene-3-carbaldehyde, under refluxion (15 minutes) with thiosemicarbazide in the presence of alcoholic KOH. Here, we present an alternate method with a better yield with extended time for refluxion without using any KOH.

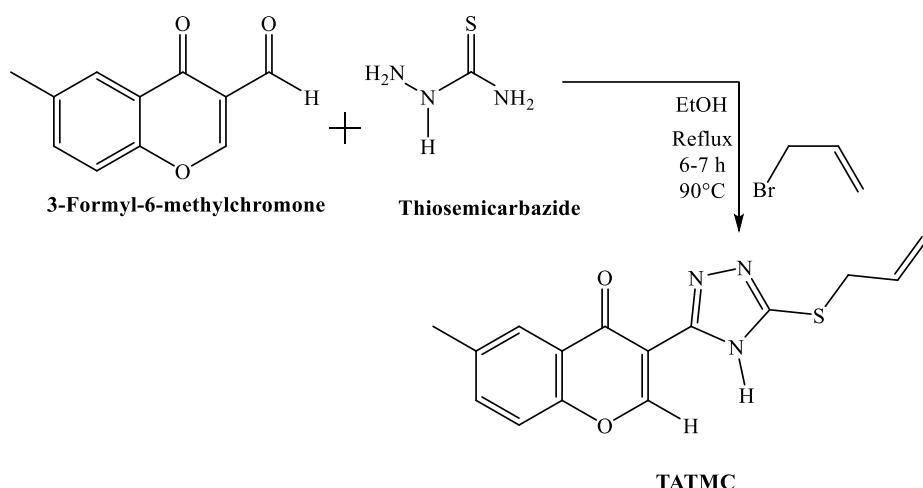
To a solution of 6-methyl-4-oxo-4H-chromene-3-carbaldehyde (0. 376 g, 2 mmole) in 20 mL of methanol, was added a solution of thiosemicarbazide (0.182 g, 2 mmole) in 10 ml of ethanol. The mixture was refluxed for 4 to 6 h. The precipitated solid, after cooling, was collected by filtration and washed with ethanol and n-hexane. The purity of the compound was monitored by TLC (**Scheme 2.3**)



Scheme 2A.3 Schematic of the preparation of **HMPM**

2A.2.4 Preparation of 3-(5-(allylthio)-4H-1,2,4-triazol-3-yl)-6-methyl-4H-chromen-4-one (TATMC)

The ligand, **TATMC** is derived from condensation of 6-methyl-3-formylchromone (2.5gr, 10 mmole) were dissolved in 25 ml hot ethanolic solution of thiosemicarbazide (1.2gr, 10 mmole) and resulting mixture was heated at 70-90 °C for about 15 min on addition of drop by drop of allyl bromide (5 ml, 1 mmole) with continuous refluxion for 6-7 h the ligand yellow solid was obtained (**Scheme 2.4**). When checked with TLC and it gave clear single spot. For better results, the reaction mixture was keep standing overnight. The needle-shaped yellow colour crystals were obtained suitable enough for an XRD analysis. The ligand was filtered off, washed with n-hexane and absolute ethanol.



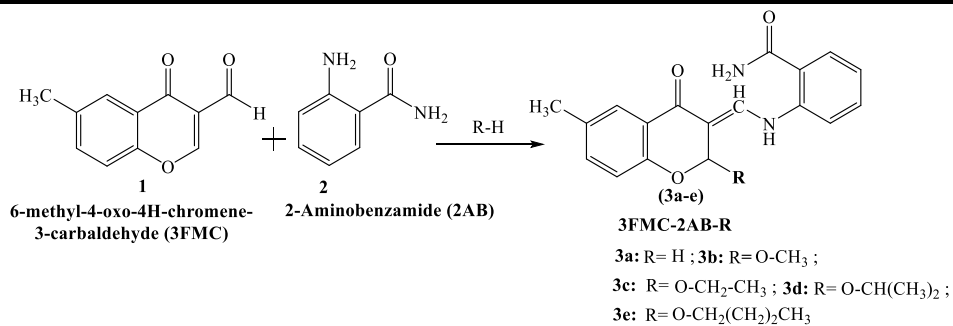
Scheme 2A.4 Schematic of the synthesis of **TATMC**

2A.2.5 Preparation of 3-formyl-6-methylchromone derivatives 3FMC-2AB-R

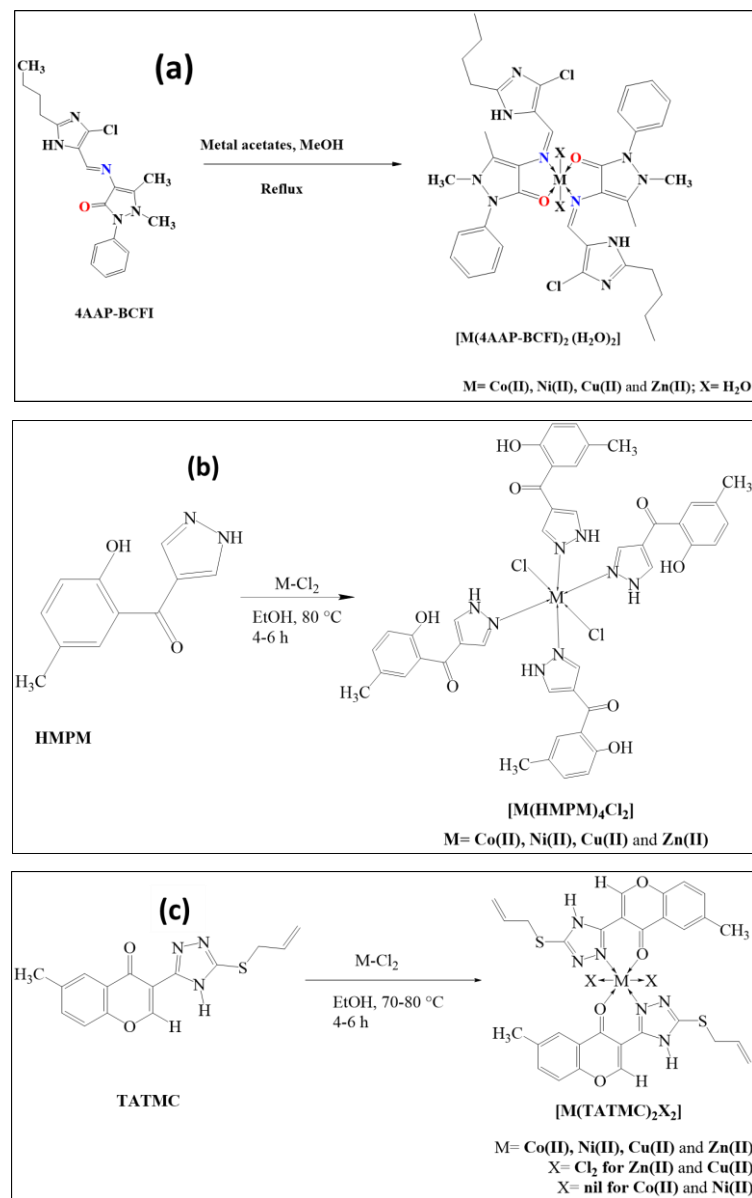
3-formyl-6-methylchromone derivatives **3FMC-2AB-R** were prepared by adding 2-aminobenzamide (1 mmole) drop wise to the 3-formyl-6-methylchromone (1 mmole) in different solvents water (a), methanol (b), ethanol (c), 2-propanol (d), and 1-butanol (e) with continuous stirring for 1 h. All the compounds (a-e) formed are yellow in colour. The products thus obtained were recrystallized from their corresponding solvents. The experimental details were given in **Scheme 2.5**.

2A.3 Preparation of Divalent Metal Complexes

The Co(II), Ni(II), Cu(II) and Zn(II) complexes were synthesized by using the respective metal acetates, while some metal salts were used as metal chlorides. In the preparation of all the metal (II) complexes the following general procedure was adopted for the ligands (**4-AAP- BCFI**), (**HMPM**) and **TATMC** as given in **Scheme 2.6**.



Scheme 2A.5 Synthesis of chromanones, 3FMC-2AB-R

Scheme 2A.6 Schematic representation of the synthesis of various complexes of (a) [M(4AAP-BCFI)₂(H₂O)₂], (b) [M(HMPM)₄Cl₂] and (c) M(TATMC)₂X₂]

To 20 ml (2 mmole) of hot methanolic solution of the ligand was added drop wise 10 ml of hot methanolic/ethanolic (1 mmole) solution of corresponding metal acetate salt of Co(II), Ni(II),

Cu(II) and Zn(II) with constant stirring. The reaction mixture was refluxed on an oil bath at 70-80 °C for about 4-6 h. After refluxing the reaction mixture gave colored solid which filtered and washed with methanol and dried in vacuum.

The recrystallized pure complexes suitable for single crystal XRD studies were obtained from their dilute solutions in test tubes, sealed with aluminum foil with one or two perforations. To avoid temperature variations, the test tubes were enclosed under a thick sheet of thermocole, which was then sealed inside a wooden chest for 3–8 days. The tubes were then removed to identify single crystals of various shapes and sizes. Through the use of a compound microscope, these crystals were sorted. For single crystal XRD studies, the best crystal was carefully chosen and washed with pure relevant solvents to get rid of any solvent residues.

The physicochemical details and characterization of the ligands and their metal complexes are presented in **Chapters, III, IV, and V**.

PART-B

METHODS

This Part covers the sampling procedures for measurements and characterization of various compounds by instrumental techniques. A brief introduction to the principles of some modern research methods that we have used is provided at the end of this part.

2B.1 The Buffers

Because the compound's spectral and electrochemical experiments were largely conducted in aqueous buffers, a series of aqueous buffer solutions with a constant ionic strength of 0.1 M and a pH range of 1.0 to 13.0 were prepared. To obtain the solution with the specified pH, the stock solutions listed in **Table 2B.1** were prepared first and then employed in various combinations according to the reported procedure.

Table 2B.1 Stock solutions for preparing the buffers

Solute	Concentration (M)
Hydrochloric Acid (HCl)	0.10
Potassium Chloride (KCl)	0.10
Sodium Chloride (NaCl)	0.10
Sodium Citrate ($\text{Na}_3\text{C}_6\text{H}_5\text{O}_7$)	0.02
Sodium Acetate	0.10
Acetic Acid (CH_3COOH)	0.10
Sodium Tetra Borate ($\text{Na}_2\text{B}_4\text{O}_7$)	0.04
Glycine ($\text{H}_2\text{NCH}_2\text{COOH}$)	0.10
Sodium Hydroxide (NaOH)	0.10

Table 2B.2 Preparation of pH buffers of range, 1.10 - 4.50

S.NO.	$\text{Na}_3\text{C}_6\text{H}_5\text{O}_7$	HCl	Capacity (ml)	pH (Calculated)	pH (Measured)
1	4.72	95.28	100	1.12	1.10
2	10.46	89.54	100	1.52	1.50
3	30.48	69.52	100	2.10	2.07
4	49.28	50.72	100	2.55	2.58
5	68.39	31.61	100	3.05	3.06
6	78.10	21.90	100	3.50	3.54
7	81.68	18.32	100	4.04	4.08
8	82.79	17.21	100	4.53	4.55

Table 2B.3 Preparation of pH buffers of range, 5.00 – 6.50

S.NO.	CH ₃ COONa	CH ₃ COOH	Capacity (ml)	p ^H (Calculated)	p ^H (Measured)
1	77.65	22.35	100	5.06	5.11
2	81.23	18.77	100	5.56	5.60
3	82.79	17.21	100	6.11	6.15
4	83.24	16.76	100	6.57	6.63

For Neutral p^H, KOH / HCl was used to pH-tune the stock KCl solution.

Table 2B.4 Preparation of pH buffers of range, 7.75 – 9.00

S.No.	Na ₂ B ₄ O ₇	HCl	Capacity (ml)	pH (Calculated)	pH (Measured)
1	12.05	87.95	100	7.74	7.77
2	18.87	81.13	100	8.05	8.11
3	38.59	61.41	100	8.58	8.62
4	55.59	44.41	100	9.07	9.12

Table 2B.5 Preparation of pH buffers of range, 9.50 – 11.00

S.No	Na ₂ B ₄ O ₇	NaOH	Capacity (ml)	pH (Calculated)	pH (Measured)
1	66.27	33.73	100	9.61	9.65
2	69.86	30.14	100	10.15	10.22
3	70.87	29.13	100	10.61	10.69
4	71.75	28.25	100	11.05	11.03

Table 2B.6 Preparation of pH buffers of range, 11.50 – 12.92

S.No.	Glycine	NaOH	Capacity (ml)	pH (Calculated)	pH (Measured)
1	0.94	99.06	100	11.64	11.71
2	0.39	99.61	100	12.15	12.22
3	0.15	99.85	100	12.54	12.59
4	0.06	99.94	100	12.96	13.00

2B.2 Sampling Methods and Instrumental Operations

A brief account of the instruments used for the characterization of the synthesized ligands and their metal (II) complexes are given below.

2B.2.1 Melting Point Determination: The melting points were determined using the Stuart SPM30 Digital Melting Point Apparatus, and the data were adjusted.

2B.2.2 Elemental Analysis: The Carlo Erba (Fisons) Instruments Model EA TCM 480 CHNS-O Elemental Analyzer has been used to evaluate the C, H, N, and S elemental analysis of the ligands and complexes.

2B.2.3 Mass Spectral Analysis: Mass spectral data of the ligands and complexes were recorded on ESI-Stove (Water synapt G2S) of high resolution mass spectrometer was used to determine electrospray ionization mass spectra (ESI-MS).

2B.2.4 Infrared Spectral Studies: The FT-IR spectra in KBr pellets were recorded using a Perkin Elmer Model Spectrum 100S Spectrophotometer in the range 4000-300 cm^{-1} .

2B.2.5 NMR Spectral Studies: The ligands and some of the soluble diamagnetic complexes were characterized using ^1H and ^{13}C NMR spectra recorded on a Bruker Advance 400 MHz NMR Spectrometer at room temperature using tetramethylsilane (TMS) as an internal reference. The ~10-12 mg/ml solutions were prepared with deuterated solvents. Several deuterated solvents were used as the locking isotope during NMR studies.

2B.2.6 ESR Spectral Studies: On the powder and solution states, EPR spectra were measured with a JEOL FA 100 X-band Spectrometer.

2B.2.7 Magnetic Susceptibility Studies: A Batington MS2 magnetometer and MS2G single frequency sample sensor were used to assess the solid state magnetic susceptibility of crystalline materials at a field of 0.1 mT. Pascal's constants were used to make diamagnetic corrections.

2B.2.8 Molar Conductance: The molar conductance of the metal complexes in 10^{-3} M DMF solution was determined using Digisun Electronics digital conductivity meter model 909.

2B.2.9 Thermal Analysis: Thermal analysis of the metal complexes were carried out on a Perkin Elmer Diamond TGA instrument at a heating rate of 10 $^{\circ}\text{C}$ and nitrogen flow rate of 20 mL/min using alumina crucible.

2B.2.10 UV-Visible Absorption Spectral Methods: In the wavelength range 200-1000 nm, the electronic spectra of all compounds were recorded on a Thermo Scientific Evolution 600 or a Perkin Elmer Lambda 25 Spectrophotometer in DMSO. The spectral variation has been used to monitor pH-metric and spectrophotometric titrations for analyzing protonation, deprotonation equilibria, and chemical kinetics.

2B.2.11 Fluorescence Emission Spectral Methods: The UV-Visible fluorescence emission spectra of all compounds were recorded on an Analytika F96pro Fluorescence Spectrophotometer in the wavelength range of 900-200 nm. With each compound, the excitation wavelength was changed.

2B.3 X-Ray Crystallographic Studies

2B.3.1 Growing Crystals: The recrystallized respective pure Schiff base compounds were dissolved in methanol (10 mg per 3ml) and the test tubes were sealed with aluminum foils with one or two

perforations. To avoid temperature variations, the test tubes were enclosed under a thick sheet of thermo coal, which was then sealed inside a wooden chest for 3-12 days. After a few weeks, the tubes were removed to identify single crystals of various shapes and sizes. Through the use of a compound microscope, these crystals were sorted. The best crystal for single crystal XRD studies was carefully chosen, cleansed with pure ether and n-hexane solvents to remove solvent residues and then air dried before, it was taken for mounting on the single crystal XRD machines.

2B.3.2 X-Ray Crystallographic Technique for an Elucidation of Structures

The experimental science of determining the arrangement of atoms in crystalline substances is known as crystallography. These techniques are used by material scientists, biologists, astronomers, and other scientists to determine the structure and other geometrical properties of crystalline materials [3]. The examination of the diffraction patterns of a sample targeted by an X-ray beam generated from an anodic material such as Cu, Mo, etc. is now used in crystallographic procedures [4]. X-rays interact with the spatial structure of crystals to produce diffraction patterns of sharp Bragg reflection spots [5], making this approach perfect for examining solid structures. In this Thesis, we discussed some Schiff base and quinoline derivative crystal structures that were used in the current research, as well as the relationship between X-ray diffraction data and molecular modeling data. **Figure 2B.1** depicts the schematic diagram of a single crystal XRD method.

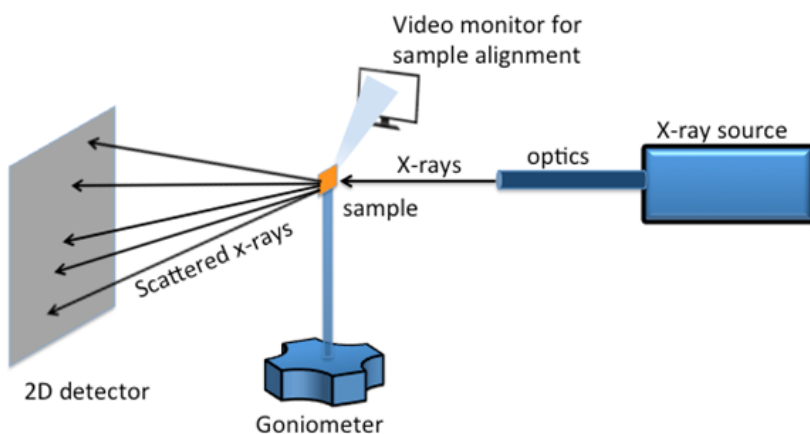


Figure 2B.1 Schematic of a single crystal X-ray diffractometer

2B.3.3 Crystallographic Data Collections

The single crystal X-ray data is collected on a Bruker-Nonius SMART APEX CCD diffractometer at 293 (2) K α using graphite-monochromated Mo K radiation ($\lambda = 0.71073$), after getting a suitable crystal for an X-ray experiment. This device is used to direct X-ray beams through a crystal, record where they diffract, and quantify the intensity of the reflection.

2B.4 Molecular Modelling

“Computational Chemistry” is the science of representing molecular structures computationally and simulating their behavior with quantum and classical physics equations [6]. Computational chemistry, often known as molecular modelling, is the simulation of chemical processes and computation of chemical characteristics employing computer-based models. The combination of two mathematical methodologies, Molecular Mechanics (MM) and Quantum Mechanics (QM), is molecular modelling. ChemOffice Ultra, HyperChem, Gaussian, Spartan, Sybyl, and other molecular modelling tools are used to calculate single point energy, geometrical optimization, and property calculations (prediction of certain physical and chemical properties like heat of formation, HOMO-LUMO, dipole moment)[7]. All methods are not capable of performing all types of calculations, and no single approach is ideal for all applications. The following is a quick overview of four major computational chemistry approaches.

2B.4.1 *Ab Initio Methods*

Quantum mechanics underlies these methods (i.e., solving the Schrodinger equation) [8]. In *Ab initio* calculations, the wave functions Hartree-Fock and Quantum Monte Carlo (QMC) are commonly used [9]. Another type of *ab initio* calculation is density functional theory, which is based on total electron density rather than wave functions [10]. It's the most promising methodology for quantum chemical calculations. For simple molecules, *ab initio* calculations produce excellent quantitative results.

The theory that all chemistry can be described in terms of interaction between electronic charges within molecules is the basis of electronic structure approaches. As a result, chemical bonding can be roughly defined as a redistribution of electrical charge that stabilizes a molecule with respect to a group of its (isolated) constituent atoms. The relative stability of a system is shown by its total energy, which is given by a differential equation.

$$\hat{H} = \hat{T} + \hat{V} \quad (2.10)$$

where \hat{H} denotes the Hamiltonian operator that sums the kinetic (\hat{T}) and potential (\hat{V}) energies. The kinetic energy of a particle in quantum mechanical systems is

$$\hat{T} = \frac{-\hbar^2}{2m} \nabla^2 \quad (2.11)$$

where m is the mass of the particle, \hbar is the Plank constant and

$$\nabla^2 = \frac{\partial^2}{\partial x^2} + \frac{\partial^2}{\partial y^2} + \frac{\partial^2}{\partial z^2} \quad (2.12)$$

The potential energy of electrostatic systems is commonly described as the pairwise interaction between charged particles.

$$\hat{V} = \frac{q_1 q_2}{4\pi\epsilon_0} \frac{1}{|r_1 - r_2|} \quad (2.13)$$

where ϵ_0 permittivity of free space and $|r_1 - r_2|$ is the distance between the charges q_1 and q_2 .

The Schrödinger equation cannot be solved exactly for systems with more than two interacting particles. As a result, all ab initio calculations for many-body systems (e.g., molecules) involve a variety of approximations. However, ab initio methods for molecular calculations must meet a number of specific requirements:

- Both the structure and electronic states of the molecule must be well defined and specified in order for solutions to be very well defined and specified.
- With respect to atomic nuclei displacements, the molecule's potential energy must vary smoothly and continuously.
- The model can't be skewed in any way, like by assuming that there is a chemical bond between two atoms.
- The model must be "size-consistent," implying that the solutions and errors must scale in proportion to the molecule's size.

The model must be "variation," which means that approximate solutions must put an upper bound on the system's "actual" energy. So, within the limits of the method, the closest fit to the real wave function is the approximate solution with the lowest energy.

2B.4.2 Semi-Empirical Methods

Ab-initio approaches are substantially slower than semi-empirical methods. These calculations involve a number of approximations and constraints, including the use of experimental data [11]. Various semi-empirical approaches are optimized according to necessity. The NDDO, MNDO, AM1, and PM3 methods are some of the approaches used to reproduce the formation temperatures and structures of massive organic compounds [12]. Some methods, like ZINDO/S, are made to predict electronic transitions in the UV/VIS range [13].

In semi-empirical calculations, the basis sets are specifically optimized minimal basis sets made up of slater-type orbitals. Hartree-Fock theory uses a simple point charge model to figure out the energy of nuclear repulsion. However, this model is not good enough for semi-empirical calculations because it only takes into account valence electrons and treats core electrons and nuclei as one effective core potential. The core-core potential employed in NDDO methods extends further the use of simple point charge modelling with lowered nuclear charges to account for some of the approximations employed in computing the attractive core-electron energies.

$$E_{AB} = Z'_A Z'_B e^{2/R_{AB}} \quad (2.14)$$

R_{AB} represents the inter-nuclear separation, while Z'_A represents the effective core charge, which includes the nuclear charge as well as all core electrons. In NDDO methods, a general equation for figuring out the energy of core-core repulsion between nuclei A and B at a distance of R_{AB} is:

$$E_{AB} = Z'_A Z'_B \langle S_A S_A, S_B S_B \rangle [1 + F(A) + F(B)] \quad (2.15)$$

The core repulsion energy is a result of both the electron-electron repulsion integral $S_A S_A$ and $S_B S_B$ atom-type dependent functions $F(A)$ and $F(B)$, both of which are dependent on the inter-nuclear spacing R_{AB} . In MNDO, the functions $F(A)$ and $F(B)$ have a relatively simple form:

$$F_A = \exp(-\alpha_A R_{AB}) \quad (2.16)$$

Some of MNDO's flaws, especially those that had to do with hydrogen bonds, were fixed by giving AM1 a slightly more complex function:

$$F_A = \exp(-\alpha_A R_{AB}) + \sum K_{Ai} \exp[L_{Ai}(R_{AB} - M_{Ai})^2] \quad (2.17)$$

The sum over supplementary exponential functions includes three or four components and provides three new parameters for each element, K_{Ai} , L_{Ai} , and M_{Ai} , which are the main differences between AM1 and MNDO (aside from the actual appropriate technique).

2B.4.3 Molecular Mechanics (MM) Method

Within those molecular mechanics (MM) calculations, Newtonian mechanics (classical physics) is used to predict the structures and properties of molecules. In this approach, nuclei are considered as spheres, and connected bonds are treated as springs. These MM techniques can be used to simulate biomolecules like DNA or proteins [14].

The potential energy (E) of a molecular system in a particular conformation is calculated as a sum of individual energy terms using the following functional approximation, known as an interatomic state equations or force field in chemistry.

$$E = E_{Covalent} + E_{Noncovalent} \quad (2.18)$$

where the following summations derive the portions of the covalent and non - covalent interaction contributions:

$$E_{Covalent} = E_{Bond} + E_{Angle} + E_{Dihedral} \quad (2.19)$$

$$E_{Noncovalent} = E_{Electrostatic} + E_{Van\ der\ Waals} \quad (2.20)$$

2B.4.4 Molecular Dynamics (MD)

To mimic the time-dependent behavior of molecules, molecular dynamics simulations are used [15]. The MD method is used to investigate how a solute molecule diffuses across a liquid. This method can be applied to computations involving big biomolecules in solutions [16].

Where the following summations derive the portions of the covalent and non-covalent interaction contributions: The variation of a set of interacting particles is quantified in MD simulations using the solution of Newton's equations of motion, eqn 2.21, wherein $r_i(t) = (x_i(t), y_i(t), z_i(t))$ is the position vector of the i^{th} particle, F_i is the force acting on the i^{th} particle at time t , and m_i is the particle's mass.

$$F_i = m_i \frac{d^2 r_i(t)}{dt^2} \quad (2.21)$$

The simultaneous forces acting on the particles, as well as their initial locations and velocities, must be provided in order to incorporate the above second-order partial differential equation. The differential equations are normalized and solved numerically due to the many nature of the case. MD trajectories reflect the time system dynamics in phase space and are described by both position and velocity vectors. As a result, numerical integrators, such as the Verlet method, are used to propagate the locations and velocities over a finite time interval. $r_i(t)$ determines the (changing over time) position of each particle in space, whereas $v_i(t)$ determines the kinetic energy and temperature in the system.

The objective of numerical integration of Newton's equations of motion is to discover an expression that specifies locations $r_i(t + \Delta t)$ at time $t + \Delta t$ in terms of positions known at time t . The Verlet algorithm is widely utilized in MD simulations due to its simplicity and stability. The essential formula for this technique is eqn 2.22, which is obtained from the Taylor expansion for the positions $r_i(t)$.

$$r_i(t + \Delta t) \cong 2r_i(t) - r_i(t - \Delta t) + \frac{F_i(t)}{m_i} \Delta t^2 \quad (2.22)$$

2B.4.5 Data Processing, 2D and 3D Graphical Presentation

MS EXCEL was routinely used for initial data processing and curve fitting. Origin was used for drawing plots. GoldenSoft's Surfer (version 12) and Grapher (version 10) were extremely used for gridding, surfaces and wireframe mesh 3D plots of data of the $z = f(x, y)$ kind where z is the domain of the acquired data for the x and y binary conditions or variables [25].

The Surfer can generate a 'z' data set for any mathematical function, $z = f(x, y)$, where 'x' and 'y' form sets of real numbers within any range that never makes the value of 'z' undefined.

The graphical forms, in 'wire frame' format from Surfer and in 'surface mat' format from Grapher platforms for the equation, $z = x^2 - y^2 + xy$, are shown in **Figure 2B.2**. It may be noted that Grapher has MOE versatile features to manipulate with the presentation and appearances of the plots.

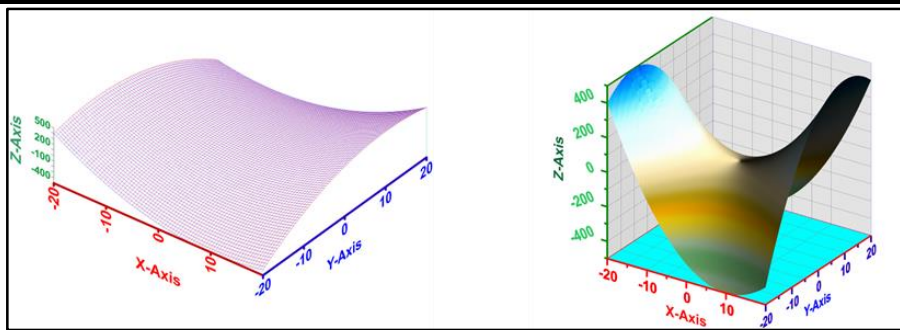


Figure 2B.2 The 3D Surfer plot (left) and Grapher plot (right) for the equation, $z = x^2 - y^2 + xy$, for the range of $-20 < x < 20$ and $-20 < y < 20$ with a gridding increment of 0.5 on each of x and y domains

2B.5 Hirshfeld Surface Analysis

Hirshfeld surface analysis is an effective method for visualizing molecular crystal interactions [17]. Crystal Explorer 17.5 is a computer application that calculates intermolecular interactions between single molecules or for the complete crystal structure [18]. The expansion of the weight function characterizing an atom in a molecule to include the function of a molecule in a crystal results in the formation of Hirshfeld surfaces [19]. The iso surface produced from these calculations, with a predetermined weight function $w(r) = 0.5$, defines the space occupied by a molecule in a crystal by dividing the electron density of the fragments [20]. Hirshfeld surfaces can disclose information on intermolecular interactions in a crystal due to the fact that the surface is determined by both the confined molecule and its nearest neighbors.

The fused sphere van der Waals and smoothed Connolly surfaces, which are used to view and quantify molecular geometries, lack this benefit because they are set only by the molecule itself. To extract accurate information on intermolecular interactions from Hirshfeld surfaces, the crystal structures that are entered into the computer must be well-characterized, with all hydrogen atoms correctly identified or organized. In crystal space, the HS is the region that separates the inner reference molecule from the outer surrounding molecules [21]. By isolating space, the HS permits the study of fingerprint intermolecular interactions in a crystalline environment. HS analysis can be used to visualize and quantify non-covalent interactions that contribute to the stability of crystal packing [22]. It is possible to map dnorm, electrostatic potential, shape index, and curvature to HS. The dnorm property is a symmetric function of nuclei's surface distances (d_i and d_e) relative to their van der Waals radii. The red and blue colored regions on the d_{norm} represent shorter and longer inter contacts, respectively, whereas the white colored regions represent contacts around the van der Waals radii [23]. Two-dimensional fingerprint plots in the crystal provide useful information on intermolecular contacts. The use of HS analysis to describe the nature of intermolecular interactions that affect the

packing of molecules in crystals has shown to be very effective. Polymorphism, crystallization, the presence of small molecules in the cavities of macromolecules, and the search for correlations between the strength of interactions and the melting point are all investigated using Hirshfeld surfaces analysis [24].

The Hirshfeld surface is a smooth, continuously differentiable 3D manifold, and the two principal curvatures of the surface. In connection with the distances between the surface and atomic nuclei inside and outside the surface, these can be utilized to define a variety of valuable surface properties at every point.

2B.6 Biological Screening Methods

2B.6.1 Antibacterial Screening

Two gram negative bacteria, *Pseudomonas aeruginosa* and *Escherichia coli*, and two gram positive bacteria *Bacillus cereus* and *Bacillus subtilis*, were employed in this study. For bacterial, the reference drug streptomycin was used. The MIC values of the investigated compounds and reference drugs were measured in μM .

2B.6.2 Anti-diabetic Activity by *in vitro* α -Amylase Assay Method

The compounds were assessed for their anti-diabetic potency by evaluating α -amylase enzyme activity inhibition by modified method of Philip *et al* [26] using glucose as control.

The percentage of inhibition values of the investigated compounds and reference drugs were measured in $\mu\text{g}/\text{ml}$. The substances were tested in triplicate, and the standard deviation was computed.

2B.6.3 Antioxidant Screening

The antioxidant activity of the synthesized compounds has attracted people's interest, and it's been tested predominantly *in vitro* systems. The antioxidant activity of the ligand and its metal complexes was investigated using the DPPH (2,2-diphenylpicryl hydrazyl) radical as a reagent in a spectrophotometric test. The antioxidant ascorbic acid is used as a standard. The substances were tested in triplicate, and the standard deviation was computed.

2B.7 Molecular Protein Docking Interactions

The goal of molecular docking approaches is to predict a ligand's optimal binding mode to a macromolecular partner (in this case, only proteins are examined) [27]. This involves the generation of a number of alternative ligand conformations/orientations, or poses, within the protein binding site. Consequently, the presence of the molecule target's three-dimensional structure is required; this structure can be experimentally solved (through X-ray crystallography or nuclear magnetic resonance, for example) or created by computational approaches. pdbqt files for protein and ligand preparation

and grid boxes (ADT) were created using the graphical user interface application AutoDock Tools [28]. ADT [29] provided the protein with polar hydrogens, Kollman charges, solvation parameters, and fragment volumes. AutoDock has saved the prepared file as a PDBQT file. Using a grid box, AutoGrid was utilized to produce a grid map. To save computation time, a score grid is computed utilizing the structure of the ligand [30]. AutoDock/Vina was docked using the protein and ligand information as well as the grid box properties in the configuration file. AutoDock-Vina and Schrodinger software employ iterative local search global optimizer [31]. During the docking step, both the protein and ligands are considered as rigid molecules. The results with a positional root-mean-square deviation (RMSD) of less than 1.0 were pooled and represented by the outcome with the lowest binding free energy. The conformation with the lowest binding energy or binding affinity was retrieved and aligned with the receptor structure for further study. RadC receptor (PDBID: 2QLC) belongs to the RadC receptor family of DNA repair proteins.

Utilizing AutoDock-Vina and Schrodinger [32] software, docking calculations were performed. Using AutoDockTools 1.5.6, water molecules are eliminated, polar hydrogens are added, and Kollman and Gasteiger partial charges are assigned to the ligand. The application AutoGrid was used to generate affinity maps with 606060 grid points and a spacing of 0.575. To comprehend the 2D structure and investigate the mechanism of binding interactions, the discovery studio visualizer software was applied.

References

[1] Khan, K. M.; Ambreen, N.; Mughal, U. R.; Jalil, S.; Perveen, S.; Choudhary, M. I. 3-Formylchromones: Potential Antiinflammatory Agents. *European Journal of Medicinal Chemistry* **2010**, 45 (9), 4058–4064. <https://doi.org/10.1016/j.ejmech.2010.05.065>.

[2] Joshi, N.S.; Karale, B.K.; Jagtap, A.P.; Shinde, S.M.; bhirud, S.B.; Gill C.H. Synthesis And Characterization of Some Heterocyclic Organo Phosphorus Compounds. *Indian Journal of Heterocyclic Chemistry* **2003**, (13), 151-154.

[3] Li, J.; Sun, J. Application of X-Ray Diffraction and Electron Crystallography for Solving Complex Structure Problems. *Accounts of Chemical Research* **2017**, 50 (11), 2737–2745. <https://doi.org/10.1021/acs.accounts.7b00366>.

[4] Hendrickson, W. A. Anomalous Diffraction in Crystallographic Phase Evaluation. *Quarterly Reviews of Biophysics* **2014**, 47 (1), 49–93. <https://doi.org/10.1017/S0033583514000018>.

[5] Petkov, V. Nanostructure by High-Energy X-Ray Diffraction. *Materials Today* **2008**, 11 (11), 28–38. [https://doi.org/10.1016/S1369-7021\(08\)70236-0](https://doi.org/10.1016/S1369-7021(08)70236-0).

[6] Genheden, S.; Reymer, A.; Saenz-Méndez, P.; Eriksson, L. A. Chapter 1. Computational Chemistry and Molecular Modelling Basics; **2017**; pp 1–38. <https://doi.org/10.1039/9781788010139-00001>.

[7] Pimentel, A. S.; Guimarães, C. R. W.; Miller, Y. Molecular Modeling: Advancements and Applications. *Journal of Chemistry* **2013**, 2013 (001), 1–2. <https://doi.org/10.1155/2013/875478>.

[8] Defranceschi, M.; Le Bris, C. Mathematical Models and Methods for Ab Initio Quantum Chemistry; Lecture Notes in Chemistry; Springer Berlin Heidelberg: Berlin, Heidelberg, 2000; Vol. 74. <https://doi.org/10.1007/978-3-642-57237-1>.

[9] Bickmore, B. R.; Wander, M. C. F. Encyclopedia of Geochemistry; White, W. M., Ed.; Encyclopedia of Earth Sciences Series; Springer International Publishing: Cham, **2018**. <https://doi.org/10.1007/978-3-319-39312-4>.

[10] Grabowski, I.; Teale, A. M.; Śmiga, S.; Bartlett, R. J. Comparing Ab Initio Density-Functional and Wave Function Theories: The Impact of Correlation on the Electronic Density and the Role of the Correlation Potential. *The Journal of Chemical Physics* **2011**, 135 (11), 114111. <https://doi.org/10.1063/1.3636114>.

[11] (a) Lewars, E. G. Semiempirical Calculations. In Computational Chemistry; Springer Netherlands: Dordrecht, **2011**; pp 391–444. https://doi.org/10.1007/978-90-481-3862-3_6; (b) Stewart, J. J. P. Optimization of Parameters for Semiempirical Methods VI: More Modifications to the NDDO Approximations and Re-Optimization of Parameters. *Journal of Molecular Modeling* **2013**, 19 (1), 1–32. <https://doi.org/10.1007/s00894-012-1667-x>.

[12] Hofmann, M.; Schaefer, H. F. Computational Chemistry. In *Encyclopedia of Phys. Science and Technology*; Elsevier, **2003**; pp 487–506. <https://doi.org/10.1016/B0-12-227410-5/00129-0>.

[13] Anouar, E. H.; Osman, C. P.; Weber, J. F.; Ismail, N. H. UV/Visible Spectra of a Series of Natural and Synthesised Anthraquinones: Experimental and Quantum Chemical Approaches. *SpringerPlus* **2014**, 3 (1), 233. <https://doi.org/10.1186/2193-1801-3-233>.

[14] Van der Kamp, M. W.; Shaw, K. E.; Woods, C. J.; Mulholland, A. J. Biomolecular Simulation and Modelling: Status, Progress and Prospects. *Journal of The Royal Society Interface* **2008**, 5 (suppl_3), 173–190. <https://doi.org/10.1098/rsif.2008.0105.focus>.

[15] Adcock, S. A.; McCammon, J. A. Molecular Dynamics: Survey of Methods for Simulating the Activity of Proteins. *Chemical Reviews* 2006, 106 (5), 1589–1615. <https://doi.org/10.1021/cr040426m>.

[16] Durrant, J. D.; McCammon, J. A. Molecular Dynamics Simulations and Drug Discovery. *BMC Biology* **2011**, 9 (1), 71. <https://doi.org/10.1186/1741-7007-9-71>.

[17] Batsanov, A. S. X-Ray Diffraction, Small Molecule Applications ☆. In *Encyclopedia of Spectroscopy and Spectrometry*; Elsevier, 2017; pp 656–666. <https://doi.org/10.1016/B978-0-12-409547-2.11370-8>.

[18] Price, S. (Sally) L. Quantifying Intermolecular Interactions and Their Use in Computational Crystal Structure Prediction. *Crystal Engeeniring Communication* **2004**, 6 (61), 344. <https://doi.org/10.1039/b406598k>.

[19] Barbour, L. J. Single-Crystal X-Ray Diffraction. In *Comprehensive Supramolecular Chemistry II*; Elsevier, 2017; Vol. 2, pp 23–43. <https://doi.org/10.1016/B978-0-12-409547-2.12493-X>.

[20] Jelsch, C.; Ejsmont, K.; Huder, L. The Enrichment Ratio of Atomic Contacts in Crystals, an Indicator Derived from the Hirshfeld Surface Analysis. *IUCrJ* **2014**, 1 (2), 119–128. <https://doi.org/10.1107/S2052252514003327>.

[21] Tojiboev, A.; Zhurakulov, S.; Englert, U.; Wang, R.; Kalf, I.; Vinogradova, V.; Turgunov, K.; Tashkhodjaev, B. Hirshfeld Surface Analysis and Energy Framework for Crystals of Quinazoline Methylidene Bridged Compounds. *Proceedings* **2020**, 62 (1), 1. <https://doi.org/10.3390/proceedings2020062001>

[22] Pook, N.-P. Supramolecular Architecture in a Ni(II) Complex with a Weakly Bonded N,N'-(1,4-Phenylenedi- Carbonyl)Diglycinate Counter-Anion: Crystal Structure Investigation and Hirshfeld Surface Analysis. *Crystals* **2019**, 9 (12), 615. <https://doi.org/10.3390/crust9120615>.

[23] Balić, T.; Perdih, F.; Počkaj, M.; Molnar, M.; Komar, M.; Balić, I. Polymorphism of Coumarin Thione-Triazole-4-Methyl-7-[(4-Phenyl-5-Thioxo-4,5-Dihydro-1H-1,2,4-Triazol-3-Yl)Methoxy]-2H-Chromen-2-One. *Journal of Molecular Structure* **2021**, 1231, 129957. <https://doi.org/10.1016/j.molstruc.2021.129957>.

[24] Turner, M. J.; Grabowsky, S.; Jayatilaka, D.; Spackman, M. A. Accurate and Efficient Model Energies for Exploring Intermolecular Interactions in Molecular Crystals. *The Journal of Physical Chemistry Letters* **2014**, 5 (24), 4249–4255. <https://doi.org/10.1021/jz502271c>.

[25] Urszula Litwin, Jacek M. Pijanowski, A. S.; Zygmunt, M. Application of Surfer Software in Densification of Digital Terrain Model (DTM) Grid with The Use. **2013**, No. 1, 51–61.

[26] Philip, J. E.; Shahid, M.; Prathapachandra Kurup, M. R.; Velayudhan, M. P. Metal Based Biologically Active Compounds: Design, Synthesis, DNA Binding and Antidiabetic Activity of 6-Methyl-3-Formyl Chromone Derived Hydrazones and Their Metal (II) Complexes. *Journal of Photochemistry Photobiology Biology* **2017**, 175, 178–191. <https://doi.org/10.1016/j.jphotobiol.2017.09.003>.

- [27] Meng, X.-Y.; Zhang, H.-X.; Mezei, M.; Cui, M. Molecular Docking: A Powerful Approach for Structure-Based Drug Discovery. *Current Computer Aided-Drug Design* **2011**, 7 (2), 146–157. <https://doi.org/10.2174/157340911795677602>
- [28] Forli, S.; Huey, R.; Pique, M. E.; Sanner, M. F.; Goodsell, D. S.; Olson, A. J. Computational Protein–Ligand Docking and Virtual Drug Screening with the AutoDock Suite. *Nature Protocols* **2016**, 11 (5), 905–919. <https://doi.org/10.1038/nprot.2016.051>.
- [29] Sivaramakrishnan, M.; Kandaswamy, K.; Natesan, S.; Devarajan, R. D.; Ramakrishnan, S. G.; Kothandan, R. Molecular Docking and Dynamics Studies on Plasmepsin V of Malarial Parasite Plasmodium Vivax. *Informatics in Medicine Unlocked* **2020**, 19, 100331. <https://doi.org/10.1016/j.imu.2020.100331>.
- [30] Feinstein, W. P.; Brylinski, M. Calculating an Optimal Box Size for Ligand Docking and Virtual Screening against Experimental and Predicted Binding Pockets. *Journal of Cheminformatics* **2015**, 7 (1), 18. <https://doi.org/10.1186/s13321-015-0067-5>.
- [31] Valdés-Tresanco, M. S.; Valdés-Tresanco, M. E.; Valiente, P. A.; Moreno, E. AMDock: A Versatile Graphical Tool for Assisting Molecular Docking with Autodock Vina and Autodock4. *Biology Direct* **2020**, 15 (1), 12. <https://doi.org/10.1186/s13062-020-00267-2>.
- [32] O’Boyle, N. M.; Banck, M.; James, C. A.; Morley, C.; Vandermeersch, T.; Hutchison, G. R. Open Babel: An Open Chemical Toolbox. *Journal of Cheminformatics* **2011**, 3 (1), 33. <https://doi.org/10.1186/1758-2946-3-33>.

CHAPTER – III

SYNTHESIS AND SPECTRAL, SINGLE CRYSTAL XRD, DFT- COMPUTATIONAL AND BIOLOGICAL ACTIVITY STUDIES OF A NEW SCHIFF BASE OF 4-AMINOANTIPYRINE AND INVESTIGATIONS OF ITS Co(II), Ni(II), Cu(II) AND Zn(II) COMPLEXES

CHAPTER-III

SYNTHESIS AND SPECTRAL, SINGLE CRYSTAL XRD, DFT-COMPUTATIONAL AND BIOLOGICAL ACTIVITY STUDIES OF A NEW SCHIFF BASE OF 4-AMINOANTIPYRINE AND INVESTIGATIONS OF ITS Co(II), Ni(II), Cu(II) AND Zn(II) COMPLEXES

In this Chapter, the studies of Schiff base, **4AAP-BCFI** synthesized from 4-aminoantipyrine and 2-butyl-4-chloro-5-formylimadazole along with those of its complexes of some bidentate metal ions such as Co(II), Ni(II) Cu(II) and Zn(II) are presented. The ligand and the complexes have been characterized by various analytical and spectroscopic methods. The studies propose the formation $[M(4AAP-BCFI)_2(H_2O)_2]$ type complex for all where **M** = **Co(II)**, **Ni(II)** **Cu(II)** and **Zn(II)** ions. Biological activity have been done for both ligand, **4AAP-BCFI** and its $[M(4AAP-BCFI)_2(H_2O)_2]$ complexes along with molecular modelling and molecular docking studies.

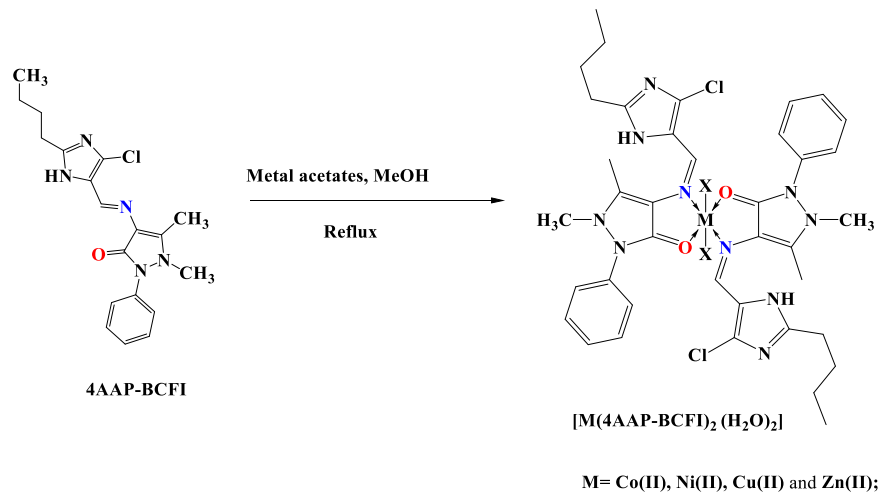
This Chapter is divided into three parts, **PART A**, **PART B**, and **PART C**. **PART A** describes in detail the physical, analytical, spectroscopic, and coordination chemistry studies of **4AAP-BCFI** and its metal complexes. **PART B** covers the single crystal X-ray analysis of **4AAP-BCFI** ligand and its metal complexes followed by correlation between empirical and molecular modelling DFT data. **PART C** describes the biological activity and protein-ligand interaction and molecular docking studies of **4AAP-BCFI** ligand and its metal complexes.

PART-A

SPECTRAL, PHYSICOCHEMICAL AND COORDINATION CHEMISTRY STUDIES OF 4AAP-BCFI

3A.1 Physical and Elemental Analysis

The physical and analytical characteristics of the **4AAP-BCFI** ligand and its metal complexes are shown in **Table 3A.1**. The data are commensurate with the chemical structures shown in **Scheme 3A.1**.



Scheme 3A.1 Schematic of the synthesis of $[M(4AAP-BCFI)_2(H_2O)_2]$ from **4AAP-BCFI**

Table 3A.1 Analytical data of **4AAP-BCFI** and its metal complexes

Compound [#]	Colour	M.P °C	Mol. Formula	Elemental Analysis % found (calculated)				
				C	H	N	M	Cl
4AAP-BCFI	White	189	$C_{19}H_{22}ClN_5O$	61.37 (61.36)	5.96 (5.94)	18.83 (18.83)	- -	9.53 (9.50)
$[Co(L)_2(H_2O)_2]$	Orange	265	$C_{38}H_{48}Cl_2N_{10}CoO_4$	54.42 (54.37)	5.77 (5.80)	16.70 (16.69)	7.03 (6.98)	8.45 (8.40)
$[Ni(L)_2(H_2O)_2]$	Green	259	$C_{38}H_{48}Cl_2N_{10}NiO_4$	54.44 (54.41)	5.77 (5.73)	16.71 (16.68)	7.00 (6.97)	8.46 (8.44)
$[Cu(L)_2(H_2O)_2]$	Brown	293	$C_{38}H_{48}Cl_2N_{10}CuO_4$	54.12 (54.11)	5.74 (5.72)	16.61 (16.60)	7.54 (7.51)	8.41 (8.37)
$[Zn(L)_2(H_2O)_2]$	Cream white	280	$C_{38}H_{48}Cl_2N_{10}ZnO_4$	54.00 (54.00)	5.72 (5.70)	16.57 (16.55)	7.74 (7.72)	8.39 (8.35)

[#] L=4AAP-BCFI

3A.2 Mass Spectral Analysis

The electrospray ionization mass spectra (MS-ESI⁺) of ligand and its complexes **4AAP-BCFI**, **[Co(L)₂(H₂O)₂]** **[Ni(L)₂(H₂O)₂]**, **[Cu(L)₂(H₂O)₂]** and **[Zn(L)₂(H₂O)₂]** have given the ion peak consistent with their formula shown in **Scheme 3A.1** representative spectra presented in **Figures 3A.1-3A.2**. The mass spectral data of ligand and its metal complexes are listed in **Table 3A.2**.

Table 3A.2 Mass spectral data of **4AAP-BCFI** and its metal complexes

S.No.	Compound	Calculated mass	Obtained mass	Peak assigned
1	4AAP-BCFI	371.86	372	[M] ⁺
2	[Co (L)₂(H₂O)₂]	836.26	837	[M+1]
3	[Ni (L)₂(H₂O)₂]	837.26	837	[M] ⁺
4	[Cu (L)₂(H₂O)₂]	841.25	843	[M+2]
5	[Zn (L)₂(H₂O)₂]	842.25	845	[M+3H]

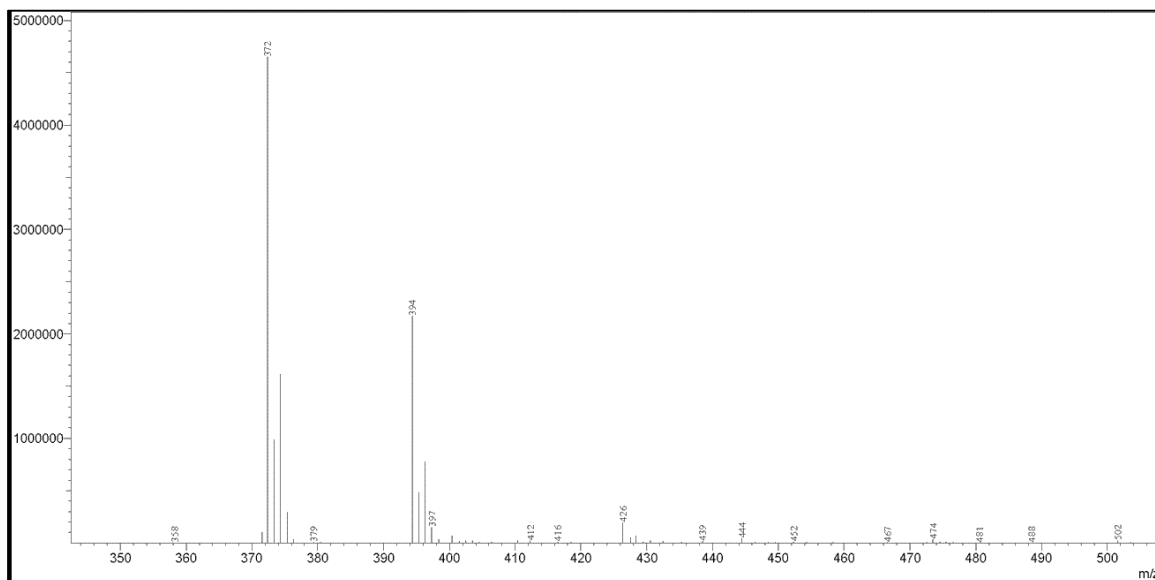


Figure 3A.1 Mass spectrum of **4AAP-BCFI**

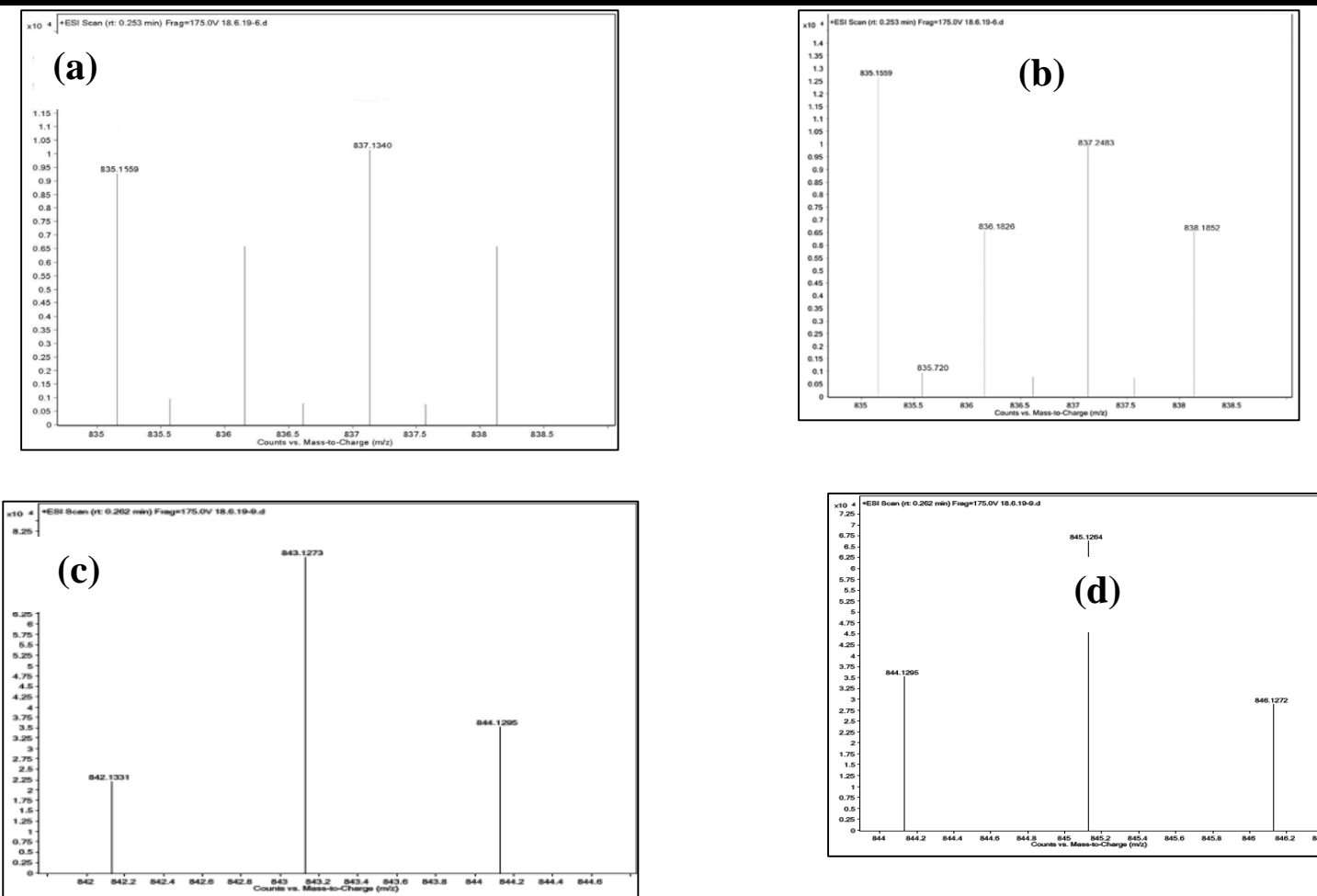


Figure 3A.2 Mass spectra of (a) Co(II), (b) Ni(II), (c) Cu(II) and (d) Zn(II) complexes of **4AAP-BCFI**

3A.3 FT-IR Spectral Studies

The FTIR spectra of the prepared complexes were compared with those of a free ligand in order to determine the coordination site involved in chelation. The important infrared spectral data of **4AAP-BCFI** and its metal complexes are listed in **Table 3A.3**. The FTIR frequencies, $\nu(\text{C=O})$ and $\nu(\text{C=N})$ (azomethine) observed at 1642 cm^{-1} and 1603 cm^{-1} of the free ligand show a downward shift in every complex, tentatively suggesting that **4AAP-BCFI** binds to metal ions as a bidentate ligand through O and N atoms [1]. The broad bands of metal complexes in the range $3450\text{-}3300 \text{ cm}^{-1}$ and then the other band $830\text{-}865 \text{ cm}^{-1}$ indicate the presence of coordinated water molecules in the metal complexes [38-39]. The participation of oxygen and nitrogen atoms in coordination is additionally confirmed by IR bands in the range $700\text{-}500 \text{ cm}^{-1}$ corresponding to $\nu(\text{M-O})$ and $\nu(\text{M-N})$ stretching frequencies. A notable point from the IR spectra of all metal complexes is the unchanged position of the $\nu(\text{N-H})$ imidazole group at 3100 cm^{-1} of free ligand band. It indicates the non-participation of the imidazole group in the complex formation [2]. Representative FTIR spectra are shown in **Figures 3A.3–3A.4**.

Table 3A.3 Some selected IR spectral data of **4AAP-BCFI** and its metal complexes (in cm^{-1})

Compound [#]	$\nu(\text{C=O})$ (Antipyrine)	ν (C=N)	$\nu(\text{O-H})$	$\nu(\text{N-H})$ (Imidazole)	$\nu(\text{M-N})$	$\nu(\text{M-O})$
4AAP-BCFI	1642	1603	---	2930	---	---
[Co(L)₂(H₂O)₂]	1616	1564	3406, 841	2928	584	641
[Ni(L)₂(H₂O)₂]	1618	1568	3421, 846	2928	577	647
[Cu(L)₂(H₂O)₂]	1644	1592	3421, 860	2930	564	668
[Zn(L)₂(H₂O)₂]	1636	1592	3377, 858	2929	598	633

[#] L = **4AAP-BCFI**

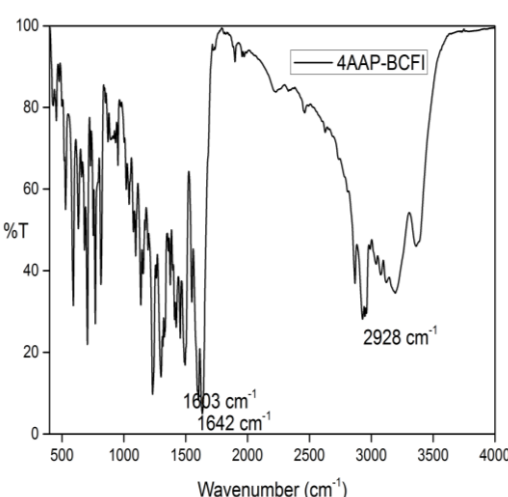


Figure 3A.3 FTIR spectrum of **4AAP-BCFI**

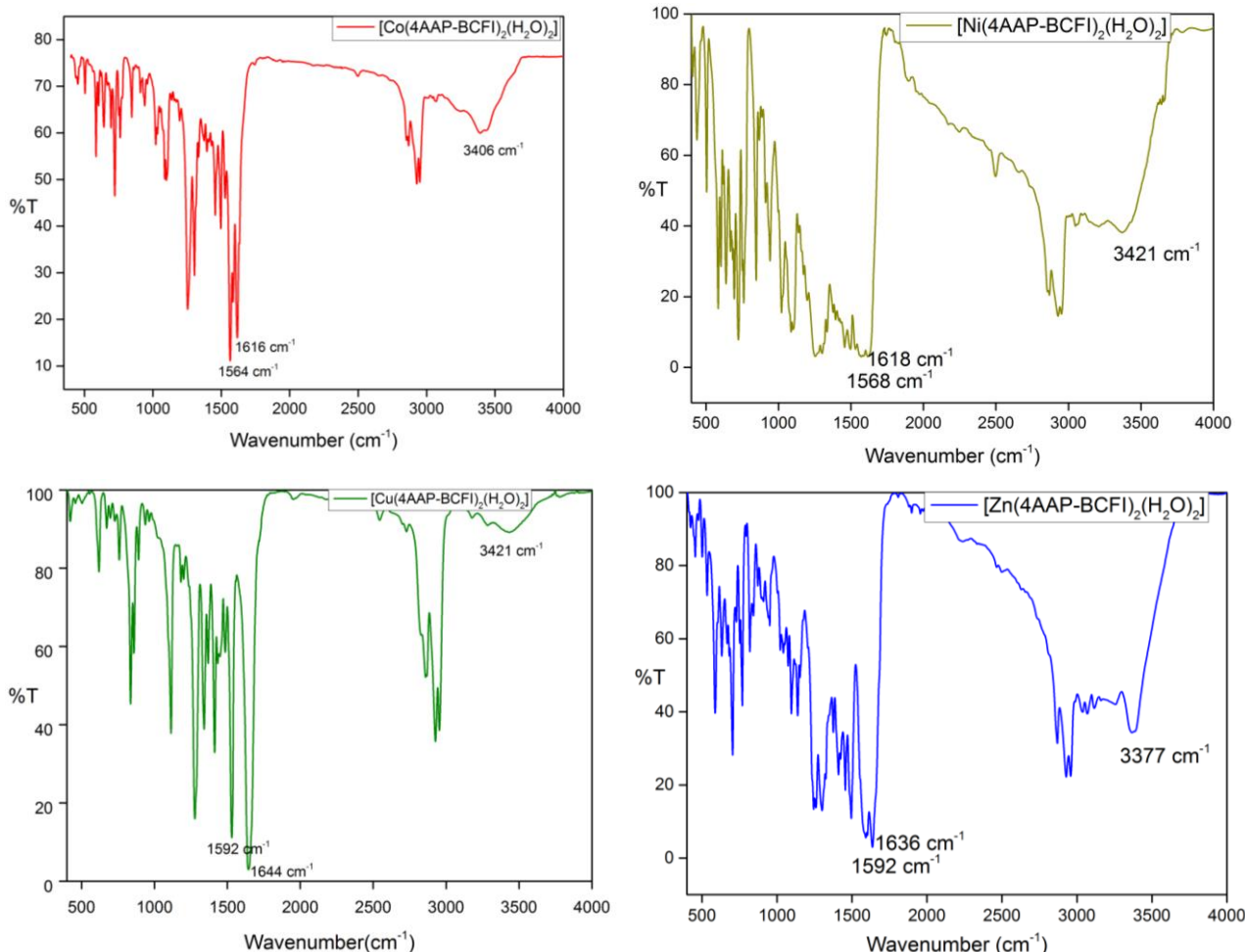


Figure 3A.4 FTIR spectra of the complexes of **4AAP-BCFI**

3A.4 Electronic Spectral Studies

The electronic spectral data of the ligand, **4AAP-BCFI** and its Cu(II), Co(II), Ni(II) and the Zn(II) complexes and magnetic moment values are collected in **Table 3A.4**. The ligand provides peaks at 210 nm, 250 nm and 350 nm due to $\pi \rightarrow \pi^*$ and $n \rightarrow \pi^*$ transitions of the azomethine and aromatic chromophores in the ligand[3]. The electronic spectrum of Cu(II) complex exhibits four bands at 208 nm, 242 nm, 342 nm and 525 nm. The band at 525 nm is assigned to $^2B_{1g} \rightarrow ^2B_{2g}$ characteristics for distorted octahedral geometry. Its magnetic moment value is 1.81BM. The electronic spectra of the Co(II) complex show bands at 220 nm and 342 nm originating from the ligand part transitions and at 406 nm due to $^4T_{1g}$ (F) \rightarrow $^4T_{2g}$ (P), characteristics of octahedral field geometry. The magnetic moment of 3.95 BM of the Co(II) complex also conforms the octahedral geometry. The Ni(II) complex also shows three band at 216 nm, 342 nm and 410 nm, the last of which is consistent with an octahedral geometry assignable to $^3A_{2g}$ (F) \rightarrow $^3T_{1g}$ (P) transition. The magnetic moment value of 3.11 BM also

supports an octahedral geometry for the Ni(II) complex. A strong band is observed at 408 nm for the Zn(II) complex could be a ligand to metal charge transfer band.

A few representative spectra are presented in **Figure 3A.5**.

Table 3A.4 Electronic spectral data of **4AAP-BCFI** and spectral and magnetic data of $[\text{M}(\text{L})_2(\text{H}_2\text{O})_2]$

Compound [#]	$\lambda_{\text{max}}(\text{nm})$ and band assignment	μ_{eff} (B.M)
4AAP-BCFI	210 (π - π^*), 250(π - π^*), 340 (n- π^*)	-
$[\text{Co}(\text{L})_2(\text{H}_2\text{O})_2]$	220 (π - π^*), 342 (n- π^*), 406 ($^4\text{T}_{1\text{g}}(\text{F}) \rightarrow ^4\text{T}_{2\text{g}}(\text{P})$)	3.95
$[\text{Ni}(\text{L})_2(\text{H}_2\text{O})_2]$	216 (π - π^*), 342 (n- π^*), 410 ($^3\text{A}_{2\text{g}}(\text{F}) \rightarrow ^3\text{T}_{1\text{g}}(\text{P})$)	3.11
$[\text{Cu}(\text{L})_2(\text{H}_2\text{O})_2]$	208 (π - π^*), 242 (π - π^*), 342 (n- π^*), 525 ($^2\text{B}_{1\text{g}} \rightarrow ^2\text{B}_{2\text{g}}$)	1.81
$[\text{Zn}(\text{L})_2(\text{H}_2\text{O})_2]$	210 (π - π^*), 340 (n- π^*), 440 (LMCT)	-

[#] L= **4AAP-BCFI**

3A.5 ^1H and ^{13}C -NMR Spectral Studies

The ^1H and ^{13}C NMR spectra of **4AAP-BCFI** recorded in DMSO are shown in **Figure 3A.6**. The ^1H -NMR aromatic protons are observed in the region of 7.26-7.51 ppm (m, 6H). Azomethine proton (s, 1H, -CH=N-) is observed at 9.61 ppm as a singlet and the protons of N-methyl of antipyrine ring observed(s, 3H, N-CH₃) and (S, 3H, C-CH₃) a singlet at 3.18 and 2.49 ppm while the aliphatic imidazole attached n-butyl protons observed at 0.92-2.72 ppm. The ^{13}C -NMR spectrum of **4AAP-BCFI** shows peaks at δ 151.60 (1C, -C=N-), 10.12, 35.83 (C, CH₃, C, N-CH₃), aromatic carbons resonates at 143.40, 134.64, 132.29, 129.20, 127.03, 125.19, 124.48, 118.12 (8C, ArC) and n-butyl carbons appears at 13.85-30.39 (4C). The spectra are in agreement with its molecular structure shown in **Scheme 3A**.

The ^1H -NMR spectrum of $[\text{Zn}(\text{4AAP-BCFI})_2(\text{H}_2\text{O})_2]$ is presented in **Figure 3A.7**. The HC=N- peak decreases to δ 9.38 from 9.68 ppm in free ligand to complex due to participation of -C=N in formation of M-O bond. All the other protons peak chemical values are shifted to downfield region.

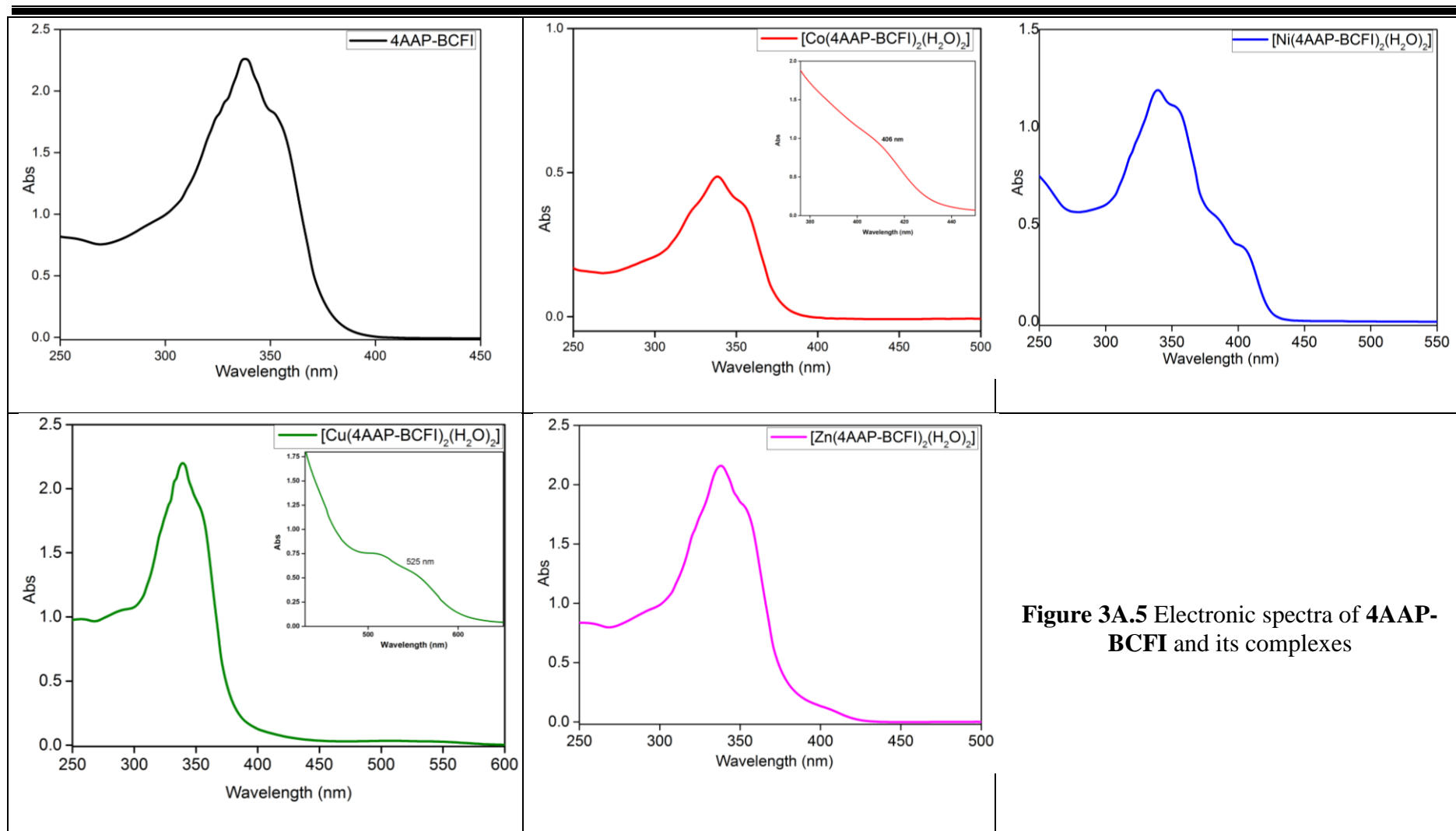


Figure 3A.5 Electronic spectra of 4AAP-BCFI and its complexes

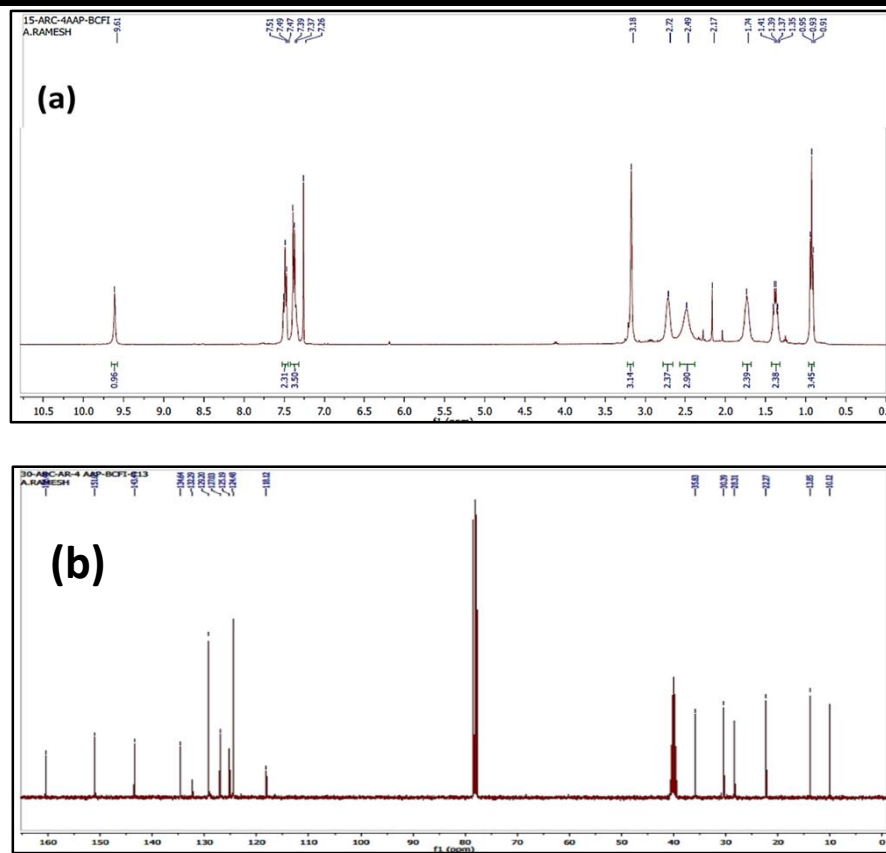


Figure 3A.6 ^1H (a) and ^{13}C (b) NMR spectra of **4AAP-BCFI**

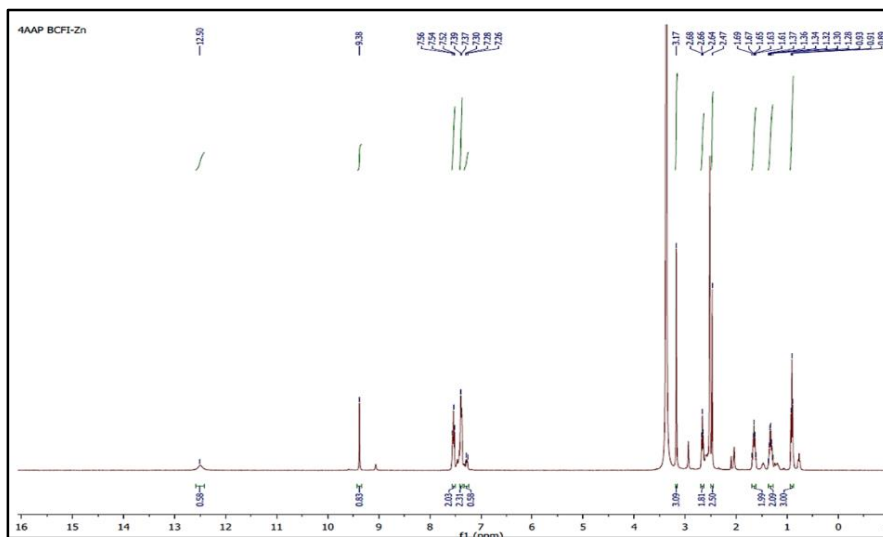


Figure 3A.7 ^1H -NMR spectrum of $[\text{Zn}(\text{4AAP-BCFI})_2(\text{H}_2\text{O})_2]^{2+}$

3A.6 Electron Spin Resonance ESR Spectral Study of $[\text{Cu}(\text{4AAP-BCFI})_2(\text{H}_2\text{O})_2]^{2+}$

The polycrystalline X-band EPR spectrum of the Cu(II) complex is shown in **Figure 3A.8**. The spectral analysis by the dedicated software reveals that the values of g_{\parallel} and g_{\perp} as 2.168 and 2.115 respectively. The g_{av} value is calculated as 2.14. The fact that $g_{\parallel} > g_{\perp} > 2.0023$

(free electron) indicates that the unpaired electron is mostly localized in the $d_{x^2-y^2}$ orbital of the Cu(II) complex [5] and that the $g_{||}$ value, in turn, being less than 2.3 indicates a covalent metal-ligand dative bond. The ESR spectral data indicate a distorted octahedral geometry with a formula of $[\text{Cu}(4\text{AAP-BCFI})_2(\text{H}_2\text{O})_2]^{2+}$ in the solid state. The proposed structure is presented in **Scheme 3A.1**.

The monovariant Job's plot studies were done to find out the metal-ligand stoichiometry. The photometric titration Job's plot is presented in **Figure 3A.9**.

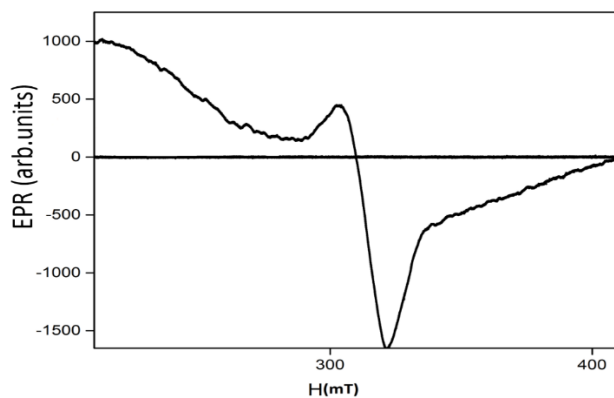


Figure 3A.8. Polycrystalline ESR spectrum of $[\text{Cu}(4\text{AAP-BCFI})_2(\text{H}_2\text{O})_2]^{2+}$

3A.7 Spectrophotometric Titration of 4AAP-BCFI

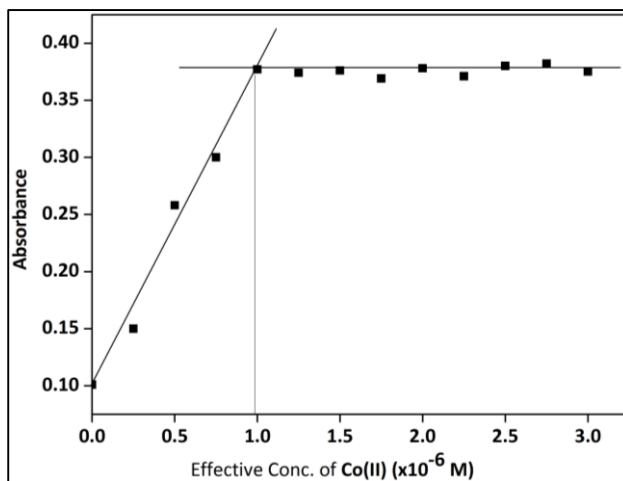


Figure 3A.9 Photometric titration (Job's plot) of Co(II) (4×10^{-6} M) against 4AAP-BCFI

3A.8 Thermal Analysis

Thermo gravimetric analysis (TGA) was performed on the complexes from ambient temperature (30 $^{\circ}\text{C}$) to 500 $^{\circ}\text{C}$. The thermo grams for ligand and complexes are presented in **Figure 3A.10-3A.11**. The studies indicate a loss of 2 water molecules per metal equivalent

between the temperatures range 120 -150 °C. However, the ligand, **4AAP-BCFI**, exhibited a loss of (CO) molecule at 135 °C whereas a broad pyrolytic decomposition takes place from 194 °C resulting in total loss by 200 °C. Weight loss to the tune of 60% was observed from the complexes from about 370 °C due to decomposition of ligand molecules. The residues at above 400 °C are found to be metal oxides. The weight loss as are in agreement with the composition of the complexes, as $[\text{M}(\text{4AAP-BCFI})_2(\text{H}_2\text{O})_2]^{2+}$. The results also indicate that these Co(II) Ni(II), Cu(II), Zn(II) complexes are thermally moderately stable solid complexes.

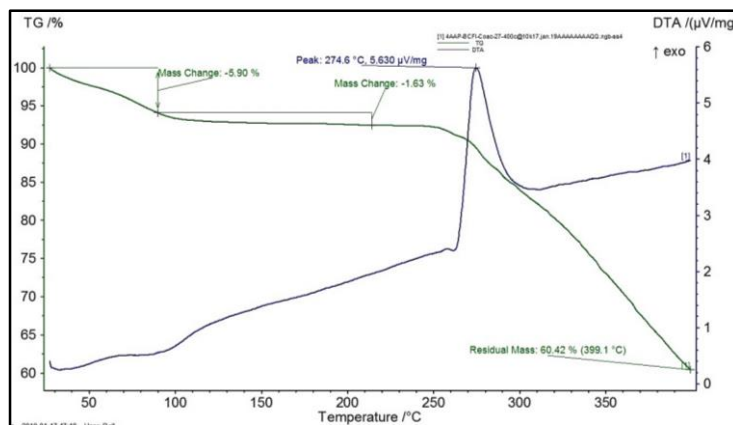


Figure 3A.10 TGDTA thermogram of **4AAP-BCFI**

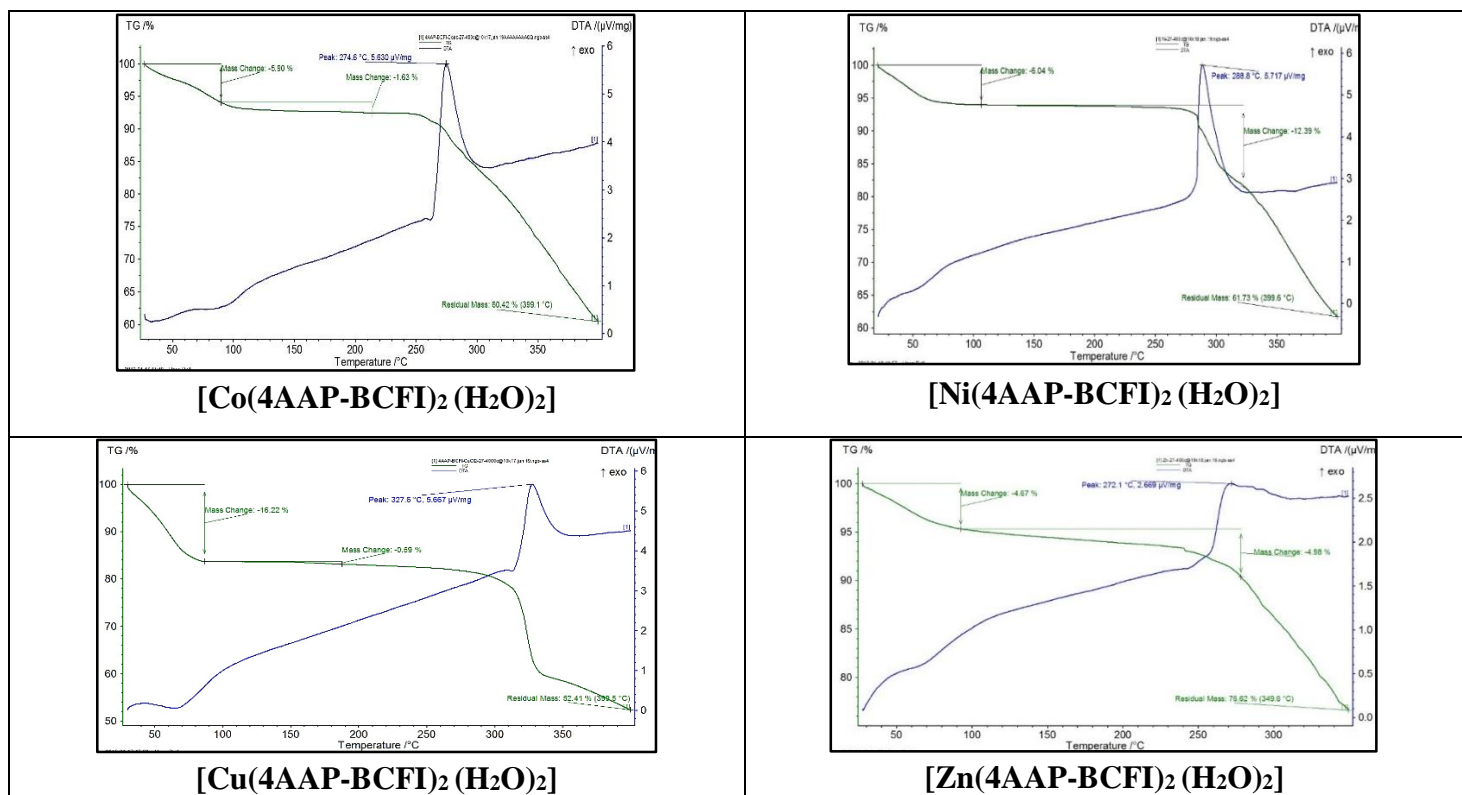


Figure 3A.11 TGA-DTA thermograms of the complexes of **4AAP-BCFI**

PART-B

**SINGLE CRYSTAL XRD STUDIES AND DFT/B3LYP CALCULATIONS
OF 4AAP-BCFI AND ITS METAL COMPLEXES: CORRELATION OF
EMPERICAL AND MODELLED DATA**

3B.1 X-Ray Crystal Structure Analysis of 4AAP-BCFI

The structure of the **4AAP-BCFI** has been solved by a single crystal X-ray diffractometry. The absolute structure parameter was determined successfully. Single crystals, suitable for structure determination, could not be obtained for the $[\text{M}(\text{4AAP-BCFI})_2(\text{H}_2\text{O})_2]$ complexes though they are quite stable to air and moisture and moderately soluble in DMSO and DMF. The **4AAP-BCFI** is found to crystallize in the centro symmetric monoclinic $P2_1/n$ space group with one molecule of ligand **4AAP-BCFI**, ($Z=4$), and one H_2O molecule in the asymmetric unit, ($Z'=1$). The pyrazole and phenyl moieties are not co-planar and the torsion (dihedral) angle between these rings (C15-C14-N5-N4) is 144.98° (or 35.02°). The crystal structure analysis also reveals that the ligand **4AAP-BCFI** forms a corrugated structure in the crystal with $\text{O}-\text{H} \dots \text{O}$, $\text{O}-\text{H} \dots \text{N}$ and $\text{N}-\text{H} \dots \text{O}$ hydrogen bonds with the crystal-held water molecules included. The ORTEP diagram of **4AAP-BCFI** is shown in **Figure 3B.1** and its relevant XRD refinements data has been provided in **Table 3B.1**. And its hydrogen bonding interactions are listed in **Table 3B.2**. The ligand molecules are interconnected with the pyrazolone carbonyl ($\text{C}=\text{O}$) group and imidazole-attached *n*-butyl $-\text{CH}_2$ *via* $\text{C}-\text{H} \dots \text{O}$ hydrogen bonds to form a helical structure along the crystallographic *b*-axis (**Figure 3B.2a and b**). The H_2O molecule interacts with the pyrazolone $\text{C}=\text{O}$ and phenyl $\text{C}-\text{H}$ groups with $\text{O}-\text{H} \dots \text{O}$ and $\text{C}-\text{H} \dots \text{O}$ hydrogen bonds. Thus, the intercalation of water molecules seems to have influenced the crystallographic packing of **4AAP-BCFI** by stabilizing the single-strand helical pattern. The helical structures are propagated into second dimension to form corrugated layered structure along the crystallographic *c*-axis (**Figure 3B.3a and b**).

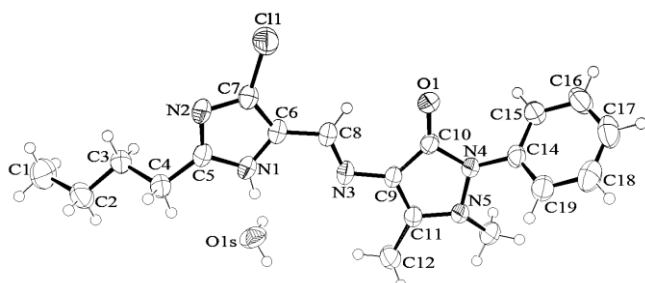


Figure 3B.1 ORTEP representation of **4AAP-BCFI.xH₂O** (the thermal ellipsoids are drawn at 50% probability level)

Table 3B.1 Crystallographic data of **4AAP-BCFI.xH₂O**

CCDC Number	2032456
Empirical formula	C ₁₉ H ₂₂ ClN ₅ O, x H ₂ O (x=0.25)
Formula weight	371.86
Temperature (K)	296(2)
Wavelength (Å)	0.71073
Crystal system, space group	Monoclinic, P2 ₁ /n
Unit cell dimensions	a (Å) = 12.1533(12); b (Å) = 13.1907(14) c (Å) = 13.5661(13); $\alpha = 90^\circ$; $\beta = 112^\circ$; $\gamma = 90^\circ$
Volume (Å ³)	2015.5(4)
Z	4
Z' (water molecules)	1
Calculated density (mg/mm ³)	1.285
Absorption coefficient (mm ⁻¹)	0.213
F(000)	824
Crystal size (mm ³)	0.350 x 0.300 x 0.300
θ range for data collection (°)	2.238 to 28.486
Limiting indices	-14 ≤ h ≤ 16; -17 ≤ k ≤ 17; -18 ≤ l ≤ 15
Reflections collected / unique	24179 / 4996
R _{int}	0.0280
Completeness to θ	25.242 100.0 %
Absorption correction	Semi-empirical from equivalents
Max. And min. transmission	0.939 and 0.929
Refinement method	Full-matrix least-squares on F ²
Data / restraints / parameters	4996 / 3 / 253
Goodness-of-fit on F ²	1.027
Final R indices [I > 2 σ (I)]	R ₁ = 0.0428, wR ₂ = 0.1110
Final R indices [all data]	R ₁ = 0.0671, wR ₂ = 0.1271
Extinction coefficient	n/a
Largest diff. peak and hole (e Å ⁻³)	0.188 and -0.264

Table 3B.2 Intermolecular donor (D) and acceptor (A) hydrogen bond lengths (Å) and angles (°) for **4AAP-BCFI**

D-H....A	d(D-H)	d (H....A)	d (D....A)	∠DHA	(Symmetry code)
C8-H....O1	0.930	2.325	3.004	129.54	O1
C3-H....N2	0.960	2.679	3.606	162.45	N2[-x+1, -y+2, -z+1]
N1-H1....O1	0.860	2.019	2.814	153.29	O1S
O1s-H....N2	0.827	2.063	2.871	165.73	N2[x+1/2, -y+3/2, z+1/2]
O1s-H....O1	0.825	1.999	2.816	170.11	O1[-x+1, -y+2, -z+1]
N1-H....O1s	0.860	2.020	2.8135	153.30	-

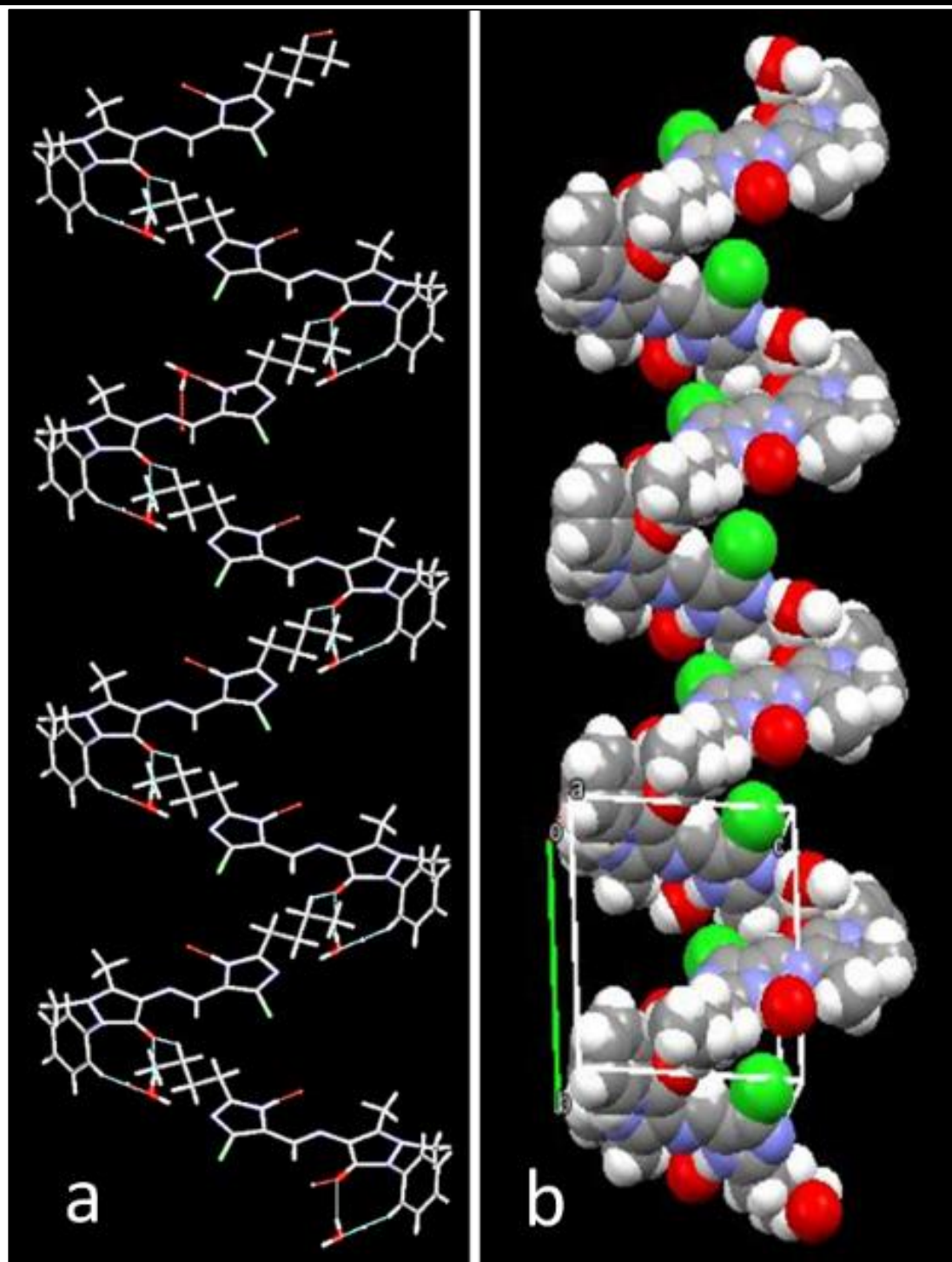


Figure 3B.2 Corrugated tapes formed by **4AAP-BCFI** molecules with C-H....O hydrogen bond interaction along the crystallographic *b*-axis, shown in stick (a) and space-filling (b) models. (The unit cell compartment is shown in the space-filled model)

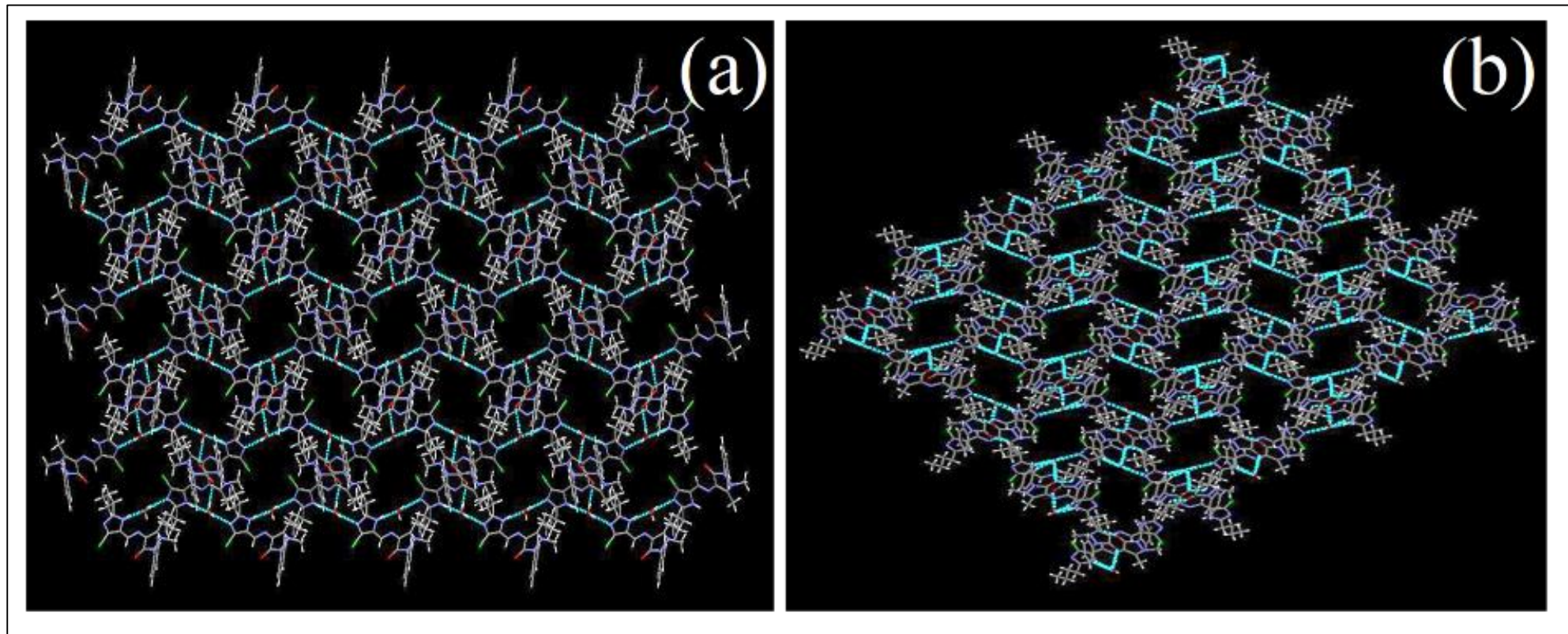


Figure 3B.3 Corrugated layer packing of **4AAP-BCFI** along the crystallographic *c*-axis shown in stick model with O–H...O, O–H...N and N–H...O hydrogen bond interactions viewed down the crystallographic *a*-axis **(a)** and *c*-axis**(b)**

3B.2 Computational Studies

3B.2.1 DFT-B3LYP Calculations

The geometries of **4AAP-BCFI** and all other complexes were fully optimized without any geometrical and symmetrical constraints using B3LYP method employing 6-31G* basis set [6]. All the calculations were performed using Gaussian 16 suit program package [7].

3B.2.2 Computational Structure Analysis Density Function Theory (DFT) Studies

To probe the structure and stability of **4AAP-BCFI** ligand and its various metal chelates, some computational studies by density functional theoretical (DFT) calculations were performed on them using the B3LYP/6-31G* level platform. A correlation between the modelled data in its (gas phase) single molecular status and the experimental single crystal XRD data of **4AAP-BCFI** would through light on how the intermolecular forces in the compounds influence the native molecular electronic and structural properties. Though no single crystals of $[M(4AAP-BCFI)_2(H_2O)_2]$ could be obtained, computational modelling on them could be possible.

3B.2.3 Torsional Energy Conformational Plots

The torsional energy conformational plots of the single dihedral rotation over C6-C8, C8-N3 and N3-C9 and those of the double dihedral over C6-C8-N3 and C8-N3-C9 bond sets performed on the MM2-way energy minimized molecules by ChemSoft Chem3D (ver 12), are shown in **Figure 3B.4**. The gridding and plotting are obtained from Surfer (ver 12) and Grapher (ver 11) tools supplied by Golden Software Inc. (vide chapter-II)

3B.2.4 Correlation of the X-Ray Crystallographic Data of Ligand and Molecular Modelled Data of Its Complexes

In **Figure 3B.5** are shown the XRD structure and the one generated by modelling of **4AAP-BCFI** with the highest possible overlapping and spatial coincidence of maximum number atoms. The geometrical parameters of ligand obtained using B3LYP/6-31G* level of calculation are compared systematically with the corresponding experimental counterparts.

Considerable deviation can be seen from the aligned geometries of **4AAP-BCFI** at the exocyclic n-butyl skeletal disposition in relation to the C-Cl bond on the imidazole ring (the solid state XRD shows a slight *syn* disposition whereas the DFT calculations favour more of *anti*).

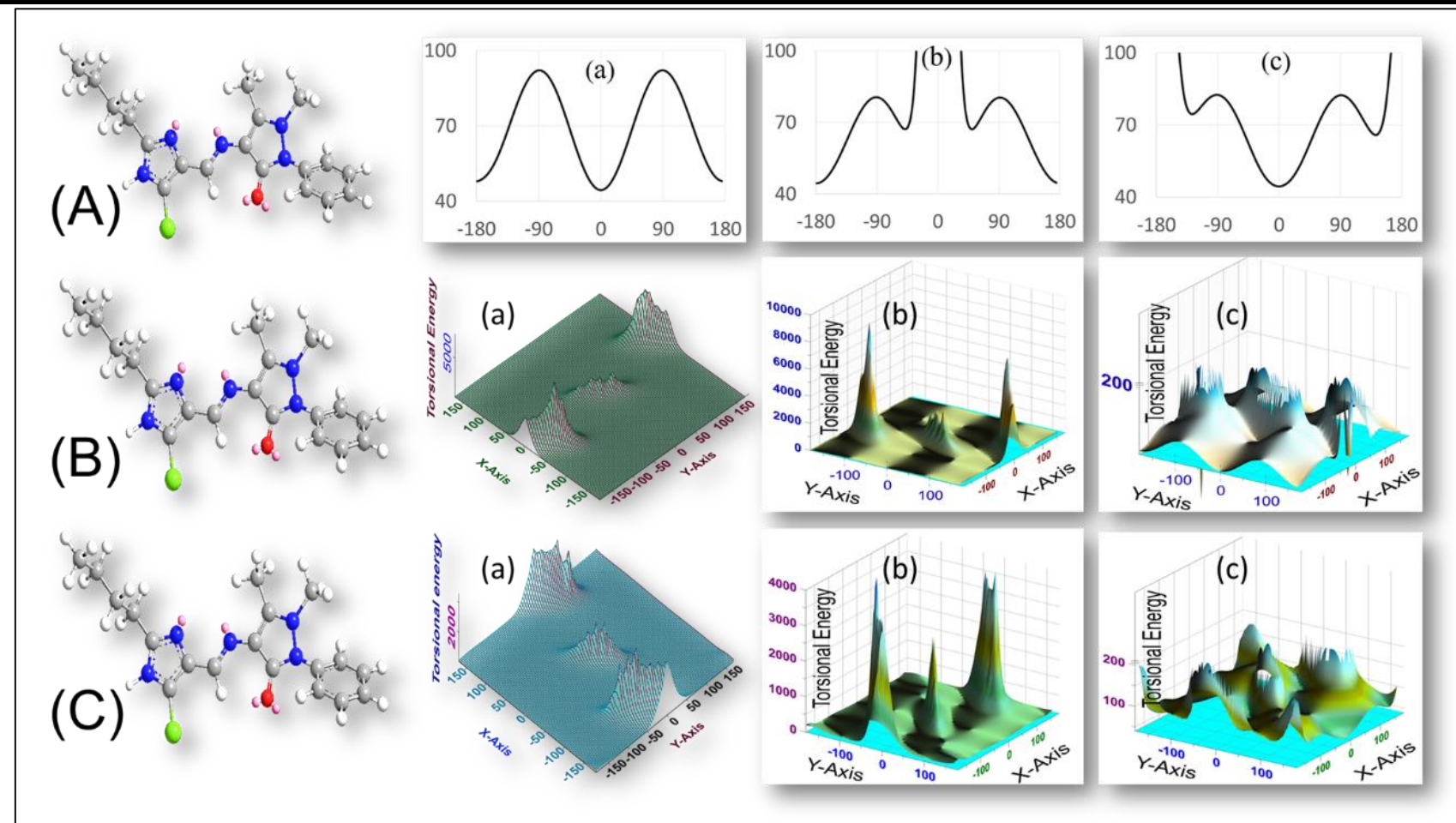


Figure 3B.4 The torsional conformation energy plots of MM2-energy-minimized **4AAP-BCFI** molecule on (A) single bond over C6-C8 (Aa), C8-N3 (Ab) and N3-C9 (Ac) and (B) double dihedral torsional energy 3D plots over C6-C8-N3 dihedral with rotation angle over C6-C8 shown on X-Axis and C8-N3 on Y-Axis and (C) double dihedral torsional energy 3D plots over C6-N3-C9 with rotation angle over C8-N3 shown on X-Axis and N3-C9 on Y-Axis both as a Surfer wireframe (Ba, Ca) and Grapher surface (Bb, Cb) and Grapher surface, truncated to 200 kJ mol⁻¹ (Bc, Cc) (Ref. *Fig. 3B.1* for atom number reference)

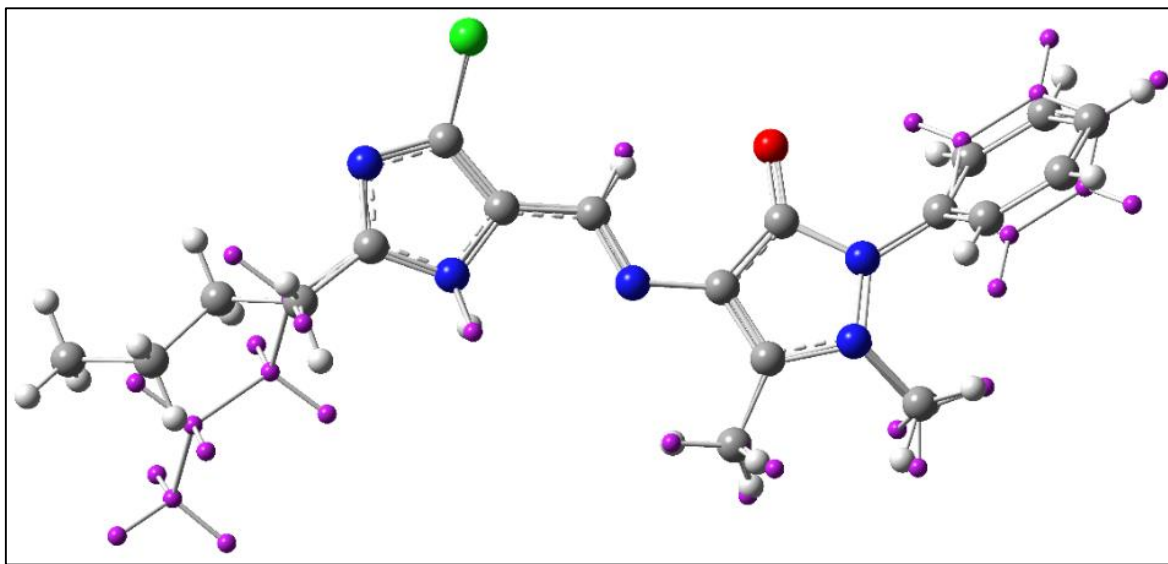


Figure 3B.5 X-ray crystal structure alignment of **4AAP-BCFI** (colour key: grey = carbon, white = hydrogen, blue = nitrogen, red = oxygen, and green = chlorine) with its modelled structure (atoms shown in pink)

Similarly, the dihedral angle between the pirazole and the benzene rings seems to be more in the solid state (XRD) whereas the free molecule (DFT) prefers near co-planarity of the two rings. Deviation in the geometry obtained using B3LYP/6-31G* level of theory when compared with its experimental XRD counterpart is attributed to the system difference, one a free gas-phase molecule and the other amidst multiple intermolecular interactions in the solid state matrix. Overall, the geometries obtained experimentally by single crystal XRD studies and DFT calculations clearly indicate that **4AAP-BCFI** holds near identical spatial disposition of its molecular framework. A list of some XRD data and DFT-modelled data of **4AAP-BCFI** along with the DFT-modelled data of its four complexes is placed in **Table 3B.3**.

Table 3B.3 Important empirical (XRD) and DFT-calculated bond lengths, bond angles and dihedral angles of **4AAP-BCFI** (**L**) and $[\mathbf{M}(\mathbf{L})_2(\mathbf{H}_2\mathbf{O})_2]$ (Ref. Fig. 3B.1 for atom number reference)

Important Bonds	Bond length (Å)					
	XRD of L	DFT on L	DFT on $[\mathbf{M}(\mathbf{L})_2(\mathbf{H}_2\mathbf{O})_2]$			
			M=Co(II)	M=Ni(II)	M=Cu(II)	M=Zn(II)
C8-N3	1.2773	1.2971	1.3174	1.3115	1.4321	1.4254
C6-C8	1.4388	1.4360	1.4205	1.4361	1.3934	1.3879
C9-N3	1.3914	1.3826	1.4067	1.3994	1.3498	1.3445
C9-C10	1.4360	1.4694	1.4353	1.4304	1.4457	1.4549
C10-O1	1.2340	1.2259	1.2906	1.2938	1.2850	1.2792
Bond Angles (°)						

N3-C8-C6	119.35	119.12	131.95	130.520	123.619	121.084
C8-N3-C9	120.14	120.54	128.88	129.884	123.560	123.400
C11-C9-N3	122.75	123.69	136.45	136.463	137.553	136.279
O1-C10-C9	131.90	130.70	125.77	126.068	123.338	124.870
N4-C10-C9	104.89	104.70	107.42	107.342	107.874	107.416
O1-C10-N4	123.20	124.56	126.79	126.590	128.719	127.712
Dihedral Angles (°)						
C7-C6-C8-N3	170.62	179.31	174.80	-37.600	178.204	176.190
N1-C6-C8-N3	-3.70	-1.075	12.89	155.337	-0.615	-4.405
C6-C8-N3-C9	-175.52	-179.47	-9.84	-11.874	103.198	116.537
C10-C9-N3-C8	2.40	5.37	150.27	155.034	171.491	174.164
N3-C9-C10-O1	-3.70	-2.30	-4.25	-2.667	-0.902	0.273
C11-C9-N3-C8	177.78	177.00	42.97	-32.838	-7.588	-5.295
N3-C9-C11-C12	8.60	5.92	-1.51	1.452	-1.681	-1.913
C8-C6-C7-C11	3.80	1.54	6.31	3.527	0.401	-1.010

3B.2.5 Modelled Data and Geometry of the Complexes

The structures of a few metal complexes, with optimized geometries obtained by DFT calculations are shown in **Figure 3B.6**. The **4AAP-BCFI** is found to act as a bidentate ligand through the N and O binding atoms preferred in all the energy-minimized complexes. Important geometric parameters at the coordination sphere of various complexes are given in **Table 3B.4** in relation to the computer (DFT) generated structures shown in **Figure 3B.6**. In **Table 3B.5** are collected the difference-data for the ligand, **4AAP-BCFI** on the basis of its existence as a pure molecule and its fate upon complexation from both empirical and modelled perspectives. Here, the ΔXRD value means, the difference between a parameter for the ligand framework in the DFT-modelled complex and the corresponding value for the pure ligand from the XRD data. Similarly, the ΔDFT value means the difference between a parameter for the ligand framework in the DFT-modelled complex and the corresponding value for the DFT-modelled pure ligand. Any finite ΔXRD value may imply a true variation of the parameter upon complexation whenever the values of the said parameter for the ligand from DFT calculations and that from XRD data are in good agreement whereas ΔDFT may imply a deviation of the specified parameter of a gas-phase single molecule upon coordination to give a gas-phase single molecule of the complex.

As expected, the bond lengths between the donor atoms and their linked atoms in the ligand molecule are slightly only different in the complexes when compared to those in the free ligand. Similarly, the bond angles of the C6-C8-N3, C8-N3-C9, N3-C9-C10 and O1-C10-C9 and where N3

and O1 are the donor atoms, are found to be affected to varied extents to account for the demands of structural stability of the complexes upon coordination. Since, the C6-C8-N3 and C9-N3-C8 moieties are exocyclic and thus flexible and the coordination is a five-membered ring with NMO angle close to 90°, the angles at these moieties are lower in the complexes than in the ligand whereas the angles at O1-C10-C9, where both the carbon atoms are endocyclic and thus are less flexible, seem to have hardly been affected upon complexation. The fact that Δ XRD and Δ DFT values of any parameter of the pure or those of the complexed ligand are very close to each other indicates the reliability of the B3LYP platform for the DFT calculations.

It can be noted from the optimized geometries that in the case of Co(II) and Ni(II) the four donor atoms of the two **4AAP-BCFI** ligands are in plane. Typically, the dative bond lengths for Co-O and Co-N are 2.12 and 2.15 Å, respectively, as shown in **Table 3B.4**. For Ni(II) complex they are 2.08 and 2.11 Å. From this data one may conclude the two axial water ligands are in equidistant with metal ions in each of the Co and Ni complexes suggesting that these complexes are in octahedral geometry with D_{2h} point group at the coordination sphere.

It is interesting to observe that the bond distance values of the two water molecules with the metal ion in the case of Zn(II) are 2.12 Å and 2.27 Å. Thus, it is to be stated that the **(Zn(4AAP-BCFI)₂(H₂O)₂)²⁺** forms a distorted octahedral complex with a C_{2v} point group for the coordination sphere (**Figure 3B.6**).

Table 3B.4 Geometrical parameters of **[M(4AAP-BCFI)₂(H₂O)₂]** calculated from **B3LYP-DFT** modeling

M(II)	d1	d2	d3	d4	d5	d6		a1	a3	a2	
Co(II)	2.12	2.15	2.12	2.15	2.11	2.11		81.6	81.6	180.0	
Ni(II)	2.08	2.11	2.08	2.11	2.08	2.08		83.9	83.9	179.9	
Zn(II)	2.17	2.12	2.15	2.18	2.27	2.15		81.1	80.8	149.4	
	d1	d2	d3	d4	a1	a3	a2	a4	ncd1	ncd2	ncd3
Cu(II)	2.04	2.01	2.00	2.03	84.5	86.2	90.6	93.0	2.22	1.69	1.67

All the symbols used herein are described in **Figure 3B.6**. The distances are in Å and angles are in (°)

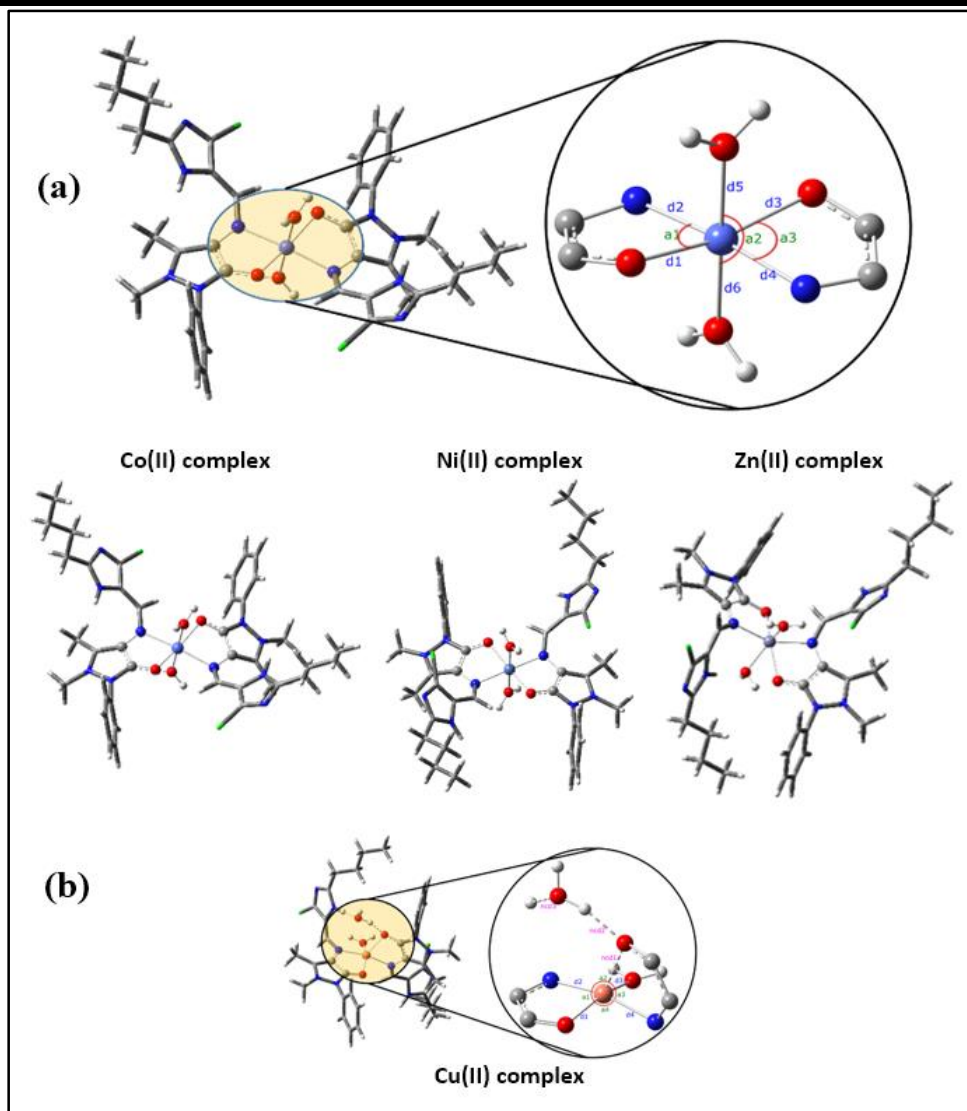


Figure 3B.6 Optimized geometries of (a) various complexes in an octahedral environment and (b) copper complex in a distorted square pyramidal geometry with primary coordination shell indicated in ball-stick model and all other atoms in tube model with colour scheme: grey (carbon), blue (nitrogen), red (oxygen) and light blue (metal) in (a) and pink (copper) in (b)

The DFT-optimized geometry of the Cu(II) complex is not only significantly different from the other three complexes but also offers structural data in disagreement with the experimental results. As mentioned above, the electronic and ESR spectral data support a distorted octahedral geometry while the thermal (TGA) and mass spectral information indicates presence of 2 water molecules per metal atom. However, in the computational studies it is observed that although two **4AAP-BCFI** ligands are involving in the bonding along with two water molecules, the binding nature of the two **4AAP-BCFI** is not chemically indistinguishable. The two **4AAP-BCFI** ligand molecules form two dissimilar chelation pattern with Cu(II) centre. Their NONO donor atoms do not define a metal atom-containing plane whereas there is a plane of NOMNO⁻ where O is the

oxygen of one of the two water molecules. The oxygen of the other **4AAP-BCFI** binds axially to the Cu(II) centre resulting in an M-O bond, considerably larger in bond length than the other one, denoted by **ncd1** and **d1** respectively, in **Figure 3B.6**. To understand the long bond properties, we have carried out **atoms in molecule theory** (AIM) and **reduced density gradient** (RDG) calculations. These calculations were carried out using the multifunctional wave function analyzer, **Multiwfn** program [7]. Calculated AIM monograph and RDG plot of Cu(II) complex are given in **Figure 3B.7**.

Table 3B.5 Comparative empirical and computational bond lengths (Å), bond angles (deg) and dihedral angles (deg) of **4AAP-BCFI (L)** and its complexes (*Ref. Fig.3B.6 for atom number reference*)

Compound/ Parameter		L	ML₂ 2H₂O with M =			
			Co(II)	Ni(II)	Cu(II)	(Zn(II))
Computed data of the complexes	String	-	Octahedral (D _{2h})	Octahedral (D _{2h})	Dist. Sq. Pyr. (c ₁)	Octahedral (c _{2v})
	M-N3	-	2.150	2.105	2.012	2.115
	M-O1	-	2.122	2.082	2.042	2.174
	M-N3-C8	-	119.337	120.500	125.930	125.778
	M-N3-C9	-	108.188	107.212	110.072	110.716
	M-O1-C10	-	107.255	105.971	107.032	106.785
ΔXRD	C8-N3	0.012	-0.040	-0.034	-0.155	-0.148
ΔDFT		-	-0.020	-0.015	-0.135	-0.128
ΔXRD	C9-N3	0.003	-0.015	0.080	-0.041	-0.034
ΔDFT		-	-0.024	0.071	-0.050	-0.043
ΔXRD	C9-C10	0.008	0.001	0.006	-0.009	-0.018
ΔDFT		-	0.034	0.004	0.024	0.015
ΔXRD	C10-O1	0.033	-0.056	-0.059	-0.051	-0.045
ΔDFT		-	-0.065	-0.068	-0.060	-0.054
ΔXRD	C10-N4	-0.008	0.024	0.024	0.033	0.028
ΔDFT		-	0.044	0.024	0.053	0.048
ΔXRD	C6-C8-N3	0.230	-12.606	-11.166	-4.270	-1.734
ΔDFT		-	-12.856	-11.396	-4.499	-1.964
ΔXRD	C9-N3-C8	-0.400	-8.761	-9.744	-3.420	-3.260
ΔDFT		-	-8.356	-9.339	-3.015	-2.855
ΔXRD	N3-C9-C11	-	-13.710	-13.713	-14.803	-13.529
ΔDFT		-	-12.769	-12.772	-13.862	-12.488
ΔXRD	O1-C10-C9	1.200	6.125	5.830	8.512	7.030
ΔDFT		-	4.928	4.633	7.315	5.833

Δ XRD	O1-C10-N4	-1.360	-3.594	-3.390	-5.519	-4.512
Δ DFT		-	-2.234	-2.030	-4.159	-3152
Δ XRD	N1-C6-C8-N3	-2.625	-16.629	-159.026	-3.085	0.705
Δ DFT		-	-11.854	-154.251	1.690	5.480
Δ XRD	C6-C8-N3-C9	3.950	-185.390	187.407	-278.718	-292.057
Δ DFT		-	-189.346	-167.589	-282.674	-296.013
Δ XRD	C8-N3-C9-C11	0.780	134.888	210.595	-170.192	183.075
Δ DFT		-	-219.813	-144.106	-169.333	-171.626
Δ XRD	N3-C9-C10-O1	-1.400	7.944	-1.031	-2.798	-3.973
Δ DFT		-	-3.744	3.169	1.402	0.227

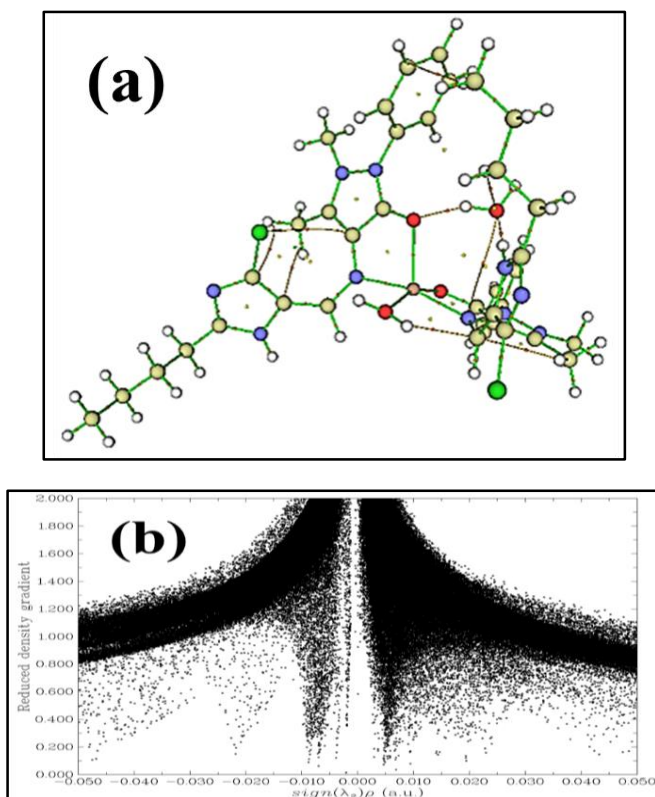


Figure 3B.7 AIM monograph **(a)** and RDG plot **(b)** of $[\text{Cu}(4\text{AAP-BCFI})_2(\text{H}_2\text{O})_2]$

The RDG plot clearly shows the existence of non-covalent interactions in Cu(II) complex. As various types of intramolecular interactions are involved in the complex, the bond critical point of Cu(II)-O is scrutinized to probe the nature of interaction at the **ncd1** bond. The calculated Laplacian electron density (LED) at the **ncd1** bond critical point is 0.040 au whereas that expected for a covalent bond is usually more than -0.20 au. The observed deficiency of LED clearly indicates that the **ncd1** bond is mostly by a non-covalent interaction. Similar kind of observation has been reported recently for some borazon and diborane complexes [8]. The DFT calculations on the Cu(II)

complex suggest that the complex cation, in gaseous state, is more stable in a marginally distorted square planar structure than in square pyramidal or trigonal pyramidal ones.

3B.3 Hirshfeld Surface Calculations

Hirshfeld surface analyses is a graphical tool for visualization and understanding of close contact intermolecular interactions in solid state [9]. Using the Crystal Explorer (ver. 17.5), an Hirshfeld surface analysis was performed on the XRD data of **4-AAP-BCFI** in the CIF format. The Hirshfeld surfaces of the crystal of **4AAP-BCFI** are shown in **Figure 3B.8**. Symbols d_i , d_e and d_{norm} are used to represent Hirshfeld surface distances from the nearest nucleus inside and outside the molecular surface and a normalized contact distance, respectively. Visualization of extent of d_{norm} is presented in shades of white, red, and blue diffuse colours. The d_{norm} values for the **4-AAP-BCFI** range from -0.59 to 1.51 \AA . Considerable depth of hydrogen bond interactions are found for C=O....H, N-H....O, N-H....Cl and C-H....O. These contacts are also shown with fingerprint plots in Fig. 10 from which one can find the density of Hirshfeld surfaces to the tune of O....H (8.0 %), N....H (9.4 %), H....Cl (13.2%), H....H (48.4%), C....H (17.4%) while other contact types, like C....C, Cl....Cl and C....Cl have negligible extent. Such representative 2D finger print plots given in **Figure 3B.9**.

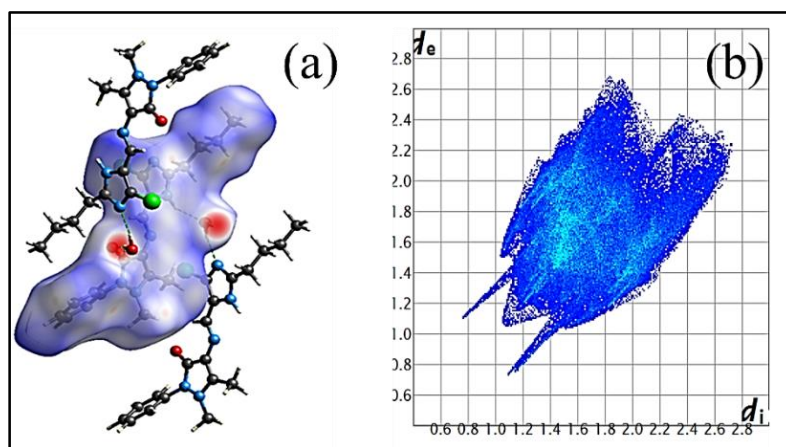


Figure 3B.8 Hirshfeld surface (d_{norm} mapped) for visualizing the (a) intermolecular interactions of the **4AAP-BCFI** (dotted lines represent hydrogen bonds) and (b) the corresponding finger print map of d_e vs d_i with 100% mapping of all its atoms

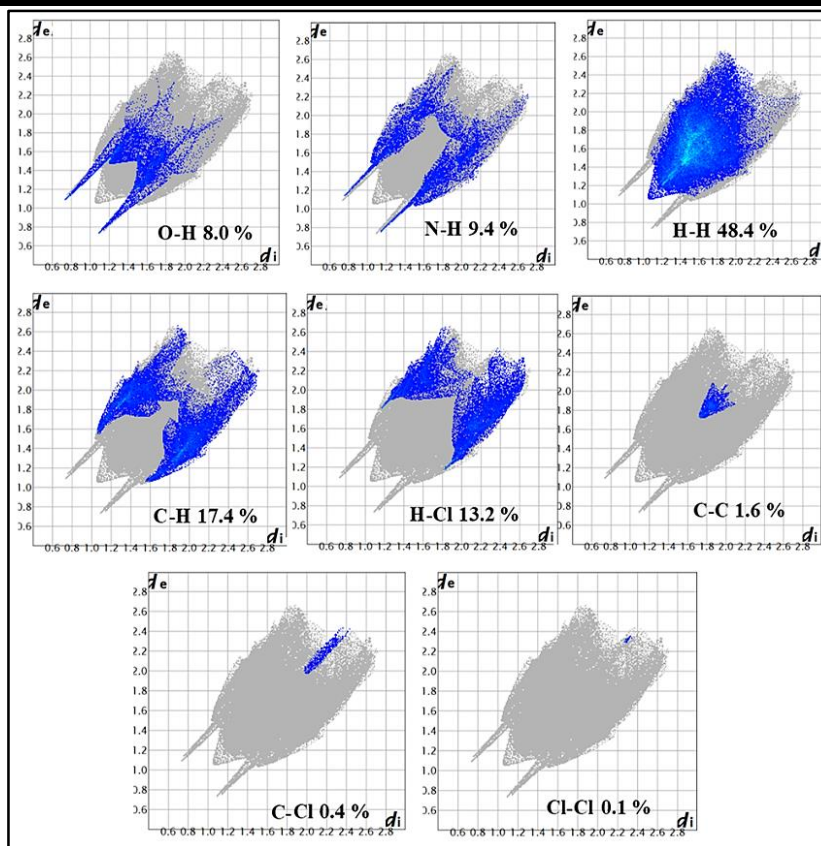


Figure 3B.9 The 2D finger print plots of inter atomic interactions of ligand **4AAP-BCFI** showing the percentage of contacts contributed to the total Hirshfeld surface area of the molecules

The Hirshfeld surface analysis manifests the importance of H-atom contacts (hydrogen bond) in stabilizing the crystal packing. The large values of N–H…O, C-Cl…H and C–H…O interactions suggests that Van der Waals interactions and hydrogen bonding interactions together play a major role in the crystal packing [10].

3B.4 Comparative Molecular Modelling Studies of $[\text{M}(\text{4AAP-BCFI})_2(\text{H}_2\text{O})_2]$ in the Light of XRD Studies of **4AAP-BCFI**

For addressing the stability aspects of the ligand **4AAP-BCFI** and its metal complexes, molecular modelling studies were used to find, the conformational visualization of the molecules in various forms. The MM2 force field method with an RMS gradient of 0.01 is used to calculate the global energy minimized structures. The MM2-energy-minimized, anaglyph and stereographic structure of **4AAP-BCFI** shown in **Figure 3B.10-3B.11**. Quantum mechanical HOMO-LUMO orbital energy estimates were used to calculate the projected gas-phase electronic transitions. The HOMO-LUMO of metal complexes $[\text{M}(\text{4AAP-BCFI})_2(\text{H}_2\text{O})_2]$ is created and illustrated obtained from DFT calculations.

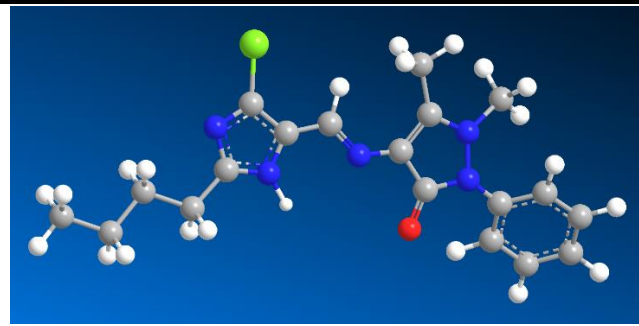


Figure 3B.10 Global minimized ball-stick model of **4AAP-BCFI**

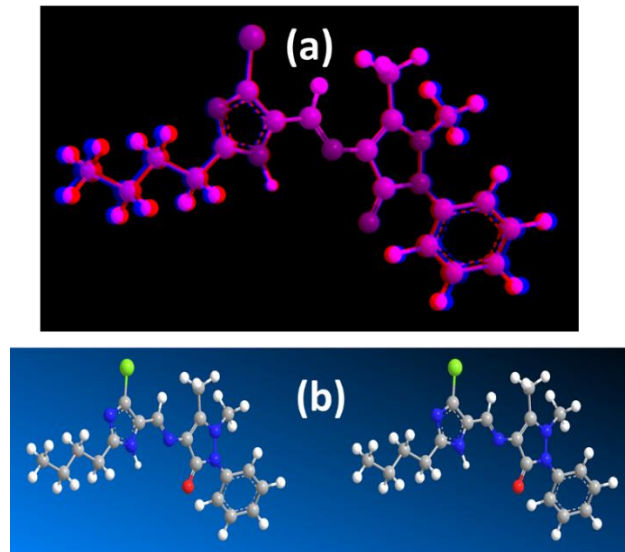


Figure 3B.11 Energy minimized images of **4AAP-BCFI** in its anaglyph (a) and stereographic perspective (b)

3B.5 Stability Analysis

3B.5.1 Frontier Orbital Analysis

The shapes of the calculated HOMOs and LUMOs and the corresponding eigen values of various complexes are shown in **Table 3B.6**. The ΔE_g ($= E_{\text{LUMO}} - E_{\text{HOMO}}$) values of Co(II), Ni(II), Cu(II), and Zn(II) are 3.70, 3.76, 2.00, and 1.82 eV, respectively and these ΔE_g values are indicative of stability of the complexes. The larger ΔE_g values for Co(II) and Ni(II) complexes are also in favour of octahedral geometries for them. The low ΔE_g values of Cu(II) and Zn(II) signify slight distortion in geometry as the results indicate.

Table 3B.6 Modelled shapes of HOMO and LUMO molecular orbitals (iso value 0.007 a.u.), their corresponding energies and expected theoretical electronic transition maxima

[M(4AAP-BCFI)₂ 2H₂O with M =			
Co(II)	Ni(II)	Cu(II)	Zn(II)
Highest Occupied Molecular Orbitas (HOMOs) and their energies (eV)			
E _{HOMO} =-10.32	E _{HOMO} =-10.25	E _{HOMO} =-8.96	E _{HOMO} =-8.71
Lowest Unoccupied Molecular Orbitas (LUMOs) and their energies (eV)			
E _{LUMO} =-6.62	E _{LUMO} =-6.49	E _{LUMO} =-6.96	E _{LUMO} =-6.89
$\Delta E_g = E_{LUMO} - E_{HOMO}$ (eV)			
3.70	3.76	2.00	1.82
Obsrvd λ_{max} = 342 nm	342 nm	525 nm	440 nm
Exptd λ_{max} =335 nm	330 nm	620 nm	482 nm

PART-C

BIOLOGICAL ACTIVITY AND MOLECULAR DOCKING STUDIES OF 4AAP-BCFI AND ITS METAL COMPLEXES

3C.1 *In-vitro* Antimicrobial Activity

The microbial activity of ligand **4AAP-BCFI** and its Schiff base complexes were screened against two gram positive and two gram negative bacteria and with *streptomycin* drug as the standard. The tested results are collected in **Table 3C.1**. A 0.5 mL of stock solution of bacterial culture was spread on a plate and the wells were filled with either 600 $\mu\text{g}/\text{ml}$ or 900 $\mu\text{g}/\text{ml}$ of the indicated compounds of ligand and its metal complexes followed by incubation at 28°C. After 24 hours, the well-diffusion was observed using DMSO as solvent. Standard streptomycin drug was used for comparing the results and activity was measured by the antimicrobial reading scale. *In vitro* antimicrobial activity of the ligand and its metal complexes were evaluated against two Gram-positive (*Bacillus subtilis*, *Staphylococcus aureus*) and two Gram-negative (*Escherichia coli*, *Salmonella paratyphi*) bacteria using disk diffusion method [11]. Zone of inhibition (ZOI) was measured by antibiotic zone scale in (mm).

The ligand, **4AAP-BCFI** and its metal complexes have been assayed for antimicrobial activity histogram are shown in **Figure 3C.1**. From the results collected the Zn(II) complex shows a good antimicrobial activity towards all the tested pathogenic bacteria. Its 600 $\mu\text{g}/\text{ml}$ dose exhibited a maximum zone of inhibition at 15 mm for *E. coli* and *Staphylococcus aureus* and least activity towards *Salmonella paratyphi* (12 mm) and *B. subtilis* (13 mm) whereas the 900 $\mu\text{g}/\text{ml}$ one showed a maximum activity (16mm) towards *E. coli* and least at about 14 mm towards *S. paratyphi*, *B. subtilis* and *S. aureus*. The ligand and its other complexes show only a moderate antimicrobial activity positive towards all the test pathogenic bacteria ranging from 11 mm to 14 mm. Among all the five compounds tried with, the zinc complex, $[\text{Zn}(\text{4AAP-BCFI})_2(\text{H}_2\text{O})_2]^{2+}$ in its 900 mg/ml comes any close, with 16 mm, to the commercial standard, streptomycin (22 mm) at its 900 mg/ml concentration. The efficiency may be shown as $\text{Zn(II)} > \text{Ni(II)} > \text{Ligand} > \text{Cu(II)} > \text{Co(II)}$.

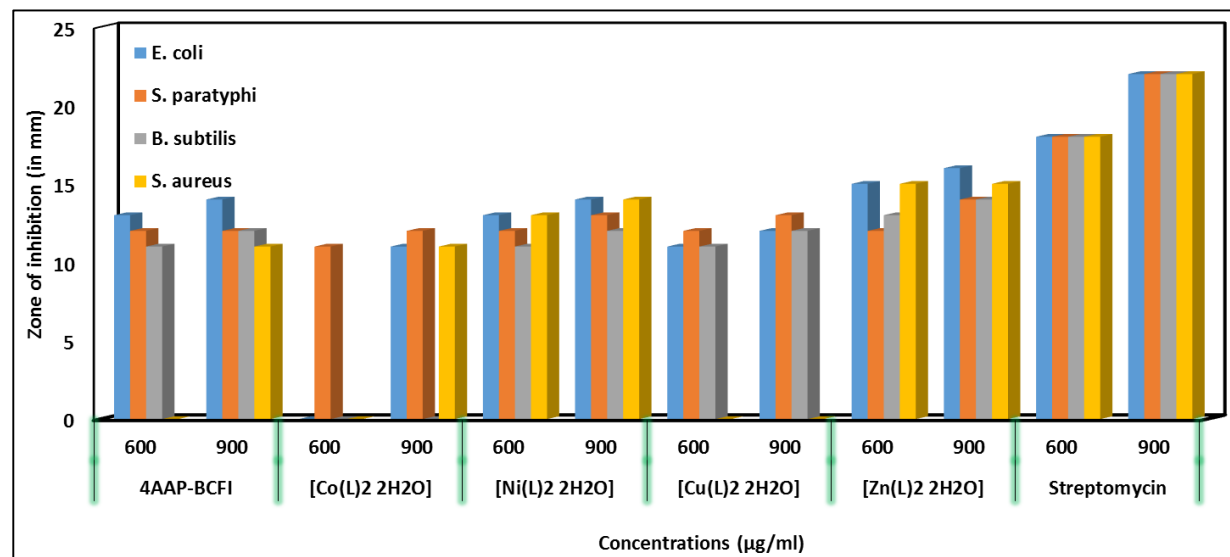
3C.2 *In-vitro* Antioxidant Property

The scavenging potential of the free radical DPPH (2,2-Diphenyl-1-picrylhydrazyl) has been investigated. The outputs are listed in **Table 3C.2**. The data indicate that $[\text{Co}(\text{L})_2(\text{H}_2\text{O})_2]$ and $[\text{Cu}(\text{L})_2(\text{H}_2\text{O})_2]$ in the same sequence has promising antioxidant action. In addition, the antioxidant activity of some of the complexes, the ligand, and the remaining complexes ranges from good to moderate (**Figure 3C.2**).

Table 3C.1 Zone of inhibition (mm) values of antimicrobial activity of the compounds

Compounds [#]	Conc. µg/ml	Zone of inhibition (in mm)			
		<i>Escherichia coli</i>	<i>Salmonella paratyphi</i>	<i>Bacillus subtilis</i>	<i>Staphylococcus aureus</i>
4AAP-BCFI	600	13	12	11	-
	900	14	12	12	11
[Co(L) ₂ (H ₂ O) ₂]	600	-	11	-	-
	900	11	12	-	11
[Ni(L) ₂ (H ₂ O) ₂]	600	13	12	11	13
	900	14	13	12	14
[Cu(L) ₂ (H ₂ O) ₂]	600	11	12	11	-
	900	12	13	12	-
[Zn(L) ₂ (H ₂ O) ₂]	600	15	12	13	15
	900	16	14	14	15
Standard (<i>Streptomycin</i>)	600	18	18	18	18
	900	22	22	22	22

L = 4AAP-BCFI

**Figure 3C.1** Histogrammatical presentation of the antibacterial activity of the **4AAP-BCFI** and its complexes

3C.3 Molecular Docking Studies

Molecular docking studies for the molecular energy-minimized ligand and its complexes of Co(II), Cu(II), Ni(II) and Zn(II) were performed using Discovery Studio, version 4.1 (Accelrys Inc., San Diego, CA, USA) under the Chemistry at Harvard Macromolecular Mechanics (CHARMM)Force Field. The three-dimensional structures were retrieved from Protein Data Bank (PDB ID: 2QLC and 3C94 with the target protein file prepared by removing the structural water

molecule, hetero atoms and co-factors while leaving only the residues associated with protein by using Accelrys Discovery Studio 4.1(ADS) tool Ligand-Fit module and the obtained results were scrutinized based on highest dock score and number of H-bonds by SS Viewer [12].

Table 3C.2 Minimum inhibition concentration (MIC) values of anti-scavenging activity of ligand and its complexes with ascorbic acid as the standard

Compound	IC ₅₀ (μM)
4AAP-BCFI (L)	43.35
[Co(L) ₂ 2H ₂ O]	21.92
[Ni(L) ₂ 2H ₂ O]	35.74
[Cu(L) ₂ 2H ₂ O]	13.53
[Zn(L) ₂ 2H ₂ O]	23.88
Standard	7.12

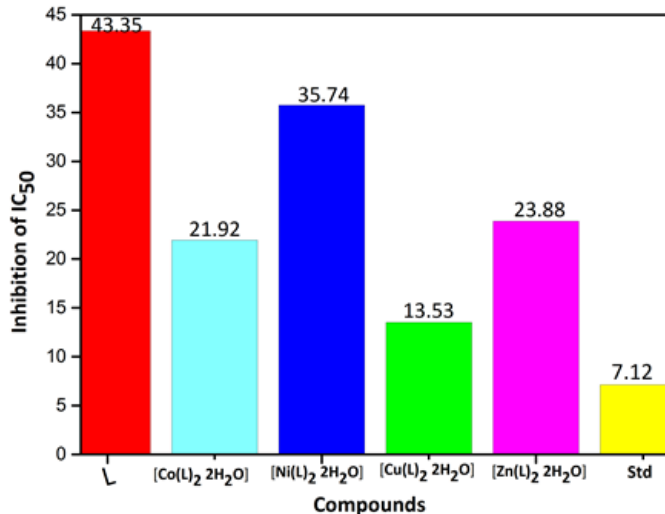


Figure 3C.2 Histogrammatical representation of the IC₅₀ inhibition values of DPPH radical scavenging activity of ligand and its complex

A DNA repair protein, (RadC) (PDB ID: 2QLC), and a spurious DNA annealing protein, ssDNA (PDB ID: 3C94) have been chosen as receptor proteins on the basis of their interesting structural nature and published information conducive to **4AAP-BCFI** and its Co(II), Ni(II), Cu(II) and Zn(II) Complexes. The ligand, **4AAP-BCFI** and its metal complexes were modelled for docking with the receptors of the DNA repair protein (RadC) (PDB ID: 2QLC) and ssDNA (PDB ID: 3C94). The results show that all the molecules interact with amino acid residues of the protein receptor through hydrogen bond interactions. The best visualized conformations are presented in **Figure 3C.3-3C.4**. While the corresponding binding energy values are summarized in **Table 3C.3-3C.4**. The affinities with the receptor, 2QLC, were found better than that with 3C94. The studies reveal that **4AAP-BCFI** (-76.624 kcal/mol) and its Zn(II) (-78.573 kcal/mol) and Ni(II) (-77.924 kcal/mol) complexes bind more strongly than the other complexes to both 2QLC and 3C94 receptors these docking studies may serve as a possible pharmacokinetic pathway mechanism to their *in vitro* antimicrobial activity.

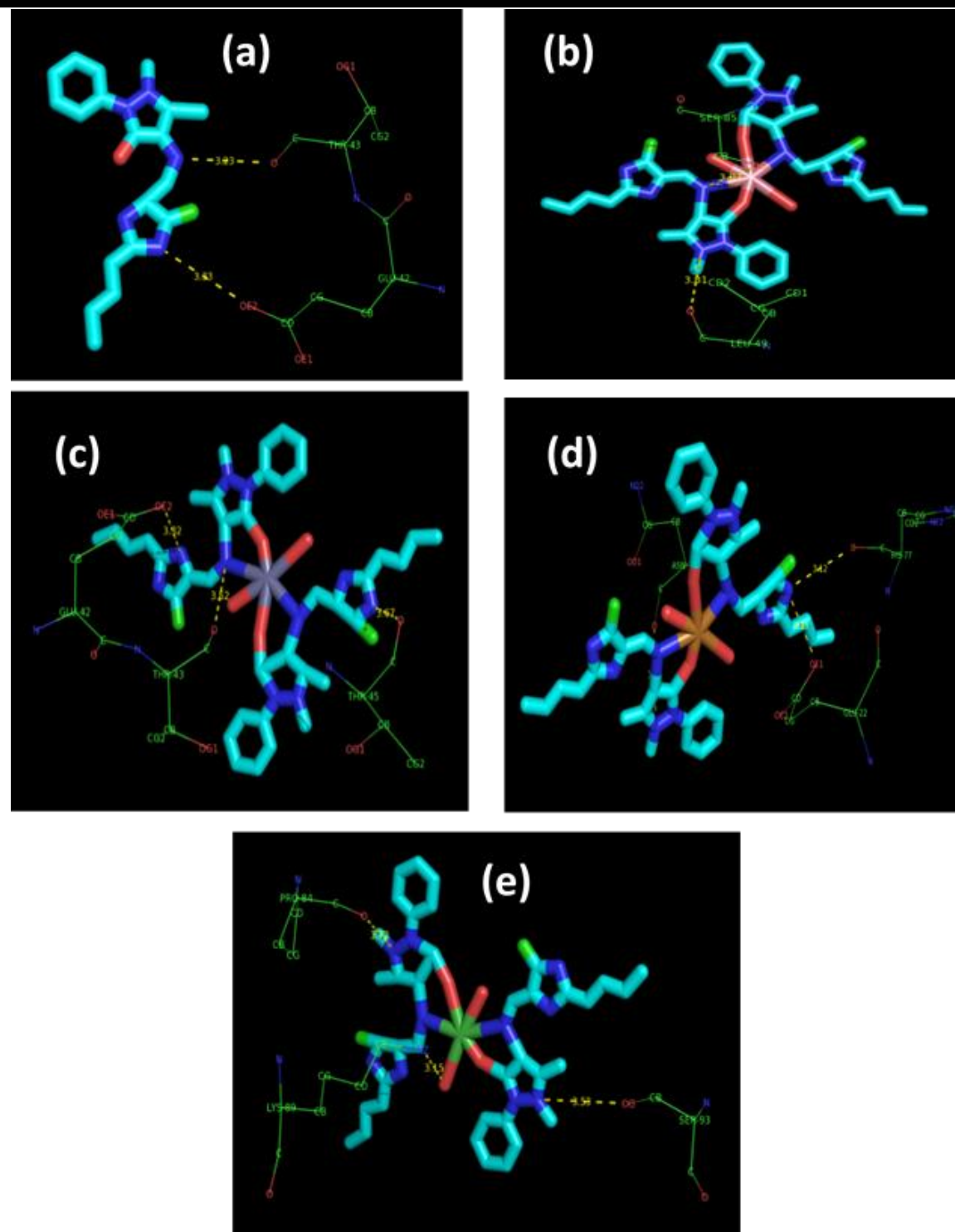


Figure 3C.3 3D docking poses of (a) 4AAP-BCFI, (b) Co(II) (c), Ni(II) (d) ,Cu(II) and (e) Zn(II) complexes with the binding site of the target protein of DNA-repair protein, RadC (PDB ID:(2QLC)

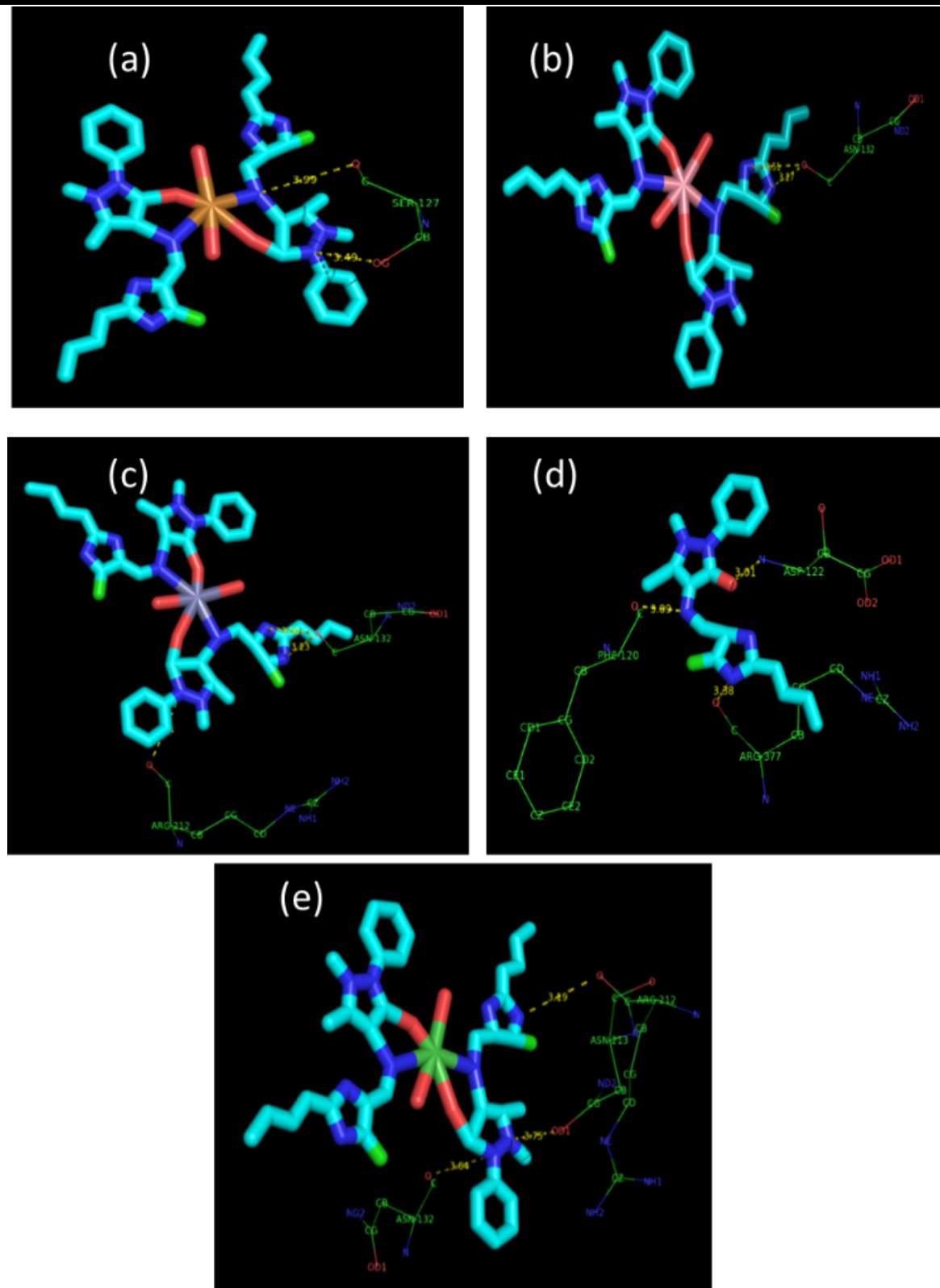


Figure 3C.4 3D docking poses of Co(II) (a), Ni(II) (b), Cu(II) (c), **4AAP-BCFI** ligand (d) and Zn(II) complexes (e) with 3C94 receptor binding protein

Table 3C.3 Molecular interactions of **4AAP-BCFI** and its metal complexes against 2QLC (DNA repair protein, RadC) binding protein (PDB ID: (2QLC)

Compounds [#]	2QLC receptors	Binder atoms	H-bond Distance (Å)	Best docking energy (kcal/mol)
4AAP-BCFI	THR43-O	NH	3.23	-76.624
	GLU42-OE2	NH	3.33	
[Co(II)(L)₂(H₂O)₂]	SER85-OG	NH	3.07	-75.968
	LEU94-O	NH	3.81	
[Ni(II)(L)₂(H₂O)₂]	LYS89-NZ	OC	3.15	-77.924
	SER93-OG	NH	3.53	
	PRO84-O	NH	3.72	
[Cu(II)(L)₂(H₂O)₂]	HIS77-O	NH	3.12	-76.121
	GLU22-OE1	NH	3.23	
	ASN114-O	NH	3.86	
[Zn(II)(L)₂(H₂O)₂]	THR45-O	NH	3.67	-78.573
	GLU42-OE2	NH	3.32	
	THR43-O	NH	3.52	

[#] L = **4AAP-BCFI****Table 3C.4** Molecular interactions of **4AAP-BCFI** and its complexes with 3C94 (Bacterial single stranded DNA) (ssDNA)-binding protein

Compounds [#]	Receptor(3C94) (Interacting atoms)	Ligand (atoms)	H-bond Distance(Å)	Docking energy (kcal/mol)
Co(II)(L)₂2H₂O]	ASN132-O	NH	3.27	-74.924
	ASN132-O	NH	3.51	
[Ni(II)(L)₂2H₂O]	ARG212-O	NH	3.19	-73.310
	ASN213-OD1	NH	3.75	
[Cu(II)(L)₂2H₂O]	ARG132-O	NH	3.64	-72.028
	ASN132-O	NH	3.23	
[Zn(II)(L)₂2H₂O]	ARG212-O	NH	3.74	-75.254
	ASN132-O	NH	3.50	
	ASN132-O	NH	3.23	
4AAP-BCFI	ASP122- O	NH	3.01	-75.024
	ARG377-O	NH	3.38	
	PHE120-O	NH	3.09	

L = **4AAP-BCFI**

3C.4 *In-silico* Drug Likeness Property of **4AAP-BCFI**

In order to assess the pharmacological potential, drug likeness metrics are determined. These characteristics have been estimated for a large number of compounds with known pharmacological properties, resulting in the construction of desirable parameter ranges. The famous Lipinski's rule of five [13], according to which absorption and penetration are more likely when the molecular weight (MW) is less than 500, is one of the usual rules to be examined for novel drug candidates. The ADME variables of the compound **4AAP-BCFI**, such as molecular weight (MW), HBA, HBD, MR, TPSA, BBB penetration, log K_p , and bioavailability score, were determined and the same are provided in **Table 3C.5**. The molecular weight (MW) is 371.86 g/mol, and the number of hydrogen bond acceptors (nHBA) and number of hydrogen bond donors (nHBD) values should be fewer than 10 and 5, respectively, according to the literature. The nHBA and nHBD values for **4AAP-BCFI** are 3 and 1, respectively. TPSA has a maximum value of 140 \AA^2 and a computed value of 67.97 \AA^2 for **4AAP-BCFI**. MR is a number that ranges between 40 -130. The **4AAP-BCFI** has an MR value of 106.50. **Table 3C.5** showed that GI absorption is high, with skin permeability (log K_p) being -5.26 and bio availability of 0.55. According to the example above, ligand **4AAP-BCFI** exhibits adequate biological properties with a drug-like character that should be investigated more in the future.

Table 3C.5. ADME properties of **4AAP-BCFI**

Molecular weight (MW)	371.86
Hydrogen Bond Donor (HBD)	1
Hydrogen bond acceptor (HBA)	3
Molar refractivity (MR)	106.50
Topological polar surface area (TPSA \AA^2)	67.97
Gastrointestinal (GI) absorption	High
Blood–brain barrier (BBB) penetration	Yes
Skin permeability (Log K_p (cm/s))	-5.26
Bioavailability	0.55

Note: The **4-AAP-BCFI** crystal part of this Chapter has been published in a Springer journal as Synthesis, DFT calculations and biological activity of a new Schiff base of 4-aminoantipyrine and its Co(II), Ni(II), Cu(II) and Zn(II) complexes and crystal structure of the Schiff base, Ajmeera Ramesh *et al*, *Research on Chemical Intermediates*, 2021, **47**, 4673-4697

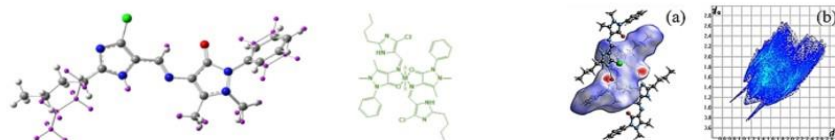
•Published: 02 August 2021

Synthesis, DFT calculations and biological activity of a new Schiff base of 4-aminoantipyrine and its Co(II), Ni(II), Cu(II) and Zn(II) complexes and crystal structure of the Schiff base

[Ajmeera Ramesh](#), [Ravinder Pawar](#), [Perugu Shyam](#) & [Allikayala Ramachandraiah](#)
Research on Chemical Intermediates volume **47**, pages 4673–4697, (2021)

Abstract

A novel Schiff base, (Z)-4-(((2-butyl-4-chloro-1H-imidazol-5-yl)methylene)amino)-1,5-dimethyl-2-phenyl-1H-pyrazol-3(2H)-one, labelled as **4AAP-BCFI**, is synthesized by adduction of 4-aminoantipyrine with 2-butyl-4-chloro-5-formylimidazole, and its molecular structure has been determined by a single-crystal X-ray diffraction studies. The cationic complexes of the **4AAP-BCFI** with Co(II), Ni(II), Cu(II) and Zn(II) metal ions are also synthesized and characterized. The mass spectral data and the spectral and other studies reveal the stoichiometry of the complexes as $[M(4AAP-BCFI)_2(H_2O)_2]^{2+}$ where M is the bivalent metal ion and that **4AAP-BCFI** acts as a bidentate ligand coordinating through the oxygen atom of the 4-aminoantipyrine ring and the nitrogen atom of the imine group.



References

- [1] Ushaiah, B.; Leela, D. S.; Ravi, M.; Anupama, B.; Perugu, S.; Kumari, C. G. Synthesis, Characterization, Antibacterial, DNA Binding and Cleavage Studies of Mixed Ligand Cu(II), Co(II) Complexes. *Journal of Fluorescence* **2014**, 24 (6), 1687–1699. <https://doi.org/10.1007/s10895-014-1456-2>.
- [2] Kavitha, P.; Laxma Reddy, K. Synthesis, Spectral Characterisation, Morphology, Biological Activity and DNA Cleavage Studies of Metal Complexes with Chromone Schiff Base. *Arabian Journal of Chemistry* **2016**, 9(4), 596–605. <https://doi.org/10.1016/j.arabjc.2012.09.001>.
- [3] Bheemarasetti, M.; Palakuri, K.; Raj, S.; Saudagar, P.; Gandamalla, D.; Yellu, N. R.; Kotha, L. R. Novel Schiff Base Metal Complexes: Synthesis, Characterization, DNA Binding, DNA Cleavage and Molecular Docking Studies. *Journl of Iranian. Chemical. Society* **2018**, 15 (6), 1377–1389. <https://doi.org/10.1007/s13738-018-1338-7>.
- [4] Kolhe, N. H.; Jadhav, S. S. Synthesis, Characterization and Biological Activity of Mixed Ligands Complexes of Quinolin-8-Ol and Substituted Chromones with Mn(II), Co(II), Ni(II) and Cu(II) Metal Ions. *Research on Chemical Intermediates* **2019**, 45 (3), 973–996. <https://doi.org/10.1007/s11164-018-3656-x>.
- [5] Ha, N. Van; Dat, D. T.; Nguyet, T. T. Stereoelectronic Properties of 1,2,4-Triazole-Derived N-Heterocyclic Carbenes - A Theoretical Study. *VNU J. Sci. Nat. Sci. Technol.* **2019**, 35 (4). <https://doi.org/10.25073/2588-1140/vnunst.4935>.
- [6] Frisch, M.J.; Trucks, G.W.; Schlegel, H.B.; Scuseria, G.E.; Robb, M.A.; J.R.; Cheeseman, et al. Gaussian 16, Revision C.01. Gaussian, Inc., Wallingford CT **2016**.
- [7] Lu, T.; Chen, F. Multiwfn: A Multifunctional Wavefunction Analyzer. *Journal of Computational Chemistry* **2012**. <https://doi.org/10.1002/jcc.22885>.
- [8] Ravinder, P.; Subramanian, V. Substitution Effects of Diborane on the Interaction with Borazine (Inorganic Benzene). *Journal of Physical Chemistry A* **2010**, 114 (17), 5565–5572. <https://doi.org/10.1021/jp910717j>.
- [9] Spackman, P. R.; Turner, M. J.; McKinnon, J. J.; Wolff, S. K.; Grimwood, D. J.; Jayatilaka, D.; Spackman, M. A. CrystalExplorer: A Program for Hirshfeld Surface Analysis, Visualization and Quantitative Analysis of Molecular Crystals. *Journal of Applied Crystallography* **2021**, 54 (3), 1006–1011. <https://doi.org/10.1107/S1600576721002910>.
- [10] McKinnon, J. J.; Jayatilaka, D.; Spackman, M. A. Towards Quantitative Analysis of Intermolecular Interactions with Hirshfeld Surfaces. *Chemical Communication* **2007**, No. 37, 3814. <https://doi.org/10.1039/b704980c>.
- [11] Osowole, A. A.; Kolawole, G. A.; Fagade, O. E. Synthesis, Physicochemical, and Biological Properties of Nickel(II), Copper(II), and Zinc(II) Complexes of an Unsymmetrical Tetradentate Schiff Base and Their Adducts. *Synthetic Reaction Inorganic, Meterials Nano-Metal Chemistry* **2005**, 35 (10), 829–836. <https://doi.org/10.1080/15533170500358168>.
- [12] Perugu, S.; Jalli, H.; Bhanoori, M.; *International Journal of Innovative Tech. Explor. Eng.* 2013, (3), 4.
- [13] Walters, W. P.; Murcko, A.; Murcko, M. A. Recognizing Molecules with Drug-like Properties. *Current Opinian in Chemical Biology* **1999**, (3), 384-387. [https://doi.org/10.1016/S1367-5931\(99\)80058-1](https://doi.org/10.1016/S1367-5931(99)80058-1).

CHAPTER – IV

SYNTHESIS, CHARACTERIZATION, CRYSTAL STRUCTURE DETERMINATION, COMPUTATIONAL MODELLING AND BIOLOGICAL STUDIES OF A NEW (2-HYDROXY-5- METHYLPHENYL)(1H-PYRAZOL-4- YL)METHANONE AND ITS Zn(II), Cu(II), Ni(II) AND Co(II) COMPLEXES

CHAPTER-IV

SYNTHESIS, CHARACTERIZATION, CRYSTAL STRUCTURE DETERMINATION, COMPUTATIONAL MODELLING AND BIOLOGICAL STUDIES OF A NEW (2- HYDROXY-5-METHYLPHENYL)(1H-PYRAZOL-4-YL)METHANONE AND ITS Zn(II), Cu(II), Ni(II) AND Co(II) COMPLEXES

In this chapter the studies of (2-hydroxy-5-methylphenyl)(1H-pyrazol-4-yl)methanone (**HMPM**) and its metal complexes are discussed. Spectral (FTIR, UV-Visible absorption, ¹H and ¹³C NMR, fluorescence), single crystal XRD, molecular modelling, molecular docking, and bioactivity studies are presented. The **HMPM**, has been prepared by condensation of 3-formyl-6-methylchromone with thiosemicarbazide. The details of synthesis of **HMPM** and its complexes have been described in **Chapter-II**.

This Chapter is divided into 3 Parts, **Part-A**, **Part-B** and **Part-C**. **Part-A** discusses the studies of **HMPM** ligand and its metal complexes. **Part-B** covers the single crystal XRD studies, molecular modelling, and Hirshfeld surface analysis of $[\text{Zn}(\text{HMPM})_4\text{Cl}_2]$ complex. Correlation of the XRD data with computational data is also described. **Part-C** presents the biological activity studies of **HMPM** and $\text{M}(\text{HMPM})_4\text{Cl}_2$ complexes and molecular docking studies on the 2QLC and 2QV4 proteins.

PART-A

SPECTRAL CHARACTERIZATION, (2-HYDROXY-5-METHYLPHENYL)(1H-PYRAZOL-4-YL)METHANONE (HMPM) AND ITS Zn(II), Cu(II), Ni(II) AND Co(II) COMPLEXES

4A.1 Physical and Elemental Analysis

Table 4A.1 summarizes the physical and analytical data for **HMPM** and its metal complexes. The chemical structures presented in **Figure 4A.1** agree well to the elemental analysis results.

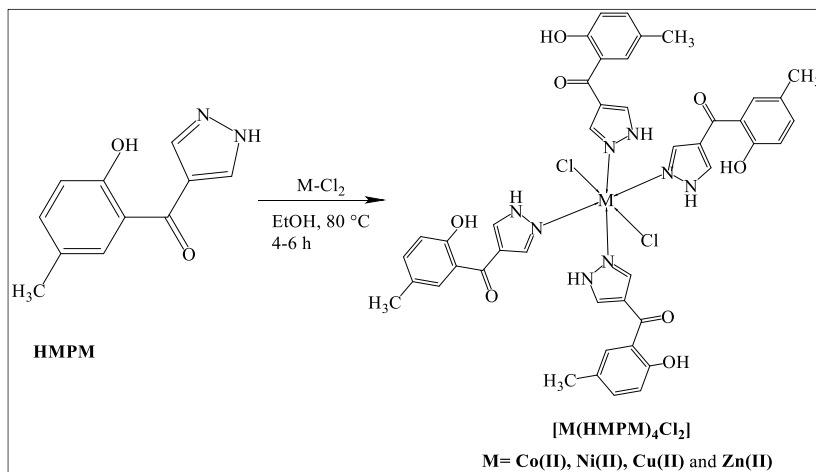


Figure 4A.1 Schematic of the synthesis of $[\text{M}(\text{HMPM})_4\text{Cl}_2]$ from **HMPM**

Table 4A.1 Physical and analytical data of **HMPM** and $[\text{M}(\text{HMPM})_4\text{Cl}_2]$

Compound	Colour	M.P (°C)	Formulae	Elemental Analysis % found (calculated)			
				C	H	N	O
HMPM	White	198.7	$\text{C}_{11}\text{H}_{10}\text{N}_2\text{O}_2$	(65.34) 65.31	(4.98) 4.96	(13.85) 13.85	(15.82) 15.80
$[\text{Co}(\text{HMPM})_4\text{Cl}_2]$	Orange	>254	$\text{C}_{44}\text{H}_{40}\text{Cl}_2\text{N}_8\text{O}_8\text{Co}$	(56.30) 56.26	(4.30) 4.28	11.94 11.96	(13.64) 13.58
$[\text{Ni}(\text{HMPM})_4\text{Cl}_2]$	Purple	255.8	$\text{C}_{44}\text{H}_{40}\text{Cl}_2\text{N}_8\text{O}_8\text{Ni}$	(56.31) 56.30	(4.30) 4.25	(11.94) 11.95	(13.64) 13.57
$[\text{Cu}(\text{HMPM})_4\text{Cl}_2]$	Deep brown	>258	$\text{C}_{44}\text{H}_{40}\text{Cl}_2\text{N}_8\text{O}_8\text{Cu}$	(56.03) 56.00	(4.27) 4.25	(11.88) 11.85	(13.57) 13.50
$[\text{Zn}(\text{HMPM})_4\text{Cl}_2]$	Cream white	>265.3	$\text{C}_{44}\text{H}_{40}\text{Cl}_2\text{N}_8\text{O}_8\text{Zn}$	(55.92) 55.91	(4.27) 4.27	(11.86) 11.86	(13.54) 13.53

4A.2 FT-IR Spectral Studies

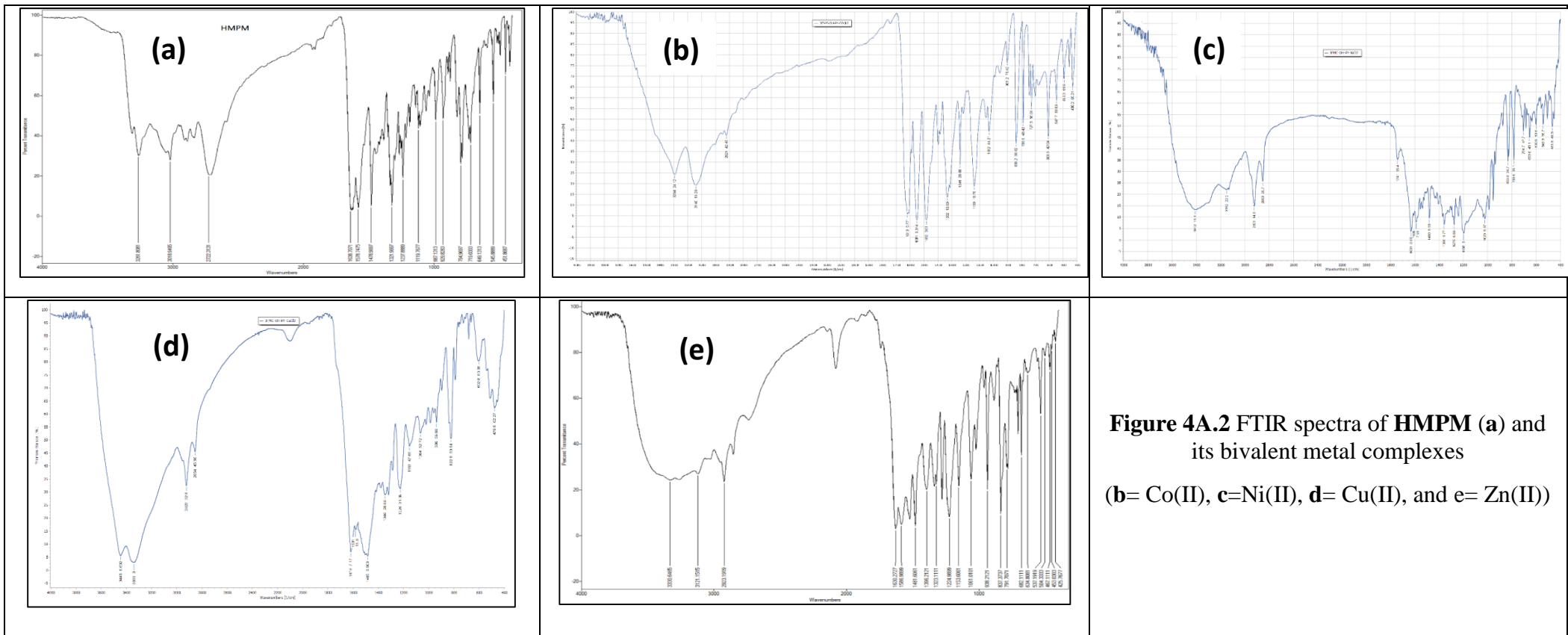
The FTIR infrared spectra of **HMPM** and a pair of its $[\text{M}(\text{HMPM})_4\text{Cl}_2]$ complexes are shown in **Figure 4A2**. The band at 1578 cm^{-1} characteristic of $\nu(\text{C}=\text{N})$ azomethine in the free ligand, is found to be unusually shifted to higher frequency at $1581\text{-}1589 \text{ cm}^{-1}$ after coordination in all $[\text{M}(\text{HMPM})_4\text{Cl}_2]$ complexes. Some important IR data are listed in **Table 4A.2**. Usually the $-\text{C}=\text{N}-$ stretching frequency of Schiff bases undergoes bathochromic shift to lower frequencies upon complexation to many of the d-block elements though this shift is less in the case of endocyclic $-\text{C}=\text{N}-$ in aromatic rings. The present feature of hypsochromic shift of $-\text{C}=\text{N}-$ stretching frequency from 1578 to 1589 cm^{-1} does not only indicate that **HMPM** binds to metal ion via the imidazole sp^2 nitrogen atom but also that there is a flow of electron cloud from the metal to the aromatic imidazole ring [1]. The complex shows additional band at 431 cm^{-1} and 425 cm^{-1} due to the asymmetric and symmetric stretching frequencies of the two M-Cl bonds and 455 to 467 cm^{-1} corresponds to M-N bonds. These low frequency bands support the involvement of chlorides in coordination. The failure of silver nitrate test and poor electrical conductivity in DMF, DMSO and water is supports this idea.

Table 4A.2 Some important FTIR spectral data of **HMPM** and its complexes in cm^{-1}

Compound	$\nu\text{C}=\text{N}$	$\nu\text{C}=\text{O}$	$\nu\text{C-H}_{\text{aliph}}$	νNH	νOH	$\nu\text{M-Cl}$	$\nu\text{M-N}$
HMPM	1578	1638	2722	3018	3261	-	-
[\text{Co}(\text{HMPM})_4\text{Cl}_2]	1581	1619	2921	3140	3294	430	463
[\text{Ni}(\text{HMPM})_4\text{Cl}_2]	1586	1630	2923	3121	3326	431	466
[\text{Cu}(\text{HMPM})_4\text{Cl}_2]	1589	1619	2923	3140	3293	430	455
[\text{Zn}(\text{HMPM})_4\text{Cl}_2]	1586	1630	2923	3121	3330	425	467

4A.3 Electronic Spectral Studies

The electronic spectra of ligand and its complexes are recorded in DMSO at room temperature. A few of them are shown in through **Figure 4A.3**. The spectrum of **HMPM** exhibits two bands at 283 nm , 323 nm . The 283 nm band is attributed to the $\pi\text{-}\pi^*$ of the whole molecule and the band at 323 nm to the $\text{n}\text{-}\pi^*$ of the pyrazole ring. However, the complexes, $[\text{M}(\text{HMPM})_4\text{Cl}_2]$ are insoluble in many organic solvents but moderately only in DMF and DMSO.



The electronic absorption spectrum of $[\text{Co}(\text{HMPM})_4\text{Cl}_2]$ complex exhibits bands at 312 nm, 380 nm due to charge transfer transitions. While absorption at 474 nm is due to d-d transitions. The results indicate are an octahedral geometry for this complex.

$[\text{Ni}(\text{HMPM})_4\text{Cl}_2]$ complex exhibits bands at 298 and 393 nm, attributed to the charge transfer transitions while the peak at 540 nm to $3\text{Ag}(\text{F}) \rightarrow 4\text{T}1(\text{F})$ d-d transitions. These findings also point to an octahedral geometry for $[\text{Ni}(\text{HMPM})_4\text{Cl}_2]$ [2].

The wak and broad band observed for $[\text{Cu}(\text{HMPM})_4\text{Cl}_2]$ complex at 292 nm, 300 nm attributable to charge transfer transitions while the peak at 443 nm corresponds to the $^2\text{B}_{1g} \rightarrow ^2\text{E}_g$ d-d transition. An octahedral geometry is tentatively assigned to this complex. Poor solubility and negative silver nitrate test also suggest this complex through **Cu-complex** prefer square planer to octahedral due to the John-Teller Effect.

Two absorption bands are observed for the $[\text{Zn}(\text{HMPM})_4\text{Cl}_2]$ complex at 321 nm and 345 nm with a shoulder at 425 nm. Since the zinc ion is not expected to show any d-d transition due to its d^{10} configuration, these two bands are attributed to be originating from the ligand's $\pi-\pi^*$ and $n-\pi^*$ transitions, respectively with a red-shift (bathochromic shift) and the shoulder at 425 nm may be from the ligand-to-metal charge transfer transition (LMCT) [3].

4A.4 ^1H and ^{13}C -NMR Spectral Studies

The ^1H and ^{13}C NMR spectra of **HMPM** presented in **Figure 4A.4** and they are consistent with the structures of the **HMPM**. The low contact-shift of many peaks, except that of the ^1H NMR chemical shift of the NH imidazole proton supports that the metal is bound to the sp^2 nitrogen and that the N-Zn bond seems to be orthogonal to the π -cloud of the aromatic ring (or coplanar to the ring).

NMR data; ^1H NMR spectrum (DMSO-d₆; δ , ppm): 2.45 (s, 3H, CH_3), 7.66-8.70 (q, 2H, $\text{C}_{\text{ar}}-\text{H}_2$), 7.91 (s, 1H, $\text{C}_{\text{ar}}-\text{H}$), 8.54 (s, 1H, $\text{C}_{\text{ar}}-\text{H}$), 9.27 (s, 1H, $\text{C}_{\text{ar}}-\text{H}$), 9.79 (s, 1H, NH), 13.30(broad, 1H, OH); ^{13}C NMR spectrum (DMSO-d₆; δ , ppm): 20.95 (CH_3), 117.28-118.32 (2 CH), 120.54 (CH), 124.91 (CH), 131.99 (CH), 134.42(C), 145.53 (CHN), 134.42(C), 163.94(C-OH), 174.80(C=O).

4A.5 Deprotonation Equilibria for HMPM and $[\text{Zn}(\text{HMPM})_4\text{Cl}_2]$

The ligand, **HMPM**, is essentially a weak acid due to the presence of the phenol moiety which would undergo deprotonation in alkaline medium. In order to know whether the deprotonation would at all result in any resonance between benzenoid phenolate and quinonoid structures as in ligand **HMPM** and complex $[\text{Zn}(\text{HMPM})_4\text{Cl}_2]$, we have pursued to check the

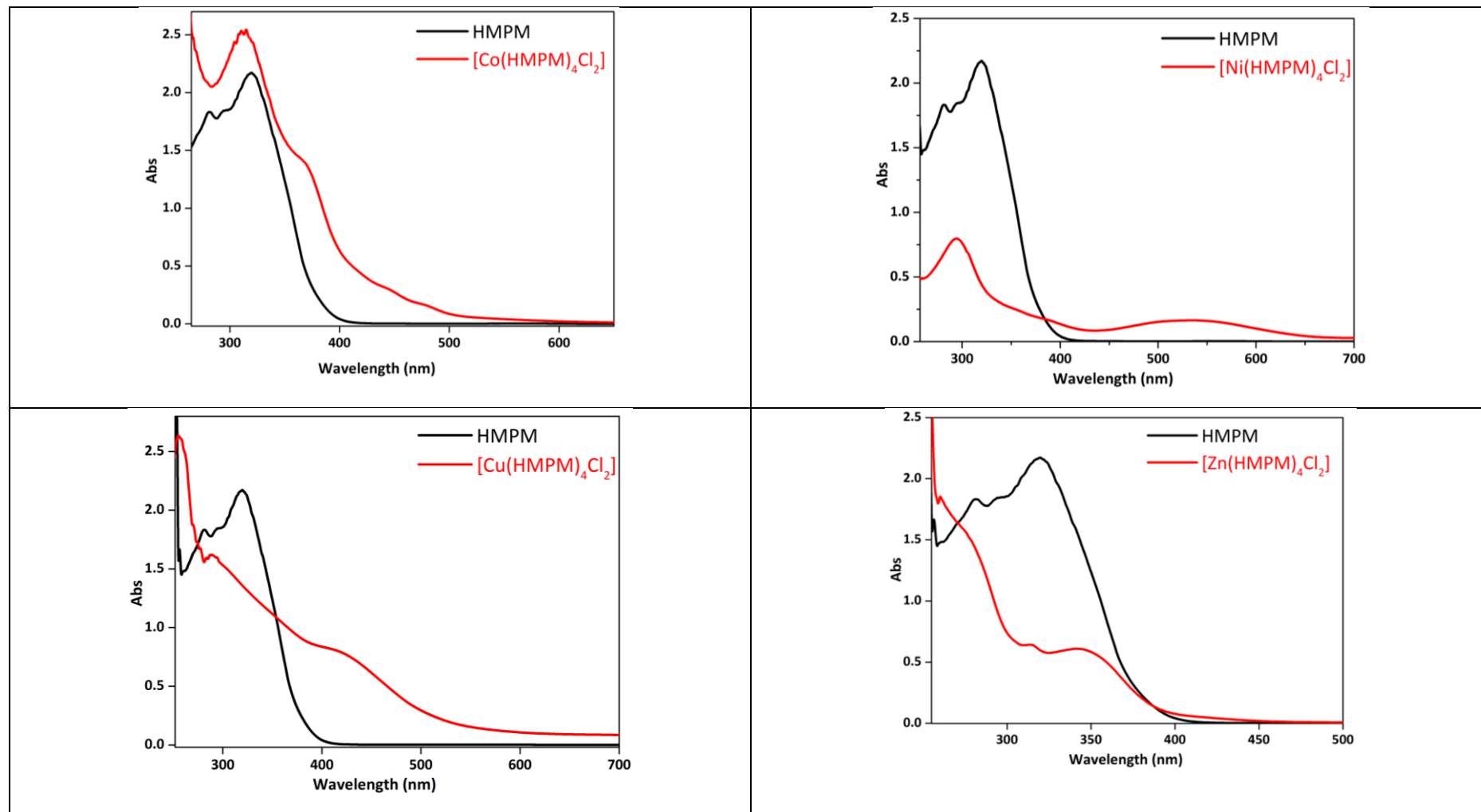


Figure 4A.3 Superimposed electronic spectra of **HMPM** and its complexes (all at their 2×10^{-5} M) in DMSO

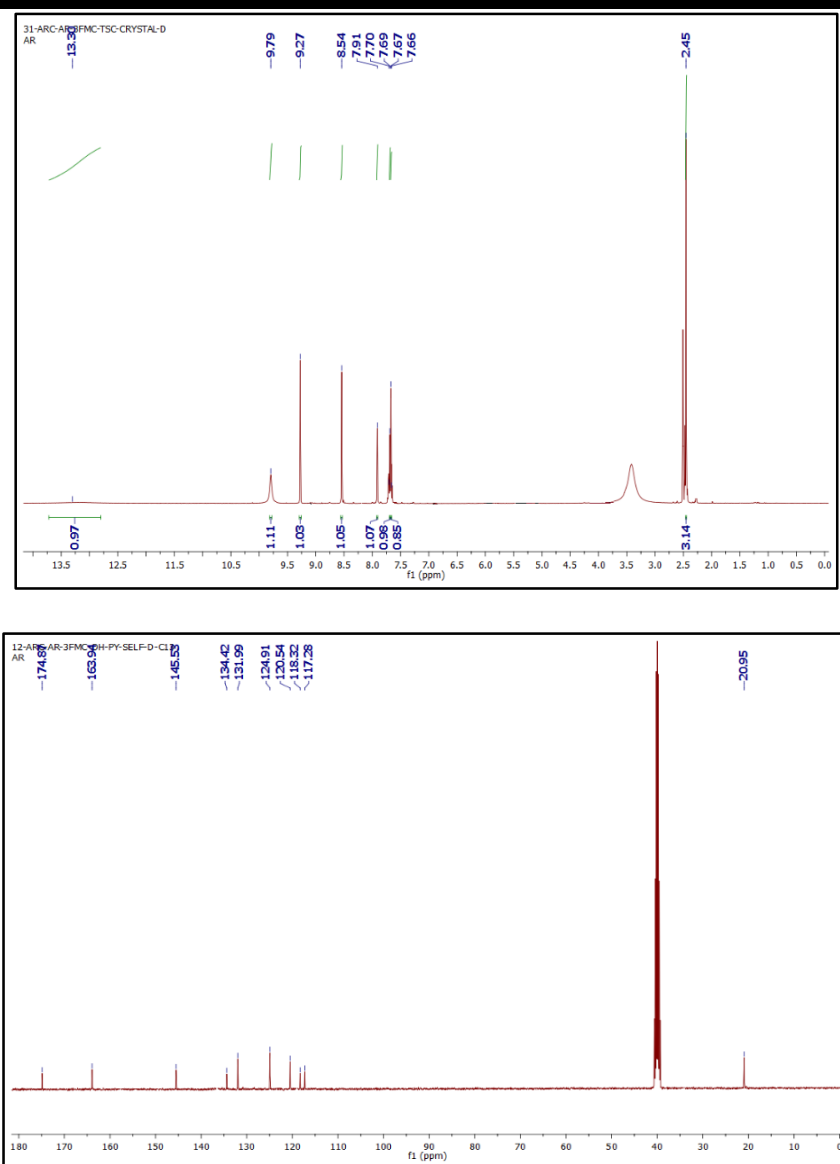
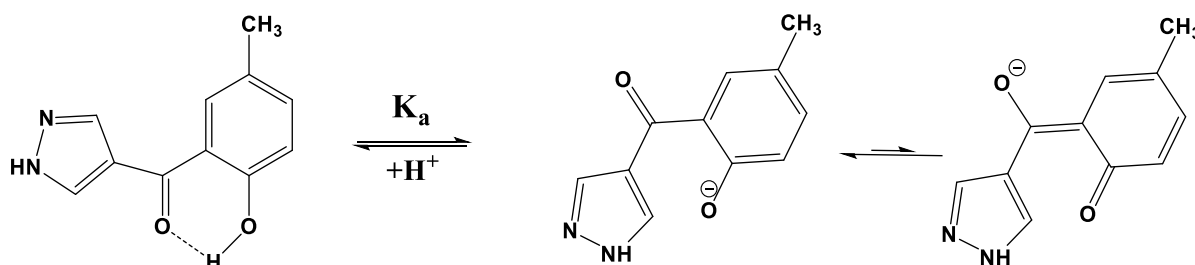


Figure 4A.4 ^1H and ^{13}C NMR spectra of **HMPM**

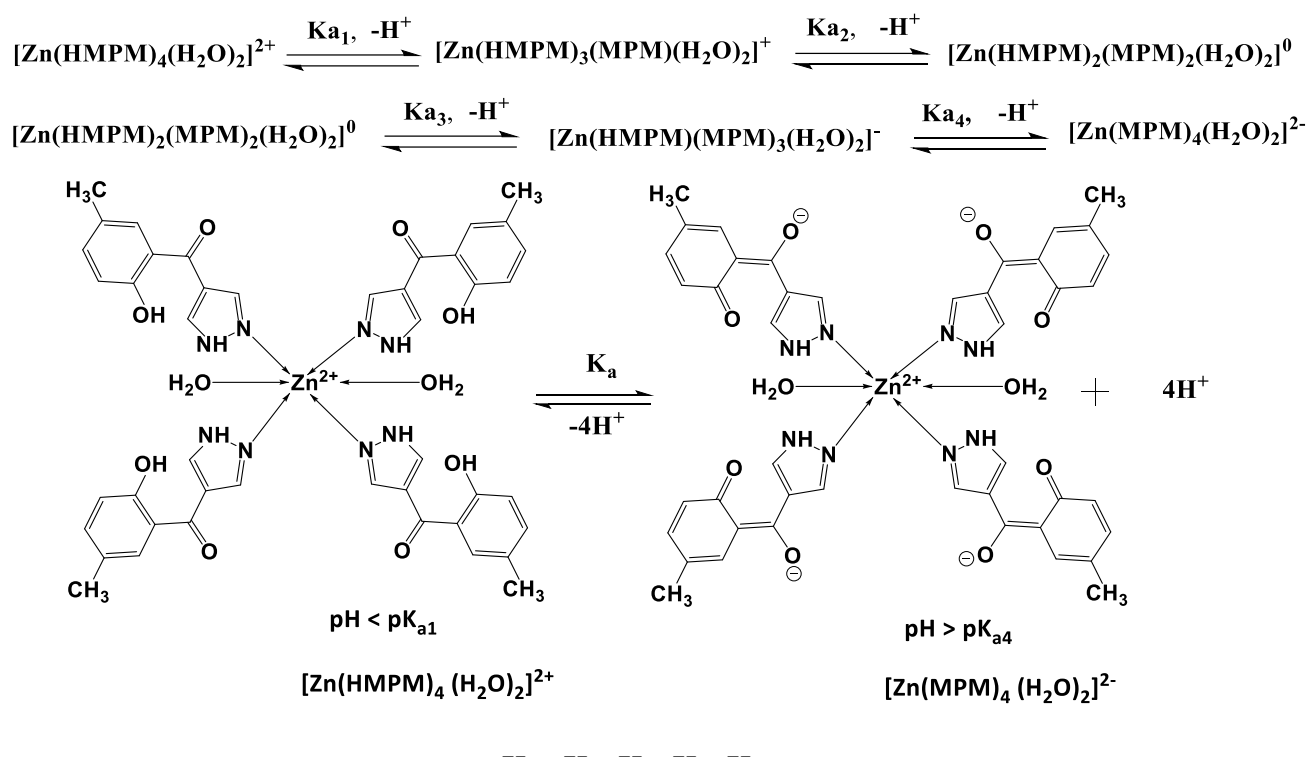
electronic spectra of the ligand and the complex at extreme low and high pHs. The electronic spectra for both **HMPM** and $[\text{Zn}(\text{HMPM})_4\text{Cl}_2]$ are shown in **Figure 4A.5(a)** at pH = 2 and pH = 12 in aqueous DMSO. The spectral patterns of **HMPM** in non-aqueous DMSO and in aqueous medium at pH = 2 look alike suggesting that the presence of excess protons along with water does not affect the gross electronic behaviour of **HMPM**. But the bathochromic shift of the λ_{max} of **HMPM** from about 350 nm in pH = 2 to about 450 nm in pH = 12 in aqueous-DMSO media. This indicates deprotonation of the phenol followed by change towards a quinonoid electronic form. Reversal of the shift by acidification of the solution of pH = 12 proves that the spectral variation is not due to any irreversible chemical reaction of **HMPM**.

The single crystal X-Ray diffraction studies of $[\text{Zn}(\text{HMPM})_4\text{Cl}_2]$ discussed in the next section proves beyond doubt that **HMPM** act as a monodentate ligand and that its phenolic group does not get deprotonated during complexation. Hence, we expect not much change in the electronic spectrum of **HMPM** in aqueous medium (DMSO) and that in an aqueous medium of low pH but some change if the pH is alkaline due to the deprotonation and possible onset of a quinonoid structure. However, we would expect ligand substitution of chloride by water as $[\text{Zn}(\text{HMPM})_4\text{Cl}_2] \rightarrow [\text{Zn}(\text{HMPM})_4(\text{H}_2\text{O})_2]^{2+}$ in aqueous buffers and also due to pH effect since water is spectrochemically stronger ligand than chloride and then due to the usual deprotonation followed by emergence of a quinonoid structure at the **HMPM** in $[\text{Zn}(\text{HMPM})_4(\text{H}_2\text{O})_2]^{2+}$.

The pH-dependent electronic spectra of $[\text{Zn}(\text{HMPM})_4\text{Cl}_2]$ are shown in **Figure 4A.5(b)**, which shows a change of spectra by both medium and pH. Thus, the spectral variation of $[\text{Zn}(\text{HMPM})_4\text{Cl}_2]$ in DMSO and aqueous solution of pH=2 is due to the formation of $[\text{Zn}(\text{HMPM})_4(\text{H}_2\text{O})_2]^{2+}$ in aqueous medium. Like in the case of **HMPM**, there is a bathochromic shift observed for $[\text{Zn}(\text{HMPM})_4(\text{H}_2\text{O})_2]^{2+}$ from pH=2 to pH=12 indicating the deprotonation of the phenol in the complex too. However, the shift is not as much as that in the ligand, indicating that the benzenoid structure is more preferred in the complex. Conductometric and pH-metric titrations of **HMPM** and $[\text{Zn}(\text{HMPM})_4(\text{H}_2\text{O})_2]^{2+}$ against a standard NaOH reveals the consumption of only one phenolic equivalents per mole of the complex while a pH-metric titration of it that the complex molecule releases the first proton readily but hardly the rest, as expected for any polybasic weak acids. In **Scheme 2** is shown the acid-base equilibria for both **HMPM** and $[\text{Zn}(\text{HMPM})_4(\text{H}_2\text{O})_2]^{2+}$ and plausible consecutive acid-base equilibria for $[\text{Zn}(\text{HMPM})_4(\text{H}_2\text{O})_2]^{2+}$. We may conclude that $K_{a1} >> K_{a2} > K_{a3} > K_{a4}$.



Scheme 4A.1 Protonation-deprotonation equilibrium for **HMPM**



$$K_a = K_{a1} \cdot K_{a2} \cdot K_{a3} \cdot K_{a4}$$

Scheme 4A.2 Consecutive protonation-deprotonation equilibria for $[\text{Zn}(\text{HMPM})_4(\text{H}_2\text{O})_2]$

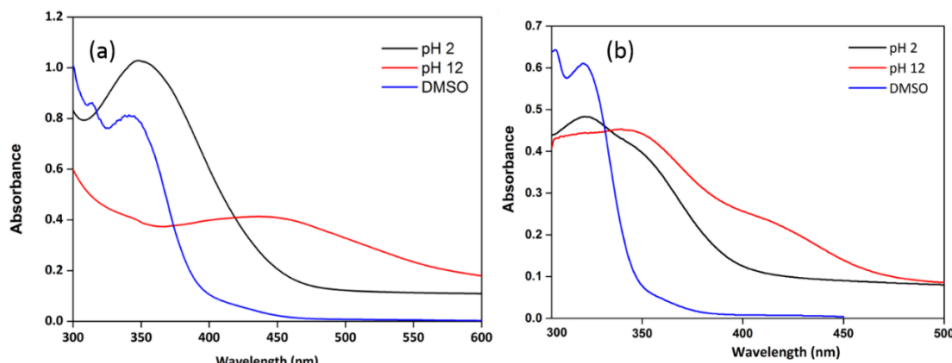


Figure 4A.5 Electronic spectra of (a) HMPM (2×10^{-4} M) and (b) $[\text{Zn}(\text{HMPM})_4\text{Cl}_2]$ (2×10^{-4} M) in aqueous buffers

4A.6 Fluorescence Spectra

The luminescence spectra of the ligand **HMPM** and complex $[\text{Zn}(\text{HMPM})_4\text{Cl}_2]$ over the wavelength range of 400 -800 nm are shown in **Figure 4A.7**. The ligand exhibits two emission bands at around 475 and 505 nm with a shoulder at about 540 nm whereas the complex fluoresces at about 510 nm [4]. A series of eye-vision photos of the solutions of **HMPM** and $[\text{Zn}(\text{HMPM})_4\text{Cl}_2]$ in varied media are presented in **Figure 4A.6** under the excitation of an UV light. The Zn(II) complex sports a faint blue tinge and the ligand a dim greenish glow to naked eye.

The unusual light blue glow displayed by $[\text{Zn}(\text{HMPM})_4\text{Cl}_2]$ complex may mean the prospective of its utility as a nonlinear optical (NLO) material for blue light emitting diode (LED) devices.

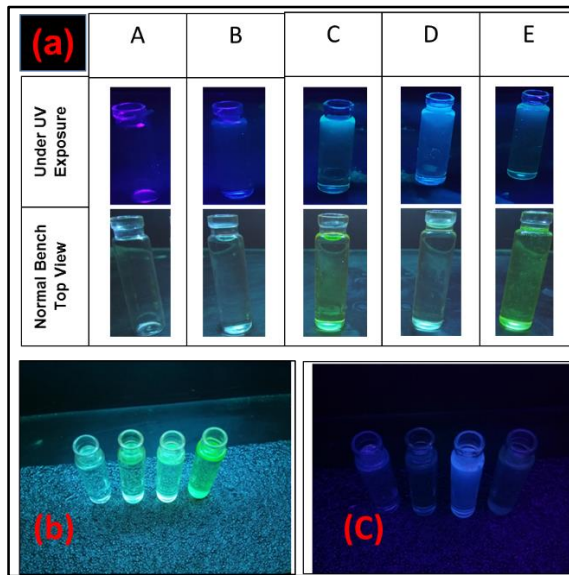


Figure 4A.6 Visual fluorescence phenomena checking (a) of individual samples of (A) empty vial, (B) HMPM in DMSO, (C) HMPM in alkaline DMSO, (D) $[\text{Zn}(\text{HMPM})_4\text{Cl}_2]$ in DMSO and (E) $[\text{Zn}(\text{HMPM})_4\text{Cl}_2]$ in alkaline DMSO; (b) relative view of (left to right) HMPM in DMSO, HMPM in alkaline DMSO, $[\text{Zn}(\text{HMPM})_4\text{Cl}_2]$ in DMSO and $[\text{Zn}(\text{HMPM})_4\text{Cl}_2]$ in alkaline DMSO and (c) relative view in pinch dark under the exposure to UV light of (left to right) HMPM in DMSO, HMPM in alkaline DMSO, $[\text{Zn}(\text{HMPM})_4\text{Cl}_2]$ in DMSO and $[\text{Zn}(\text{HMPM})_4\text{Cl}_2]$ in alkaline DMSO

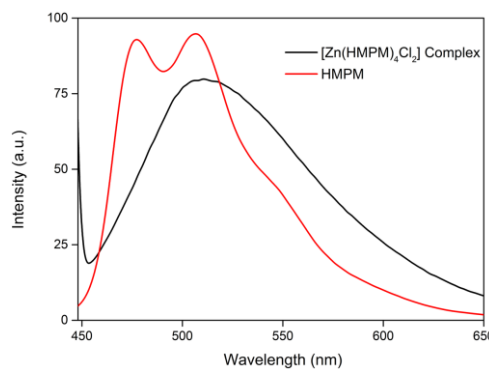


Figure 4A.7 Superimposed fluorescence emission spectra of HMPM (4×10^{-4} M) and $[\text{Zn}(\text{HMPM})_4\text{Cl}_2]$ (1×10^{-4} M) in DMSO

4A.7 Electron Spin Resonance Spectroscopic Studies of $\text{Cu}(\text{HMPM})_4\text{Cl}_2$ Complex

The polycrystalline ESR spectrum of the $\text{Cu}(\text{HMPM})_4\text{Cl}_2$ complex is shown in **Figure 4A.8**. The computer simulation calculates g_{\parallel} and g_{\perp} to be 2,396 and 2,220, respectively. The presence of unpaired electrons in the dx^2-y^2 (ground state) metal orbital is indicated by the fact that $g_{\parallel} > g_{\perp} > 2.0023$ which also suggests an octahedral around the Cu(II) core [5]. The fact that the,

provided value 2.3 is less than 2.3 indicates that the metal and ligand are covalently bound. G, commonly known as the magnetic exchange interaction parameter, is derived using the following formula,

$$G = \frac{g_{\parallel} - 2.0023}{g_{\perp} - 2.0023}$$

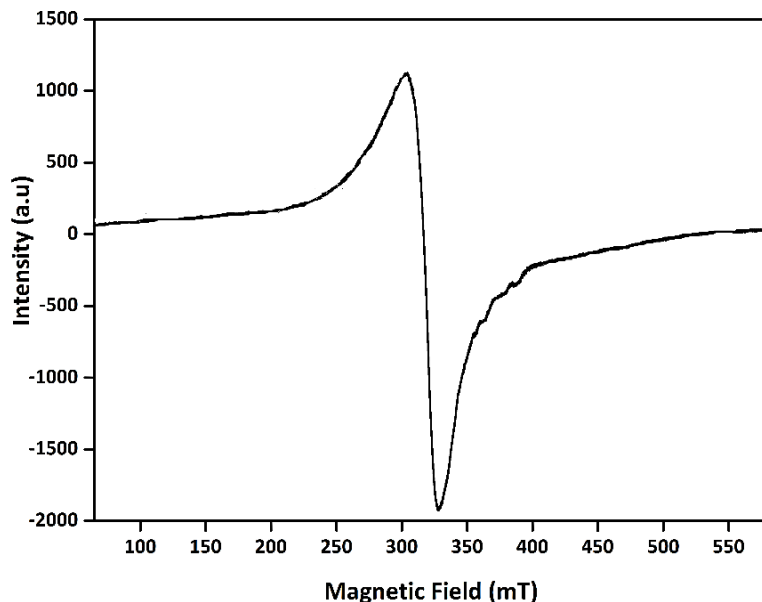


Figure 4A.8 Polycrystalline X-band ESR spectrum of $[\text{Cu}(\text{HMPM})_4\text{Cl}_2]$

is determined to be around 1.07. Moreover, it is widely known, as stated by Hathaway and Billing, that a value of $G < 4$ indicates a significant magnetic connection between nearby metal centres in solid state, whereas a value of $G > 4$ indicates weak interactions [6].

PART-B

MOLECULAR STRUCTURE DETERMINATION BY SINGLE CRYSTAL X-RAY DIFFRACTION AND HIRSHFELD SURFACE ANALYSIS OF $[\text{Zn}(\text{HMPM})_4\text{Cl}_2]$ AND MOLECULAR MODELLING OF $[\text{M}(\text{HMPM})_4\text{Cl}_2]$ COMPLEXES

4B.1 Crystal Structure Analysis of $[\text{Zn}(\text{HMPM})_4\text{Cl}_2]$

Single crystals suitable for XRD studies could not be successful for **HMPM** and **$[\text{M}(\text{HMPM})_4\text{Cl}_2]$** Where, M is other than Zn.

The complex, **$[\text{Zn}(\text{HMPM})_4\text{Cl}_2]$** , crystallizes in the centrosymmetric monoclinic $P2_1/n$ space group with half complex molecule in the asymmetric unit. The crystallographic unit cell and the molecular structure of **$[\text{Zn}(\text{HMPM})_4\text{Cl}_2]$** in its ORTEP mode are shown in **Figure 4B.1** and **4B.2** representing the number scheme of atoms shown here is used throughout the discussion.

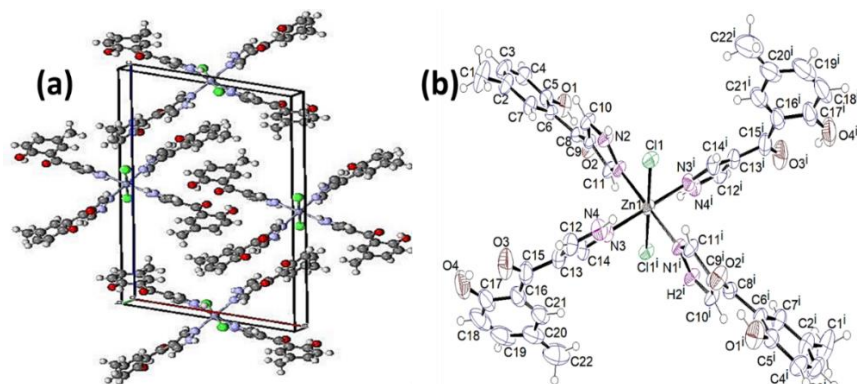


Figure 4B.1 Unit cell and molecular packing pattern **(a)** and ORTEP representation **(b)** of $[\text{Zn}(\text{HMPM})_4\text{Cl}_2]$ in its crystalline state. The thermal ellipsoids are drawn at 50% probability level

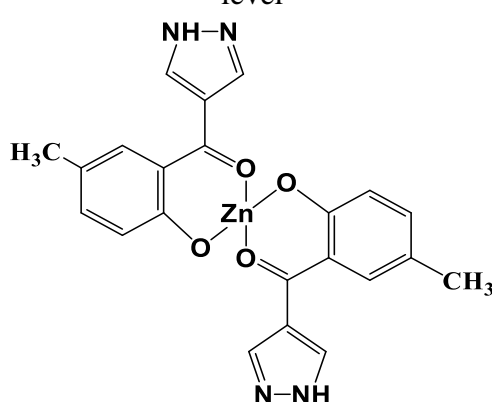


Figure 4B.2 Speculatively expected structure for $[\text{Zn}(\text{HMPM})_2]$ complex

It is surprising that the complex is not formed as the one shown in **Figure 4B.2** though there is no issue against it. The complex $[\text{Zn}(\text{HMPM})_4\text{Cl}_2]$ comprises of one Zn(II) cation, two chloride anions and four monodentate **HMPM** ligands in a distorted octahedral structure having a butterfly disposition. As can be seen from the stereographic representation in **Figure 4B.3**, the molecule in the solid state appears in a c_i point group rather than in any other higher symmetry group due to the fact that all the N-Zn bond lengths and N-Zn-N bond angles are not identical even though they are very close and that the **HMPM** molecular skeletons are in an inverse disposition.

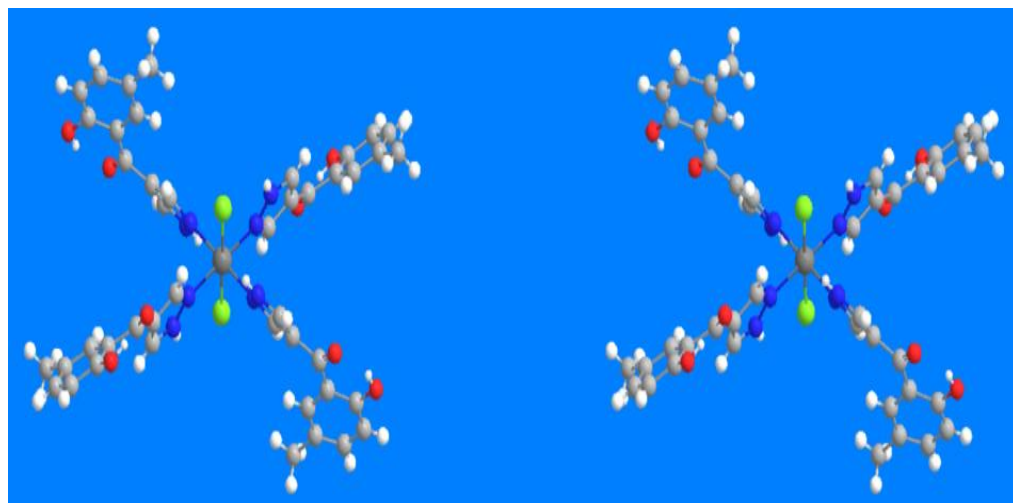


Figure 4B.3 Stereographic view of the $[\text{Zn}(\text{HMPM})_4\text{Cl}_2]$

The confinement of the molecule to a mere c_i is also evident from the differential Zn-N bond lengths of the Zn^{2+} and N-atoms of the pyrazole rings of the **HMPMs**. In one trans pair (Zn1-N1 and Zn1-N1i) the Zn-N bond length is about 2.170 Å whereas in the other (Zn1-N3 and Zn1-N3i), it is about 2.166 Å. Further, the two trans pairs of N-Zn-N bond angles also slightly differ such that one pair (N1-Zn1-N3 and N1i-Zn1-N3i) has it at about 89° whereas the other (N1-Zn1-N3i and N1i-Zn1-N3) at about 90° . However, the axial Zn-Cl bond lengths, viz., Cl1-Zn1 and Cl1i-Zn1 are near similar at 2.434 Å and with the Cl-Zn1-Cl bond angle at about 180.0° . The dissimilarity of Zn-N coordination is further seen in the dissimilarity of the Cl-Zn-N bond angles away from 90° . One pair (N1-Zn1-Cl1 and N1i-Zn1-Cl1i) shows it at about 91° and the other (N3-Zn1-Cl1 and N3i-Zn1-Cl1) at about 89° . Relevant crystallographic and structure refinement parameters of the complex is presented in **Table 4B.1**. Sets of some selected bond lengths, bond angles and dihedral angles are shown in **Table 4B.3** through **4B.7** respectively. The pyrazole moiety and benzoyl moiety are not co-planar to each other. One pair of ligands in trans position, has their C5-C6-C8-C9 and C5i-C6i-

C8i-C9i dihedral angle of about -159° whereas the other trans pair of the ligands, their C13-C15-C16-C17 and C13i-C15i-C16i-C17i of about 162° . This indicates that the 4 ligands are present in two distinct pairs of conformations in the solid state of $[\text{Zn}(\text{HMPM})_4\text{Cl}_2]$. The non-coplanarity of pyrazole and hydroxybenzoyl rings seems to be favouring an intramolecular hydrogen bonding between the phenolic O-H and C=O moieties of the benzoyl group [(O1-H1....O2=C8 and O1i-H1i....O2i=C8i; $D = 2.573 \text{ \AA}$; $d = 1.859 \text{ \AA}$, $\theta = 144.86^\circ$) and (O4-H4....O3=C15 and O4i-H4i....O3i=C15i; $D = 2.555 \text{ \AA}$; $d = 1.839 \text{ \AA}$, $\theta = 145.29^\circ$)]. This structural feature is also found to facilitate intramolecular hydrogen bonding with the axially coordinated Cl-atoms and the nearest pyrazole's imine hydrogen (-NH-). The NH4....Cl1 hydrogen bonds are found as $\text{NH}_2 \cdots \text{Cl1}$; $D = 3.145 \text{ \AA}$, $d = 2.582 \text{ \AA}$, $\theta = 124.11^\circ$; $\text{NH}_4 \cdots \text{Cl1}$; $D = 3.203 \text{ \AA}$, $d = 2.726 \text{ \AA}$, $\theta = 114.14^\circ$. As expected, the hydrogen bonds of Cl1....H-N- are near vertical to those of C=O....H-O-. All the relevant data of various hydrogen bonds are placed in **Table 4B.2**.

The crystal structure analysis unveils the fact that the $[\text{Zn}(\text{HMPM})_4\text{Cl}_2]$ molecules form close packed structure in the crystal. Any two $[\text{Zn}(\text{HMPM})_4\text{Cl}_2]$ neighbour molecules in their inversion space relation are engaged in interaction with each other to form a dimer as homodimer synthon consisting of N-H \cdots O and C-H \cdots O hydrogen bonds **Figure 4B.4**. These dimers extend to form a one-dimensional (1D) tape along the crystallographic *b*-axis **Figure 4B.5**. The molecules which are in 1D-tapes further interact with one another as *n*-glide-related molecules with similar interactions and form a close-packed structure.

4B.2 Computational Modelling Studies on $[\text{Zn}(\text{HMPM})_4\text{Cl}_2]$ and HMPM by Extended Tight Binding (xTB)

In order to have an insight into how the structural aspects of **HMPM**, influenced upon complexation, i.e., in $[\text{Zn}(\text{HMPM})_4\text{Cl}_2]$, we have taken up computational DFT modelling studies of **HMPM** and $[\text{Zn}(\text{HMPM})_4\text{Cl}_2]$ on Extended Tight Binding (xTB) platform. An anaglyph picture and stereographic image of the **HMPM** ligand generated by ChemSoft Chem3D platform after energy minimization through SCF-MM2 calculations are shown in **Figure 4B.6** since we could not generate a single crystal for the ligand. It is worthwhile to compare these pictures with the experimental crystallographic stereographic image of $[\text{Zn}(\text{HMPM})_4\text{Cl}_2]$ in order to judge the spatial orientation of the ligand, **HMPM**, in free and complexed states shown in **Figure 4B.7**. Dihedral conformational energy plots over its C6-C8 and C8-C9 bonds and double dihedral surface plots over C6-C8-C9 bonds of **HMPM** are presented in **Figure 4B.8** and **Figure 4B.9** respectively. The optimized geometries of the ligand and the complex are shown in **Figure 4B.10**. It can be seen from this figure that in both the ligand and the complex that the phenol and the benzoyl carbonyl are engaged in intramolecular hydrogen bond (-O-H \cdots O=C) suggestive of two important structural

and chemical viewpoints, viz., one, that the **HMPM** does not serve as a bidentate ligand like the one shown in **Figure 4B.2** and two, that the bivalent zinc ion prefers a Zn-N₄ coordination sphere to a Zn-O₄ (**Figure 4B.1**).

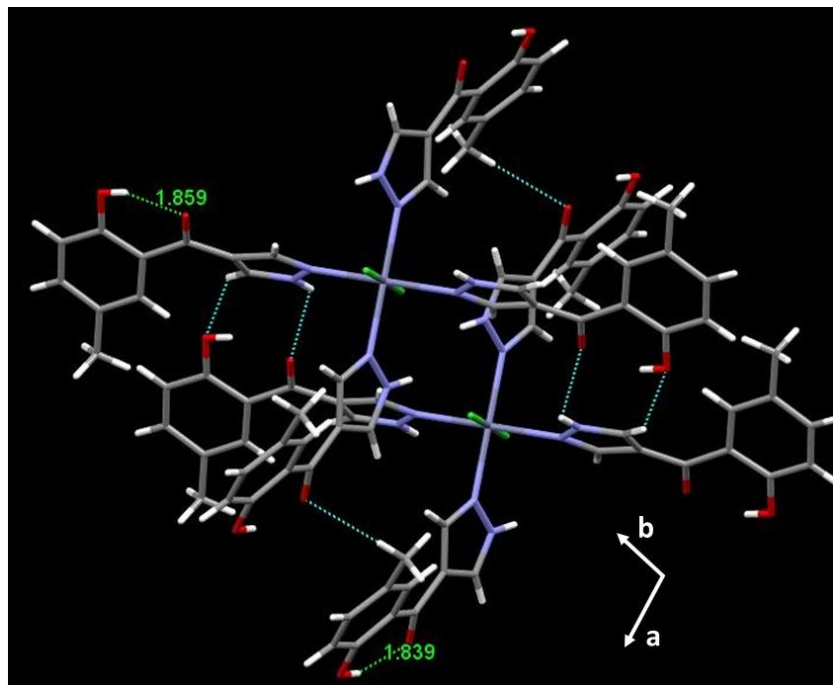


Figure 4B.4 Formation of inverse-related homo-dimer synthone from a close pair of $[\text{Zn}(\text{HMPM})_4\text{Cl}_2]$ molecules with the help of intermolecular N-H \cdots O hydrogen bonds and C-H \cdots O hydrogen bonds (Intramolecular hydrogen bonds with different bond lengths (O-H \cdots O=C) can also be seen)

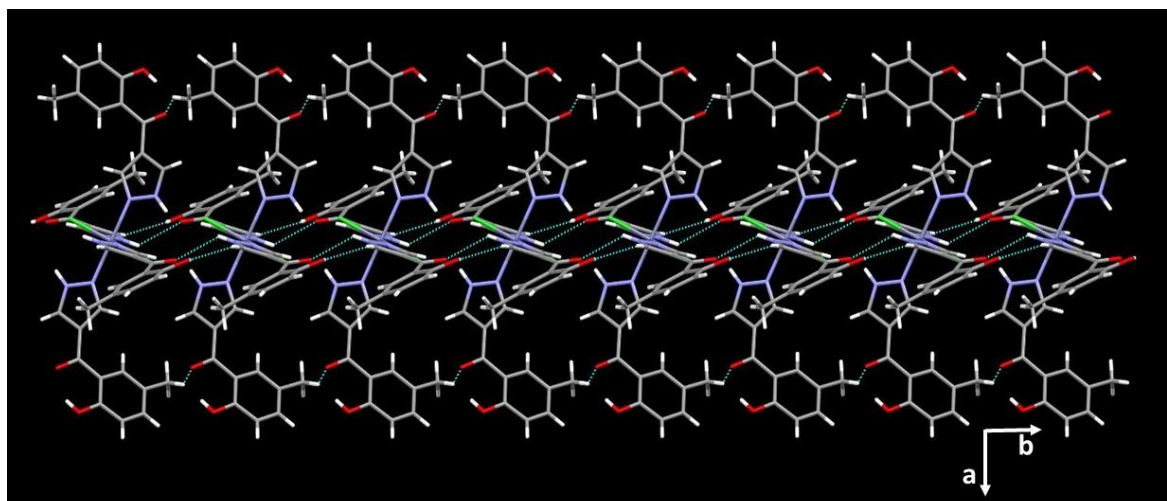


Figure 4B.5 One-dimensional (1D) tape formation of $[\text{Zn}(\text{HMPM})_4\text{Cl}_2]$ synthones (shown in **Figure 4A.4**) along the crystallographic b-axis through N-H \cdots O and C-H \cdots O hydrogen bonds

Table 4B.1 Crystallographic data of $[\text{Zn}(\text{HMPM})_4\text{Cl}_2]$

Empirical formula	$\text{C}_{44}\text{H}_{40}\text{Cl}_2\text{N}_8\text{O}_8\text{Zn}$
Formula weight	945.11
Temperature(K)	296(2)
Wavelength (Å)	0.71073
Crystal system	Monoclinic
Space group	$P2_1/n$
Unit cell dimensions (Å)	$a = 13.2068; b = 7.0763; c = 23.5910$
Angle (°)	$\alpha = 90; \beta = 102.327; \gamma = 90$
Volume (Å ³)	2153.9(3)
Z	2
Calculated density (g/cm ³)	1.457
F(000)	976
Crystal size(mm)	0.300 x 0.250 x 0.200
θ range for data collection (°)	1.636-28.407
Limiting indices	-17≤h≤14, -8≤k≤8, -31≤l≤31
Reflections collected/unique [$I > 2\sigma(I)$]	17130/5268 [R(int) = 0.0300]
Completeness to θ	25.242(99.0%)
Absorption correction	Semi-empirical from equivalents
Max. and min. transmission	0.863 and 0.805
Refinement method	Full-matrix least-squares on F^2
Data/restraints/parameters	5268/0/294
Goodness-of-fit on (F^2)	1.150
Final R indices [$I > 2\sigma(I)$]	$R_1 = 0.0390, wR2 = 0.1044$
R indices (all data)	$R_1 = 0.0640, wR2 = 0.1317$
Extinction coefficient	n/a
Largest diff. peak and hole(e/Å ³)	0.414 and -0.528
CCDC number	2124698

A modelling study forced on the structure shown in **Figure 12** gave an optimized energy far higher than the one evaluated for the structure in **Figure 5**. In this connection, comparison of the structural parameters of the organic skeleton in both the free ligand and that in the complex in their optimised (stabilised with global eigen value) structures obtained by computational modelling and that, in turn, with those of the XRD structure are relevant. Despite trials on different methods, we were unable to develop a single crystal for **HMPM** and hence the computational data acquired on the pure **HMPM** suffer lack of an empirical counterpart to be juxtaposed with. However, the computational structural data obtained on both **HMPM** and $[\text{Zn}(\text{HMPM})_4\text{Cl}_2]$ are compared with the corresponding XRD experimental data of $[\text{Zn}(\text{HMPM})_4\text{Cl}_2]$. **Table 4B.2** lists a few selected

structural parameters for modelled HMPM and modelled $[\text{Zn}(\text{HMPM})_4\text{Cl}_2]$, such as bond lengths, bond angles, and dihedral angles.

Table 4B.2 Bond distances and angles of some hydrogen bonding interactions in $[\text{Zn}(\text{HMPM})_4\text{Cl}_2]$

String*	Bond distance (Å)			Bond angle (°)
	D…A	H…A	D…H	D-H…A
C4-H4...Cl1i	3.655(3)	2.87	0.93	142.8
C11-H11...Cl1i	3.441(2)	2.98	0.93	112.5
N2-H2...Cl1	3.145(19)	2.58	0.86	124.1
O1-H1O...O2	2.573(2)	1.86	0.82	144.8
O4-H4O...O3	2.555(4)	1.84	0.82	145.3
N4-H4N...Cl1	3.203(2)	2.73	0.90	114.0
N4-H4N...Cl1i	3.107(2)	2.36	0.90	140.0
C4-H4...Cl1i	3.655(3)	2.87	0.93	142.8
C11-H11...Cl1i	3.441(2)	2.98	0.93	112.5
N2-H2...Cl1	3.145(19)	2.58	0.86	124.1
O1-H1O...O2	2.573(2)	1.86	0.82	144.8
O4-H4O...O3	2.555(4)	1.84	0.82	145.3
N4-H4N...Cl1	3.203(2)	2.73	0.90	114.0
N4-H4N...Cl1i	3.107(2)	2.36	0.90	140.0

* Atom numbering as per **Figure 4B.1 (b)**

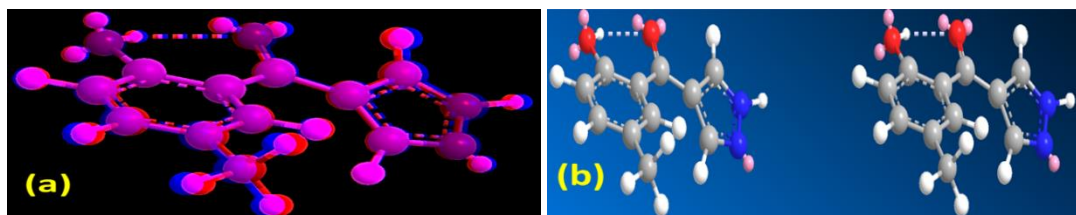


Figure 4B.6 Molecular modelled and energy minimised images of **HMPM** in its anaglyph (a) and stereographic (b) perspectives

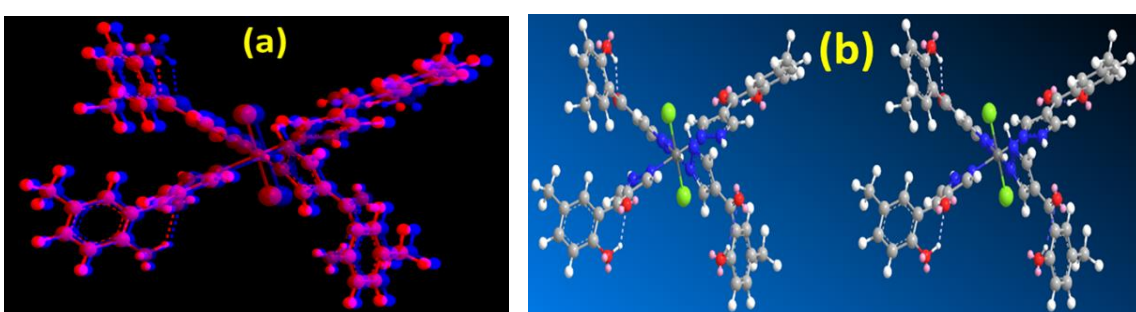


Figure 4B.7 Molecular modelled and energy minimised images of $[\text{Zn}(\text{HMPM})_2\text{Cl}_2]$ in its anaglyph (a) and stereographic (b) perspectives

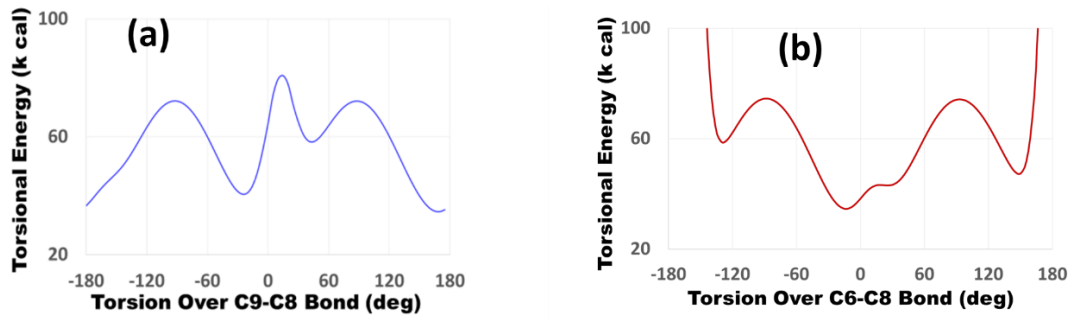


Figure 4B.8 Torsional energy plots of **HMPM** over its (a) C6-C8 and (b) C8-C9 bonds

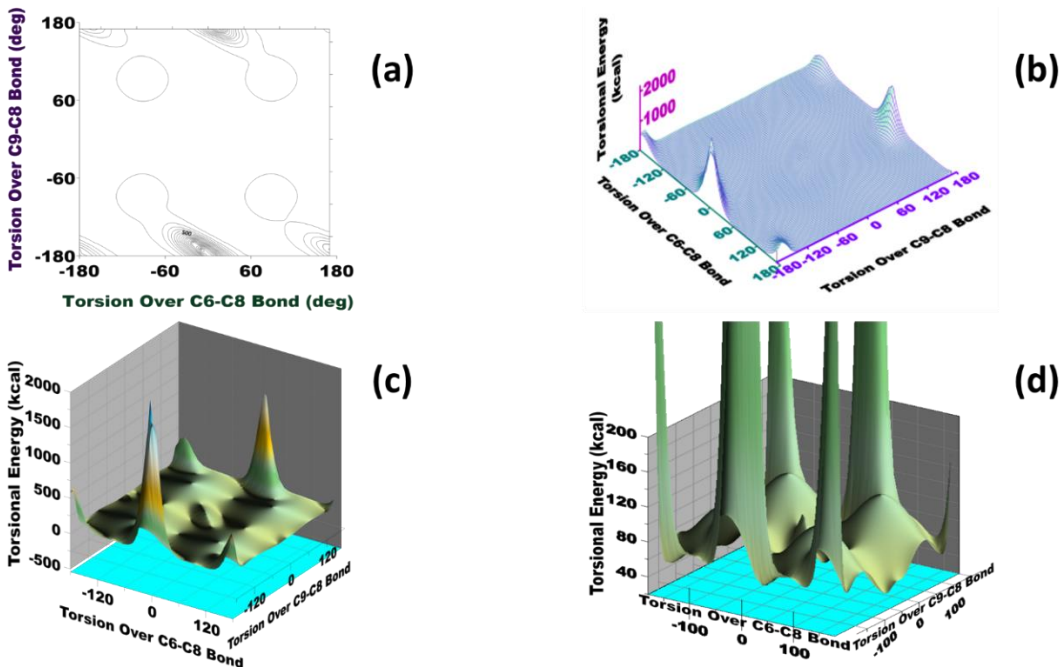


Figure 4B.9 Double dihedral 3D plots over C6-C8-C9 bonds of **HMPM** in (a) iso-energy contour (b) wireframe and (c) total surface and (d) truncated surface (max scaled energy is housed to 200 kcal) formats

Table 4B.3 shows some selected structural parameters such as, bond lengths, bond angles and dihedral angles of modelled and XRD experimental structures of $[\text{Zn}(\text{HMPM})_4\text{Cl}_2]$ whereas **Table 4B.4** displays and compares selected bond lengths, bond angles and dihedral angles of modelled **HMPM** and those of **HMPM** ligand in the XRD structure of $[\text{Zn}(\text{HMPM})_4\text{Cl}_2]$. In all the cases, the bond distances of the **HMPM** parts are near similar but for a slight variation only at the O-H....OC hydrogen bond bond length which in modelled $[\text{Zn}(\text{HMPM})_4\text{Cl}_2]$ (2.621 Å) is shown to be stronger upon complexation than in modelled **HMPM** (2.680 Å). However, the O-H....OC hydrogen bond bond length in the XRD structure of $[\text{Zn}(\text{HMPM})_4\text{Cl}_2]$ (2.688 Å) is in good agreement with the uncomplexed **HMPM**. It is amazing that the optimized geometry of modelled $[\text{Zn}(\text{HMPM})_4\text{Cl}_2]$ complex clearly reveals that all the four Zn-N bonds are not identical

but set into 2 pairs of bond distances as 2.303 and 2.238 Å which when compared with the XRD structure of $[\text{Zn}(\text{HMPM})_4\text{Cl}_2]$ relate to 2.170 and 2.166 Å respectively though the differences in the pairs are 0.065 and 0.004 Å respectively. The XRD structure of $[\text{Zn}(\text{HMPM})_4\text{Cl}_2]$ shows the two Zn-Cl bonds with similar bond distance of 2.434 Å whereas the modelled one also show similar bond length of 2.319 Å. The unusually large difference (0.115 Å) between the Zn-Cl bonds of the computed and experimental $[\text{Zn}(\text{HMPM})_4\text{Cl}_2]$ must be due to the prevalence of intramolecular inter-ligand and intermolecular inter-ligand hydrogen bonds involving the chlorides mentioned above which seem to have been ignored in the modelled isolated complex. It is also interesting to note that the calculated various bond distances of $[\text{Zn}(\text{HMPM})_4\text{Cl}_2]$ in its crystal structure shown in **Figure 4** deviate only marginally from the modelled counterpart shown in **Figure 13**. However, the bond angles and dihedral angles proximate to the coordinating nitrogen, viz., exocyclic carbonyl O=C-C(pyrazole) (O2-C8-C9-) and its linked endocyclic (C8-C9-C11) and C9-C11-N1 are a bit largely different between the experimental and calculated (modelled) data as seen from the **Tables 3** through **Table 7**. Since the carbonyl oxygen and indulges in intermolecular hydrogen bonding whereas the coordinated chlorine also does the same feat any molecular structural parameters of **HMPM** would be more affected closer to the coordination sphere than those of atomic strings farther to the metal centre and more so in the solid state (XRD) than those farther to. Further, though the four **HMPM** ligands form two distinct pairs, the structural data of the modelled **HMPM** ligand and its counterparts in the two pairs of the ligand in the complex do not differ alarmingly. Thus, it is worth to mention that tight binding (GFN-xTB) method provides crystal geometry with minimum deviation. The empirical and modelled data shown in **Table 4B. 3** through **Table 4B. 8** are in support of this inference in all the complexes.

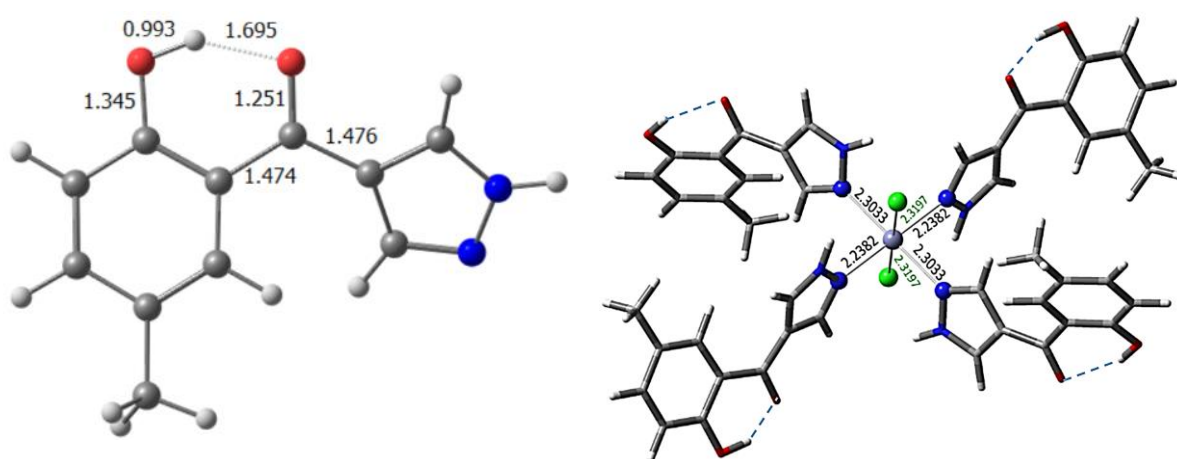


Figure 4B.10 DFT-optimized geometries of **HMPM** and $[\text{Zn}(\text{HMPM})_4\text{Cl}_2]$ molecules

TABLE 4B.3 Comparative structural parameters of DFT-modelled **HMPM** and **[Zn(HMPM)₄Cl₂]**

Bond Lengths (Å)			
Atomic String	HMPM	[Zn(HMPM) ₄ Cl ₂]	Difference
N1-N2	1.353	1.341	-0.012
C11-N1	1.316	1.318	0.002
C11-C9	1.393	1.411	0.018
C9-C8	1.469	1.464	-0.005
C8-C6	1.457	1.471	0.014
C6-C5	1.400	1.415	0.015
C8-O2	1.221	1.237	0.016
C5-O1	1.345	1.340	-0.005
O1-H1	0.993	1.001	0.008
O2...H1	1.695	1.620	-0.075
O1i-H1i	0.993	1.001	-0.008
O2i...H1i	1.695	1.620	-0.075
O4-H4	0.993	0.986	-0.075
O3...H3	1.695	1.936	0.241
O4i-H4i	0.993	0.986	-0.075
O3i...H3i	1.695	1.936	0.241
Bond Angles (°)			
N2-N1-C11	104.430	106.403	1.973
N1-C11-C9	111.647	110.490	-1.157
C11-C9-C8	132.769	122.785	-9.984
C11i-C9i-C8i	132.769	122.785	-9.984
C14-C13-C15	132.769	133.351	0.582
C14i-C13i-C15i	132.769	133.351	0.582
C9-C8-C6	121.667	120.587	-1.081
C6-C5-O1	122.253	121.434	-0.819
C5-O1-H1	109.506	105.855	-3.651
O1-H1...O2	145.291	149.502	4.211
C9-C8-O2	177.155	118.677	-58.478
C8-O2...H1	100.373	101.377	1.004
C8-C6-C7	122.591	123.267	0.676
Dihedral Angles (°)			
N1-C11-C9-C8	173.103	-179.387	-6.284
C11-C9-C8-C6	-161.739	-159.577	-2.162
C10-C9-C8-C6	-161.739	-167.256	-5.280
C9-C8-C6-C5	-161.976	-164.951	2.975
C9i-C8i-C6i-C5i	-161.976	164.951	-2.975
C13-C15-C16-C17	-162.958	151.807	-11.151
C13i-C15i-C16i-C17i	-162.958	-151.807	11.151
C11-C9-C8-O2	19.545	21.078	-1.533

C8-C6-C5-O1	-2.530	-2.182	-0.348
C9-C8-C6-C5	-161.976	-164.951	-2.975
C13-C15-C16-C17	-161.560	-162.958	1.398
N2-C10-C9-C8	-174.427	178.693	-4.266
C8-O2-H1...O1	8.019	16.923	8.904
C5-O1-H1...O2	4.008	-6.553	-2.545
C9-C8-C6-C7	18.583	15.628	-2.955

4B.3 Molecular Electrostatic Potential (MESP) of HMPM and $[\text{Zn}(\text{HMPM})_4\text{Cl}_2]$

To gain further insight into the analysis of the Zn-N bond, molecular electrostatic potential (MESP) and charge density analysis on the nitrogen atoms of both **HMPM** and $[\text{Zn}(\text{HMPM})_4\text{Cl}_2]$ have been carried out. The chromo-contour pictures of the electrostatic potential distribution on **HMPM** and $[\text{Zn}(\text{HMPM})_4\text{Cl}_2]$ obtained xTB platform are shown in **Figure 4B.11** wherein a denser yellow region means greater electron density. It can be noticed from the MESP patterns that the azomethine nitrogen ($=\text{N}-$) and the phenolic and carbonyl oxygen atoms of **HMPM** possess larger electron density, as expected in the free ligand and that the density is more decreased on the bonded nitrogen atoms than elsewhere. The calculated charge on these N atom of ligand **HMPM** is found to be -0.134 a.u. whereas that in the complex it is 0.272 a.u and 0.292 a.u. on opposite pairs of ligands. The results obtained using charge analysis clearly reinforce the outcome of the MESP. The reduction of electron density on the nitrogen atoms from **HMPM** to $[\text{Zn}(\text{HMPM})_4\text{Cl}_2]$ further supports the reason why the sp^2 - nitrogen is preferred to the oxygen donors or the imine nitrogen for coordination. As the O atoms are involved in intramolecular H-bonding, the N atom of the ligand binds with the metal ion.

TABLE 4B.4 Comparative empirical (XRD) and DFT-modelled structural parameters of $[\text{Zn}(\text{HMPM})_4\text{Cl}_2]$

Atomic string	XRD	DFT	Difference ($\Delta(\text{XRD}-\text{DFT})$)
Bond Lengths (Å)			
N1-N2	1.341	1.342	0.001
C11-N1	1.318	1.308	0.010
C11-C9	1.411	1.399	-0.012
C9-C8	1.464	1.465	0.001
C8-C6	1.471	1.475	0.004
C6-C5	1.415	1.407	-0.008
C8-O2	1.237	1.233	-0.004
C5-O1	1.340	1.356	0.016

O1-H1	1.001	0.820	-0.181
O2...H1	1.620	1.600	-0.020
O1i-H1i	1.001	0.820	-0.181
O2i...H1i	1.620	1.600	-0.020
O3...H3	1.936	2.070	0.134
O3i...H3i	1.936	2.070	0.134
O4-H4	0.986	0.820	0.166
O4i-H4i	0.986	0.820	-0.166
Zn-N1	2.238	2.170	-0.068
Zn-N1i	2.238	2.170	-0.068
Zn-N3	2.303	2.166	-0.137
Zn-N3i	2.303	2.166	-0.137
Zn-Cl1	2.311	2.434	0.123
Zn-Cl1i	2.311	2.434	0.123
Bond Angles (°)			
N2-N1-C11	106.403	104.992	-1.411
N1-C11-C9	110.490	111.725	1.235
C11-C9-C8	112.785	123.991	11.206
C11i-C9i-C8i	122.785	-123.991	-11.206
C14-C13-C15	133.351	132.812	0.539
C14i-C13i-C15i	133.351	-132.812	-0.539
C9-C8-C6	120.587	121.202	0.615
C6-C5-O1	121.434	121.820	0.386
C5-O1-H1	105.855	109.053	3.198
O1-H1...O2	149.502	148.561	-0.941
C9-C8-O2	118.677	118.129	-0.548
C8-02...H1	101.377	100.582	-0.795
C8-C6-C7	123.267	123.023	-0.244
M-N1-N3	124.856	118.215	6.641
N3i-Zn-N1i	89.856	89.129	-0.727
N3-Zn-N1i	90.144	90.870	0.726
N3i-Zn-N1	90.144	90.880	0.736
Cl1-Zn-Cl1i	180.001	180.001	0.001
N3i-Zn-Cl1	90.170	90.791	0.621
N3-Zn-Cl1i	90.170	90.791	0.621
N1-Zn-Cl1	89.830	89.111	-0.719
N1i-Zn-Cl	90.350	90.890	0.540
N3-Zn-Cl1i	90.170	90.791	0.621
Dihedral Angles (°)			
N1-C11-C9-C8	-179.387	177.029	-2.358
C11-C9-C8-C6	-159.577	162.920	-3.343
C9-C8-C6-C5	-164.951	-159.001	-5.950

C9i-C8i-C6i-C5i	164.951	159.001	5.950
C13-C15-C16-C17	151.807	-162.001	10.194
C13i-C15i-C16i-C17i	-151.807	-162.001	-10.194
C11-C9-C8-O2	21.078	-19.333	-1.745
C8-C6-C5-O1	-2.182	3.330	-1.148
C9-C8-C6-C5	-164.951	159.020	-5.931
C13-C15-C16-C17	-162.958	-162.001	-0.957
N2-C10-C9-C8	178.693	-176.221	-2.472
C8-O2-H1...O1	16.923	15.885	-1.038
C5-O1-H1...O2	-6.553	-5.987	-0.566
C9-C8-C6-C7	15.628	-22.730	-7.102
Zn-N1-N3-N4	114.463	112.230	-2.233
Zn-N1i-N3i-C14i	-52.198	-59.610	-7.412
Zn-N1-N2-C10	177.320	175.645	-1.675
Zn-N1-C11-C9	177.082	174.602	-2.48
Zn-N1i-N2i-C10i	-177.326	-175.652	-1.674
Zn-N3i-N4i-C12i	-177.321	-173.079	-4.242
Zn-N3i-C14i-C13i	-177.320	-172.356	-4.964
N3i-Zn-N1i-N2i	-78.001	-76.088	-1.913
N3i-Zn-N1i-C11i	-105.202	-98.795	-6.407
CL1-Zn-N3-N4	155.365	156.910	1.545
CL1-Zn-N3-C14	37.970	31.382	-6.588
CL1i-Zn-N1i-N2i	-10.972	-13.209	-2.237
CL1-Zn-N1-C11	-165.628	-172.110	-6.482

TABLE 4B.5 Comparative structural parameters of modelled **HMPM** and those of it in **XRD** structure of **[Zn(HMPM)₄Cl₂]** complex

Atomic string	Modelled HMPM	XRD of [Zn(HMPM) ₄ Cl ₂]	Difference
Bond Lengths (Å)			
N1-N2	1.353	1.342	-0.011
C11-N1	1.316	1.308	-0.008
C11-C9	1.393	1.399	-0.006
C9-C8	1.469	1.465	0.004
C8-C6	1.457	1.475	-0.018
C6-C5	1.400	1.407	0.007
C8-O2	1.221	1.233	0.012
C5-O1	1.345	1.356	0.011
O1-H1	0.993	0.820	-0.173
O1i-H1i	0.993	0.820	0.173
O2...H1	1.695	1.600	-0.095

O2i...H1i	1.695	1.600	0.095
O3...H3	0.993	2.070	1.077
O3i...H3i	0.993	2.070	-1.077
O4-H4	0.993	0.820	0.173
O4i-H4i	0.993	0.820	-0.173
Zn-N3	---	2.166	---
Zn-N3i	---	2.166	---
Zn-Cl1	---	2.434	---
Zn-Cl1i	---	2.434	---
Bond Angles (°)			
N2-N1-C11	104.430	104.992	0.562
N1-C11-C9	111.647	111.725	0.078
C9-C8-C6	121.667	121.202	-0.465
C11-C9-C8	132.769	123.991	-8.778
C11i-C9i-C8i	132.769	-123.991	8.778
C14-C13-C15	132.769	132.812	0.043
C14i-C13i-C15i	132.769	-132.812	-0.043
C6-C5-O1	122.253	121.820	-0.433
C5-O1-H1	109.506	109.053	-0.453
O1-H1...O2	145.291	148.561	3.270
C9-C8-O2	177.155	118.129	-59.026
C8-O2...H1	100.373	100.582	0.209
C8-C6-C7	122.591	123.023	0.432
Dihedral Angles (°)			
N1-C11-C9-C8	173.103	177.029	3.926
C11-C9-C8-C6	-161.739	162.920	-2.181
C11-C9-C8-O2	19.545	-19.333	-0.212
C8-C6-C5-O1	-2.530	3.330	-0.8
C9-C8-C6-C5	-161.976	159.020	-2.956
C9i-C8i-C6i-C5i	-161.976	159.001	-2.956
C13-C15-C16-C17	-161.560	-162.001	0.441
C13i-C15i-C16i-C17i	-161.560	-162.001	0.441
N2-C10-C9-C8	-174.427	-176.221	-1.794
C8-O2-H1...O1	8.019	15.885	7.866
C5-O1-H1...O2	4.008	-5.987	-1.979
C9-C8-C6-C7	18.583	-22.730	-4.147

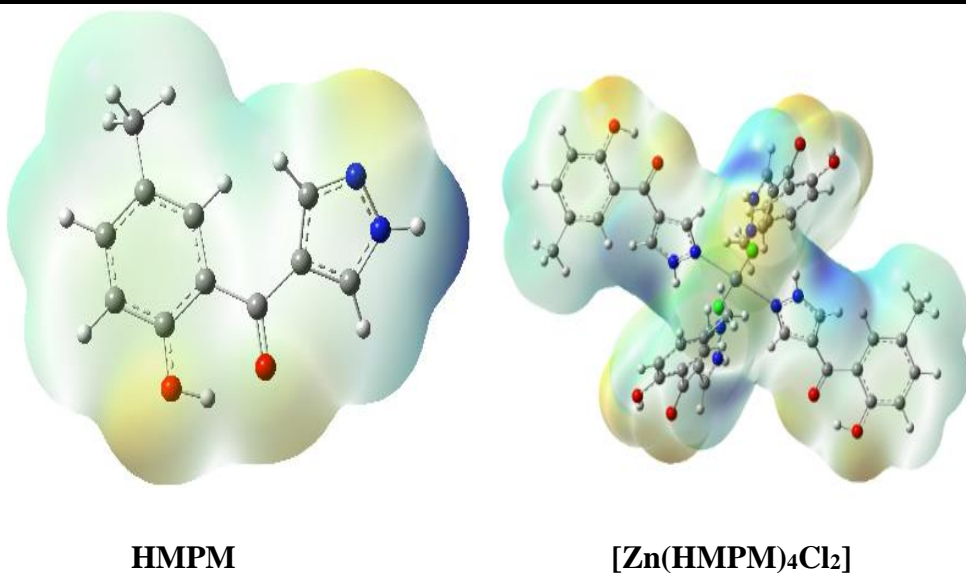


Figure 4B.11 Electrostatic potential (MESP) surfaces of **HMPM** and $[\text{Zn}(\text{HMPM})_4\text{Cl}_2]$ (highest at dark yellow and lowest at dark blue)

Table 4B.6 Comparative empirical (XRD) and MM2-modelled structural parameters of $[\text{Zn}(\text{HMPM})_4\text{Cl}_2]$

Atomic string	XRD	MM2	Difference ($\Delta(\text{XRD-MM2})$)
Bond Lengths (Å)			
N1-N2	1.341	1.394	-0.053
C11-N1	1.318	1.457	-0.139
C11-C9	1.411	1.513	-0.102
C9-C8	1.464	1.510	-0.046
C8-C6	1.471	1.378	0.093
C6-C5	1.415	1.420	-0.005
C8-O2	1.237	1.385	-0.148
C5-O1	1.340	1.54	-0.200
O1-H1	1.001	1.057	-0.056
O2...H1	1.620	1.678	-0.058
O1i-H1i	1.001	1.089	-0.088
O2i...H1i	1.620	1.712	-0.092
O3...H3	1.936	1.889	0.047
O3i...H3i	1.936	1.102	0.834
O4-H4	0.986	1.05	-0.064
O4i-H4i	0.986	1.10	-0.114
Zn-N1	2.238	1.940	0.298
Zn-N1i	2.238	1.935	0.303
Zn-N3	2.303	1.941	0.362
Zn-N3i	2.303	1.938	0.365

Zn-Cl1	2.311	2.254	0.057
Zn-Cl1i	2.311	2.251	0.060
Bond angle (°)			
N2-N1-C11	106.403	106.841	-0.438
N1-C11-C9	110.490	118.051	-7.561
C11-C9-C8	112.785	112.854	-0.069
C11i-C9i-C8i	122.785	128.024	-5.239
C14-C13-C15	133.351	133.823	-0.472
C14i-C13i-C15i	133.351	133.251	0.100
C9-C8-C6	120.587	119.840	0.747
C6-C5-O1	121.434	124.021	-2.587
C5-O1-H1	105.855	105.233	0.622
O1-H1...O2	149.502	154.201	-4.699
C9-C8-O2	118.677	118.895	-0.218
C8-02...H1	101.377	110.229	-8.852
C8-C6-C7	123.267	123.422	-0.155
N3-Zn-N1	124.856	129.151	-4.295
N3i-Zn-N1i	89.856	89.895	-0.039
N3-Zn-N1i	90.144	90.860	-0.716
N3i-Zn-N1	90.144	90.454	-0.310
Cl1-Zn-Cl1	180.001	180.12	-0.119
N3i-Zn-Cl1	90.170	90.120	0.050
N3-Zn-Cl1i	90.170	90.452	-0.282
N1-Zn-Cl1	89.830	90.201	-0.371
N1i-Zn-Cl	90.350	91.250	-0.900
N3-Zn-Cl1i	90.170	97.101	-6.931
Dihedral angle (°)			
N1-C11-C9-C8	-179.387	-180.420	1.033
C11-C9-C8-C6	-159.577	-161.100	1.523
C9-C8-C6-C5	-164.951	182.546	-17.595
C9i-C8i-C6i-C5i	164.951	154.427	-2.620
C13-C15-C16-C17	151.807	-157.450	5.643
C13i-C15i-C16i-C17i	-151.807	28.1200	-7.042
C11-C9-C8-O2	21.078	-5.246	3.064
C8-C6-C5-O1	-2.182	-168.104	3.153
C9-C8-C6-C5	-164.951	-162.45	-0.508
C13-C15-C16-C17	-162.958	179.122	-0.429
N2-C10-C9-C8	178.693	15.123	1.800
C8-O2-H1...O1	16.923	-9.010	2.457
C5-O1-H1...O2	-6.553	15.526	0.102
C9-C8-C6-C7	15.628	114.510	-0.047
Zn-N1-N3-N4	114.463	-51.128	-1.07

Zn-N1i-N3i-C14i	-52.198	173.800	3.520
Zn-N1-N2-C10	177.320	177.000	0.082
Zn-N1-C11-C9	177.082	-171.000	-6.326
Zn-N1i-N2i-C10i	-177.326	-179.781	2.460
Zn-N3i-N4i C12i	-177.321	-172.551	-4.769
Zn-N3i-C14i-C13i	-177.320	-84.529	6.528
N3i-Zn-N1i-N2i	-78.001	-94.54	-10.662
N3i-Zn-N1i-C11i	-105.202	171.421	-16.056
CL1-Zn-N3-N4	155.365	42.500	-4.530
CL1-Zn-N3-C14	37.970	-11.127	0.155
CL1i-Zn-N1i-N2i	-10.972	-168.17	2.542
CL1-Zn-N1-C11	-165.628	-180.42	1.033

Table 4B.7. Selected structural parameters of $[M(HMPM)_4Cl_2]$ calculated on MM2 platform in comparison with those of the $[Zn(HMPM)_4Cl_2]$ obtained from the XRD studies

Important atomic string	Bond lengths (Å)				
	XRD on $ZnL_4Cl_2^*$	MM2 on $ZnL_4Cl_2^*$	MM2 on $[M(HMPM)_4Cl_2]$		
			$M=Co(II)$	$M=(Ni(II))$	$M=Cu(II)$
N1-N2	1.341	1.394	1.394	1.422	1.249
C11-N1	1.318	1.457	1.445	1.482	1.287
C11-C9	1.411	1.513	1.525	1.510	1.344
C9-C8	1.464	1.519	1.531	1.507	1.334
C10-N2	1.478	1.451	1.451	1.458	1.268
N1i-N2i	1.415	1.388	1.397	1.428	1.253
C11i-C9i	1.325	1.458	1.448	1.460	1.289
C9i-C10i	1.340	1.529	1.519	1.513	1.348
C10i-N2i	1.352	1.448	1.456	1.522	1.332
M-N1	2.238	1.940	1.854	1.407	1.477
M-N1i	2.238	1.935	1.854	1.390	1.471
M-N3	2.303	1.941	1.856	1.392	1.496
M-N3i	2.303	1.938	1.854	1.403	1.489
M-Cl1	2.311	2.254	2.168	2.196	2.212
M-Cl1i	2.311	2.251	2.167	2.195	2.211
Bond angle (°)					
N1-M-N2	122.1	8.1	82.5	91.2	95.2
M-N1-C11	121.9	120.2	121.5	124.9	126.9
M-N1-N3	124.8	90.1	119.4	127.1	124.2
N1i-M-N2i	109.8	86.2	83.9	90.6	90.2
M-N1i-C11i	129.2	120.2	120.5	128.4	120.9
M-N1i-N2i	122.8	119.8	119.4	120.8	123.9
Dihedral angle (°)					

M-N1-C11-C10	-179.4	-177.0	-176.0	-139.1	-144.4
M-N1-N2-C9	-174.2	-173.8	-170.4	152.0	143.5
M-N1i-N2i-C11i	183.3	171.1	-171.5	172.2	-176.6
M-N1i-C9i-C10i	176.1	160.5	-173.5	-179.1	175.2

* HMPM

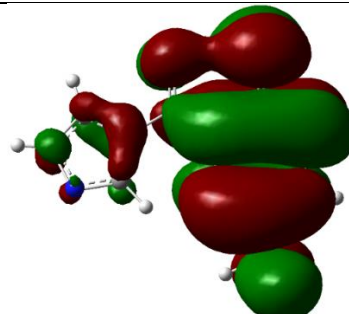
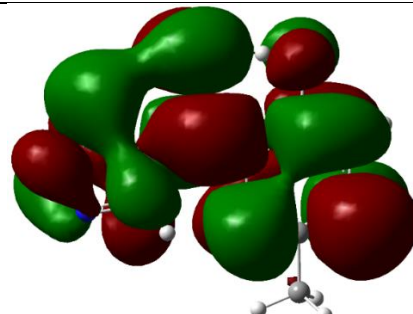
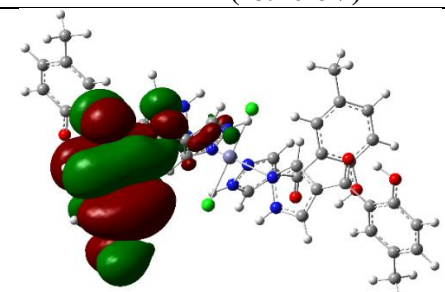
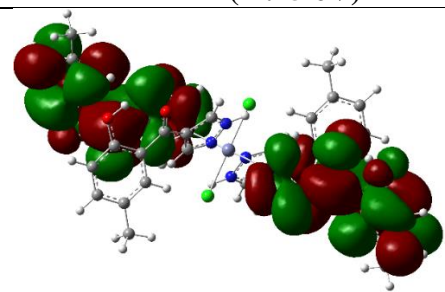
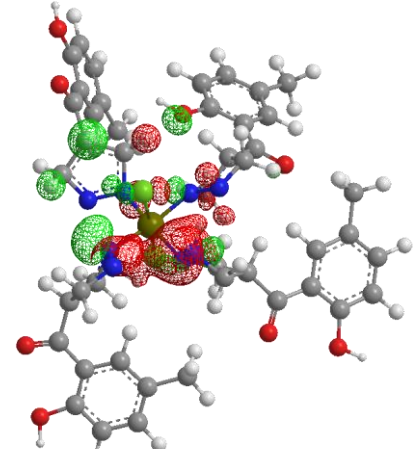
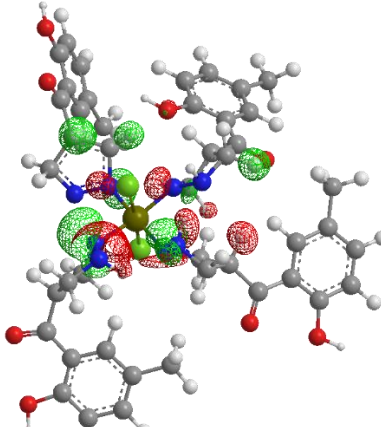
Table 4B.8 Computational (from MM2 platform) geometric parameters of $[M(HMPM)_4Cl_2]$ correlated as difference with the experimental XRD data of $[Zn(HMPM)_4Cl_2]$

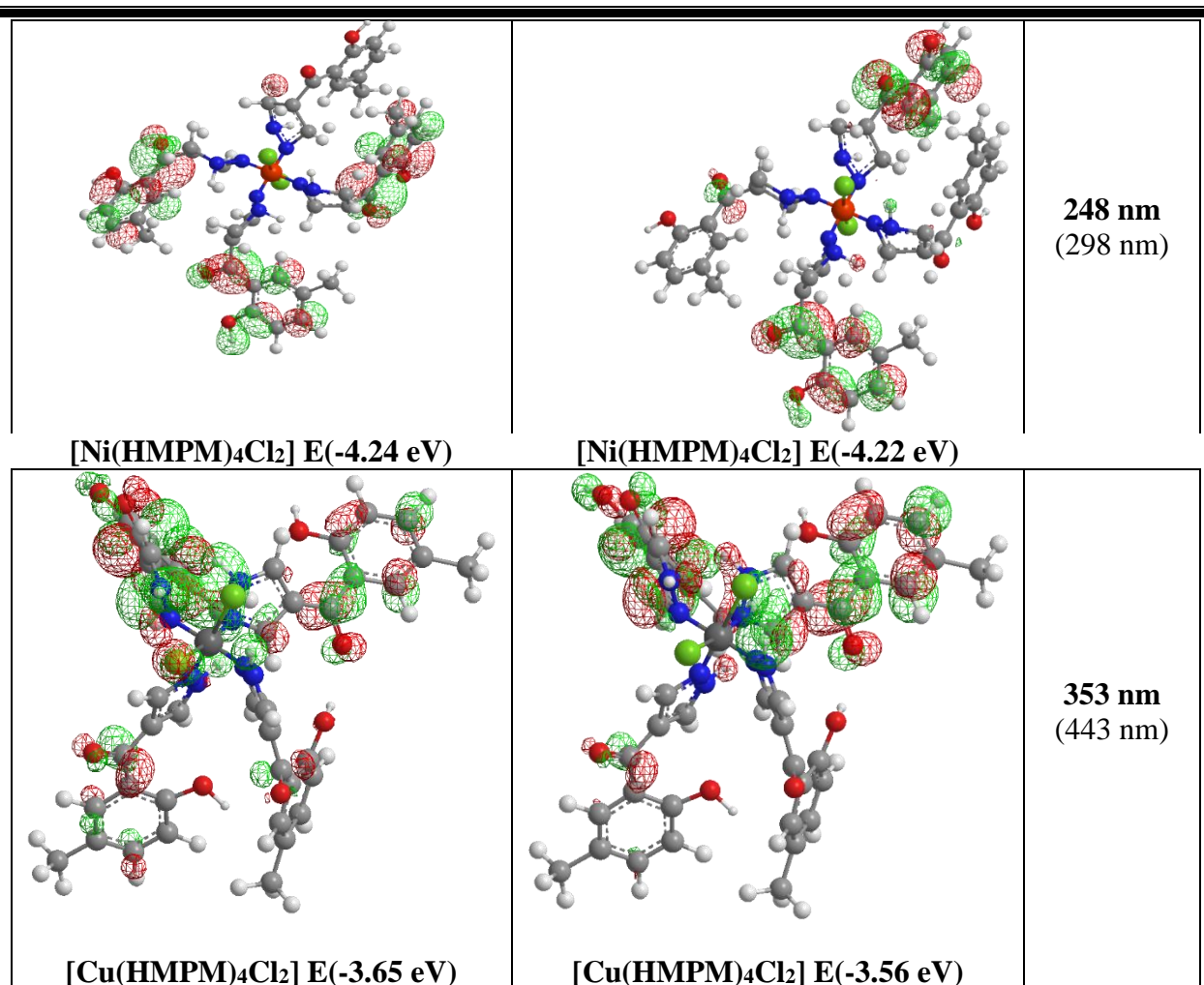
Compound/ Parameter		Differential difference of XRD-DFT and XRD-MM2 of ZnL_4Cl_2	MM2-Computational data of $[M(HMPM)_4Cl_2]$			
XRD-MM2	String		$M=Zn(II)$	$M=Co(II)$	$M=Ni(II)$	$M=Cu(II)$
Bond lengths (Å)						
ΔXRD	M-N1	0.366	-0.068	0.384	0.831	0.761
$\Delta MM2$			0.298	0.086	0.533	0.463
ΔXRD	M-N3	0.499	-0.137	0.447	0.911	0.807
$\Delta MM2$			0.362	0.085	0.549	0.445
ΔXRD	M-N3i	-0.502	-0.137	0.449	0.903	-0.814
$\Delta MM2$			0.365	0.084	0.535	0.449
ΔXRD	M-Cl1	0.066	0.123	-0.143	-0.115	-0.099
$\Delta MM2$			0.057	-0.086	-0.058	-0.042
ΔXRD	M-Cl1i	0.063	0.123	-0.144	-0.116	-0.100
$\Delta MM2$			0.060	-0.084	-0.056	-0.040
ΔXRD	N1-N2	0.054	0.001	0.053	0.081	-0.092
$\Delta MM2$			-0.053	0.000	0.028	-0.145
ΔXRD	C11-N1	0.149	0.010	0.127	0.164	-0.031
$\Delta MM2$			-0.139	-0.012	0.025	-0.170
ΔXRD	C11-C9	0.090	-0.012	0.114	0.099	-0.067
$\Delta MM2$			-0.102	0.012	-0.003	-0.169
ΔXRD	C9-C8	0.047	0.001	0.07	0.046	-0.127
ΔDFT			-0.046	0.012	-0.012	-0.185
Bond angles (°)						
ΔXRD	N1-M-N3	22.40	34.00	-39.6	-30.9	-26.9
$\Delta MM2$			11.70	-5.6	3.1	7.1
ΔXRD	M-N1-C11	-8.90	4.70	-0.4	3.0	5.0
$\Delta MM2$			13.60	1.3	4.70	6.70
ΔXRD	M-N1-N2	-2.50	-7.40	-5.2	2.50	-0.40
$\Delta MM2$			9.90	1.2	8.90	6.00
ΔXRD	N1i-M-N2i	33.0	-34.70	-25.9	-19.2	-19.60
$\Delta MM2$			1.70	-2.3	4.4	4.00
Dihedral angles (°)						
ΔXRD	M-N1-C11-C10	-0.08	1.60	3.40	40.30	35.00
$\Delta MM2$			-2.40	10.00	37.90	32.600
ΔXRD	M-N1-N2-C9	4.20	5.600	3.80	-22.20	-30.700

ΔMM2			-1.40	3.40	-21.80	-30.30
ΔXRD	M-N1i-N2i-C11i	10.70	-12.60	-11.80	-11.10	-6.70
ΔMM2			1.90	0.40	1.10	5.50
ΔXRD	M-N1i-C9i-C10i	-14.10	-1.50	-2.60	30	-0.90
ΔMM2			15.60	130	18.60	14.70

4B.4 Frontier Orbitals of HMPM and $[\text{Zn}(\text{HMPM})_4\text{Cl}_2]$

Parr and co-workers have shown that the Density Functional Theory (DFT) may be used to justify almost the whole frontier molecular theory [7, 8]. The concept of the Frontier Molecular Orbitals (FMO), particularly the Lowest Unoccupied Molecular Orbital (LUMO) and the Highest Occupied Molecular Orbital (HOMO), supports much of theoretical chemistry relating to reactivity (HOMO). The interaction of these orbitals generally allows for a good description of the systems' reactivity and spectroscopic manifestation. The orbital energy gap and the FMO theory not only help us estimate a molecule's chemical reactivity and kinetic stability, but also that an electrophilic species attacks where the HOMO is denser, and a nucleophilic species attacks where the LUMO is denser. A molecule with a small frontier orbital gap is more polarizable and is often associated with strong chemical reactivity and low kinetic stability, and is considered to be a soft molecule. The HOMO orbital serves predominantly as an electron donor, while the LUMO orbital serves mostly as an electron acceptor. According to DFT-xTB theory, the HOMO and LUMO energies, as well as their presented contour maps energy gap (EHOMO - ELUMO), of the **HMPM** ligand are (-6.20 eV) and (-2.15 eV) and -4.05 eV, respectively, whereas those of $[\text{Zn}(\text{HMPM})_4\text{Cl}_2]$ are (-6.21 eV) and (-2.39 eV) and 3.82 eV and (-3.65 eV) and (-3.56 eV) and -0.09 eV found to be $[\text{Cu}(\text{HMPM})_4\text{Cl}_2]$ and (-4.24 eV) and (-4.22 eV) and -0.02 eV for $[\text{Ni}(\text{HMPM})_4\text{Cl}_2]$ and (-6.56 eV) and (-6.34 eV) and -0.22 eV difference energy for $[\text{Co}(\text{HMPM})_4\text{Cl}_2]$. Figure 4B.12 depicts the computed highest occupied molecular orbital (HOMO) and lowest unoccupied molecular orbital (LUMO) of the ligand **HMPM** and the complex $[\text{Zn}(\text{HMPM})_4\text{Cl}_2]$, as well as their relative energy values.

HOMO	LUMO	λ_{\max} Expected (Observed)
 HMPM E(-6.20 eV)*	 HMPM E(-2.15 eV)*	306.6 nm (323 nm)
 [Zn(HMPM)4Cl2] E(-6.21 eV)*	 [Zn(HMPM)4Cl2] E(-2.39 eV)*	325.1 nm (345 nm)
 [Co(HMPM)4Cl2] E(-6.56 eV)	 [Co(HMPM)4Cl2] E(-6.34 eV)	244 nm (312 nm)



* values obtained from DFT calculations

Figure 4B.12 Modelled shapes and energies of HOMO and LUMO molecular orbitals of **HMPM** and **[M(HMPM)4Cl₂]** (mostly on MM2 platform) along with their energies and expected electronic transitions (the observed λ_{\max} are also given for comparison)

4B.5 Hirshfeld Surface Analysis

Crystal Explorer 17.5 (Turner et al., 2017) [9,10] has been used to map Hirshfeld surfaces with normalised contact distance d_{norm} and generate two-dimensional fingerprint plots for **[Zn(HMPM)4Cl₂]**. **Figure 4B.13** depicts surfaces that have been mapped over d_{norm} (-0.4 to 1.6) and shows the d_{norm} -mapped finger print Hirshfeld map of **[Zn(HMPM)4Cl₂]** as well as the percentage interaction exerted by each atomic pair **Figure 4B.14** shows the Hirshfeld diagrams for shape index (1.0 to 1.0), curvedness (-0.4 to 1.6), and fragment patch (0.0 to 17.0), while **Figure 4B.15** shows the 2D fingerprint plots of interatomic interactions of the complex. The 2D-fingerprint plots provide quantitative information on the contributions to Hirshfeld surfaces resulting from various intermolecular interactions. The d_{norm} parameter of **[Zn(HMPM)4Cl₂]** shows the surface with a red-white-blue colour scheme, with deep red patches corresponding to close contact

interactions such hydrogen bonding contacts like N-H....Cl and O-H....O. The white spots show contacts near van der Waals interactions, such as H....H contacts, but the blue sections indicate no such close contacts. Red concave regions with 'butterfly patterns' as C-H interactions and the presence of aromatic (π π) stacking interactions are shown in the shape index of complex **[Zn(HMPM)4Cl₂]**. The extent of electron density around different chemical interactions is represented by the curvature of the surface. The red spots are crowded around nitrogen, carbon, hydrogen, and oxygen atoms, as displayed on the 3D d_{norm} surface. The values of 5.2%, 0.5%, and 4.3% of C....C, C....N, and C....O, respectively, show the involvement of π π , N.... π , and O.... π interactions within the crystal packing of the compound, based on the localizations of the red spots on this surface. Intermolecular hydrogen bond interactions for N....H, C....H, OH, and H....Cl, on the other hand, assume values of 4.3%, 20%, 16.8%, and 5.9% of the 2D fingerprint histograms, respectively. Finally, according to 2D fingerprint histograms, Van der Waals (VdW) interactions (H....H) within crystal packing of the title molecule represent for 42% of overall interactions [60-61]. The Hirshfeld studies imply additional intermolecular hydrogen bonds through CH....Cl and NH....Cl, in addition to the intermolecular stacking through hydrogen bonds of N-H \cdots O and C-H \cdots O as suggested by the XRD studies (**Figure 4B.16**).

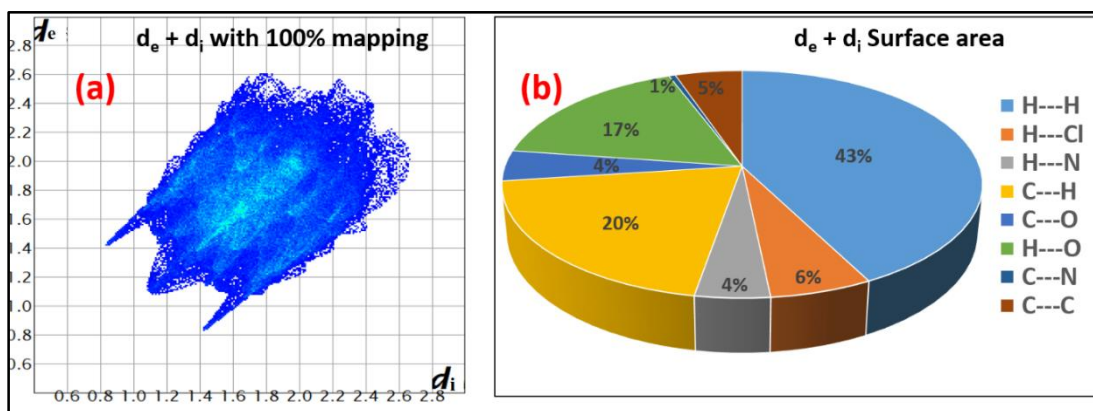


Figure 4B.13 Hirshfeld surface (d_{norm} mapped) for visualizing the (a) finger print map of d_e vs d_i with 100% mapping of all its atoms and (b) the corresponding atoms intermolecular interactions of **[Zn(HMPM)4Cl₂]** (represented in pie chart).

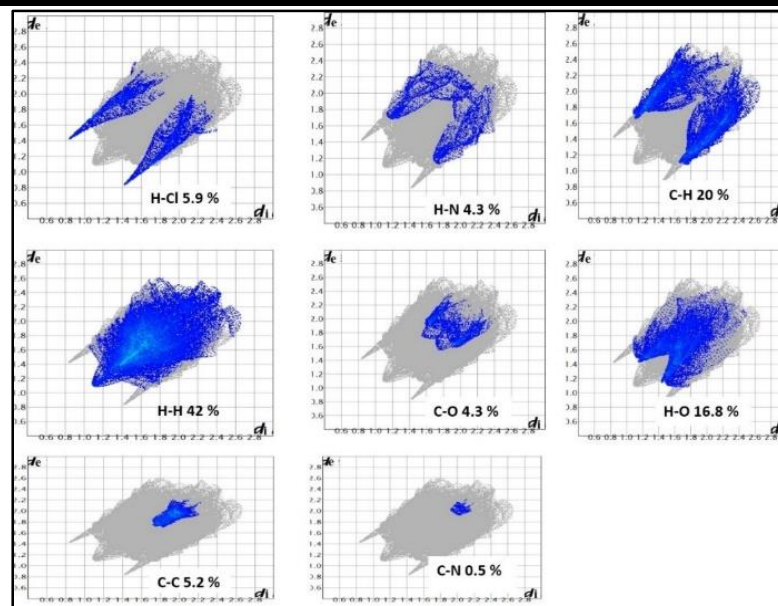


Figure 4B.14 Illustrative 2D fingerprint plots of interatomic interactions of $[\text{Zn}(\text{HMPM})_4\text{Cl}_2]$ showing percentage of contacts contributing to the overall Hirshfeld surface area (the distances from the Hirshfeld surface to the nearest atom within and exterior to the surface are d_e and d_i)

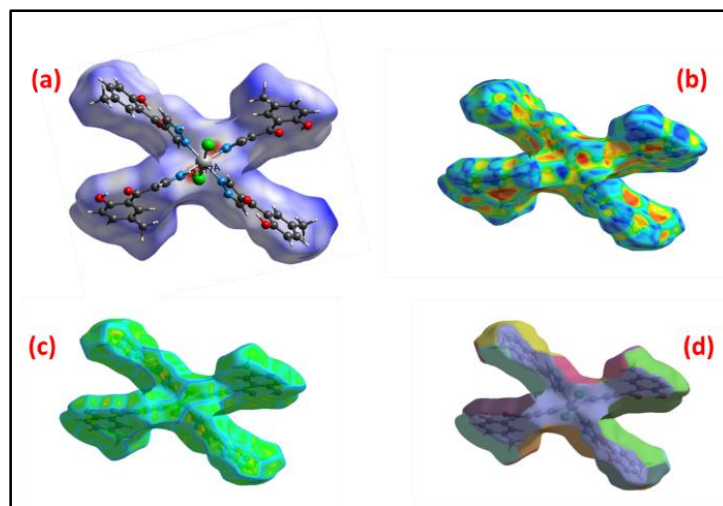


Figure 4B.15 Hirshfeld hydrogen interaction surfaces of $[\text{Zn}(\text{HMPM})_4\text{Cl}_2]$ mapped with (a) d_{norm} (b) shape index, (c) curvedness and (d) fragment patch

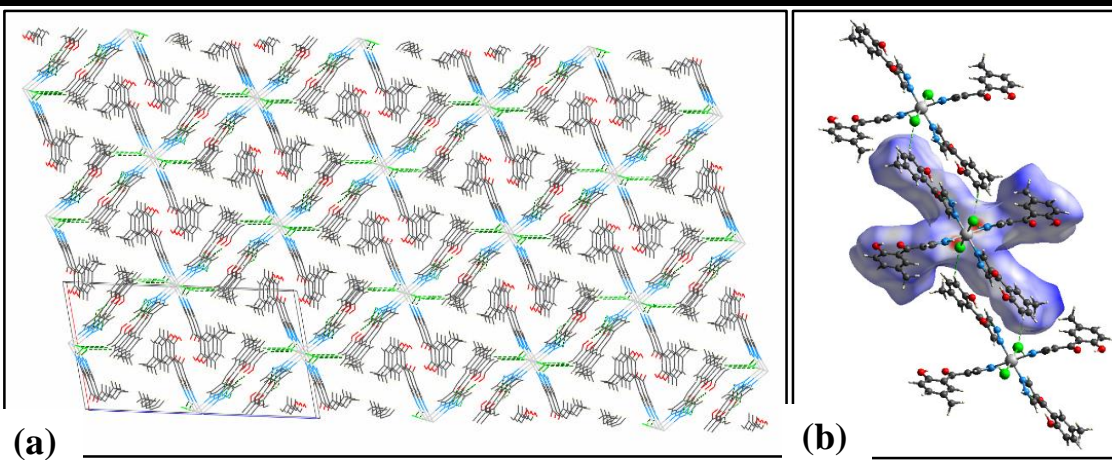


Figure 4B.16 Crystal structure (a) stacking facilitated by (b) C-H...Cl and N-H...Cl and hydrogen bonding of complex $[\text{Zn}(\text{HMPM})_4\text{Cl}_2]$

PART-C

BIOLOGICAL ACTIVITY STUDIES OF HMPM AND $[M(HMPM)_4Cl_2]$ COMPLEXES

HMPM and its various Schiff base complexes were tested for microbiological activity against two gram positive and two gram negative bacteria, along with streptomycin as a standard drug. The anti-fungal, antioxidant activity and antidiabetic assay for ligand **HMPM** and $[M(HMPM)_4Cl_2]$ complex have been carried out. As the anti-bacterial activity is enhanced in all the systems, as the concentrations of the complexes increased.

4C.1 Biological Studies

4C.1.1 Antibacterial Activity

The *in vitro* Anti-bacterial activity of both **HMPM** and $[M(HMPM)_4Cl_2]$ were assayed against two gram-positive bacteria, *Bacillus subtilis* and *Bacillus cereus* and two gram-negative bacteria, *Escherichia coli* and *Pseudomonas aeruginosa* with two different concentrations of 200 and 400 $\mu\text{g}/\text{mL}$. The complex $[Zn(HMPM)_4Cl_2]$ shown good zone of inhibition of 14 and 16 mm respectively for those two doses against gram-positive bacteria, *Bacillus subtilis* and for the same doses, 11 and 13mm respectively against gram-negative bacteria, *Escherichia coli*.

The complex, $[Cu(HMPM)_4Cl_2]$ exhibits good zone of inhibition of 16 and 15 mm respectively for those two doses against gram-positive bacteria, *Bacillus subtilis* and for the same doses, 15 and 12 mm respectively against gram-negative bacteria, *Escherichia coli*.

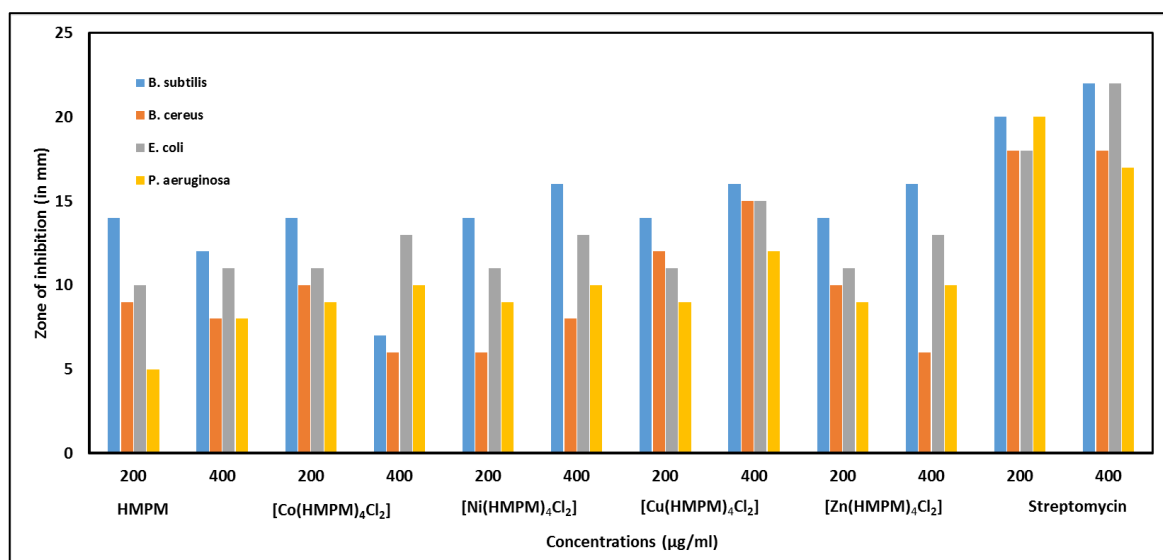


Figure 4C.1 Histogramographic representation of the antibacterial activities of **HMPM** and $[M(HMPM)_4Cl_2]$ against streptomycin as the standard

The ligand, **HMPM**, at 200 and 400 $\mu\text{g/mL}$ showed an inhibition of 14 and 12mm respectively against *Bacillus subtilis* and of 10 and 11mm respectively against the *Escherichia coli*. **Table 4C.1** holds the results which reveal that the ligand shows less activity against both gram negative and gram positive microorganism's histographical pictures are shown in **Figure 4C.1**. The remaining complexes $[\text{Ni}(\text{HMPM})_4\text{Cl}_2]$ and $[\text{Co}(\text{HMPM})_4\text{Cl}_2]$, shown moderate to good activity due to chelation theory concept [11]. Furthermore, the factors such as electronic properties, dipole moment conductivity and nature of secondary ligand may also contribute for the increased activity of complexes compared to unbound **HMPM**.

Table 4C.1 Results of antibacterial activity of **HMPM** and $[\text{M}(\text{HMPM})_4\text{Cl}_2]$

Compound	Conc. ($\mu\text{g/ml}$)	Zone of inhibition (in mm)			
		Gram positive-bacteria		Gram-negative bacteria	
		<i>Bacillus subtilis</i>	<i>Bacillus cereus</i>	<i>Escherichia coli</i>	<i>Pseudomonas aeruginosa</i>
HMPM	200	14	9	10	5
	400	12	8	11	8
$[\text{Co}(\text{HMPM})_4\text{Cl}_2]$	200	14	10	11	9
	400	7	6	13	10
$[\text{Ni}(\text{HMPM})_4\text{Cl}_2]$	200	14	6	11	9
	400	16	8	13	10
$[\text{Cu}(\text{HMPM})_4\text{Cl}_2]$	200	14	12	11	9
	400	16	15	15	12
$[\text{Zn}(\text{HMPM})_4\text{Cl}_2]$	200	14	10	11	9
	400	16	6	13	10
Standard (<i>streptomycin</i>)	200	20	18	18	20
	400	22	18	22	17

4C.1.2 *In vitro* Antifungal Activity

In vitro antifungal activity studies of **HMPM** and its complexes are conducted using two fungal strains, *Aspergillusniger* and *Penicilliumnotatum*, as well as the ketoconazole drug as a control. The results are furnished in **Table 4C.2**. For both fungal strains, the antifungal activities of $[\text{Zn}(\text{HMPM})_4\text{Cl}_2]$ and $[\text{Ni}(\text{HMPM})_4\text{Cl}_2]$ are reasonably close to the standard.

4C.1.3 *In vitro* Antioxidant Property

The scavenging activity has been studied reaction between antioxidant molecule and free radical *DPPH* (2,2-Diphenyl-1-picrylhydrazyl) occurs [12]. The data suggest some reasonable antioxidant activity for $[\text{Zn}(\text{HMPM})_4\text{Cl}_2]$, $[\text{Cu}(\text{HMPM})_4\text{Cl}_2]$, in the same order. Further, the

activity of some of the complexes, $[\text{Co}(\text{HMPM})_4\text{Cl}_2]_2$ and $[\text{Ni}(\text{HMPM})_4\text{Cl}_2]_2$, are lower than that of the DPPH has shown in **Figure 4C.2**.

Table 4C.2 MIC values of antifungal activity of **HMPM** and $[\text{M}(\text{HMPM})_4\text{Cl}_2]$ ($\mu\text{g/ml}$)

Compound	<i>Aspergillusniger</i>	<i>Pencilliumnotatum</i>
$[\text{Zn}(\text{HMPM})_4\text{Cl}_2]$	5.32	7.28
$[\text{Cu}(\text{HMPM})_4\text{Cl}_2]$	18.67	16.93
$[\text{Ni}(\text{HMPM})_4\text{Cl}_2]$	7.86	10.33
$[\text{Co}(\text{HMPM})_4\text{Cl}_2]$	56.73	42.12
HMPM	55.13	62.38
Ketoconazole (std)	3.64	3.49

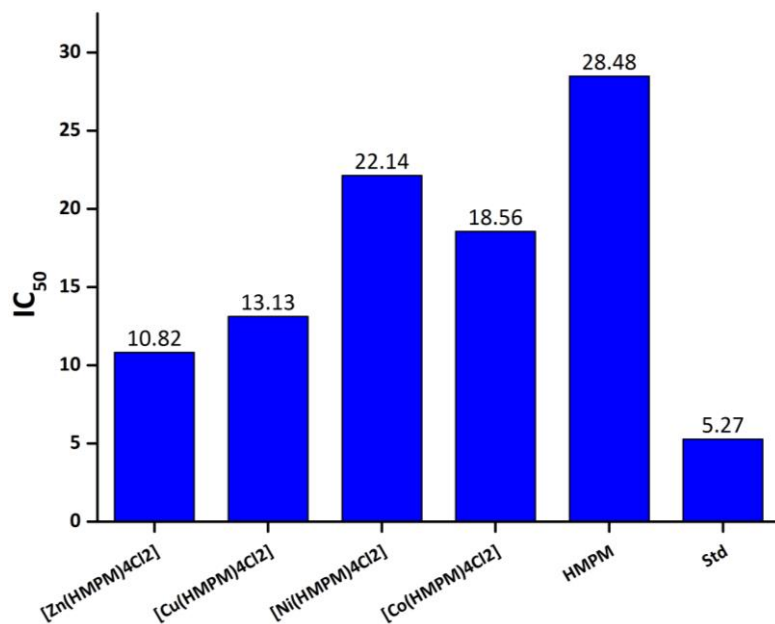


Figure 4C.2 Histogramical representation of the scavenging activity of **HMPM** and $[\text{M}(\text{HMPM})_4\text{Cl}_2]$ with IC₅₀ inhibition values of DPPH free radical

4C.1.4 *In vitro* Alpha-Amylase Inhibitory Assay

The *in-vitro* anti-diabetic study of the **HMPM** and $[\text{M}(\text{HMPM})_4\text{Cl}_2]$ was done by alpha-amylase inhibition assay results are given **Table 4C.4**. The $[\text{Zn}(\text{HMPM})_4\text{Cl}_2]$ exhibited greater anti-diabetic inhibition activity of alpha-amylase assay at 54.34 % at 50 $\mu\text{g/ml}$ concentration than **HMPM** just, 17.02 % at 50 $\mu\text{g/ml}$. This is possible that the interaction between the enzyme's active sites and the metal complex generates the observed inhibition of α -amylase activity. The different structural configurations possible for the substrates around the metal ion contribute to the enhanced activity of metal complexes. This allows them to occupy important regions of the enzyme's active

sites that the two-dimensional **HMPM** cannot reach. From the **Figure 4C.3** calculated graphical linear plots of **HMPM** ($IC_{50} = 195.20 \mu\text{g/ml}$) and $[\text{Zn}(\text{HMPM})_4\text{Cl}_2]$ ($IC_{50}=45.55 \mu\text{g/ml}$). Complexes **Co(II)**, **Cu(II)**, and **Ni(II)** exhibited significant inhibitory activity against amylase and was comparable with that of ligand exhibited at 50 ($\mu\text{g/ml}$) maximum inhibitory activity. Thus, Ligand, **HMPM** and its **M(II)** complex, $[\text{M}(\text{HMPM})_4\text{Cl}_2]$, can be considered as possible anti-diabetic agents though further studies may be essential to optimize.

Table 4C.3 Alpha-amylase enzyme inhibitory activity of **HMPM** and $[\text{M}(\text{HMPM})_4\text{Cl}_2]$ at different doses with glucose as the control

S. No.	Test Compound	% Inhibition				
		10 ($\mu\text{g/ml}$)	20 ($\mu\text{g/ml}$)	30 ($\mu\text{g/ml}$)	40 ($\mu\text{g/ml}$)	50 ($\mu\text{g/ml}$)
1	HMPM	6.38	7.4	10.6	12.76	17.02
2	$[\text{Zn}(\text{HMPM})_4\text{Cl}_2]$	6.52	23.9	32.6	43.47	54.34
3	$[\text{Cu}(\text{HMPM})_4\text{Cl}_2]$	6.30	22.0	35.0	44.86	55.0
4	$[\text{Ni}(\text{HMPM})_4\text{Cl}_2]$	4.89	27.0	31.0	37.0	52.0
5	$[\text{Co}(\text{HMPM})_4\text{Cl}_2]$	5.56	37.0	45.0	52.0	67.2

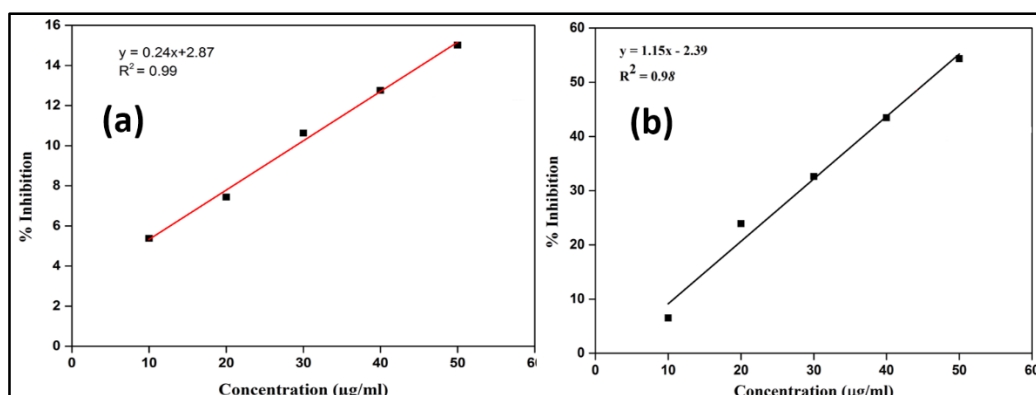


Figure 4C.3 Alpha-amylase enzyme inhibitory activity of (a) **HMPM** and (b) $[\text{Zn}(\text{HMPM})_4\text{Cl}_2]$

4C.2 Molecular Docking Analysis

Molecular docking studies of $[\text{M}(\text{HMPM})_4\text{Cl}_2]$ and **HMPM**, on the protein, **2QLC**, and on alpha-amylase enzyme **2QV4** were undertaken. The results exhibit excellent binding energies towards the receptor active sites as briefly reported hereunder:

4C.2.1 Molecular Docking with **2QLC** Protein

The interaction energy in kcal/mol of a few selective bonding interactions of the compound in $[\text{Zn}(\text{HMPM})_4\text{Cl}_2]$ with amino acid residues of the enzymes (PDB ID; **2QLC**) are collected in

Table 4C.5. The complex $[\text{Zn}(\text{HMPM})_4\text{Cl}_2]$ shows a good binding energy with a docking score -95.358 kcal/mol whereas the ligand, **HMPM** exhibited a binding energy docking score of -85.671 **Figure 4C.4** shows the pictures of prominent docked binding sites which is optimized with Schrodinger software. Furthermore docking interactions optimized on the Autodock vina results of receptor atoms, ligand atoms interactions and their H-bond distances with best docking energy scores in (Kilo calories) have been listed in detailed in **Table 4C.6**. The receptor to ligand interactions of 2D and 3D view of ligand **HMPM** and its complexes $[\text{M}(\text{HMPM})_4\text{Cl}_2]$ interactions like H, Pi-Pi and other bond interactions in the molecules are presented in **Figure 4C.5-4C.9**.

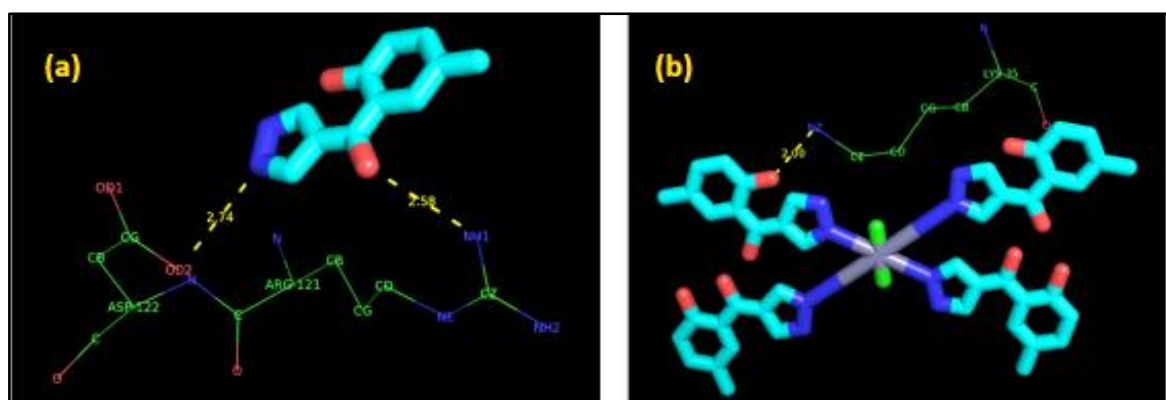


Figure 4C.4 Molecular 3D binding site poses of (a) **HMPM** and (b) $[\text{Zn}(\text{HMPM})_4\text{Cl}_2]$ with 2QLC DNA repair protein receptor

Table 4C.5. Molecular docking interaction parameters of **HMPM** and $[\text{Zn}(\text{HMPM})_4\text{Cl}_2]$ with DNA repair protein receptor (PDB ID: (2QLC)

Receptor	Ligands	Receptor (Host) Interaction Atoms	Guest Atoms	Distance (Å)	Energy (kcal/mol)
2QLC	HMPM	ASP122-OD2	NH	2.74	-85.671
		ARG121-NH1	O	2.58	-85.671
	$[\text{Zn}(\text{HMPM})_4\text{Cl}_2]$	LYS35-NZ	OH	2.00	-95.358

Table 4C.6 Molecular interactions with **ligands** against DNA RadC repair protein receptor (PDB ID: (2QLC)

Ligands	Receptor Interaction Atoms	Ligand Atoms	Hydrogen Bonding Distance (Å)	Docking Score (kcal/mol)
HMPM	OC-THR -50	HO	2.86	-5.9
	OC-GLY B-47	HO	2.14	
	OC-ASP B-88	HN	1.85	
	HN-HIS B-75	N	2.40	
$[\text{Co}(\text{HMPM})_4\text{Cl}_2]$	OC-ARG C-121	OH	2.24	-8.2

	HN-ARG C-121	O	2.24	
	OC-GLU- C-105	HO	2.14	
	HN-GLN B-90	O	2.9	
	HN-GLN G-90	O	1.89	
[Ni(HMPM)4Cl₂]	HN-ARG H-21	O	2.79	-8.2
	OC-ARG H-21	HO	2.39	
	OC-GLU G-25	HO	2.5	
	OC-ALA G-51	HO	2.28	
[Cu(HMPM)4Cl₂]	HN-GLN E-103	O	2.52	-8.6
	HN-GLN E-103	O	2.93	
	HN-ARG B-57	O	2.13	
	HN-HIS C-69	O	2.94	
	HN-ARG C-121	O	2.35	
	HN-LYS C-96	O	2.38	
	O-ASP C-100	HO	2.59	
[Zn(HMPM)4Cl₂]	HN-LYS G-89	O	1.95	-8.3
	O -ASP C-122	HN	2.70	
	HN-ARG C-57	O	2.04	
	HN-ALA C-8	O	2.44	
	HN-ALA C-8	O	2.99	
	O-THR B-48	HO	2.30	

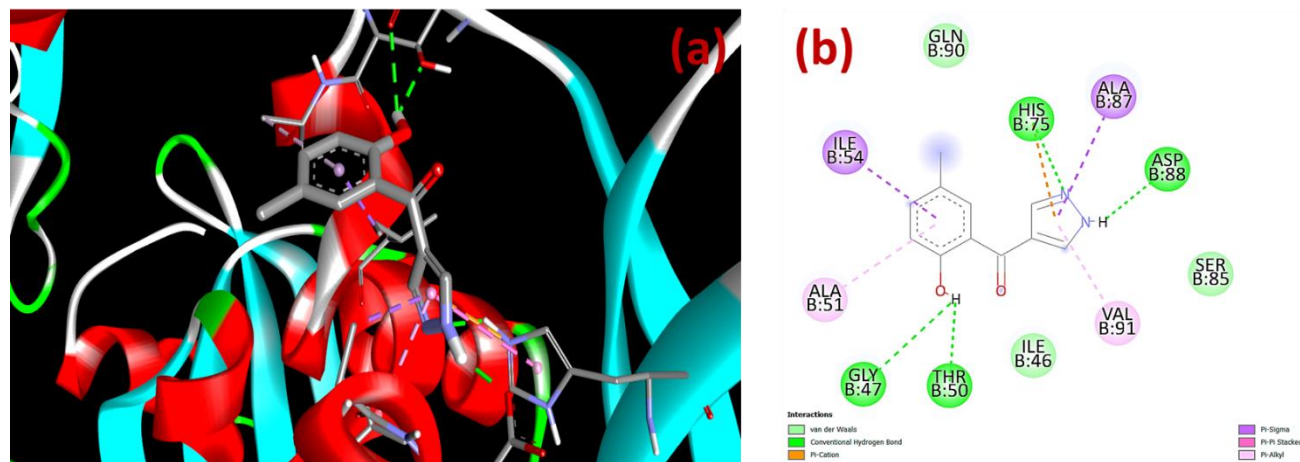


Figure 4C.5 Molecular docking interactions of **HMPM** with RadC protein (PDB: 2QLC); 3D **(a)** and 2D **(b)** presentation of ligand-receptor binding interactions with amino acid residues

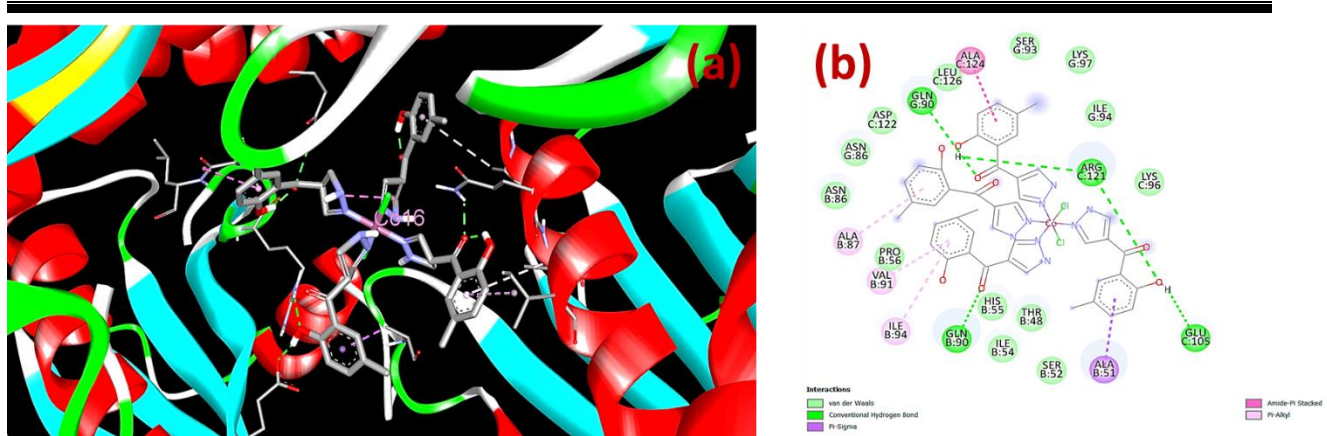


Figure 4C.6 Molecular docking interactions of $[\text{Co}(\text{HMPM})_4\text{Cl}_2]$ with RadC protein (PDB: 2QLC); 3D (a) and 2D (b) presentation of ligand-receptor binding interactions with amino acid residues

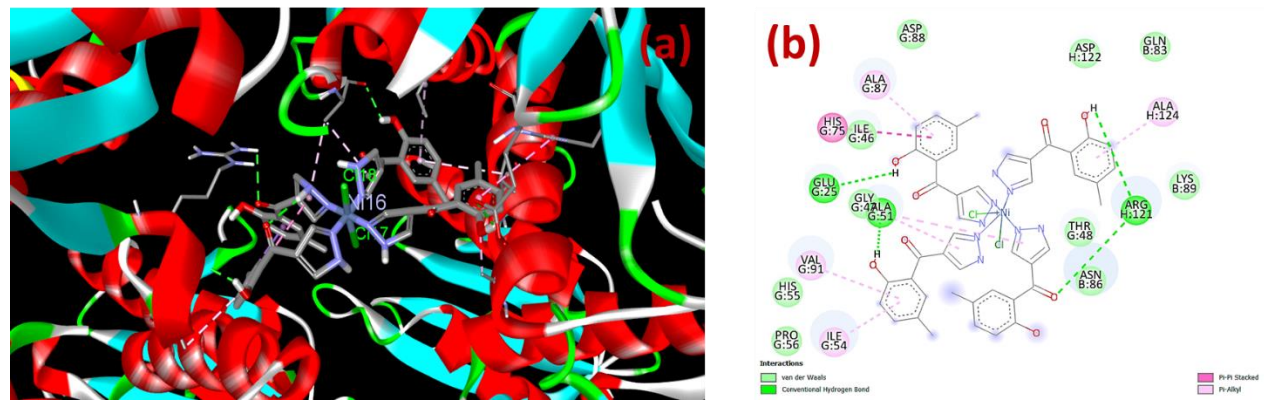


Figure 4C.7 Molecular docking interactions of $[\text{Ni}(\text{HMPM})_4\text{Cl}_2]$ with RadC protein (PDB: 2QLC); 3D (a) and 2D (b) presentation of ligand-receptor binding interactions with amino acid residues

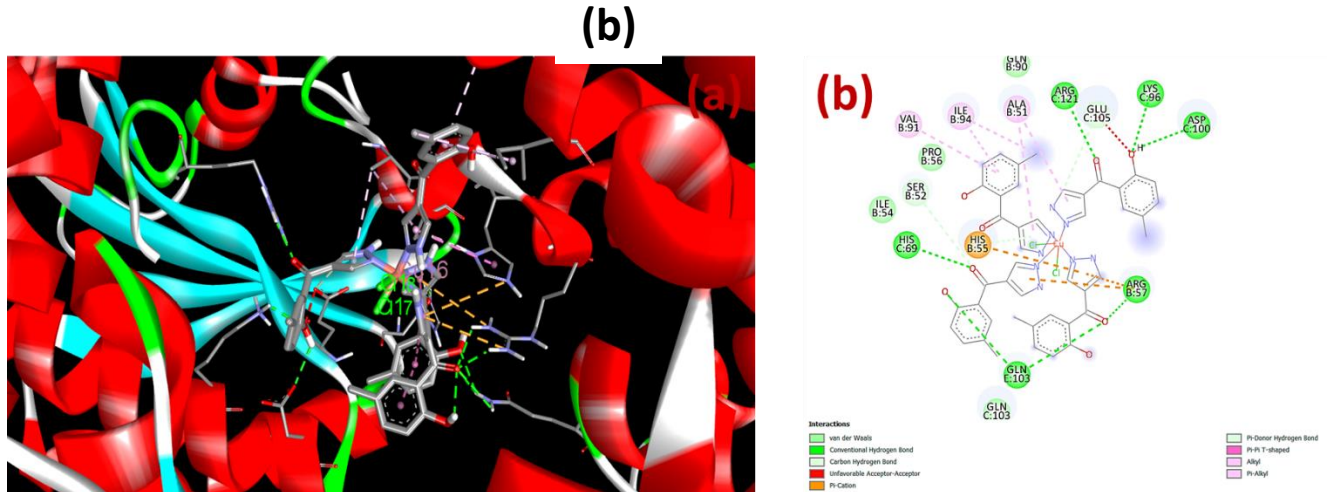


Figure 4C.8 Molecular docking interactions of **[Cu(HMPM)4Cl₂]** with RadC protein (PDB: 2QLC); 3D (a) and 2D (b) presentation of ligand-receptor binding interactions with amino acid residues

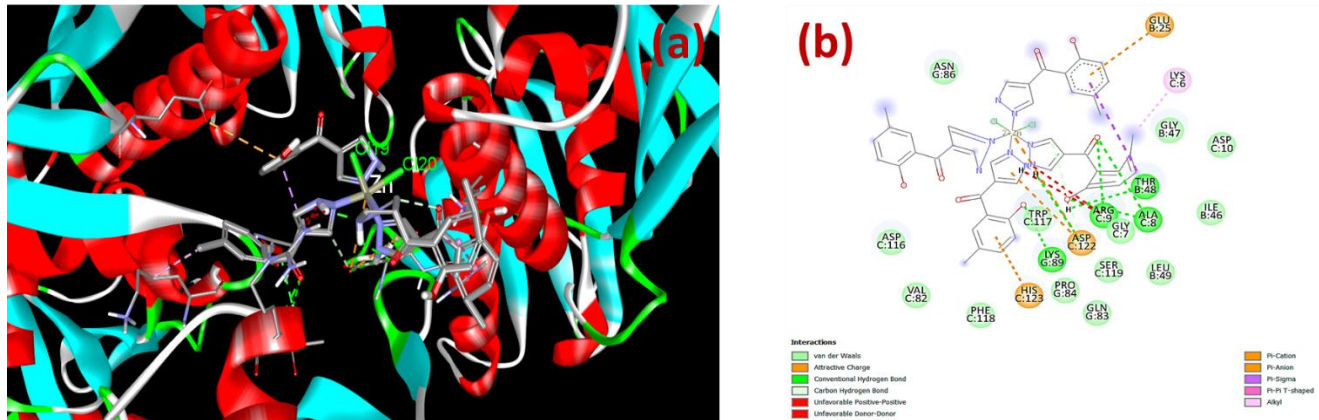


Figure 4C.9 Molecular docking interactions of **[Zn(HMPM)4Cl₂]** with RadC protein (PDB: 2QLC); 3D (a) and 2D (b) presentation of ligand-receptor binding interactions with amino acid residues

4C.2.2 Molecular Docking with Alpha-Amylase Enzyme

The α -amylase crystal structure was retrieved from the Protein Data Bank (PDB ID: 2QV4). The docking energy of the complex **[Zn(HMPM)4Cl₂]** is higher than that of **HMPM**. The binding posture and interactions responsible for the activity against human pancreatic α -amylase were determined using this assay (PDB ID: 2QV4) [63]. As a result, molecular docking study was done using these two compounds, and the results are listed in **Table 4C.7**. The ligand, **HMPM** with docking score of -7.0 was found to be showing three hydrogen bond interactions with amino acid residues ARG-398, ARG-398 and GLY-334, two pi-pi interactions with PRO-4, PHE-335 (T shaped) and hydrophobic contacts with PRO-4, PHE-335, GLY-334 and ARG -398. The binding pose of ligand **HMPM** and its complex are shown in **Figure 4C.10**. The complex, **[Zn(HMPM)4Cl₂]**, with docking score of -9.0 binds to the active site of α -amylase with an orientation and interactions similar to that of **HMPM** ligand.

It shows two hydrogen bond interactions with amino acid residues, OC-LYS-457 of OH, HN-LYS-457 of O of complex atom, and other two H bond contacts with PRO-34 and with different bond distances, such as 2.37 and 1.96 Å with NH...OC and NH....OC, respectively. One H bond distance with ASN-399 is 1.96 Å via NH...OC and three π - π interactions with ILE-396, two π - π interactions with VAL-400, LYS-457 and with hydrophobic contacts with LYS-457, ASP-456 and PRO-34.

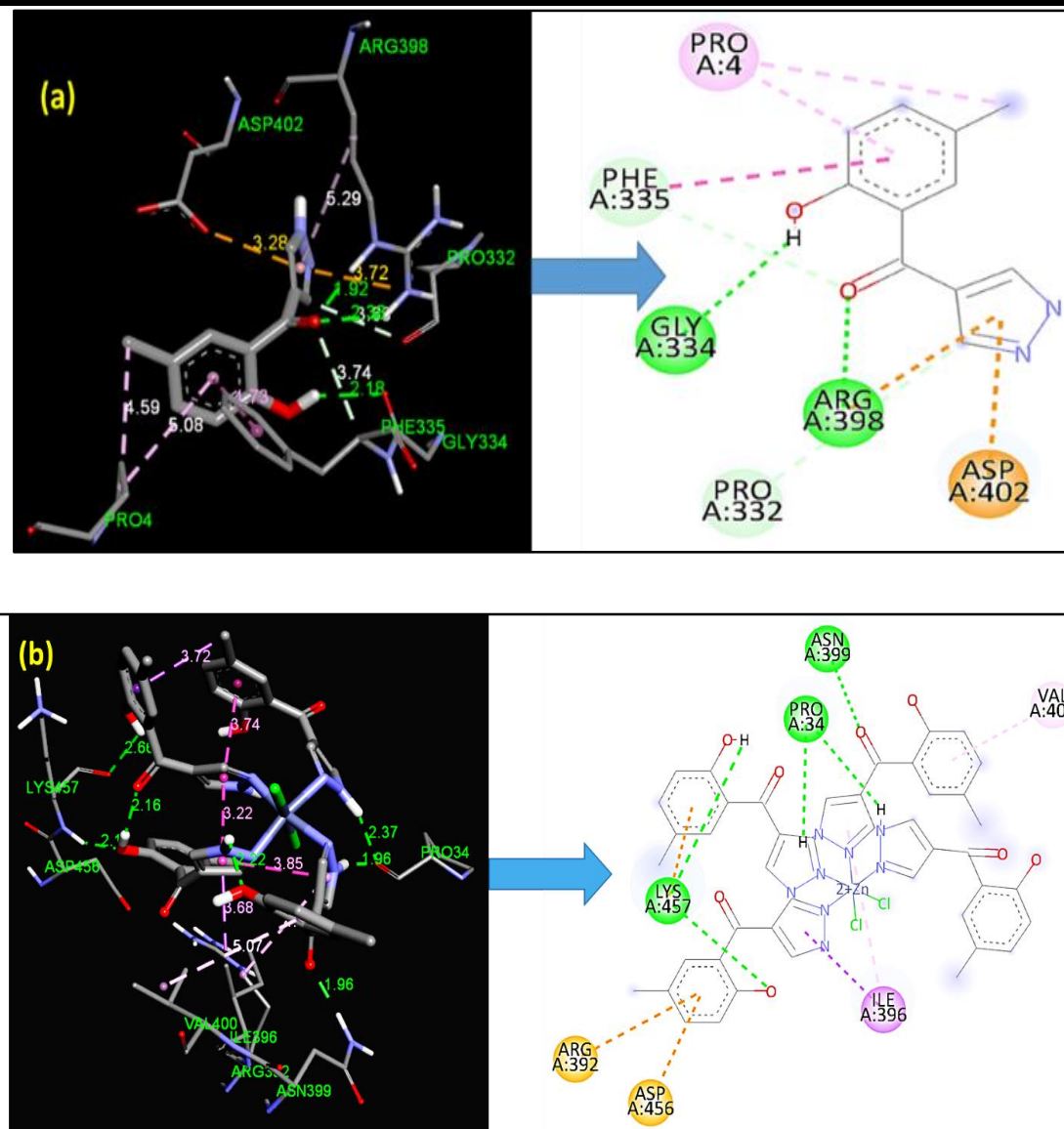
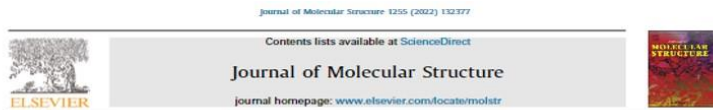


Figure 4C.10 Molecular docking interactions poses of 3D-2D HMPM (a) and $[\text{Zn}(\text{HMPM})_4\text{Cl}_2]$ (b) with alpha-amylase enzyme (PDB ID: 2QV4)

Table 4C.7 Molecular docking interaction parameters of HMPM and $[\text{Zn}(\text{HMPM})_4\text{Cl}_2]$ against *human pancreatic α -amylase* enzyme (PDB ID: 2QV4) receptor

Receptor	Ligands	Receptor (Host) Interaction atoms	Guest atoms	Distance (Å)	Energy (kcal/mol)
2QV4	HMPM	HN-ARG-398	O	1.92	-7.0
		HN-ARG-398	OH	2.38	
		OC-GLY-334	OH	2.18	
	$[\text{Zn}(\text{HMPM})_4\text{Cl}_2]$	OC-LYS-457	OH	2.66	-9.0
		HN-LYS-457	O	2.11	
		OC-PRO34	NH	2.37	
		OC-PRO-34	NH	1.96	
		OC-ASN-399	NH	1.96	

Note: The Crystal Zn(II) complex part of this Chapter has been published in a Elsevier journal as Synthesis, characterization, crystal structure determination, computational modelling and biological studies of a new tetrakis-(2-hydroxy-5-methylphenyl)(1H-pyrazol-4-yl)methanonezinc(II) complex, Ajmeera Ramesh *et al*, *Journal of Molecular Structure*, 2022, 1255, 132377.



Synthesis, characterization, crystal structure determination, computational modelling and biological studies of a new tetrakis-(2-hydroxy-5-methylphenyl)(1H-pyrazol-4-yl)methanonezinc(II) complex

Ajmeera Ramesh, Basavujo Srinivas, Ravinder Pawar, Allikayala Ramachandraiah*

Department of Chemistry, National Institute of Technology Wonnagat, Wonnagat, Karnataka 560 004, India

ARTICLE INFO

Article history:
Received 29 November 2021
Revised 16 December 2021
Accepted 7 January 2022
Available online 9 January 2022

Keywords:
Octahedral Zn(II) complex
Single crystal XRD
Molecular modelling
Antibacterial and anti-damatic activity
Docking Studies/Statistical Analysis

ABSTRACT

A new four-blade propeller with axial kind zinc complex, dichloro-tetrakis-(2-hydroxy-5-methylphenyl)(1H-pyrazol-4-yl)methanonezinc(II) complex, $[\text{Zn}(\text{HMPM})_4\text{Cl}_2]$, has been synthesized and characterized by spectral, structural and biological studies. Its crystal structure was solved by single crystal XRD. The ligand, 3-formyl-6-methyl chromone with thiosemicarbazide (HMPM), has been prepared by condensation of 3-formyl-6-methyl chromone with thiosemicarbazide. The $[\text{Zn}(\text{HMPM})_4\text{Cl}_2]$ complex crystallizes in the centrosymmetric monoclinic $P2_1/m$ space group with unit cell dimensions: $a = 12.425$ Å, $b = 10.063$ Å, $c = 15.910$ Å, $\beta = 102.32^\circ$. From the XRD data it follows that $[\text{Zn}(\text{HMPM})_4\text{Cl}_2]$ is a slightly distorted octahedral complex. The ligand, 4 HMPM serves as monodentate ligands through their pyrazole's sp^2 nitrogens and the 2 chlorides occupying the trans positions. Each of the $[\text{Zn}(\text{HMPM})_4\text{Cl}_2]$ molecules in the crystal assumes a $c\text{-}c$ plane group of symmetry. Both the ligand and the complex, have been characterized by FT-IR, ^1H NMR, ^{13}C NMR, ^{63}Zn NMR, XRD, and XTB platforms and the computationally obtained structural parameters were found to be in very good agreement with the XRD data. The calculated electronic spectral bands of HMPM and the Zn(II) complex are also found to be very close to the experimental results. The ligand and the complex are also found to exhibit considerable anti-bacterial activity. Protein-docking studies have also been carried out for both HMPM and $[\text{Zn}(\text{HMPM})_4\text{Cl}_2]$.

© 2022 Elsevier B.V. All rights reserved.

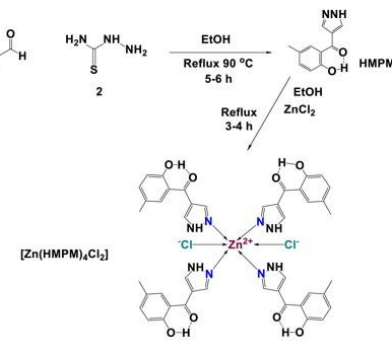
1. Introduction

The interaction between various transition metal complexes and DNA has been intensively explored due to their improved bioactivity use in the areas of DNA structural probes and anticancer medicines [1,2]. Researchers are interested in metal complexes with a variety of donor ligands because of a wide range of pharmacological features [3–4] and its role as a potential monodentate and bridging ligand in a variety of bioinorganic chemical processes [5–7]. Amongst transition metals, zinc is the second most abundant element found in (human) biological cells, behind iron, mostly in its Zn(II) which is found in diverse biological processes [8]. Zinc (II) ions gain popularity due to its interesting structural properties and activities as a catechol oxidase inhibitor, schizonticidal, antimalarial, antibacterial, photosensitizer, and agricultural biocidal [9–13]. It's also essential for structural co-factors, DNA binding or recognition, gene expression, apoptosis, catalytic

centres, immune system function, neural signal transmission, and enzyme control, amongst other things [14–20]. Pyrazolone ligandes are present in anti-tuberculosis [21], antidiabetic [22,23], anticancer [24,25], antioxidant [26,27], antibacterial [28–29], and antimicrobial activities [30–32] natural alkaloids and pharmaceuticals. Pyrazoles (narrowly defined with hydrazine, semicarbazone, and bissemicarbazone series) have recently been investigated as photochromic materials that can be employed in high-density information storage systems and optical switching devices [33–35], as well as photoluminescent materials [36–40].

This article reports the results of the synthesis, molecular structure, determined by XRD, single crystal XRD, FT-IR, ^1H NMR, ^{13}C NMR, ^{63}Zn NMR, DNA docking and biological activity studies of a new complex, $[\text{Zn}(\text{HMPM})_4\text{Cl}_2]$, i.e., [dichloro-tetrakis-(2-hydroxy-5-methylphenyl)(1H-pyrazol-4-yl)methanonezinc(II)] wherein, the ligand, (2-hydroxy-5-methylphenyl)(1H-pyrazol-4-yl)methanone, and hereafter mentioned as HMPM, is a condensate of 3-formyl-6-methyl chromone and thiosemicarbazide (Scheme 1).

* Corresponding author.



References

- [1] Hsieh, C.-C.; Lee, C.-J.; Horng, Y.-C. Effects of the Counteranion on the Pyrazole–Nitrile Coupling Reaction Mediated by Nickel(II) Ions. *Organometallics* **2009**, 28 (17), 4923–4928. <https://doi.org/10.1021/om9004753>.
- [2] Patel, R. N.; Singh, Y.; Singh, Y. P.; Butcher, R. J. Synthesis, Crystal Structure and DFT Calculations of Octahedral Nickel(II) Complexes Derived from N'-(E)-Phenyl(Pyridin-2-Yl)Methylidene]Benzohydrazide. *Journal of Coordination Chemistry* **2016**, 69 (15), 2377–2390. <https://doi.org/10.1080/00958972.2016.1189543>.
- [3] Chai, L.-Q.; Zhang, J.-Y.; Chen, L.-C.; Li, Y.-X.; Tang, L.-J. Synthesis, Crystal Structure, Spectroscopic Properties and DFT Calculations of a New Schiff Base-Type Zinc(II) Complex. *Research on Chemical Intermediates*. **2016**, 42 (4), 3473–3488. <https://doi.org/10.1007/s11164-015-2226-8>.
- [4] Chai, L.-Q.; Zhang, J.-Y.; Chen, L.-C.; Li, Y.-X.; Tang, L.-J. Synthesis, Crystal Structure, Spectroscopic Properties and DFT Calculations of a New Schiff Base-Type Zinc(II) Complex. *Research on Chemical Intermediates*. **2016**, 42 (4), 3473–3488. <https://doi.org/10.1007/s11164-015-2226-8>.
- [5] Yernale, N. G.; Bennikallu Hire Mathada, M. Preparation of Octahedral Cu(II), Co(II), Ni(II) and Zn(II) Complexes Derived from 8-Formyl-7-Hydroxy-4-Methylcoumarin: Synthesis, Characterization and Biological Study. *Journal of Molecular Structure*. **2020**, 1220, 128659. <https://doi.org/10.1016/j.molstruc.2020.128659>.
- [6] (a) Rabindra Reddy, P.; Shilpa, A. Synthesis, Characterization, and DNA-Binding and - Cleavage Properties of Dinuclear Cu(II) Salophen/Salen Complexes. *Chemistry & Biodiversity* **2011**, 8 (7), 1245–1265. <https://doi.org/10.1002/cbdv.201000153>.
- [7] Miehlich, B.; Savin, A.; Stoll, H.; Preuss, H. Results Obtained with the Correlation Energy Density Functionals of Becke and Lee, Yang and Parr. *Chemical Physics Letters* **1989**, 157 (3), 200–206. [https://doi.org/10.1016/0009-2614\(89\)87234-3](https://doi.org/10.1016/0009-2614(89)87234-3).
- [8] Lee, C.; Yang, W.; Parr R.G. Development of the Colle-Salvetti Correlation-Energy Formula into a Functional of the Electron Density. *Physical Review B* **1988**, (37), 785-789. <https://doi.org/10.1103/PhysRevB.37.785>.
- [9] Turner, M.J.; MacKinnon, J.J.; Wolff, S.K.; Grimwood, D.J.; Spackman, P.R.; Jayatilaka, D.; Spackman M.A. Crystal Explorer, Version 17.5, *University of Western Australia: Pert* **2017**.
- [10] Spackman, P. R.; Turner, M. J.; McKinnon, J. J.; Wolff, S. K.; Grimwood, D. J.; Jayatilaka, D.; Spackman, M. A. CrystalExplorer : A Program for Hirshfeld Surface Analysis, Visualization and Quantitative Analysis of Molecular Crystals. *Journal of Applied Crystallography* **2021**, 54 (3), 1006–1011. <https://doi.org/10.1107/S1600576721002910>.
- [11] Nasiri Sovari, S.; Zobi, F. Recent Studies on the Antimicrobial Activity of Transition Metal Complexes of Groups 6–12. *Chemistry* **2020**, 2 (2), 418–452. <https://doi.org/10.3390/chemistry2020026>.
- [12] Hazra, B.; Biswas, S.; Mandal, N. Antioxidant and Free Radical Scavenging Activity of Spondias Pinnata. *BMC Complementary and Alternative Medicine* **2008**, 8 (1), 63. <https://doi.org/10.1186/1472-6882-8-63>

CHAPTER – V

SPECTRAL AND BIOLOGICAL STUDIES OF A NOVEL SERIES OF CHROMANONES AND THEIR METAL COMPLEXES AND CORRELATION OF THEIR COMPUTATIONAL STUDIES WITH THE SINGLE CRYSTAL XRD MOLECULAR STRUCTURE OF ONE CHROMANONE OF THE SERIES

CHAPTER-V**SPECTRAL AND BIOLOGICAL STUDIES OF A NOVEL SERIES OF CHROMANONES
AND THEIR METAL COMPLEXES AND CORRELATION OF THEIR
COMPUTATIONAL STUDIES WITH THE SINGLE CRYSTAL XRD MOLECULAR
STRUCTURE OF ONE CHROMANONE OF THE SERIES**

A new series of chromanone-based organic molecules has been synthesized and characterized by various spectroscopic techniques have been presented in this Chapter.

This Chapter is divided into three parts: **PART-A**, **PART-B**, and **PART-C**. Among them, **PART A**, describes in detail the physical, analytical, spectroscopic, morphological and coordination chemistry studies of 3-(5-(allylthio)-4H-1,2,4-triazol-3-yl)-6-methyl-4H-chromen-4-one, **TATMC** and the other chromanone derivatives, **3FMC-2AB-R**.

In **Part-B**, we discuss the single crystal XRD and computational chemistry analysis studies of **TATMC** and correlate the empirical XRD data with the computational data of the modelled molecules, **3FMC-2AB-R(3a-e)** from their fully optimized semi empirical AM1 calculations by MOPAC, MM2 and DFT/B3LYP calculations besides, Hirshfeld surface analysis.

PART-C covers the biological and molecular docking studies of **TATMC** and its metal complexes along with those of the chromanones, **3FMC-2AB-R (3a-e)**. The details of synthesis of these compounds are described in Chapter-II.

PART-A**SPECTRAL, COORDINATION CHEMISTRY STUDIES OF TATMC AND 3FMC-2AB-R****SECTION-A1****5A.1 Studies of TATMC and Its Metal Complexes**

The general schematic of the synthesis of **TATMC** and its metal complexes is presented in **Figure 5A.1**. The physical and analytical data of **TATMC** and $[\text{M}(\text{TATMC})_2\text{X}_2]$ are presented in **Table 5A.1**. The chemical structures shown in the scheme are in good agreement with the results of the elemental analysis. All the complexes are coloured, powdered and stable at room temperature. The complexes decompose on heating without melting. They are insoluble in water and many of the common organic solvents. However, their solubility in DMF and DMSO solvents ranges from minimal to moderate. The molar conductance of the complexes in a 10^{-3} M DMF solution ranges between 0.7 and $2.2 \Omega \text{ cm}^{-1} \text{ mol}^{-1}$, indicating that these metal complexes are not electrolytes.

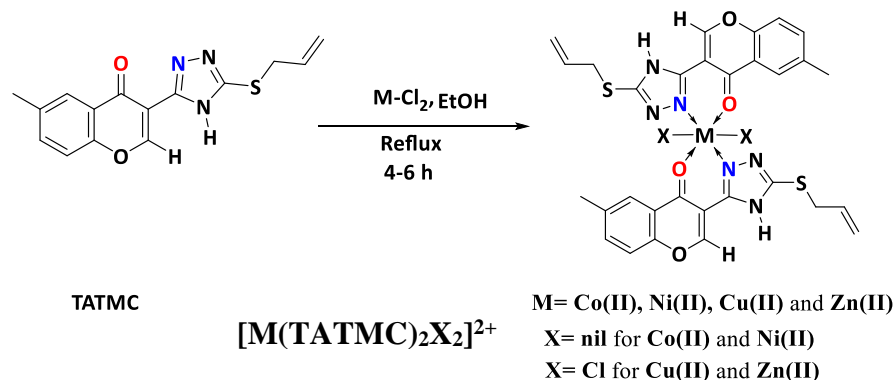


Figure 5A.1 Schematic for the synthesis of $[\text{M}(\text{TATMC})_2\text{X}_2]$ complexes from **TATMC**

Table 5A.1 Physical and analytical data of **TATMC** and $[\text{M}(\text{TATMC})_2\text{X}_2]$

Compound	Colour	M.P °C	Mol. Formulae	Elemental Analysis % found(calculated)			
				C	H	N	S
TATMC	Orange	223	$\text{C}_{15}\text{H}_{13}\text{N}_3\text{O}_2\text{S}$	(6.19) 6.16	(4.38) 4.35	(14.04) 14.03	(10.71) 10.68
[Co(TATMC)₂]	Red	>450	$\text{C}_{30}\text{H}_{26}\text{CoN}_6\text{O}_4\text{S}_2$	(54.79) 50.75	(3.99) 3.95	(12.78) 12.80	(9.75) 9.72
[Ni(TATMC)₂]	Green	>450	$\text{C}_{30}\text{H}_{26}\text{NiN}_6\text{O}_4\text{S}_2$	(54.81) 50.50	(3.99) 3.88	(12.78) 12.77	(9.75) 9.73
[Cu(TATMC)₂Cl₂]	Brown	>450	$\text{C}_{30}\text{H}_{26}\text{CuCl}_2\text{N}_6\text{O}_4\text{S}_2$	(49.15) 49.08	(3.57) 3.55	(11.46) 11.45	(9.72) 9.65
[Zn(TATMC)₂Cl₂]	Cream white	>450	$\text{C}_{30}\text{H}_{26}\text{ZnCl}_2\text{N}_6\text{O}_4\text{S}_2$	(54.26) 54.16	(3.95) 3.85	(12.66) 12.68	(9.66) 9.57

5A.2 ESI-Mass Spectrum of TATMC

The ESI-Mass spectrum of **TATMC** is shown in **Figure 5A.2**. The molecular weight of the **TATMC** is confirmed by ESI-Mass spectral analysis. The molecular ion peak appears at $m/z = 300.08$ [M+H], which is equivalent to its calculated molecular weight at $m/z = 299.07$ consistent with the molecular formulae, ($C_{15}H_{13}N_3O_2S$).

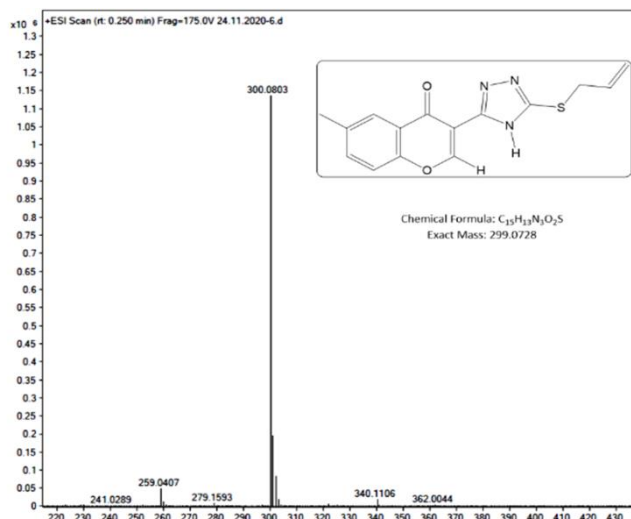


Figure 5A.2 ESI-Mass spectrum of **TATMC** is positions are consistent with the structure of **TATMC**.

Table 5A.2 ^1H and ^{13}C NMR spectral data of TATMC

5A.3 NMR Spectral Studies of TATMC

5A.3.1 ^1H and ^{13}C NMR Spectral Analysis

The ^1H -NMR spectrum of TATMC is presented in **Figure 5A.3**. The peak positions are consistent with the structure of **TATMC**. The important chemical shift δ values of ^1H and ^{13}C NMR spectral data have been provided in **Table 5A.2**.

The ^{13}C NMR spectrum of **TATMC** is presented in **Figure 5A.4**. The peak

¹ H NMR (ppm)	¹³ C NMR (ppm)
2.45 (s, 1H), 4.03-4.05 (d, 2H), 5.24-5.41 (m, 2H), 5.87-5.97 (m, 1H), 7.65-7.92 (m, 2H), 8.52 (s, 1H), 9.70 (s, 1H)	20.98, 34.41, 112.94, 118.35, 118.99, 123.44, 124.92, 131.96, 134.40, 136.48, 145.63, 149.52, 154.38, 158.00, 174.15

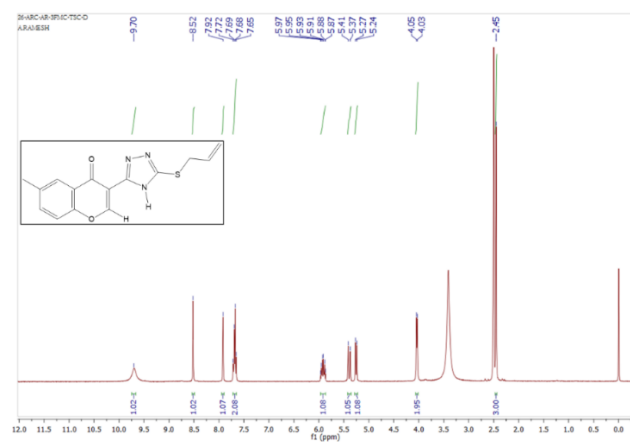


Figure 5A.3 ^1H NMR spectrum of TATMC

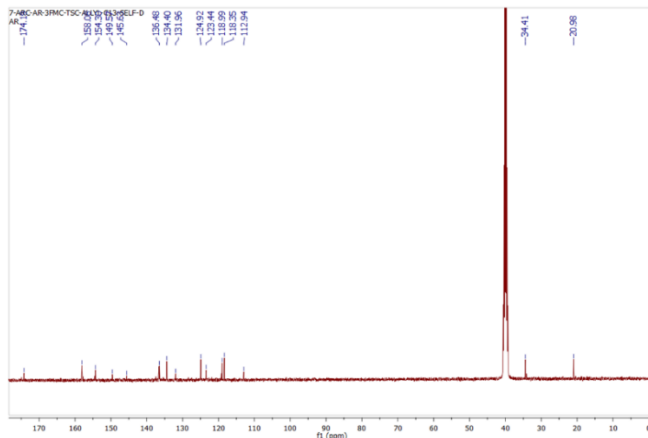


Figure 5A.4 ^{13}C NMR spectrum of TATMC

5A.4 FTIR Spectral Studies of TATMC and Its Metal Complexes

The FTIR spectrum of TATMC is shown in **Figures 5A.5**. In **Figures 5A.6** through **Figure 5A.9** are shown those of $[\text{M}(\text{TATMC})_2\text{X}_2]$

The IR frequencies of the TATMC and its respective metal complexes bands are presented in **Table 5A.3**. A decrease in the absorption bands to 1595–1627 due to the chromone C=O group at 1630 cm^{-1} of TATMC indicates the formation of a bond between metal ion and chromone oxygen atom [1, 2]. The frequency of the azomethine $\nu(\text{--CH}=\text{N})$ group is shifted to a lower frequency and appears in the region of 1523–1596 cm^{-1} . This is supported by the involvement of the azomethine group ligand's nitrogen atom in coordination with M^{2+} ion as $[\text{M}(\text{TATMC})_2\text{X}_2]^{2+}$.

Table 5A.3 Infrared spectral data of TATMC and its complexes (cm^{-1})

Compound	$\nu\text{C}=\text{N}$	$\nu\text{C}=\text{O}$	$\nu\text{C-O}$	$\nu\text{C-Haliph}$	$\nu\text{N-H}$	$\nu\text{C-S aliph}$	$\nu\text{M-O}$	$\nu\text{M-N}$
TATMC	1578	1630	1322	2719	3363	714	-	-
$[\text{Co}(\text{TATMC})_2]$	1562	1616	1319	2921	3314	681	547	470
$[\text{Ni}(\text{TATMC})_2]$	1576	1595	1335	2921	3389	710	544	495
$[\text{Cu}(\text{TATMC})_2\text{Cl}_2]$	1596	1628	1358	2920	3392	682	545	470
$[\text{Zn}(\text{TATMC})_2\text{Cl}_2]$	1523	1621	1348	2925	3400	707	539	468

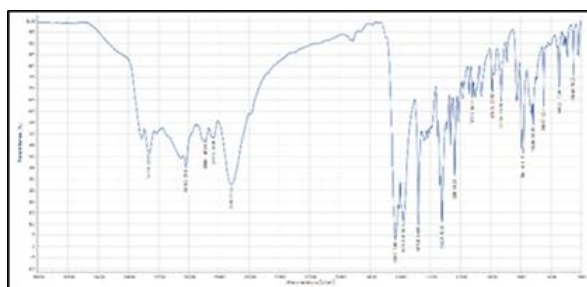


Figure 5A.5 FTIR spectrum of TATMC

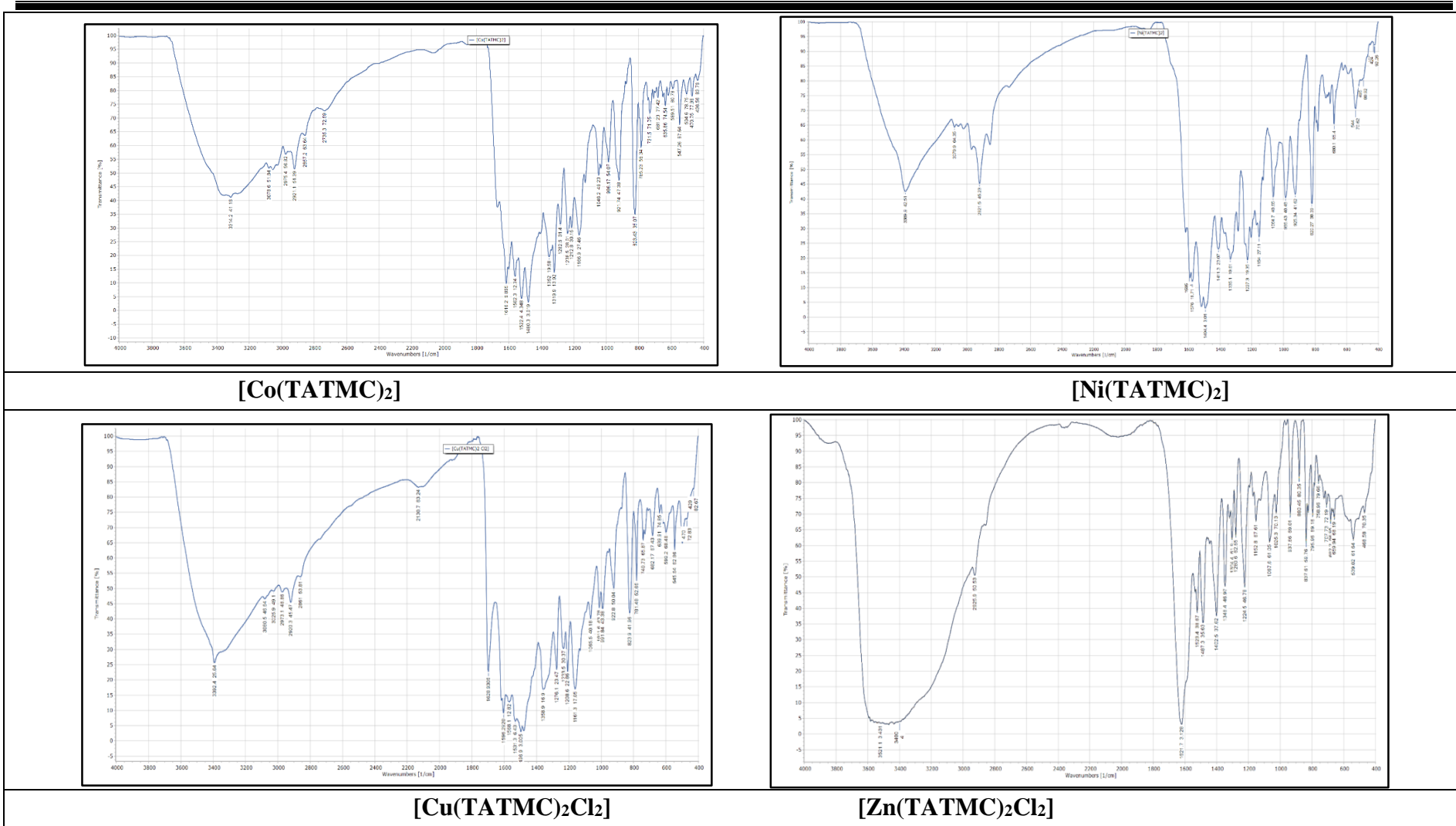


Figure 5A.6 FTIR spectra of complexes of TATMC

5A.5 Electronic Spectral Analysis of TATMC and Its Metal Complexes

In **Figure 5A.10** through **5A.14** is shown the uv-vis spectra of **TATMC** along the spectra of the $[\text{Co}(\text{TATMC})_2]$ results are given in **Table 5.A.4**.

The band at 325-334 nm is attributed to the $n \rightarrow \pi^*$ transition of the C=N imine group [3]. In **TATMC**, two bands are observed at 295 and 320 nm, which are attributed to $\pi \rightarrow \pi^*$ transition of the heterocyclic moieties and the $n \rightarrow \pi^*$ transition of the azomethine group of the ligand respectively. As a consequence of coordination to the metal center, the $\pi \rightarrow \pi^*$ and $n \rightarrow \pi^*$ transition energies in metal complexes are pushed to longer wavelengths [4].

Table 5A.4 Electronic spectral data of **TATMC** and $[\text{M}(\text{TATMC})_2]$

Compounds	$\lambda_{\text{max}} \text{ (nm)}$	Bands Assignments
TATMC	289, 326	$\pi \rightarrow \pi^*$, $n \rightarrow \pi^*$
$[\text{Co}(\text{TATMC})_2]$	325, 440	$\pi \rightarrow \pi^*$, $n \rightarrow \pi^*$
$[\text{Ni}(\text{TATMC})_2]$	317, 441	$\pi \rightarrow \pi^*$, $n \rightarrow \pi^*$
$[\text{Cu}(\text{TATMC})_2\text{Cl}_2]$	367, 430, and 427	$\pi \rightarrow \pi^*$, $n \rightarrow \pi^*$
$[\text{Zn}(\text{TATMC})_2\text{Cl}_2]$	332, 425	$\pi \rightarrow \pi^*$, LMCT

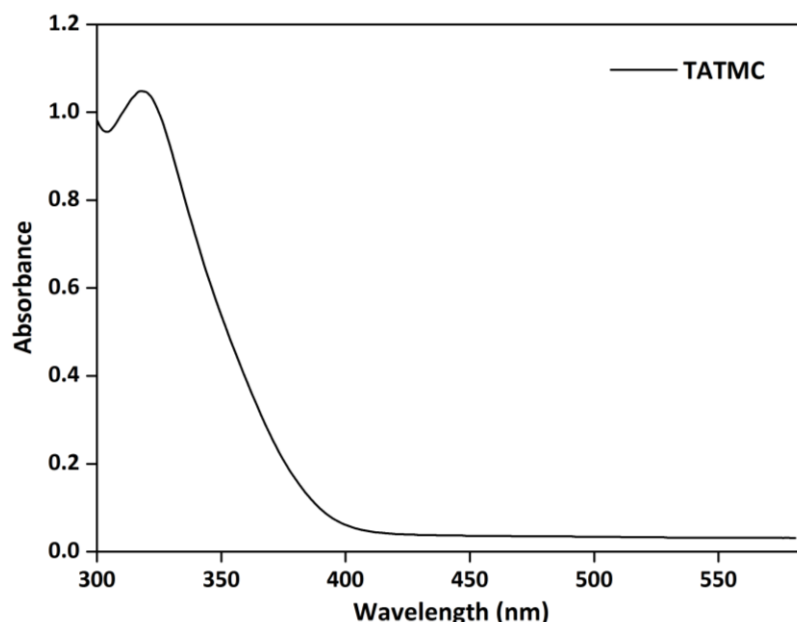


Figure 5A.6 Electronic spectrum of **TATMC**

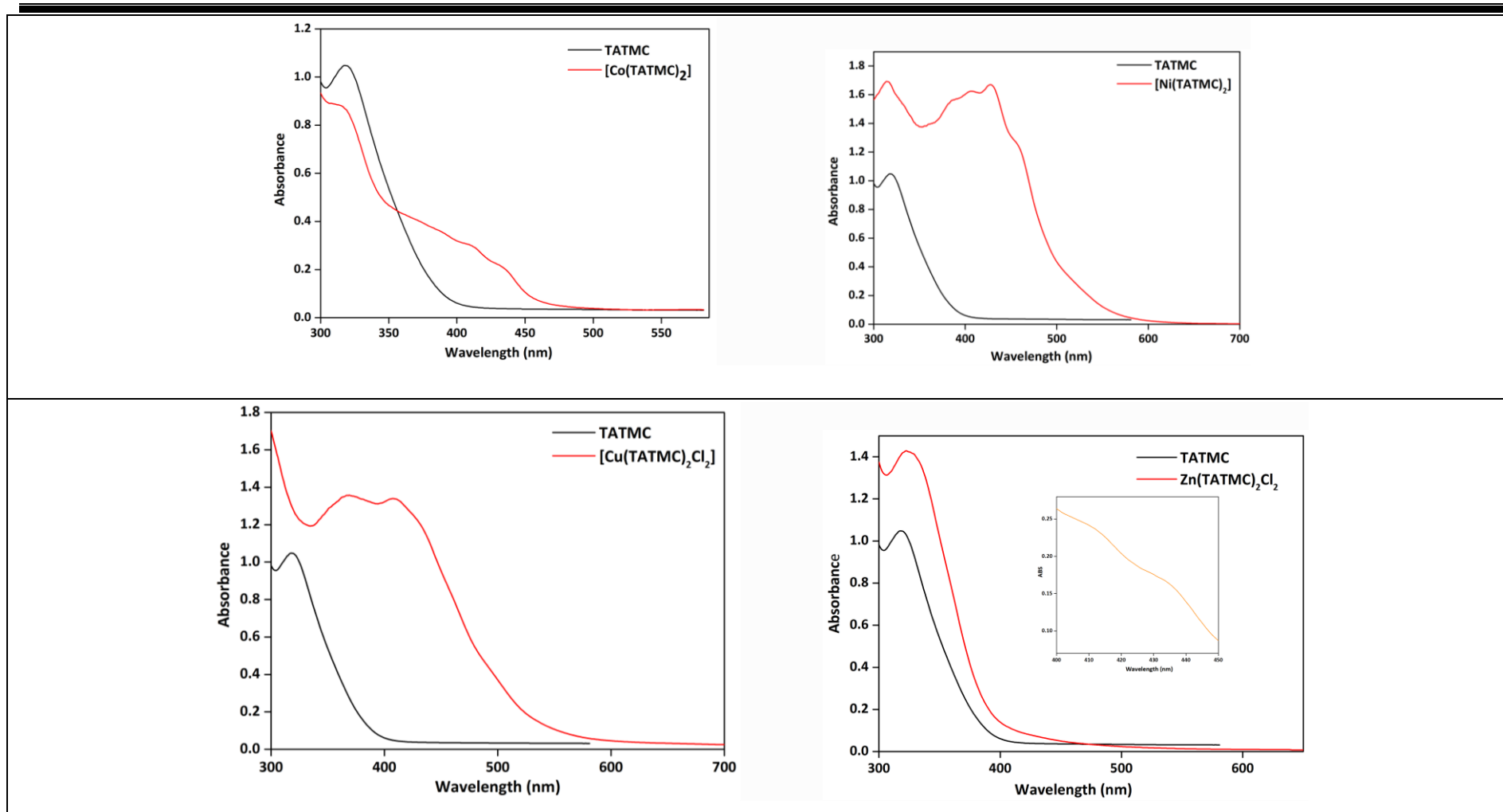


Figure 5A.7 Electronic spectra of complexes of TATMC

5A.6 Fluorescence Spectral Studies of TATMC and Its Complexes

TATMC and its complexes, $[\text{M}(\text{TATMC})_2]^{2+}$ and $[\text{M}(\text{TATMC})_2\text{Cl}_2]$ exhibit fluorescence luminescence in the range of 410-555 nm where excited by the uv radiation of about 315 nm. Metal ions results, quench the fluorescence emission of TATMC in **Table 5A.5**. However, enhancement of fluorescence through complexation is observed in the case, $[\text{M}(\text{TATMC})_2]^{2+}$ complex.

Table 5A.5 Fluorescence spectral data of TATMC and its complexes

Compounds	Excitation Wavelength (nm)	Luminescence Wavelength (nm)
TATMC	316	307
$[\text{Co}(\text{TATMC})_2]$	412	565
$[\text{Ni}(\text{TATMC})_2]$	198	410, 555
$[\text{Cu}(\text{TATMC})_2\text{Cl}_2]$	350	403, 510
$[\text{Zn}(\text{TATMC})_2\text{Cl}_2]$	-	-

5A.7 ESR Spectral Study of $[\text{Cu}(\text{TATMC})_2\text{Cl}_2]$

The polycrystalline room temperature ESR spectrum of $[\text{Cu}(\text{TATMC})_2\text{Cl}_2]$ is shown in **Figure 5A.15**. The Cu(II) complex exhibits a g_{\parallel} value of 2.356 and a g_{\perp} values of 2.172. The g values of (g_{\parallel} and g_{\perp}) both values are higher than the standard g_e Cu(II) value for free electrons, which is 2.0023. This indicates an octahedral environment around Cu(II). This g value order also indicates the presence of an unpaired electron in a dx^2-y^2 orbital with distorted octahedral geometry [5].

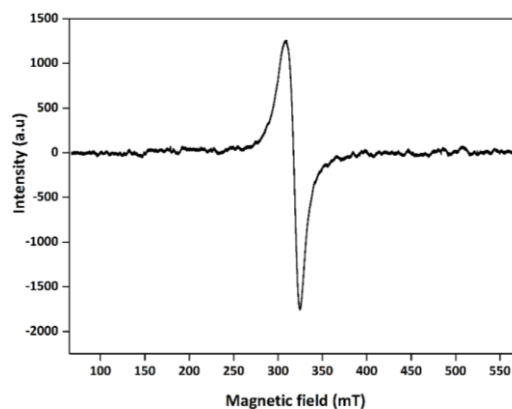


Figure 5A.8 X-band ESR spectrum of $[\text{Cu}(\text{TATMC})_2\text{Cl}_2]$

Hathaway's expression $G = g_{\parallel} - 0.0023/g_{\perp} - 2.0023$ clarifies the exchange coupling interaction. According to Hathaway, if the value of G is greater than four ($G > 4$), the exchange

interaction is negligible, whereas a significant exchange interaction is indicated when G is less than four ($G < 4$). The $[\text{Cu}(\text{TATMC})_2\text{Cl}_2]^{2+}$ complexes $G = 1.72$ is less than four ($G < 4$), showing a considerable exchange interactions in L-M.

5A. 8 Spectrophotometric Titration of TATMC (Job's Monovariation Method)

The ligand, **TATMC**, has a certain set of suitably poised donor atoms for metal coordination to metal ions. The stoichiometry of the complexation between ligand **TATMC** and equimolar concentration of metal ion $\text{Co}(\text{II})$ has been determined using Job's monovariation method, and it was discovered that the complex confirms a 1:2 stoichiometry to M: L shown in **Figure 5A.9**.

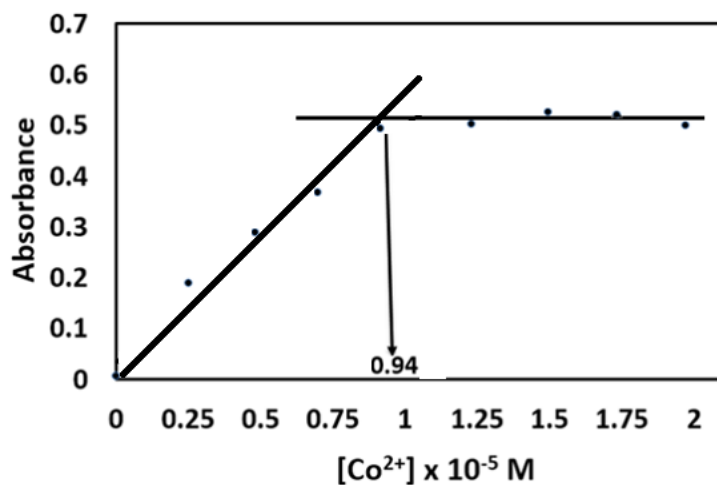


Figure 5A.9 Photometric titration of **TATMC** ($2 \times 10^5 \text{ M}$) against Co^{2+}

5A.9 SEM-EDX Morphological Study of TATMC and Its Complexes

The surface morphology and the grain size of the metal complexes have been illustrated by the scanning electron micrograph. The SEM micrograph of the ligand and all the metal complexes is shown in **Figure 5A.17**. The Energy-Dispersive X-Ray Analyzer (EDX) and SEM are considered good methods for describing the surface morphology [6,7]. Based on EDX, the presence of C, N, O, Cl, S, and the metal in each complex was confirmed by the structure of the complexes. It also confirmed the chelation of metals of $\text{Co}(\text{II})$, $\text{Ni}(\text{II})$, $\text{Cu}(\text{II})$, and $\text{Zn}(\text{II})$ to the **TATMC** ligand. The SEM images of **TATMC** in **Figure 5A.17a** showed a crystal cluster like morphology with four different sizes of $2\mu\text{m}$ - $20\mu\text{m}$, respectively. While the $[\text{Co}(\text{TATMC})_2]$ has a spherical ball-like morphology **Figure 5A.17b**, $[\text{Ni}(\text{TATMC})_2]$ images revealed irregular rock particle shapes **Figure 5A.17c**, and $[\text{Cu}(\text{TATMC})_2\text{Cl}_2]$ images have a cracked ice surface **Figure 5A.17d**. The SEM images of the $[\text{Zn}(\text{TATMC})_2\text{Cl}_2]$ complex displayed granular morphology **Figure 5A.17e**. The SEM micrographs are taken at

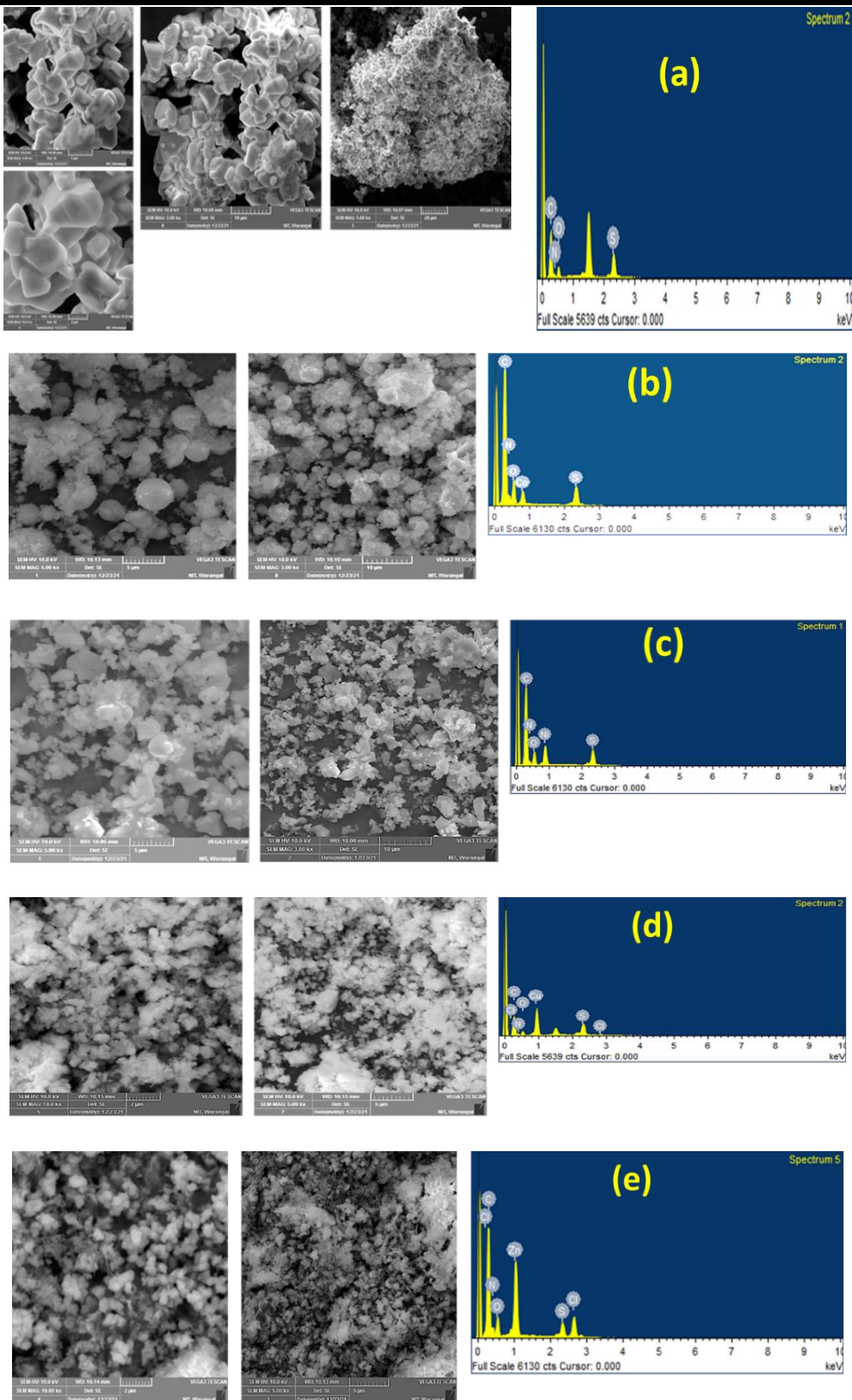


Figure 5A. 10 SEM-EDX pictures of TATMC (a), Co(II) (b), Ni(II) (c), Cu(II) (d) and Zn(II) (e) complexes

Two different scales of a ligand having 2 μm , 5 μm , 10 μm , and 20 μm where other complexes are 5 μm , 10 μm and 20 μm . From the SEM analysis, Co(II), Ni(II), Cu(II) and Zn(II) complexes have been shown to be nano-crystalline in nature, and the each complex have been unique morphologies are investigated.

5A.10 Proposed Structures of TATMC and Its Complexes

Based on all the spectral studies like analytical, molar conductivity data, electronic, infrared and morphological SEM-EDX studies, some possess tetrahedral geometry of Co(II) and Ni(II) and Cu(II), Zn(II) complexes has been proposed octahedral geometry. The proposed structures are shown in **Figure 5A.11**.

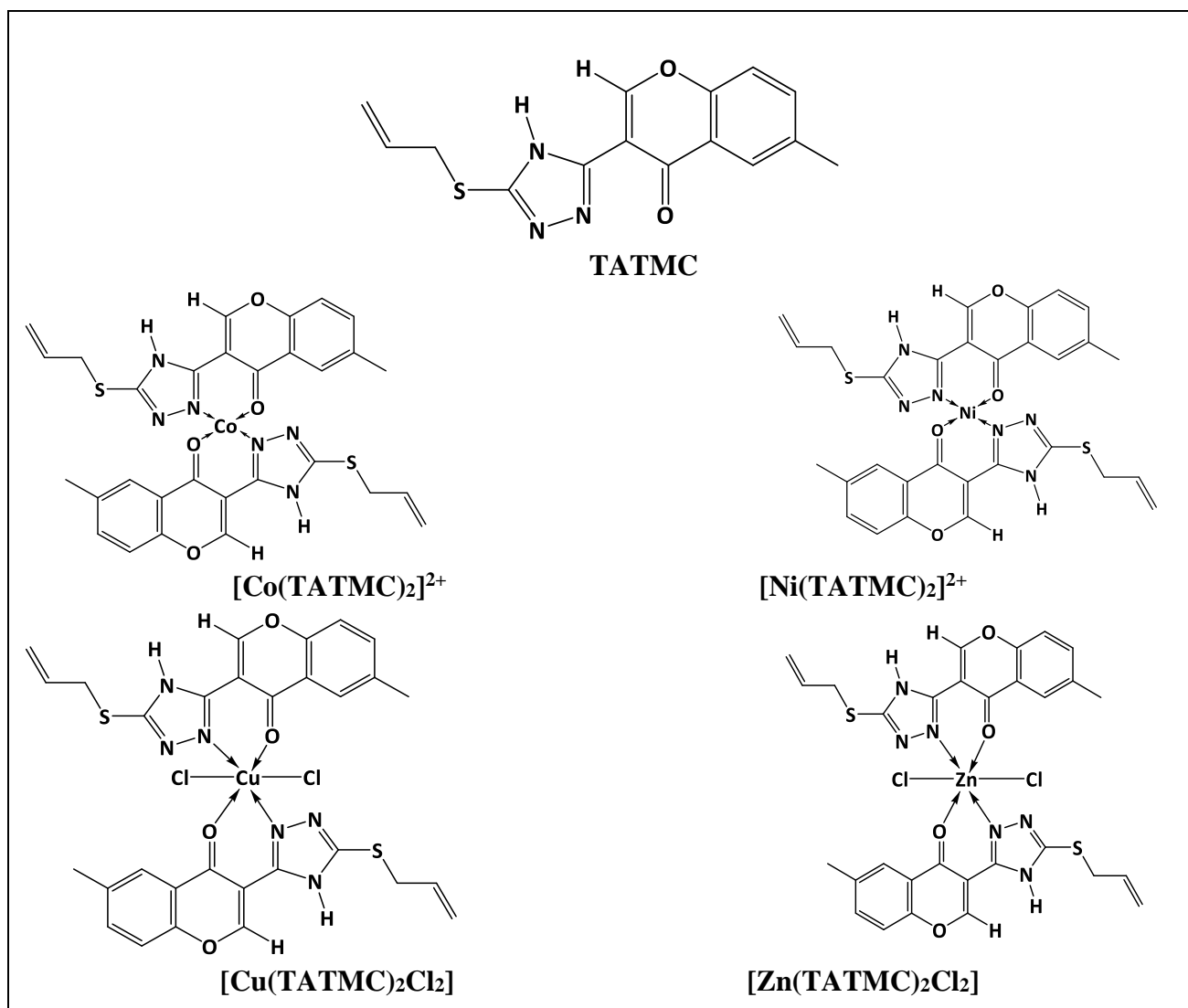


Figure 5A.11 Proposed structures of TATMC and its bivalent metal complexes

SECTION-A2

5A.1 Physical Characteristics of Chromanones 3FMC-2AB-R

Ligand derivatives from 3-Formyl-6-methylchromone and 2-aminobenzamide include **3FMC-2AB-H**, **3FMC-2AB-OMe**, **3FMC-2AB-OEt**, **3FMC-2AB-O(iPr)**, and **3FMC-2AB-O(n-But)**. All the compounds are sparingly soluble in common organic solvents like methanol, ethanol, CHCl_3 , and completely in DMSO and DMF but insoluble in water. **Table 5A.1** contains the physical and analytical properties of the compounds. The analytical data confirms the chemical composition and their proposed structures in **Figure 5A.1**

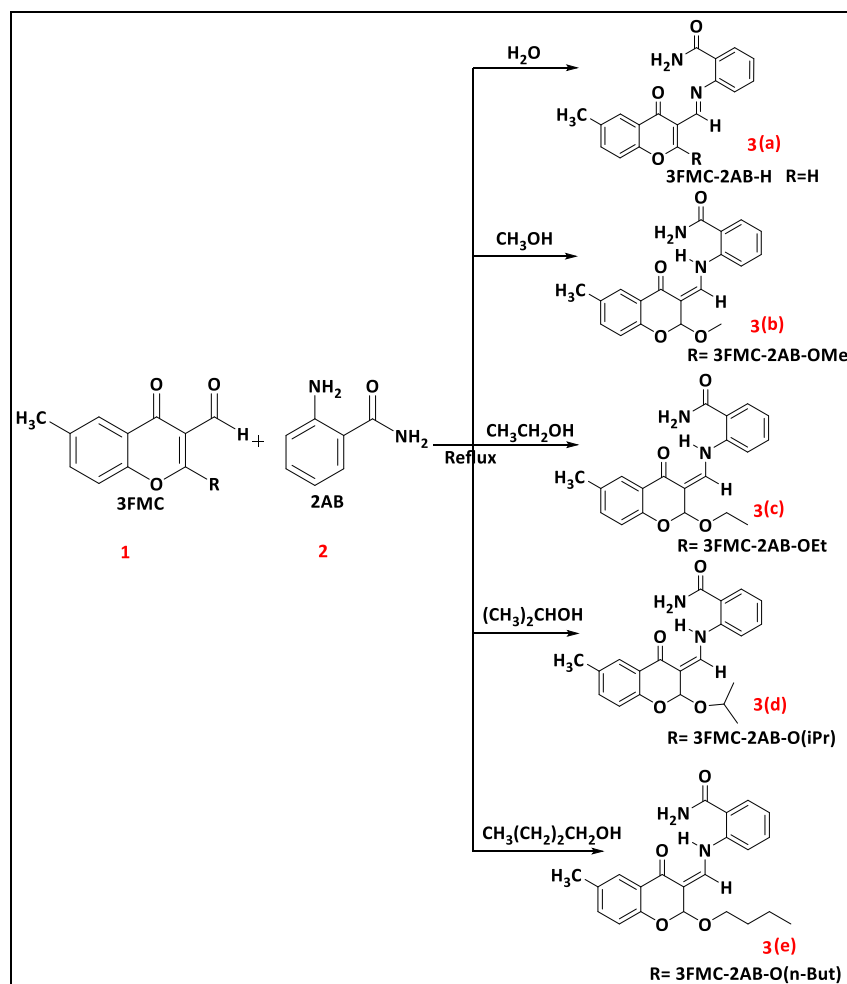


Figure 5A.1 Schematic of the synthesis of chromanone compounds, **3FMC-2AB-R** (3a-e)

Table 5A.1 Physical and analytical data of **3FMC-2AB-R (3a-e)**

Compound	Colour	M.P °C	Mol. Formula	Elemental Analysis % found (calculated)			
				C	H		O
3FMC-2AB-H (3a)	Yellow	200-202	[C ₁₈ H ₁₄ N ₂ O ₃]	(70.58) 70.49	(4.61) 4.58	(09.15) 09.14	(15.67) 15.68
3FMC-2AB-OMe (3b)	Yellow	230-232	[C ₁₉ H ₁₈ N ₂ O ₄]	(67.45) 67.43	(5.36) 5.35	(08.28) 08.25	(18.91) 28.88
3FMC-2AB-OEt (3c)	Yellow	229-233	[C ₂₀ H ₂₀ N ₂ O ₄]	(68.17) 68.15	(5.72) 5.68	(07.95) 07.93	(17.47) 17.45
3FMC-2AB-O(iPr) (3d)	Yellow	233-235	[C ₂₁ H ₂₂ N ₂ O ₄]	(68.84) 68.83	(6.05) 6.05	(07.65) 07.62	(17.48) 17.45
3FMC-2AB-O(n-But) (3e)	Yellow	236-238	[C ₂₂ H ₂₄ N ₂ O ₄]	(69.46) 69.46	(6.36) 6.35	(07.36) 07.33	(16.82) 16.80

5A.2 Infrared Spectral Analysis of 3FMC-2AB-R (3a-e)

A few FTIR spectra are presented in **Figure 5A.2** and some of the important groups are in **Table 5A.2**. The IR N-H stretching frequencies are found in the range of 3315–3189 cm⁻¹. Similarly, the stretching frequencies around 1277 cm⁻¹ conform to the presence of C-N group in **3a-e** compounds. The presence of these N-H and C-N stretching frequencies indicate that the imine CH=N group exists in its tautomeric structure (=C–NH) [8]. The other stretching frequencies are found in the range of 3439-3381cm⁻¹ and at 1642-1615 cm⁻¹ corresponds to the benzamide, NH₂, C=O and that at 1663-1638 cm⁻¹ corresponds to the chromanone C=O group in the **3a-e** compounds [9].

Table 5A.2 Infrared spectral data of chromanones **3FMC-2AB-R (3a-e)** in (cm⁻¹)

Compound	vC-N	vC=Ochrom	vC=Oami	vC-H _{ar}	vNH	vNH2	vC-O-C
3FMC-2AB-H(3a)	1279	1638	1683	3180	3315	3436	1050
3FMC-2AB-OMe(3b)	1277	1638	1661	2955	3315	3418	1063
3FMC-2AB-OEt (3c)	1276	1331	1663	2973	3205	3381	1066
3FMC-2AB-O(iPr) (3d)	1277	1642	1659	3075	3189	3305	963
3FMC-2AB-O(n-But) (3e)	1276	1615	1638	2954	3311	3419	1075

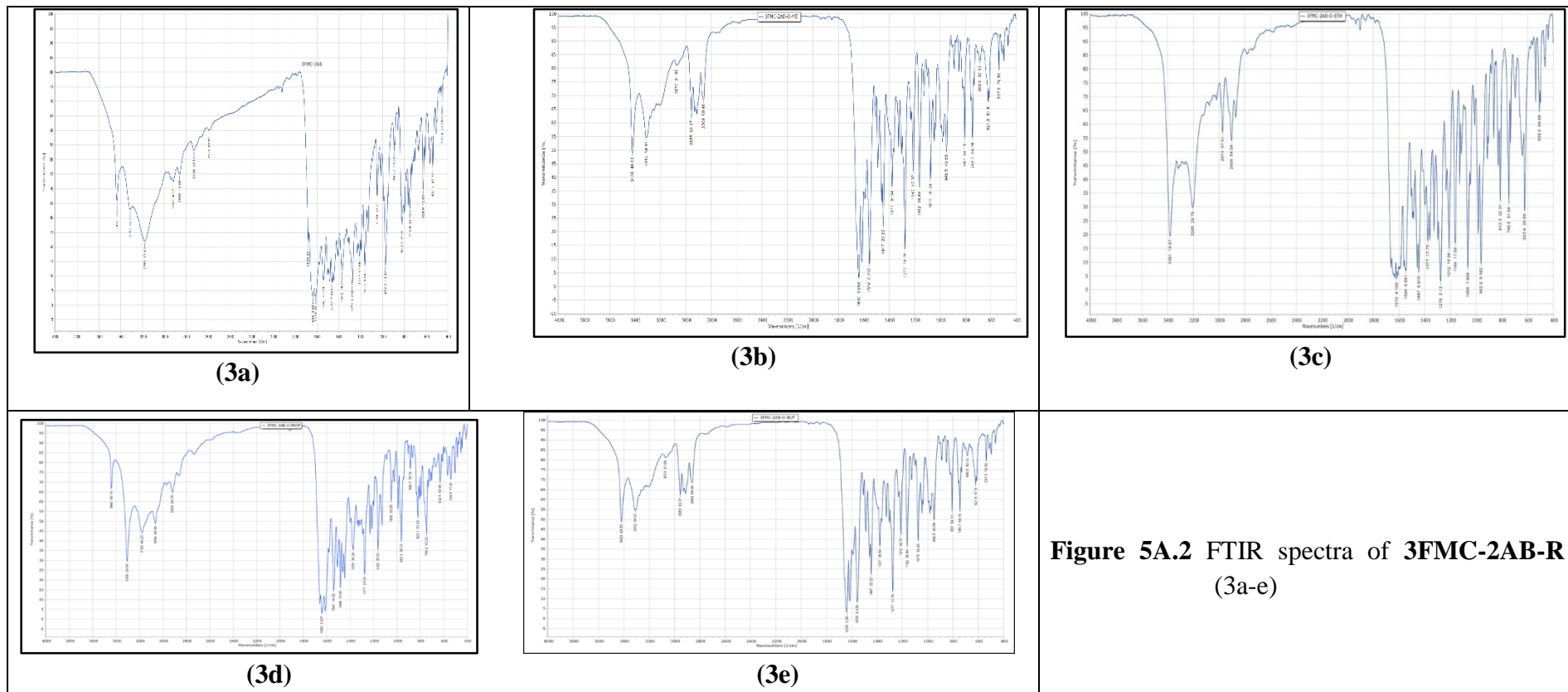


Figure 5A.2 FTIR spectra of **3FMC-2AB-R**
(3a-e)

5A. 3 ESI-Mass Spectral Study of 3FMC-2AB-R

The mass spectra of chromanone compounds **3FMC-2AB-R (3a-e)** are presented in **Figure 5A.3** through **Figure 5A.7**. The mass spectral data corresponds to the expected mass in the compounds listed in **Table 5A.3**.

Table 5A.3 Mass spectral data of chromanone compounds **3FMC-2AB-R**

S. No.	Compound	Calculated mass (amu)	Obtained mass (amu)	Peak assigned
1	3FMC-2AB-H (3a) [C ₁₈ H ₁₄ N ₂ O ₃]	306.10	307.10	(M+H) ⁺
2	3FMC-2AB-OMe (3b) [C ₁₉ H ₁₈ N ₂ O ₄]	338.12	361.11	(M+Na)
3	3FMC-2AB-OEt (3c) [C ₂₀ H ₂₀ N ₂ O ₄]	352.14	375.13	(M+Na)
4	3FMC-2AB-O(iPr) (3d) [C ₂₁ H ₂₂ N ₂ O ₄]	366.15	389.14	(M+Na)
5	3FMC-2AB-O(n-But) (3e) [C ₂₂ H ₂₄ N ₂ O ₄]	380.17	403.16	(M+Na)

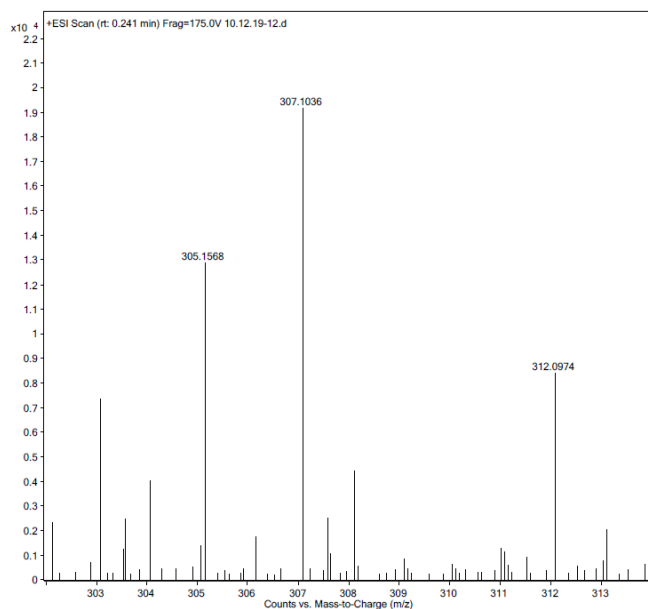


Figure 5A.3 Mass spectrum of 3FMC-2AB-H (3a)

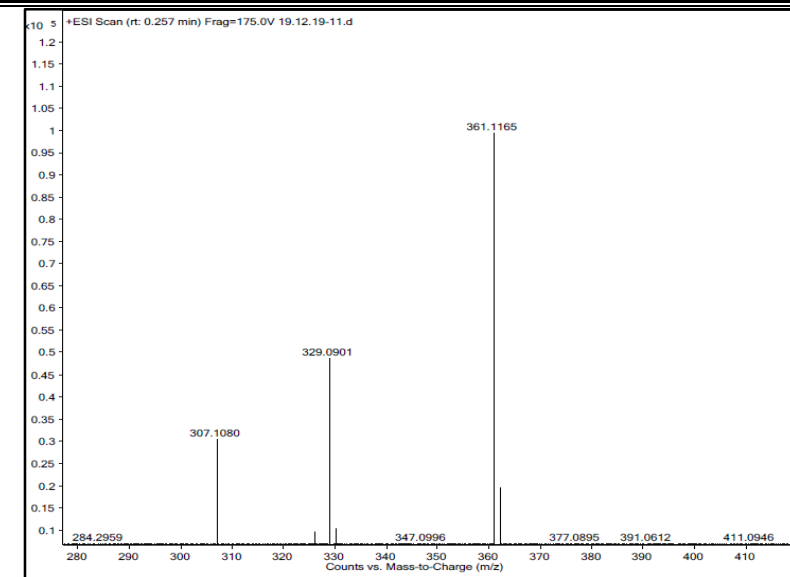


Figure 5A.4 Mass spectrum of 3FMC-2AB-OMe (3b)

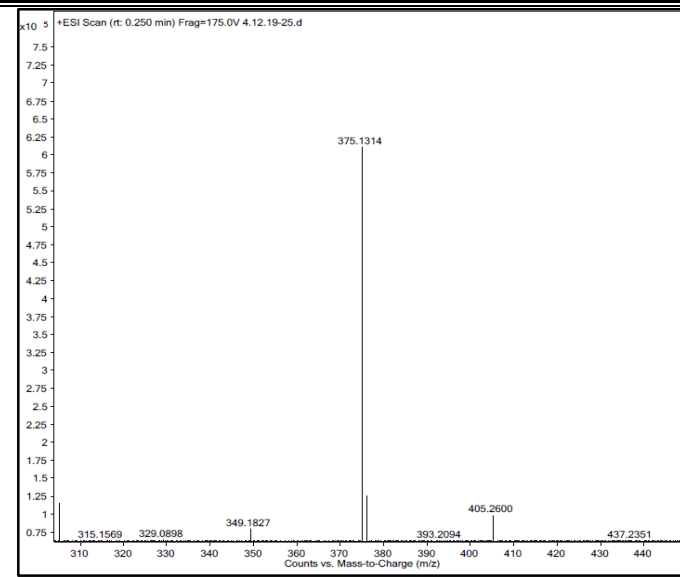


Figure 5A.5 Mass spectrum of 3FMC-2AB-OEt (3c)

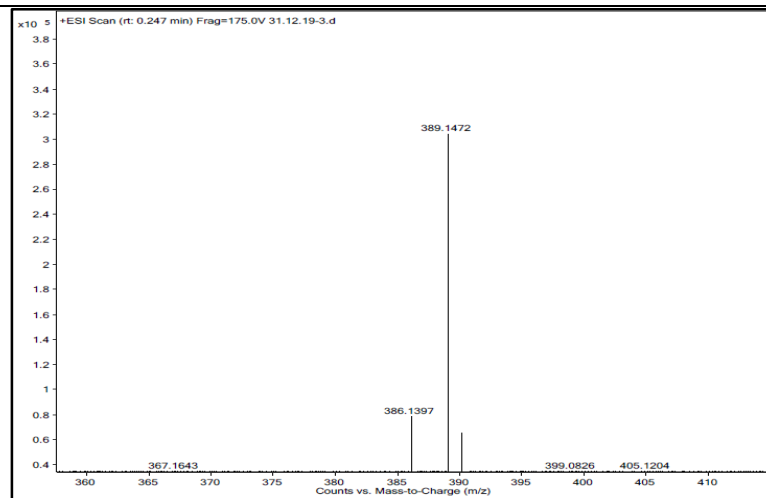


Figure 5A.6 Mass spectrum of 3FMC-2AB-O(iPr) (3d)

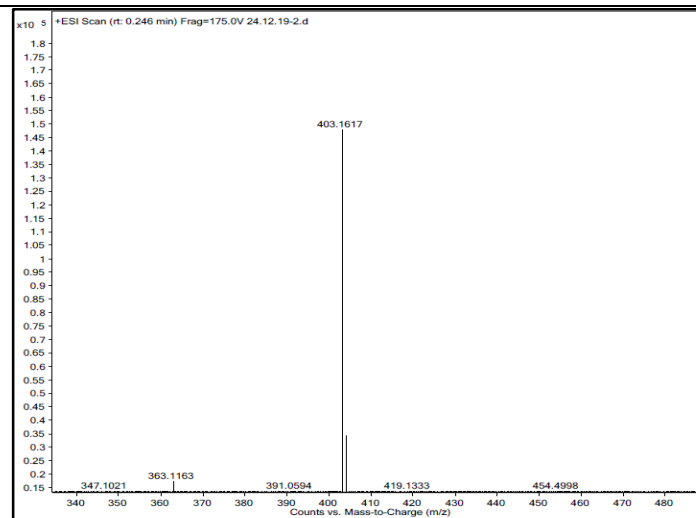


Figure 5A.7 Mass spectrum of 3FMC-2AB-O(n-But) (3e)

5A.4 Absorption Spectral Studies of 3FMC-2AB-R

The electronic spectra of all of **3FMC-2AB-R(3a-e)** recorded in DMSO are presented in **Figure 5A.8**. The intense bands at the region of 260-360 nm and 390-457 nm are due to $\pi\rightarrow\pi^*$ and $n\rightarrow\pi^*$ transitions of the compounds, respectively.

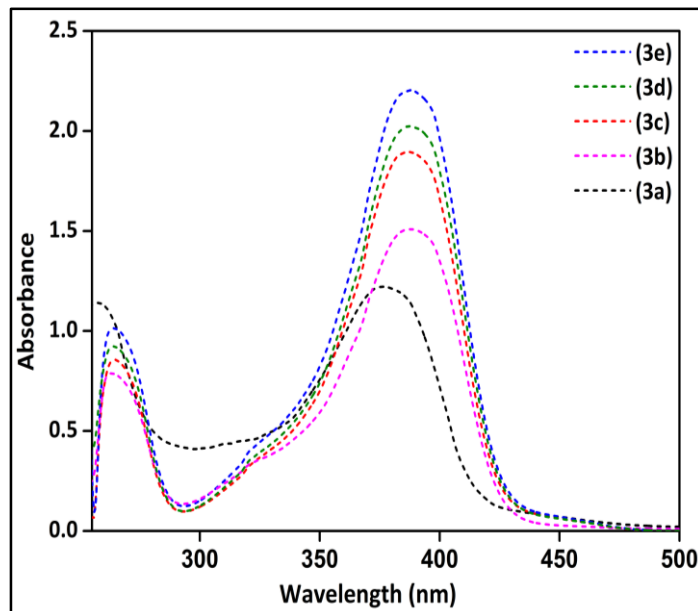


Figure 5A.8 Electronic spectra of **3FMC-2AB-R** ($R = 3a$ through $3e$ as per **Figure 5A.3**)

5A.5 Fluorescence Spectral Analysis of Chromanones 3FMC-2AB-R

The visual fluorescence emission phenomena of **3FMC-2AB-R** are presented in **Figure 5A.9**. Though all these series of compounds exhibit a finite luminescence intensity, the compound **3FMC-2AB-OEt** shown in bright intensity to naked eye in dark when exposed to uv-light in non-polar solvent like n-hexane [10].



Figure 5A.9 Visual fluorescence picture of **3FMC-2AB-OEt** in acetonitrile (1), tetrahydrofuran (2), chloroform (3), methanol (4), ethanol (5), propanol (6), n-hexane (7), dichloromethane (8), dimethylsulphoxide (9), dimethylformamide (10), acetone (11) and water (12)

Figure 5A.10 shows the emission spectra of all the **3a-e** compounds that have been recorded in DMSO solution. Upon photoexcitation at 406 nm, the chromanones **3a-e** exhibited emission bands at 490, 480, 485, 478 and 500 nm. The emission bands in the region of green light have been seen for all five compounds. Compared to the other chromanones, the chromanone (**3e**) exhibits a significant level of hyperchromic shift. When more alkoxy carbons are bonded to the 2-position of an alpha-beta unsaturated chromanone ring, the intensity of the chromanones emission bands also goes up [11].

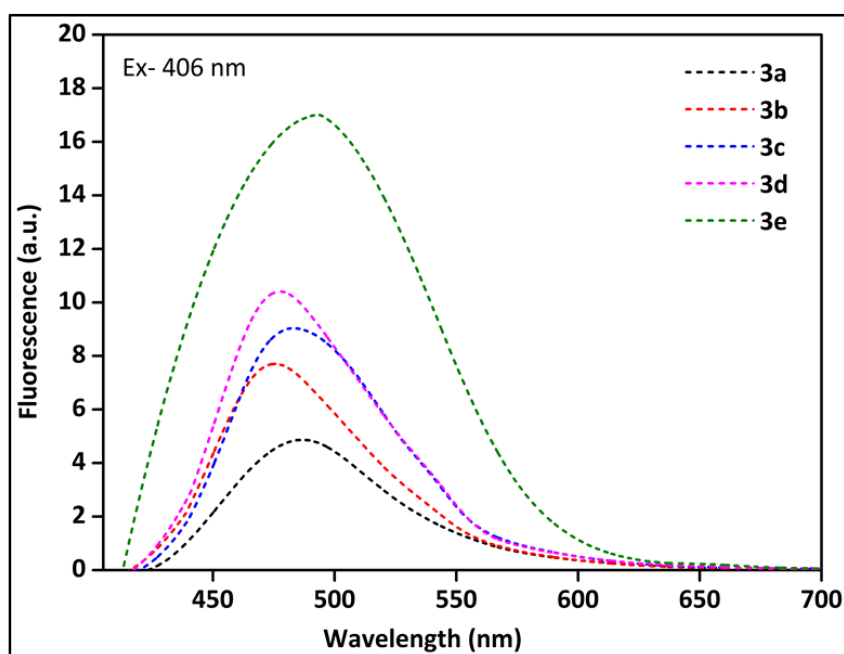


Figure 5A.10. Fluorescence spectra of chromanones (**3a-e**) with excitation at 406 nm.

5A.6 NMR Spectral Data Analysis of 3FMC-2AB-R (**3a-e**)

5A.6.1 $^1\text{H-NMR}$ Spectra

The ^1H NMR spectrum of the **3FMC-2AB-R** were recorded with DMSO-d₆ as solvent and a few of them are shown in **Figure 5A.11**. The aromatic (OCH) proton was detected at the C2(β) carbon of chromanone **3FMC-2AB-H** (**3a**), resulting in a singlet at 5.81 ppm. The solvent-substituted methoxy ($-\text{OCH}_3$) group at the C2(β) carbon of chromanone **3FMC-2AB-OMe** (**3b**) showed up as a singlet at δ 3.36 ppm, which shows that the methanol went through a Michael addition with 2-aminobenzamide. Similar multiplets at δ values of 3.74 (2H) and δ 1.09 ppm (3H) with identical coupling constant values ($J = 7.2$ Hz) in compound **3FMC-2AB-OEt** (**3c**) also point to the presence of an ethoxy group that was derived from ethanol.

The presence of an isopropoxy group is confirmed in compound, **3FMC-2AB-O(iPr)** (**3d**) by a multiplet at a δ value of 4.09 (1H) and two doublets at δ values of 1.18 and 1.02 (2CH₃) with the same coupling constant values (J = 6.0 Hz). A multiplet at a δ value of 3.69 (2H), a quintet at a value of 1.46 (2H), a triplet at a δ value of 1.22 (2H), and a triplet at a δ value of 0.81 (3H) with the same coupling constant values (J = 7.6 Hz) in compound **3FMC-2AB-O(n-But)** (**3e**) were found, confirming the presence of an n-butoxy group at the C2-position of the chromanone moiety. However, the hydrogen atom at the 2-position of the parent chemical 3-formyl-6-methylchromone serves as confirmation of the Michael addition of solvent molecules (alcohols) at the 2-position.

While in the case of the compounds **3FMC-2AB-OMe** (**3b**), **3FMC-2AB-OEt** (**3c**), **3FMC-2AB-O(iPr)**, (**3d**) and **3FMC-2AB-O(n-But)** (**3e**), the proton at 2-position carbon gave a singlet at δ values 5.81, 5.92, 6.01 and 6.94, respectively, i.e., the values were shifted to the downfield region, the proton at 2-position carbon in 3-formyl-6-methylchromone exhibits a singlet at 8.56, i.e., in the aromatic region. Alcohols (solvents) at the C2(β) carbon undergo the Michael addition, which is the cause of this.

5A.6.2 ¹³C NMR Spectra of Chromanone 3FMC-2AB-R

The proton decoupled ¹³C NMR spectra were recorded using DMSO-d₆ as the solvent. A few of them are shown in **Figures 5A.12**. The existence of a -OCH aromatic carbon at the 2-position of the chromanone moiety is confirmed by the signal at δ 167.88 ppm is due to the presence of electronegative atom in the ¹³C NMR spectra of compounds displayed. Whereas in the compound **3b** show one peaks at δ 55.18 ppm confirms the presence of the -OCH₃ group at the relevant C2-position carbon of the chromanone moiety. Similarly, δ 56.51 and 19.02 in compound **3c** indicates the presence of -OCH₂-CH₃. The presence of an isopropoxy group in compound **3d** is supported by the presence of the aliphatic peaks at δ 20.93, 25.95, and 60.2 ppm. According to the values at δ 14.04, 19.22, 31.49, and 67.46 ppm in compound **3e**, the chromanone moiety at C2-position carbon has O-CH₂-CH₂-CH₃.

In contrast, the carbon atom at position 2nd in the parent compound, 3-formyl-6-methylchromone exhibits a peak downfield at 172.5 [34]. However, the peak for carbon atom at 2-position carbon appeared resonate at δ 102.13, 115.30, 115.24, and 101.12 ppm because of the attached oxygen atoms in the compounds **3a**, **3b**, **3c**, and **3d**, respectively. The δ values are shifted to the upfield region in the final compounds compared to 3-formyl-6-methylchromone. This is due to Michael's addition of alcohol at the C2(β) position carbon.

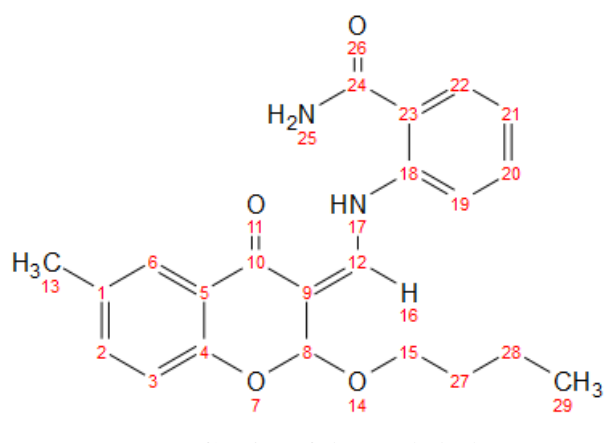
5A.6.3 ^{13}C -DEPT-135 NMR Spectral Analysis

The ^{13}C -DEPT-135 NMR spectra of compounds (**3c** and **3e**) recorded in dimethylsulphoxide (DMSO) solvent are shown in **Figure 5A.13-5A.14** and peak assignments are given in **Table 5A.4**. The spectrum of the compound **3c** shows positive peaks at δ (155.61, 143.18, 122.97, 136.13, 118.09, 124.70, 60.02, 133.83, 115.30, 132.63, 118.78 and 129.45 ppm for C-H carbon of the benzene ring, two positive peaks at δ (20.93 and 19.02) due to one CH_3 attached to the benzene ring and the other from aliphatic ethoxy substitution which is attached to C2(β)carbon of the chromanone ring and an absorbance negative peak at δ (56.51) due to methylene carbon of ethoxy substitution to.

The spectrum of the compound **3e** shows positive peaks at δ (155.62, 143.11, 118.20, 126.01, 101.12, 135.41, 115.99, 132.66, 122.97, and 129.45 for C-H carbon of the benzene ring; two positive peaks at δ (20.70 and 14.05) due to one CH_3 attached to the benzene ring and the other from an aliphatic butoxy substitution which is attached to C2(β) of the chromanone ring; and the absorbance of three negative peaks at δ (67.46, 31.49, and 19.22) due to methylene carbon of the butoxy substitution group.

Table 5A.4 Assignment of ^{13}C -DEPT-135 spectral data of chromanones (**3c** and **3e**)

Compound	(Positive/ Negative peaks	(δ) in ppm	Assignment
 3FMC-2AB-OEt (3c)	Positive(C)	155.69	C ₄
	Positive(C)	143.18	C ₁₈
	Positive (CH)	122.97	C ₅
	Positive (CH)	136.13	C ₂
	Positive (CH)	118.09	C ₃
	Positive (CH)	124.70	C ₆
	Positive (CH)	60.02	C ₈
	Positive (CH)	133.83	C ₁₂
	Positive (C)	115.30	C ₉
	Positive (C)	132.63	C ₁
	Positive (CH)	118.78	C ₁₉
	Positive (CH)	126.02	C ₂₁
	Positive (CH)	129.45	C ₂₂
	Positive (C)	127.92	C ₂₃
	Negative (CH ₂)	56.51	C ₁₅
	Positive(Ch ₃)	20.93	C ₁₃
	Positive (CH ₃)	19.02	C ₂₇
	Positive (C)	143.11	C ₁₈
	Positive (CH)	118.20	C ₃



Positive (CH)	155.62	C ₄
Positive (CH)	126.01	C ₆
Positive (CH)	101.12	C ₈
Positive (CH)	135.41	C ₁₂
Positive (CH)	115.99	C ₁₅
Positive (CH)	132.66	C ₂₀
Positive (CH)	122.97	C ₅
Positive (CH)	129.45	C ₂₂
Negative (CH ₂)	67.46	C ₁₅
Negative (CH ₂)	31.49	C ₂₇
Negative (CH ₂)	19.22	C ₂₈
positive(CH ₃)	14.05	C ₂₉
positive(CH ₃)	20.70	C ₁₃

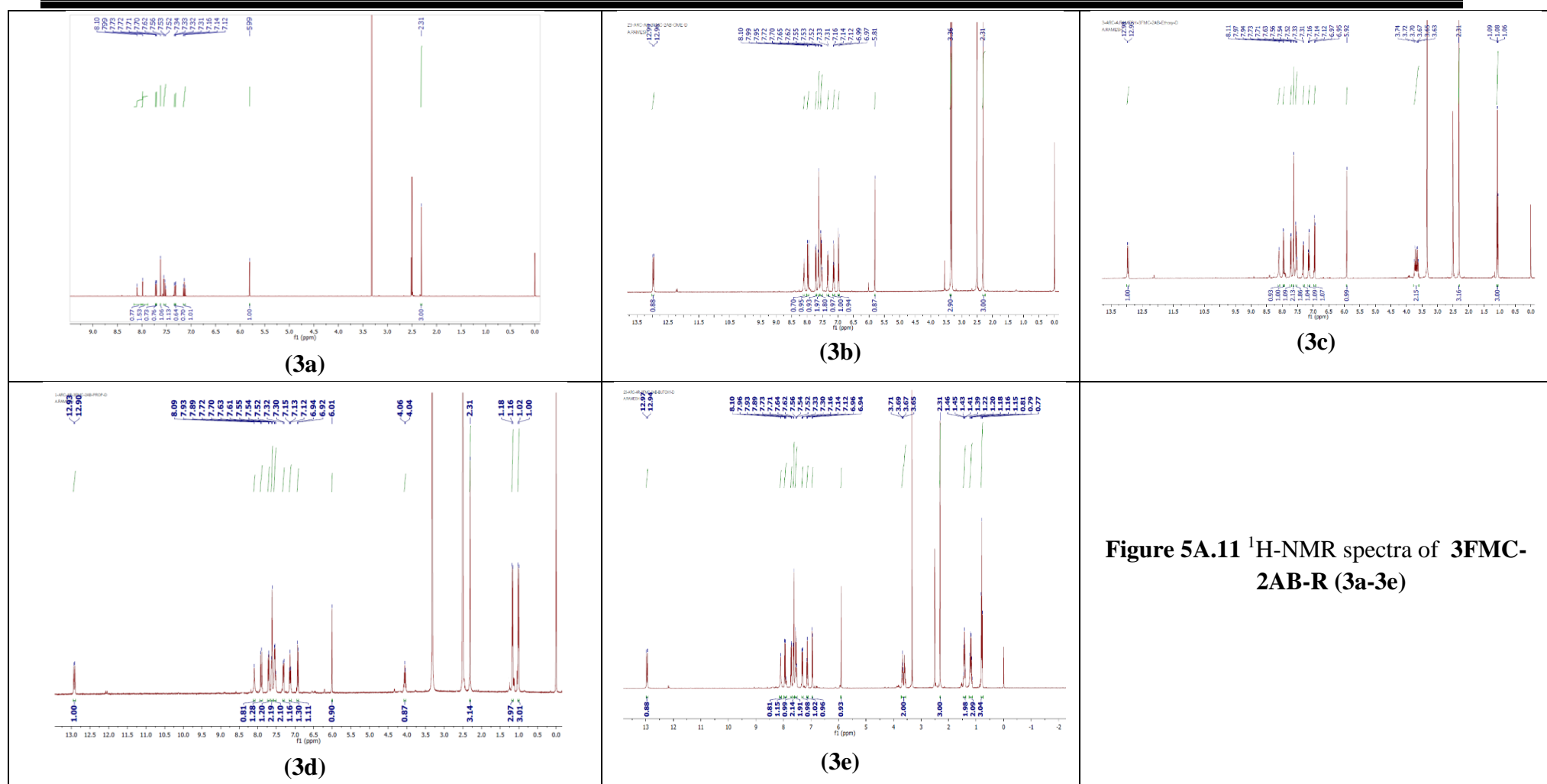


Figure 5A.11 ^1H -NMR spectra of 3FMC-2AB-R (3a-3e)

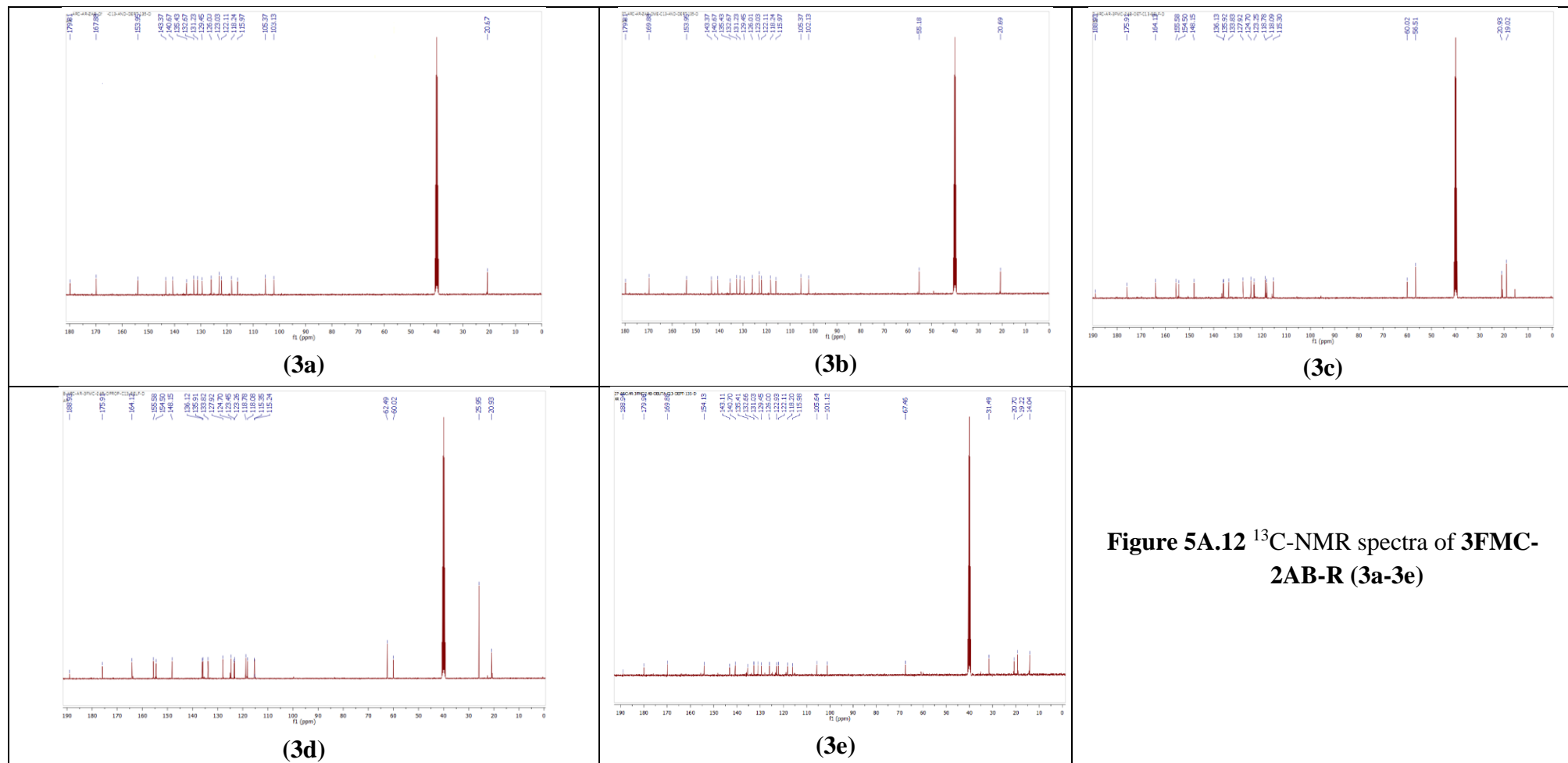


Figure 5A.12 ^{13}C -NMR spectra of **3FMC-2AB-R (3a-3e)**

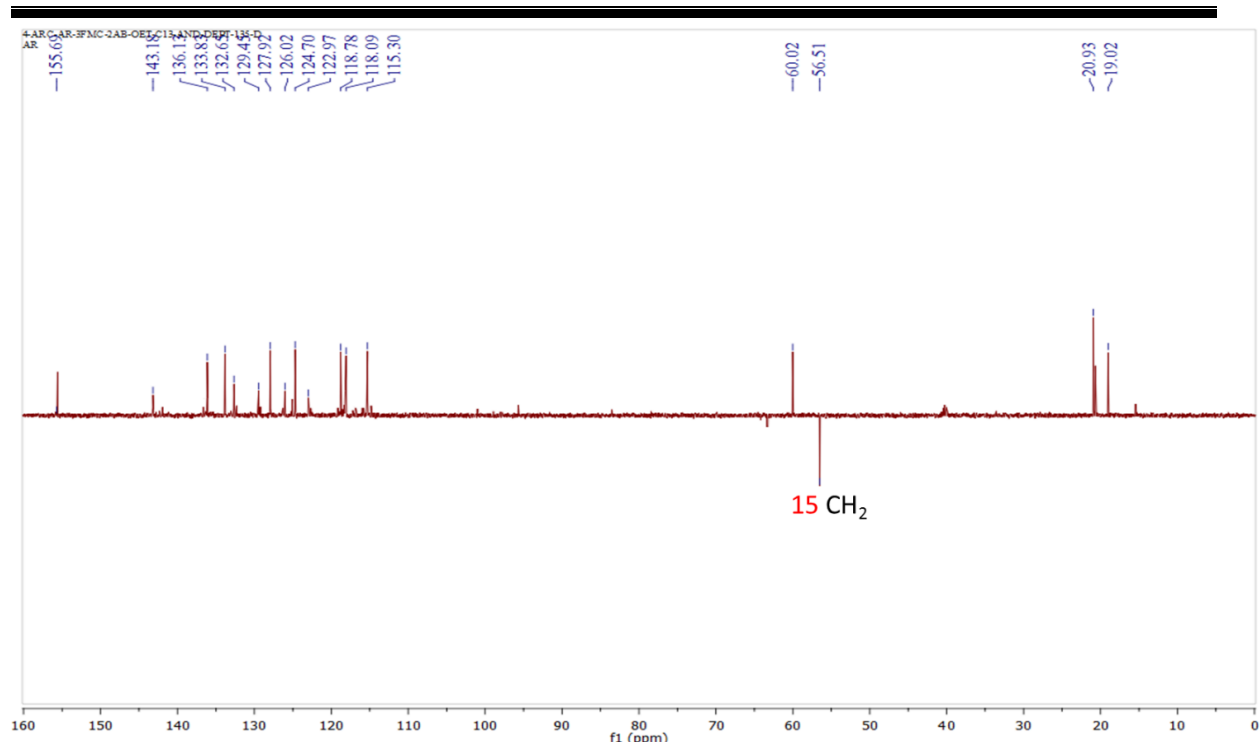


Figure 5A.13 ^{13}C -DEPT-135 spectrum of 3FMC-2AB-OEt (**3c**)

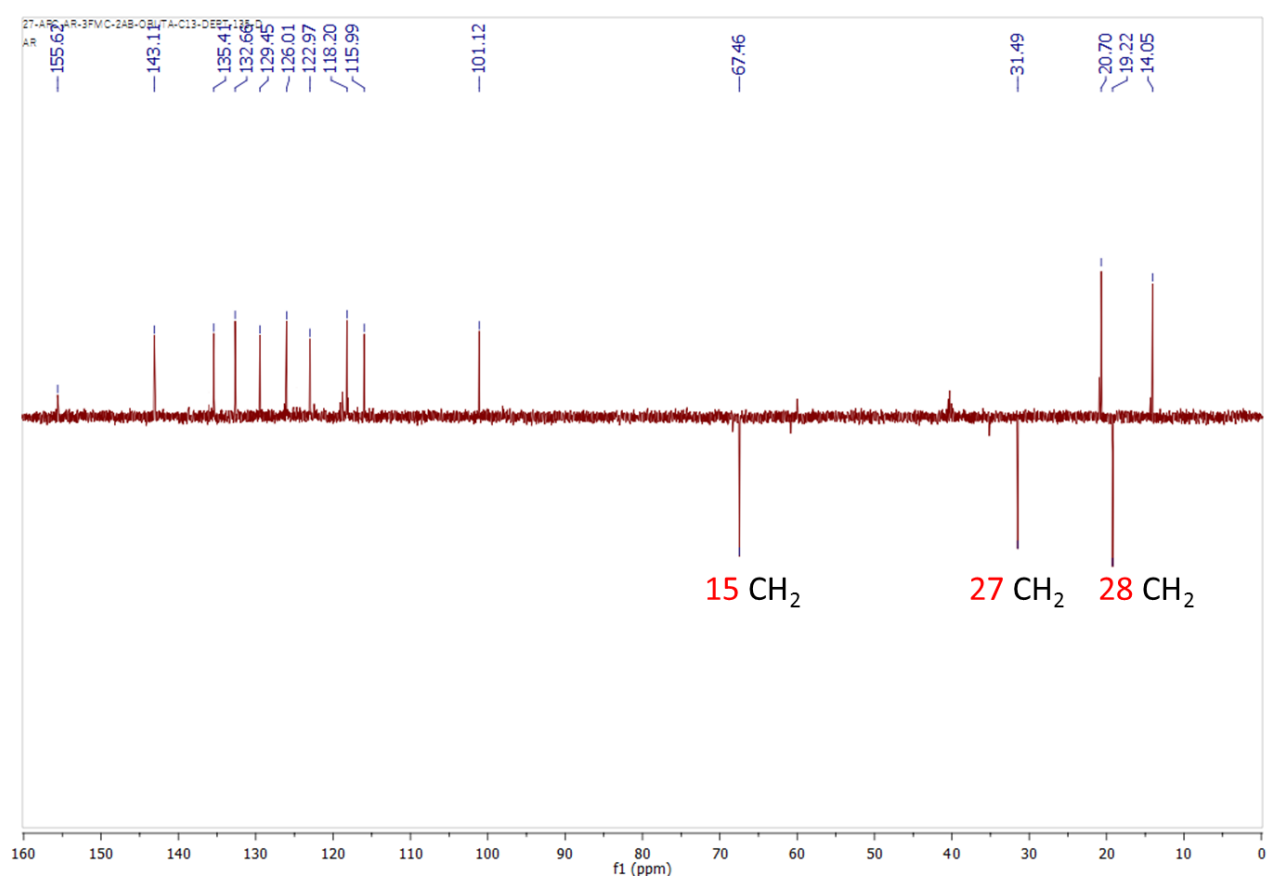


Figure 5A.14 ^{13}C -DEPT-135 spectrum of 3FMC-2AB-O(n-But) (**3e**)

PART-B**SINGLE CRYSTAL XRD AND COMPUTATIONAL STUDIES OF TATMC AND 3FMC-2AB-R AND CORRELATION OF THE EMPERICAL AND MODELLED DATA****SECTION-B1****5B.1 Crystal Structure Analysis of TATMC**

The molecular structure of **TATMC** was solved by single crystal XRD. The details of procedure are in chapter-II. The ORTEP format of **TATMC** is shown in **Figure 5B.1**. Single crystals, suitable for structure determination, could not be obtained for the $[M(TATMC)_2X_2]$ complexes, nor for **3FMC-2AB-R**. Though they are quite stable to air and moisture and moderately soluble in DMSO and DMF. The ligand, **TATMC** is found to crystallize in the unsymmetrical with $0.350 \times 0.300 \times 0.100$ crystal size, $a = 6.7984(10)$; $b = 8.7676(12)$; $c = 13.472(2)$ (Å) unit cell dimensions and $\alpha = 72.335(7)$; $\beta = 88.406(8)$; $\gamma = 68.993(7)$ angles. The chromenone and triazole moieties are planer and the bond distance between these rings at C8-O2 and C11-N1 are 1.329 and 1.228 Å, respectively. The bond angles for O2-C8-C9 and C9-C11-N1 are 122.1 and 124.6°, respectively whereas the dihedral (torsion) angle of C10-C9-C11-N1 is -174.2°. All other geometrical parameters of **TATMC** are normal and agree well with the literature values [11]. The crystallographic data of **TATMC** are summarized in **Table 5B.1**. A few selected bond lengths, bond angles and dihedral angles are presented in **Table 5B.2**.

The crystal packing layer structure analysis also reveals that, **TATMC** forms a rhombus like extended pattern in the crystal with O....N, N....O....N and N....O....O pi bonds and van der Waals contacts. The packing view of molecules within the unit cell down to c-axis is shown in **Figure 5B.2**. Careful analysis of the crystal packing shows that there exists both intra and intermolecular pi...pi bond contacts of O....N = (3.027 Å), N....O....N = (111.62°) and N....O....O = (68.38°).

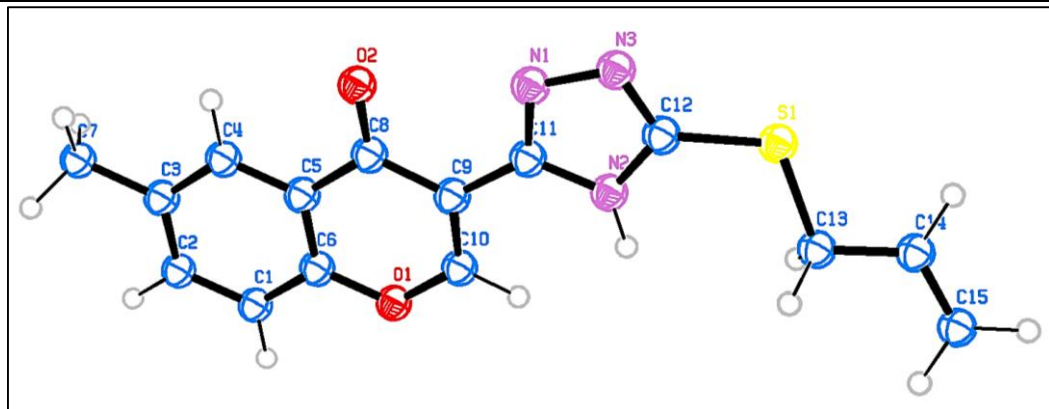


Figure 5B.1 ORTEP view of TATMC with atom labelling drawn at 50% probability level

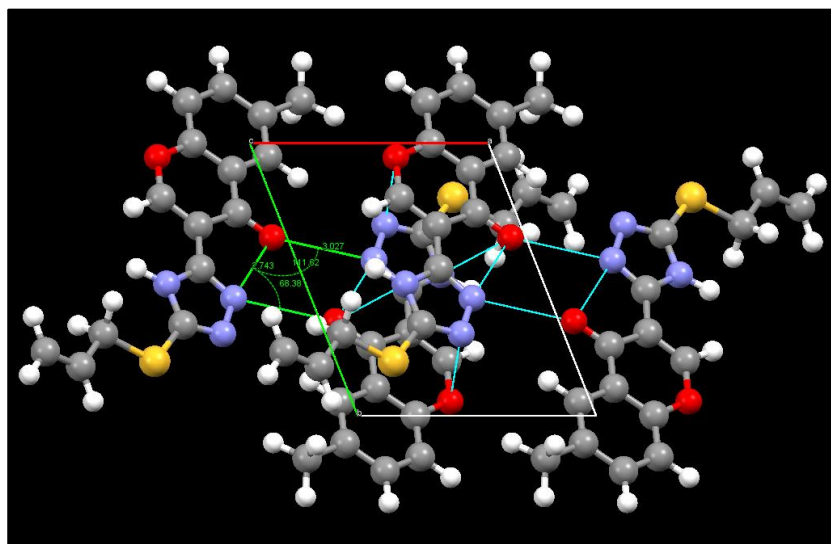


Figure 5B.2 Packing view of molecules viewed along the c-axis.

Table 5B.1 Crystallographic data of TATMC

Chemical formula	C ₁₅ H ₁₃ N ₃ O ₂ S
Formula weight	299.34
Temperature(K)	296(2)
Wavelength (Å)	0.71073
Crystal system	Triclinic
Space group	<i>P</i> -1
Unit cell dimensions (Å)	<i>a</i> = 6.7984(10); <i>b</i> = 8.7676(12); <i>c</i> = 13.472(2)
Angle (°)	α = 72.335(7); β = 88.406(8); γ = 68.993(7)
Volume (Å ³)	711.35(19)
Z	2
Calculated density (g/cm ³)	1.393
F(000)	310
Crystal size(mm)	0.350 x 0.300 x 0.100

θ range for data collection (°)	1.593 to 24.999
Limiting indices	-8 ≤ h ≤ 7, -10 ≤ k ≤ 9, -16 ≤ l ≤ 16
Reflections collected/unique [I > 2σ(I)]	7149/2498 [R(int) = 0.0275]
Completeness to θ	99.7 %
Absorption correction	Semi-empirical from equivalents
Min. and Max. transmission	0.922 and 0.977
Refinement method	Full-matrix least-squares on F ²
Data/restraints/parameters	2498/0/214
Goodness-of-fit on (F ²)	1.011
Final R indices [I > 2σ(I)]	R ₁ = 0.0501, wR2 = 0.1584
R indices (all data)	R ₁ = 0.0703, wR2 = 0.1766
Extinction coefficient	n/a
Largest diff. peak and hole(e/(Å ³))	0.416 and -0.612

5B.2 Hirshfeld Surface Analysis

Hirshfeld surface study using the Crystal Explorer 2.1 program reveals the crystalline environment, intermolecular interactions, and quantitative 2D fingerprint plot [12, 13]. The d_i and d_e represents, respectively, the atom inside to the Hirshfeld surface and the atom exterior to the Hirshfeld surface. **Figure 5B.3** shows dnorm Hirshfeld map. In the Hirshfeld surface map scale (0.6781 to 1.6656), the dark red and blue regions indicate that the intermolecular contact distance is relatively shorter and longer than the sum of van der wall radii, respectively, while the white spots represent a distance that is nearly equal to van der wall radii. The dark-red dots in the d norm represent stronger O –H •••O and C –O •••H hydrogen bonding between the water molecule and oxalate anion.

In addition, the amino group of N-H-O-H forms a hydrogen bond with carboxylate anions. As depicted in **Figure 5B.4**, the quantitative intermolecular interactions and their distributions are analyzed using a 2D fingerprint plot. The sharp spikes show that the O •••H/H •••O hydrogen bonds are closer to each other (36.9%), and the H •••H intermolecular interactions make up 20.7% of how the crystal is packed. The impact of the Br atom on intermolecular interactions is determined by 2D finger-print plots, and the interactions C •••Br/Br •••C (10.8%), H •••Br/Br •••H (12.1%), and O •••Br/Br •••O (3.5%) make moderate contributions to crystal packing.

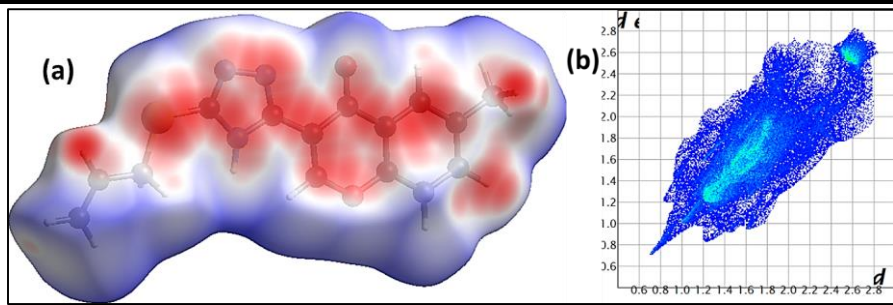


Figure 5B.3 Hirshfeld surface (d norm) mapped over visualizing the transparent of **TATMC** (a), and 2D fingerprint map of de vs di with 100% mapping of all its atoms (b)

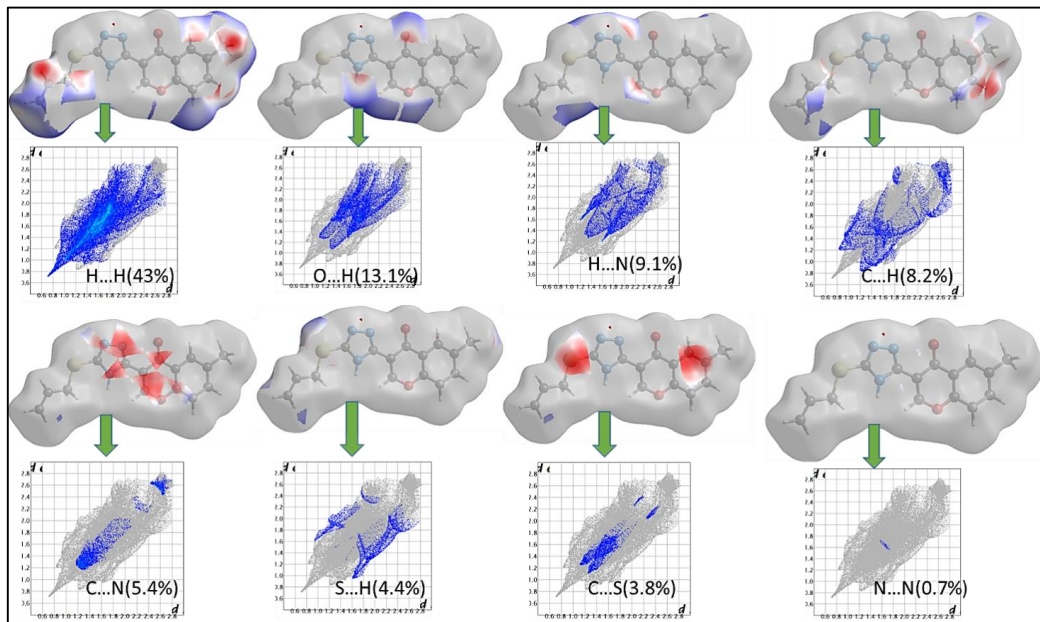


Figure 5B.4 Illustrative 2D fingerprint plots of interatomic interactions of **TATMC** showing percentage of contacts contributing to the overall Hirshfeld surface area (the distances from the Hirshfeld surface to the nearest atom within and exterior to the surface are de and di)

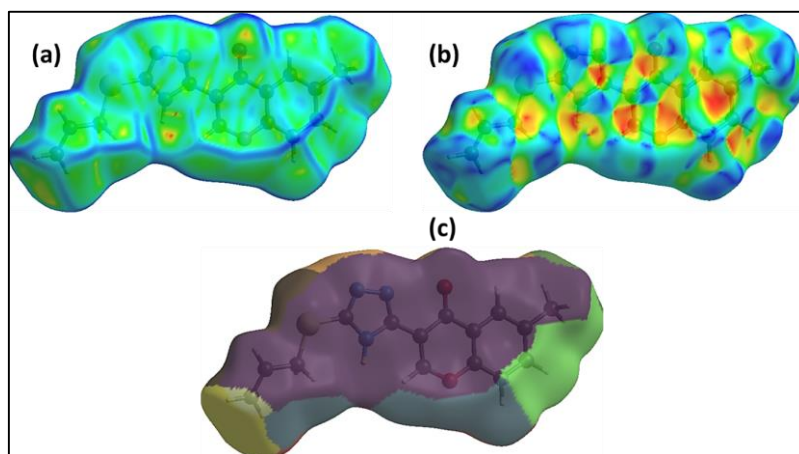


Figure 5B.5 Hirshfeld hydrogen interaction surfaces of **TATMC** mapped with curvedness (a), the shape surface (b), and the fragment patch surface property (c)

Figure 5B.5 represents (a) the curvedness surface property scale (-4.0 to 0.40), (b) the shape-index surface (-1.0 to 1.0), and (c) fragment patch surface property (0.0 to 13.0). The small blue regions surrounding the bright-red spots represent-stacking between the chromone and triazole rings, whereas the green shade in the flat region represents - stacking around the chromone and triazole rings and the fragment patch surface with purple, green, and gray parts, with each stacking interaction color-coded around the molecule.

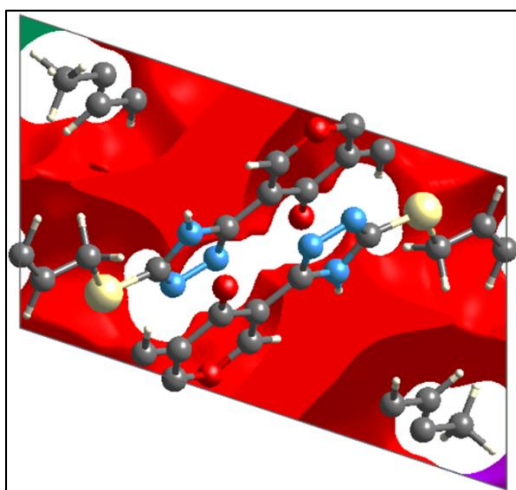


Figure 5B.6 Crystal voids structure of **TATMC** seen along the a-axis

The void surface is supplied by Crystal Explorer and illustrated in **Figure 5B.6** of ligand, **TATMC**. The void surface is determined by the sum of spherical atomic electron concentrations at the corresponding nuclear positions. The crystal void calculation (results under 0.002 a.u. iso value) reveals that **TATMC** has a void volume of 120.26 \AA^3 and a surface area of about 404.92 \AA^2 .

The small size of the cavities is confirmed by the calculated porosity of 10.72%. In places where interspecies approaches are observed in O...H, the electron density iso surfaces are not entirely closed around the components but rather are open.

5B.3 Molecular Electrostatic Potential

Molecular electrostatic potential (MESP) is a very useful way to figure out where electrophilic and nucleophilic attacks are most likely to happen in bio molecular structures, show the shape and size of molecules, and see how their charges are spread out. The MESP surface is coded with various colours with different values, in the order of red (most electronegative region), green (zero potential region) and blue (most electropositive region). The colour code of the MESP contour map of **TATMC** is shown in **Figure 5B.7**, which clearly suggests that the most

electropositive regions (blue) spots are localized over the oxygen atoms of the chromo-pyrazole ring and on the hydrogen atoms, which are the strongest attractive regions of nucleophilic attack.

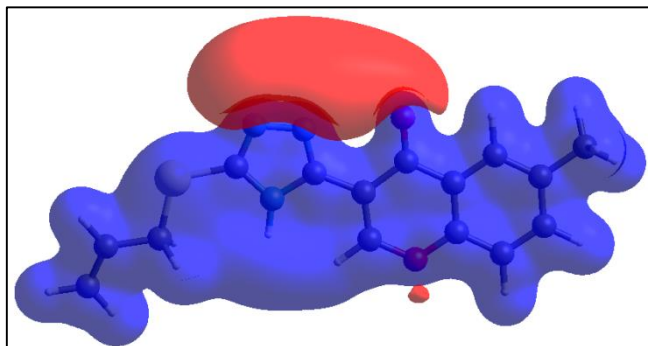


Figure 5B.7 Electrostatic potential surface of ligand **TATMC**

5B.4 Molecular Modelling Studies of TATMC and M(TATMC)₂ Complexes

The structural properties of molecules, including bond lengths, bond angles, torsional energies, dihedral angles, and HOMO-LUMO energies, have been calculated.

On the basis of the empirical XRD studies of **TATMC**, molecular modeling was performed with **TATMC** and its complexes. The MM2 force field method with an RMS gradient of 0.01 is used to calculate the global energy minimized structures. In any structural analysis the bond length, bond angles and torsional angles are some of the most essential structural factors. The global-energy-minimized structure of **TATMC** is shown in **Figure 5B.8-5B.10** are in ball-stick, stereo and anaglyph formats. Selected bond lengths, bond angles and dihedral angles are presented in **Table 5B.3**. There is a great degree of consistency between the experimental and simulated data of the global-energy-minimized structure of **TATMC**.

Quantum mechanical HOMO-LUMO orbital energy assessments were used to calculate the projected gas-phase electronic transitions from the of the energy-minimized free molecular energy diagrams of **TATMC** ligand and its corresponding metal complexes

Figure 5B.11 depicts the structure of the energy-minimized free molecules of **TATMC** and its Co(II), Ni(II), Cu(II) and Zn(II) complexes. As shown in **Figure 5B.12**, the global minimum for zero torsional angles on the bonds C11-N1 and C12-S1 indicates that the ligand, **TATMC** is planar.

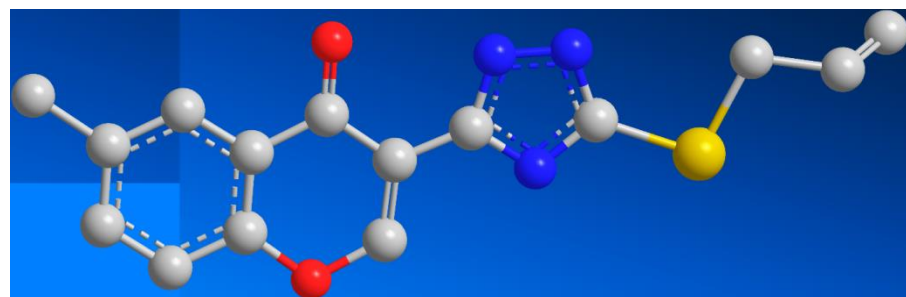


Figure 5B.8 MM2-energy-minimized structure of **TATMC**

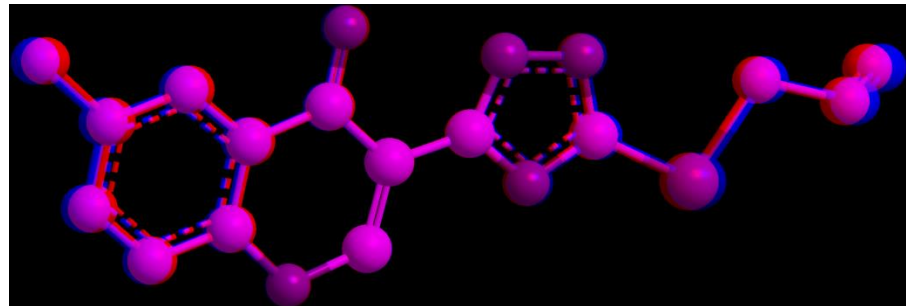


Figure 5B.9 Anaglyph structure of TATMC obtained from ChemDrawPro



Figure 5B.10 Stereographic projection of TATMC obtained from ChemDraw Pro

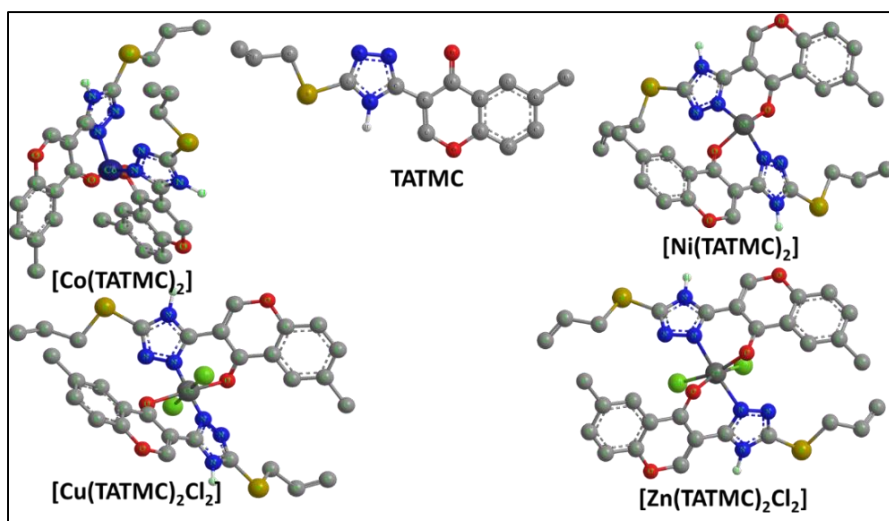


Figure 5B.11 Ball-stick model of energy-minimized structures of TATMC and its complexes

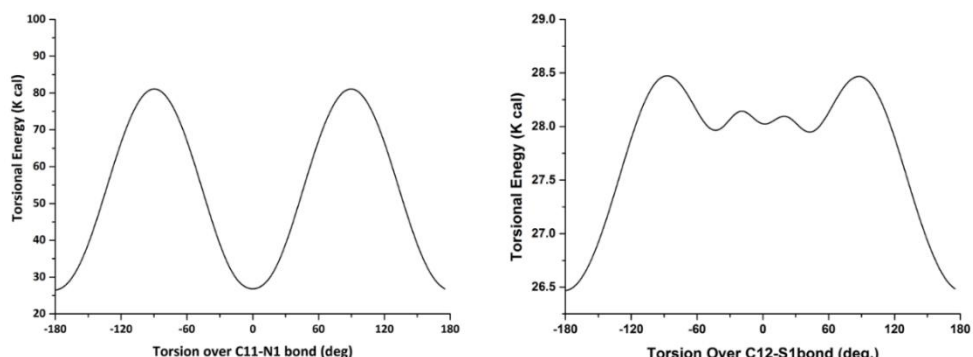
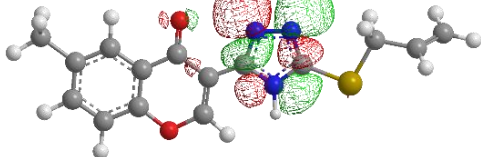
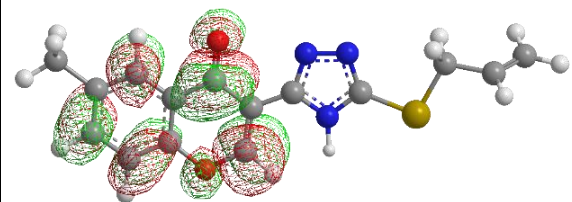
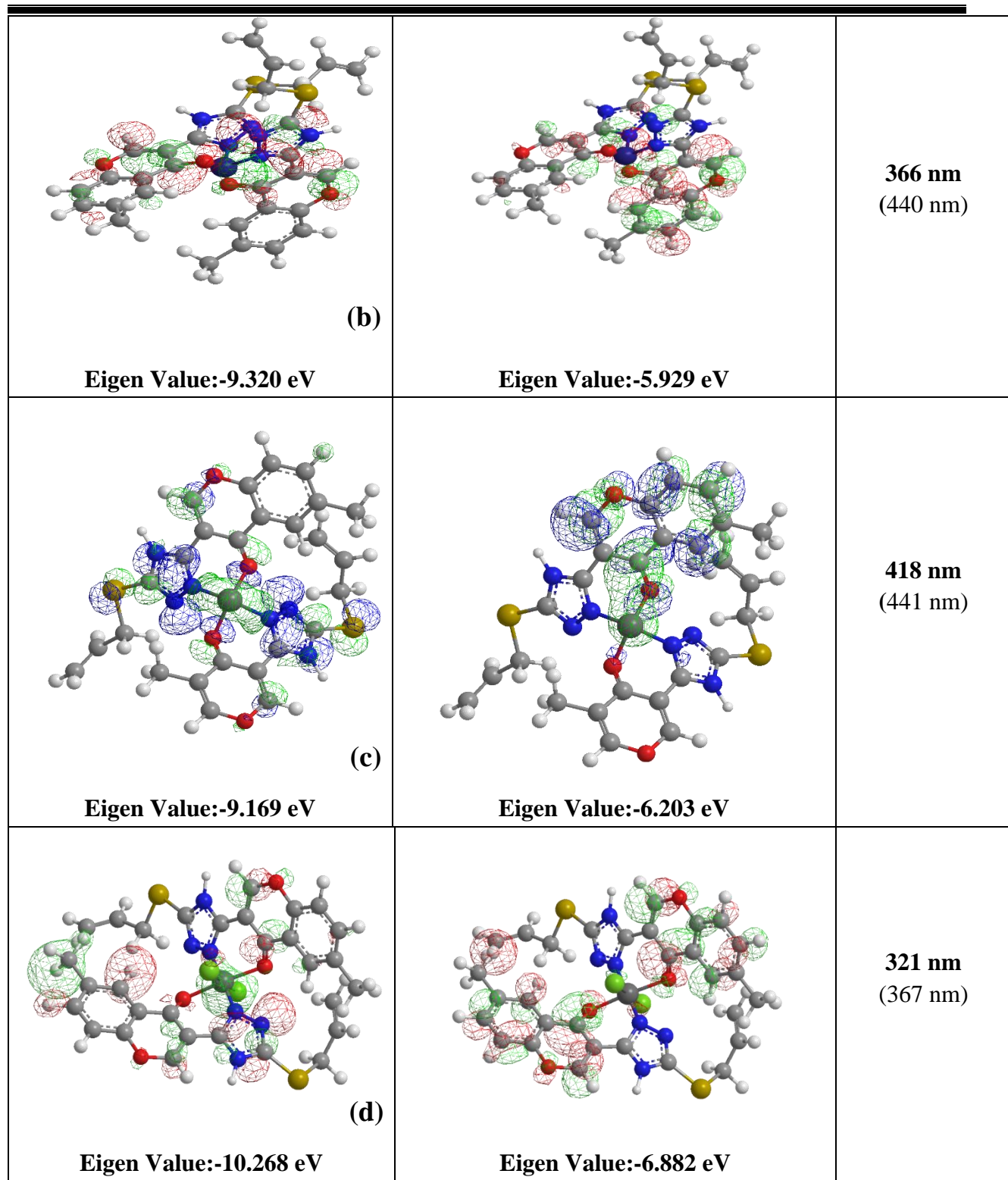


Figure 5B.12 Conformational single dihedral energy plots of TATMC

5B.5 Molecular Orbital Properties

The frontier molecular orbital energies, viz., (E_{HOMO} and E_{LUMO}) are significant parameters for the prediction of the reactivity of a chemical species. The E_{HOMO} is often associated with the electron-donating ability of a molecule. The E_{LUMO} indicates the ability of the molecule to accept electrons. The minus Eigen value of E_{HOMO} corresponds to the binding energy value for E_{HOMO} electrons present in HOMO energy levels. As a result, the lower the binding energy value for E_{HOMO} electrons, the greater the proclivity for electron(s) donation to the appropriate acceptor molecule with low energy and empty molecular orbitals, as shown in **Figure 5B.13**. The counter maps presented below indicate the orientation of HOMO and LUMO orbitals, both in molecular orbitals. The value of E_{HOMO} , E_{LUMO} and $E_{LUMO}-E_{HOMO}$ were found to be -6.423 eV, -4.011 eV and -2.412 eV of **TATMC**. wherein complexes -5.320 eV, -3.929 eV and -1.391 eV and -6.169 eV, -4.203 eV and -1.966 eV and -4.68 eV, -3.882 eV and -0.386 eV and -5.201 eV, -4.146 eV and -1.055 eV respectively Eigen values corresponds to Co(II), Ni(II), Cu(II) and Zn(II) complexes. The large difference in energy between HOMO and LUMO orbitals indicates higher stability in molecular orbitals. The low energy difference ($E_{LUMO}-HOMO$) in molecular orbitals indicates its high labile character.

HOMO	LUMO	λ_{max} Expected (Observed)
 (a) Eigen Value:-6.423 eV	 Eigen Value:-4.011 eV	415 nm (336 nm)



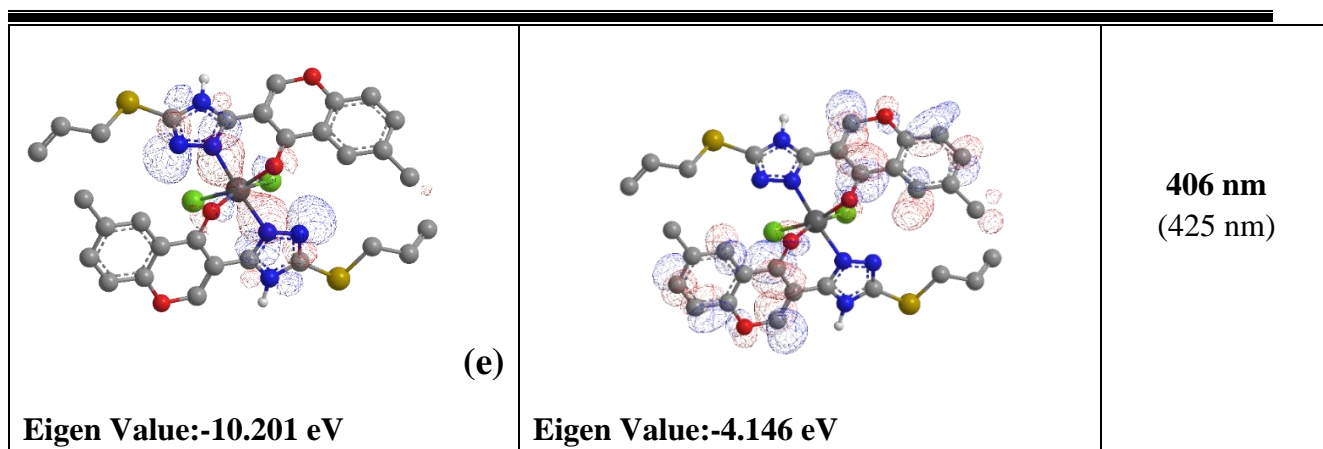


Figure 5B.13 Modelled shapes and energies of HOMO and LUMO molecular orbitals of **TATMC** and $[\text{M}(\text{TATMC})_2\text{X}_2]$ (mostly on MM2 platform) along with their energies and expected electronic transitions (the observed λ_{max} are also given for comparison)

Considerable deviation can be seen from the aligned geometries of **TATMC** at the exocyclic alkene skeleton disposition in relation to the C-S bond on the pyrazole ring (the solid state XRD shows a slight *syn* disposition whereas the MM2 calculations favour more of *anti*). Similarly the dihedral angle between the triazole and the benzene rings seems to be more in the solid state (XRD) whereas the free molecule (MM2) prefers near co-planarity of the two rings. Deviation in the geometry obtained using MM2 of theory when compared with its experimental XRD counterpart is attributed to the system difference, one a free gas-phase molecule and the other amidst multiple intermolecular interactions in the solid state matrix. Overall, the geometries obtained experimentally by single crystal XRD studies and MM2 calculations clearly indicate that **TATMC** holds near identical spatial disposition of its molecular framework. A list of some XRD data and MM2-modelled data of **TATMC** along with the MM2-modelled data of its four complexes are presented in **Table 5B.2**.

Table 5B.2 Some important structural parameters of experimental (XRD) and MM2-calculated bond lengths, bond angles and dihedral angles of **TATMC** and $[\text{M}(\text{TATMC})_2]$

Important atomic string(*)	Bond length (Å)					
	XRD of TATMC	MM2 on TATMC	MM2 on $[\text{M}(\text{TATMC})_2]$			
			M=Co(II)	M=Ni(II)	M=Cu(II)	M=Zn(II)
C8-O2	1.228	1.216	1.309	1.238	1.239	1.239
C8-C9	1.450	1.371	1.387	1.358	1.354	1.365
C9-C11	1.454	1.354	1.337	1.339	1.338	1.342
C11-N1	1.329	1.271	1.266	1.278	1.283	1.270
M-N1	-	-	1.830	1.844	1.396	1.939
M-O2	-	-	0.863	1.803	1.858	1.917

	Bond Angles (°)					
O2-C8-C9	122.1	121.6	124	122.9	120.4	121.4
C8-C9-C11	121.9	122.8	112.5	112.7	113.6	119.0
C9-C11-N1	124.6	129.2	116.5	124.0	126.3	125.2
C11-N1-N2	109.8	110.0	106.9	103.6	101.6	108.0
N1-M-N1	-	-	107.2	120.6	177.6	151.9
O2-M-O2	-	-	123.8	125.0	169.1	140.4
	Dihedral Angles (°)					
C10-C9-C8-O2	-179.4	-180.0	-164.6	-163.2	-162.9	-161.0
C10-C9-C11-N1	-174.2	-180.0	-164.7	-161.6	-161.9	-158.6
O2-C8-C9-C11	0.3	0.1	12.6	12.8	16.1	17.6
C8-C9-C11-N1	6.1	0.0	18.0	22.6	19.1	22.8
C9-C11-N1-M	-	-	-135.5	4.8	-3.5	-6.0
C9-C8-O2-M	-	-	-66.4	-74.3	-52.1	-64.2

(*) Atom numbering is as per the **Figure 5B.1**.

5B.6 Molecular Modelled Data and Geometry of the Complexes

The structures of a few metal complexes, with optimized geometries obtained by MM2 calculations.

The **TATMC** is found to act as a bidentate ligand through the N and O binding atoms preferred in all the global-energy-minimized complexes. Important geometric parameters at the coordination sphere of various complexes are given in **Table 5B.2**. In relation to the computer (MM2) generated structures shown in **Figure 5B.12**. In **Table 5B.3** are collected the difference-data for the ligand, **TATMC** on the basis of its existence as a pure molecule and its fate upon complexation from both empirical and modelled perspectives.

Table 5B.3 Comparative experimental and computational geometric parameters of **TATMC** with the MM2-modelled data of **[M(TATMC)₂X₂]**

Compound/ Parameter		TATMC	Co(II)	Ni(II)	Cu(II)	(Zn(II))
Computed data of the complexes	Geometry	-	Tetrahedral	Tetrahedral	Octahedral	Octahedral
	M-N1	-	1.830	1.844	1.396	1.939
	M-O2	-	0.863	1.803	1.358	1.917
	N1-M-N1	-	107.2	120.6	177.6	151.9
	O2-M-O2	-	123.8	125.0	169.1	140.4
	C9-C11-N1-M	-	-135.5	4.8	-3.5	-6.0
	C9-C8-O2-M	-	-66.4	-74.3	-52.1	-64.2
	C8-O2	0.012	0.081	0.01	0.011	0.011
		-	0.093	0.02	0.023	0.023
	C8-C9	0.08	-0.063	-0.092	-0.096	-0.085
		-	0.016	-0.013	-0.017	-0.006
Δ XRD	C9-C11	0.1	0.117	0.115	0.116	0.112
		-	0.017	0.015	0.016	0.012
Δ XRD	C11-N1	0.058	0.063	0.051	0.046	0.059
		-	0.005	-0.007	-0.012	0.001
Δ XRD	O2-C8-C9	0.5	1.9	0.8	-1.7	-0.7
		-	2.4	1.3	-1.2	-0.2
Δ XRD	C8-C9-C11	-0.9	9.4	9.2	8.3	2.9
		-	10.3	10.1	9.2	3.8
Δ XRD	C9-C11-N1	-4.6	8.1	0.6	-1.7	-0.6
		-	12.7	5.2	2.9	4
Δ XRD	C11-N1-N2	-0.2	-2.9	-6.2	-8.2	-1.8
		-	3.1	6.4	8.4	2
Δ XRD	C10-C9-C8-O2	0.6	-14.8	-16.2	-16.5	-18.4
		-	-15.4	-16.8	-17.1	-19
Δ XRD	C10-C9-C11-N1	5.8	-9.5	-12.6	-12.3	-15.6
		-	-15.3	-18.4	-18.1	-21.4
Δ XRD	O2-C8-C9-C11	0.2	-12.3	-12.5	-15.8	-17.3
		-	-12.5	-12.7	-16	-17.5
Δ XRD	C8-C9-C11-N1	6.1	-11.9	-16.5	-13	-16.7
		-	18	22.6	19.1	22.8

Here, the Δ XRD value means, the difference between a parameter for the ligand framework in the MM2-modelled complex and the corresponding value for the pure ligand from the XRD data. Similarly, the Δ MM2 value means the difference between a parameter for the ligand framework in

the MM2-modelled complex and the corresponding value for the MM2-modelled pure ligand. Any finite Δ XRD value may imply a true variation of the parameter upon complexation whenever the values of the said parameter for the ligand from DFT calculations and that from XRD data are in good agreement whereas Δ DFT may imply a deviation of the specified parameter of a gas-phase single molecule upon coordination to give a gas-phase single molecule of the complex.

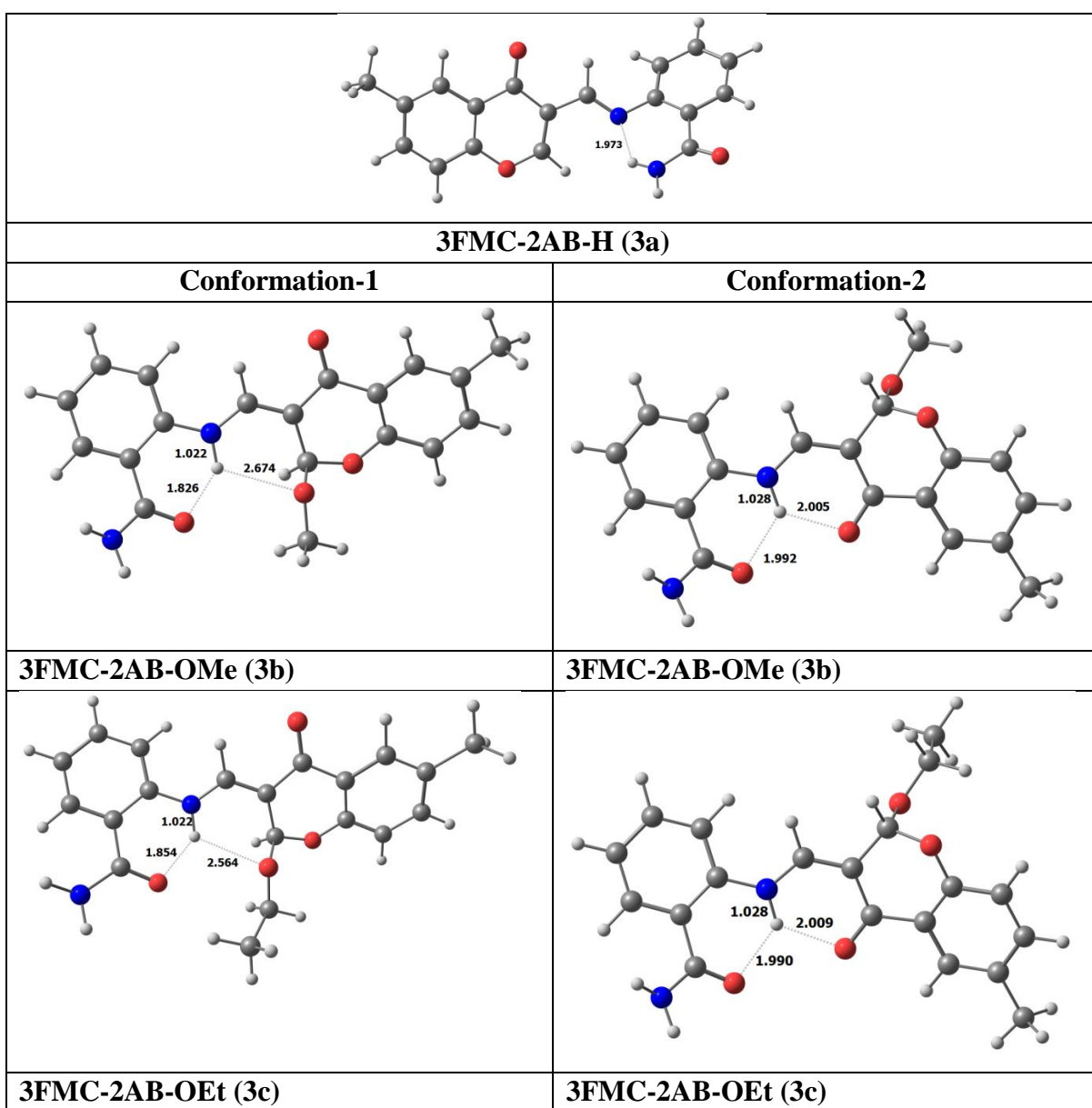
As expected, the bond lengths between the donor atoms and their linked atoms in the ligand molecule are slightly only different in the complexes when compared to those in the free ligand. Similarly, the bond angles of the C9-C11-N1, C8-N1-C11, N2-N1-C11 and O2-C8-C9 and where N1 and O2 are the donor atoms, are found to be affected to varied extents to account for the demands of structural stability of the complexes upon coordination. Since, the C9-C11-N1 and C11-N1-N2 moieties are exocyclic and thus flexible and the coordination is a five-membered ring with NMO angle close to 90° , the angles at these moieties are lower in the complexes than in the ligand whereas the angles at O2-C8-C9, where both the carbon atoms are endocyclic and thus are less flexible, seem to have hardly been affected upon complexation. The fact that Δ XRD and Δ MM2 values of any parameter of the pure or those of the complexed ligand are very close to each other vindicates the reliability of the ChemDraw platform for the MM2 calculations.

It can be noted from the optimized geometries that in the case of Cu(II) and Zn(II) the four donor atoms of the two **TATMC** is in plane. Typically, the dative bond lengths for Cu-O and Cu-N are 1.358 and 1.396 Å respectively, as shown in **Table 5B.3**. For Zn(II) complex they are 1.917 and 1.939 Å. From this data one may conclude the two chloride ligands are in equidistant with metal ions in each of the Cu(II) and Zn(II) complexes suggesting that these complexes are in octahedral geometry at the coordination sphere.

SECTION-B2

5B.1 Molecular Modelling Studies of Chromanone 3FMC-2AB-R 3a-e

For addressing the stability aspects of the chromanone **3FMC-2AB-R 3a-e** molecular modelling studies were used to find the conformational visualization of the molecules in various forms. The DFT B3LYP method with an RMS gradient of 0.01 is used to calculate the global energy minimized structures. The optimized structures of the chromanones are shown in **Figure 5B.14**, which depicts the global minimized structures of the quantum mechanical HOMO-LUMO orbital energy estimates that were used to calculate the projected gas-phase electronic transitions. Given the HOMO-LUMO of chromanones (**3a-e**), is created and illustrated in **Figures 5B.15**.



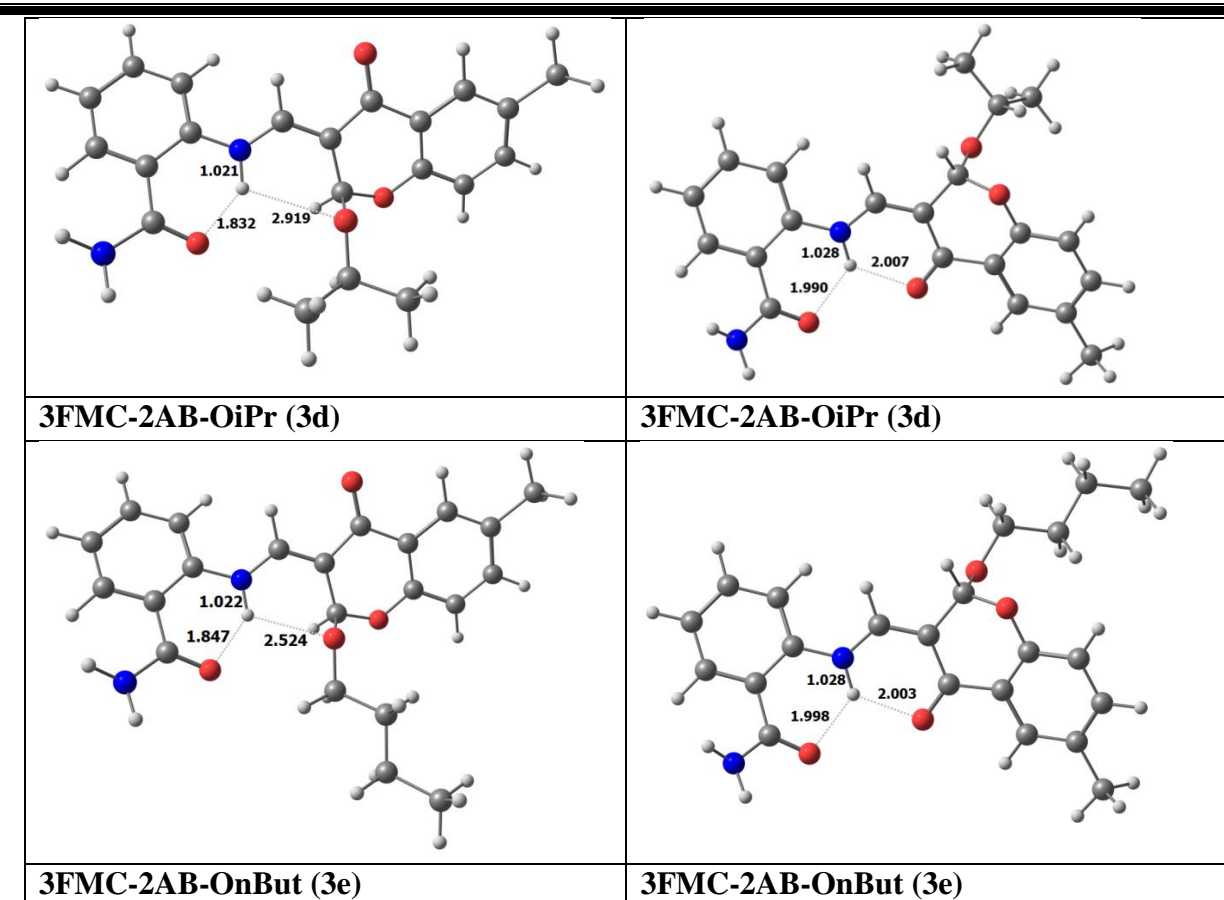


Figure 5B.14 DFT-optimized ball-stick model structures of most stable conformers of chromanones (**3a-e**) (Color Key: Grey = C, white = H, Blue = N, and Red = O atoms)

5B.2 Density Functional Theory Calculations

All the chromanones geometries are optimized using density functional theory based on Becke's three parameter hybrid exchange functional and the Lee–Yang–Parr correlation functional (B3LYP) method. In order to assess the stable structure of each synthesized chromone, in this investigation, optimization of different confirmations was carried out. The nature of critical point structures was characterized as local minima by the frequency calculations at the same level of theory. A systematic comparison of the energies of both conformations was carried out. All these calculations are performed using the Gaussian 16 program package.

Optimized geometries of both stable conformations are revealed in **Figure 5B.14**. The energy difference ($\Delta E = E_{\text{Conformation-1}} - E_{\text{Conformation-2}}$) values are given in **Table 5B.4**.

Table 5B.4 Energy difference between the two stable conformers, using B3LYP/6-31G* level of calculations

System	ΔE (kcal/mol)
3FMC-2AB-OMe	-0.63
3FMC-2AB-OEt	-1.12
3FMC-2AB-O(i-Pr)	-0.96
3FMC-2AB-O(n-But)	-0.95

It is interesting to note that **conformation-1** is energetically more stable when compared with Conf-2. It can be noted that the N-H distance involving intramolecular hydrogen bonding varies in both conformations. Typically, the calculated N-H distance value in conf-1 is \sim 1.02 Å, the same value in conf-2 is \sim 1.03 Å. It is also interesting to mention that the distance between C=O of amide group and NH group is considerably smaller in conf-1 when compared with conf-2. Calculated values C=O of amide group and NH group in **conformation-1** are 1.826, 1.854, 1.832, and 1.847 Å for 3FMC-2AB-O-ME, 3FMC-2AB-O-ETH, 3FMC-2AB-O-PROP, and 3FMC-2AB-O-BUT, respectively. Corresponding values in **conformation-2** are 1.992, 1.990, 1.990, 1.998 Å.

5B.3 HOMO-LUMO Analysis

HOMO-LUMO analysis includes both the highest occupied molecular orbital (HOMO) and the lowest unoccupied molecular orbital (LUMO). The electrons are transferred from electronic absorption (ground state) to electronic transition (first excited state). The electron donor is represented by HOMO, and the electron acceptor is represented by LUMO, which can be used to describe the transition of electron density between these orbitals. HOMO and LUMO of chromanone derivatives (**3a-3e**) viz., **3FMC-2AB-OMe**, **3FMC-2AB-OEt**, **3FMC-2AB-O(iPr)** and **3FMC-2AB-O(n-But)** delocalized is spread over with the green to red colour as shown in **Figure 6B.2**. Wherein, HOMO of substituted oxygen position covered with Red and green and in LUMO only red colour which is responsible for the electron density transfer from HOMO to LUMO in the molecules. The HOMO, LUMO energies were calculated with the same level as DFT approach. The energy gap, for the **3a-3e** chromanone molecules is determined by the difference in HOMO and LUMO energy among the all, **3FMC-2AB-OEt** having more energy i.e., -1.12 (kcal/mol). These provides information on electrical properties as well as the stability of the complete crystal structure to demonstrate the charge transfer process between these molecules.

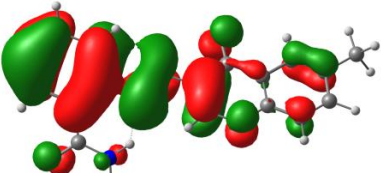
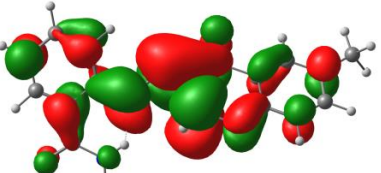
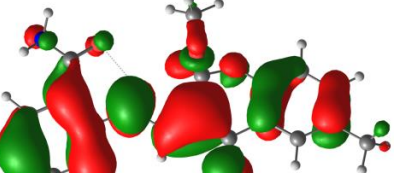
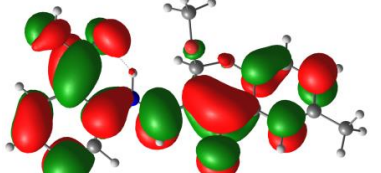
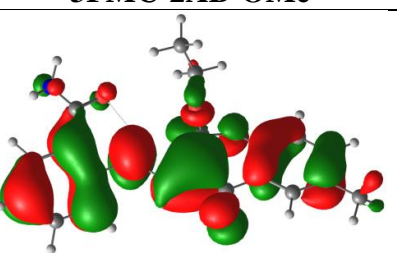
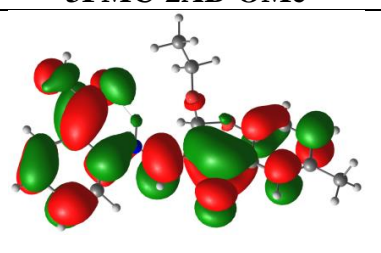
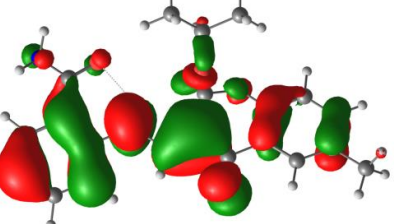
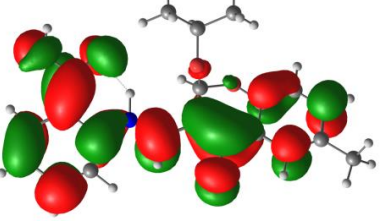
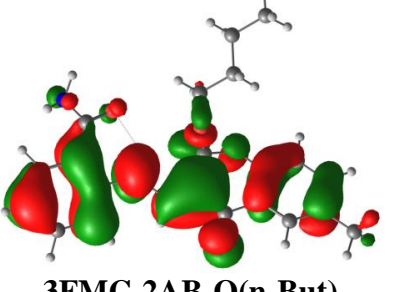
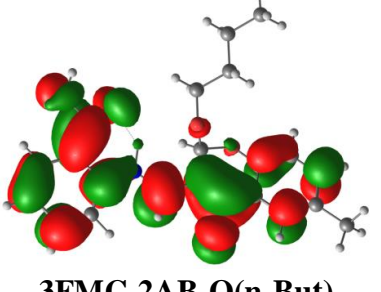
HOMO	LUMO	λ_{\max} Expected (Observed)
		342 nm (361 nm)
		206 nm (282 nm)
		206 nm (285 nm)
		207 nm (289 nm)
		208 nm (293 nm)

Figure 5B.15 Modelled shapes and energies of HOMO and LUMO molecular orbitals of **3FMC-2AB-R** (DFT platform) along with their energies and expected electronic transitions (the observed λ_{\max} are also given for comparison)

To verify the observed wavelengths of **3FMC-2AB-R**, we have calculated the λ values from HOMO, LUMO energy values and their molecular orbitals HOMO and LUMO surfaces are shown in **Figure 5B.2**. The minor deviations are understood to be due to the fact that the molecular modeling does not take the crystal packing and multidirectional intermolecular interactions into reliable consideration for the compounds.

Table 5B.4 Comparative list of bond lengths, bond angles between experimental XRD and DFT, MM2 Calculations of TATMC and **3FMC-2AB-R**

Atomic string	XRD	DFT	MM2	$\Delta(\text{XRD-DFT})$	$\Delta(\text{XRD-MM2})$
Bond Lengths (Å)					
C9-C10	1.345	1.412	1.351	-0.067	-0.006
C10-O1	1.332	1.578	1.513	-0.246	-0.181
O1-C6	1.377	1.510	1.405	-0.133	-0.028
C6-C5	1.375	1.58	1.350	-0.205	0.025
C5-C8	1.455	1.459	1.382	-0.004	0.073
C8-C9	1.450	1.521	1.352	-0.071	0.098
C8-O2	1.228	1.352	1.660	-0.124	-0.432
C5-C4	1.398	1.423	1.349	-0.025	0.049
C4-C3	1.369	1.386	1.344	-0.017	0.025
C3-C7	1.503	1.540	1.511	-0.037	-0.008
C3-C2	1.401	1.653	1.341	-0.252	0.06
C2-C1	1.365	1.498	1.339	-0.133	0.026
C1-C6	1.382	1.442	1.346	-0.06	0.036
Bond Angles (°)					
C8-C9-C10	119.92	118.70	119.26	1.22	0.64
O2-C8-C5	123.10	120.00	124.50	3.10	-1.4
C5-C6-O1	121.97	122.90	125.36	-0.93	-3.46
C6-O1-C1	116.26	118.70	120.79	-2.44	-4.59
O1-C10-C9	124.84	121.50	118.47	3.34	6.33
C5-C6-C1	121.92	118.40	122.52	3.52	-0.62
C6-C1-C2	118.44	122.30	123.86	-3.86	-5.46
C1-C2-C3	121.70	119.80	120.89	1.90	0.81
C2-C3-C7	120.20	121.50	121.85	-1.30	-1.65
C7-C3-C4	121.27	120.50	123.21	0.77	-2.01
C4-C5-C8	121.43	120.20	122.36	1.23	-0.96

5B.4 Conformational Analysis and Consideration of Tautomerism in **3FMC-2AB-R**

The compound-series, **3FMC-2AB-R** has a possibility of exhibiting 4 tautomeric equilibria profile structures as shown schematically in **Figure 5B.16**. The MM2 calculations done on each of

these structures and their energies in (kcal/mol) are presented in **Figure 5B.23** along with all chromanones possible tautomers shown in **Figure 5B.24**. All the **3a-3e** structures reveals that the tautomers have their reactive stabilities as follows:

3FMC-2AB-H (3a)

$T_1 = 29.03$ kcal/mol < $T_4 = 21.53$ kcal/mol < $T_2 = 14.15$ kcal/mol < $T_3 = 13.50$ kcal/mol

3FMC-2AB-OMe (3b)

$T_1 = 35.84$ kcal/mol < $T_4 = 22.51$ kcal/mol < $T_2 = 16.52$ kcal/mol < $T_3 = 4.80$ kcal/mol

3FMC-2AB-OEt (3c)

$T_1 = 33.94$ kcal/mol < $T_4 = 24.80$ kcal/mol < $T_2 = 19.12$ kcal/mol < $T_3 = 17.77$ kcal/mol

3FMC-2AB-O(iPr) (3d)

$T_1 = 38.48$ kcal/mol < $T_4 = 24.85$ kcal/mol < $T_2 = 22.66$ kcal/mol < $T_3 = 17.83$ kcal/mol

3FMC-2AB-O(n-But) (3e)

$T_1 = 37.56$ kcal/mol < $T_4 = 25.83$ kcal/mol < $T_2 = 21.96$ kcal/mol < $T_3 = 17.94$ kcal/mol

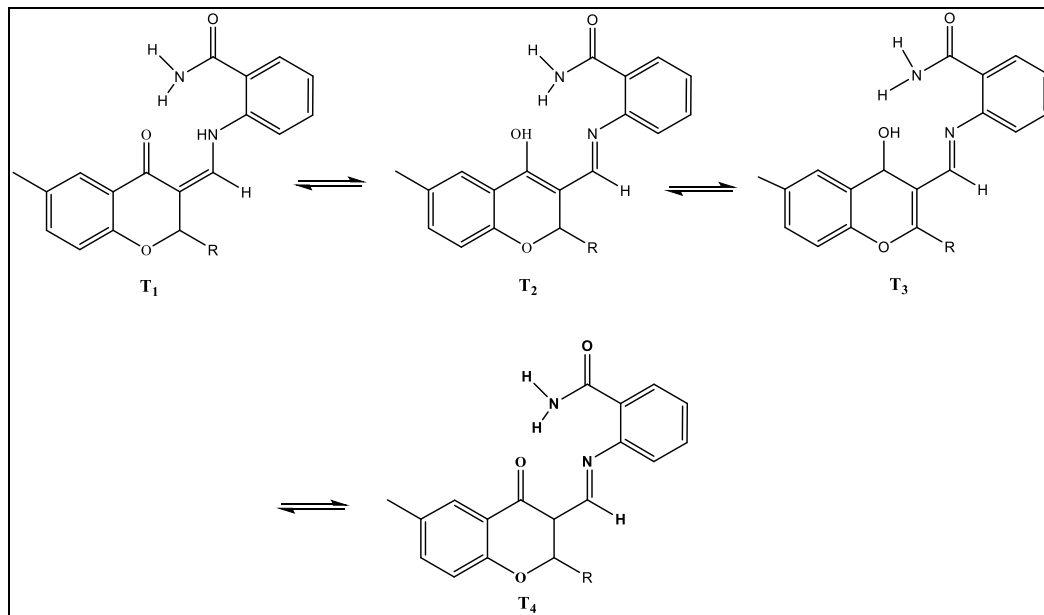


Figure 5B.16 Possibility of tautomerism in **3FMC-2AB-R**

The possible MM2-energy-minimized structures of **3FMC-2AB-H** and **3FMC-2AB-OMe** along with anaglyph and stereographic projection and double dihedral torsional energy Surfer and grapher plots is shown in **Figure 5B.17** through **Figure 5B.22**.

The global-energy-minimized MM2 structures of **3FMC-2AB-H** and **3FMC-2AB-OMe**, **3FMC-2AB-OEt**, **3FMC-2AB-O(iPr)** and **3FMC-2AB-O(n-But)** chromanones atom numbering

scheme are shown in **Figure 5B.23** along with each chromanone tautomer presented in **Figure 5B.25** and their corresponding conformational single dihedral energy plots are presented in **Figure 5B.26-5B.27**. Figure **5B.24** of **3FMC-2AB-OMe** Anaglyph and MM2-energy-minimized structure obtained from ChemDrawPro.

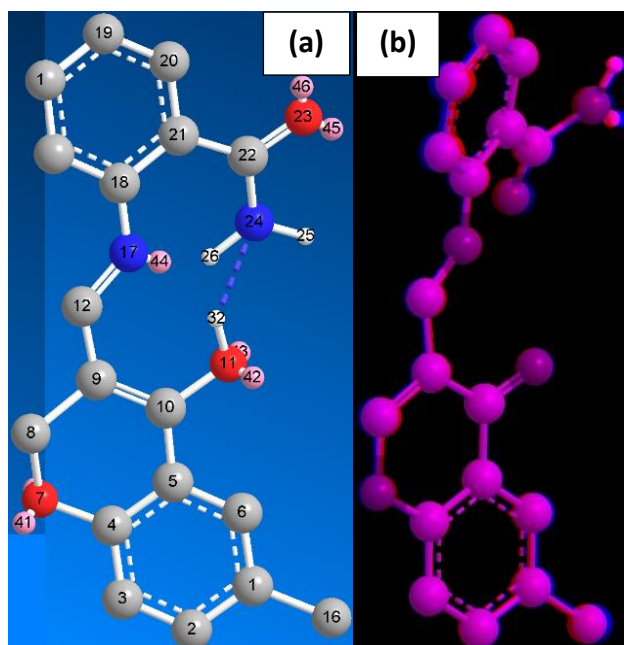


Figure 5B.17 MM2-energy-minimized structures (a) and anaglyph (b) of **3FMC-2AB-H**



Figure 5B.18 Stereographic projection of **3FMC-2AB-H** obtained from ChemDraw Pro

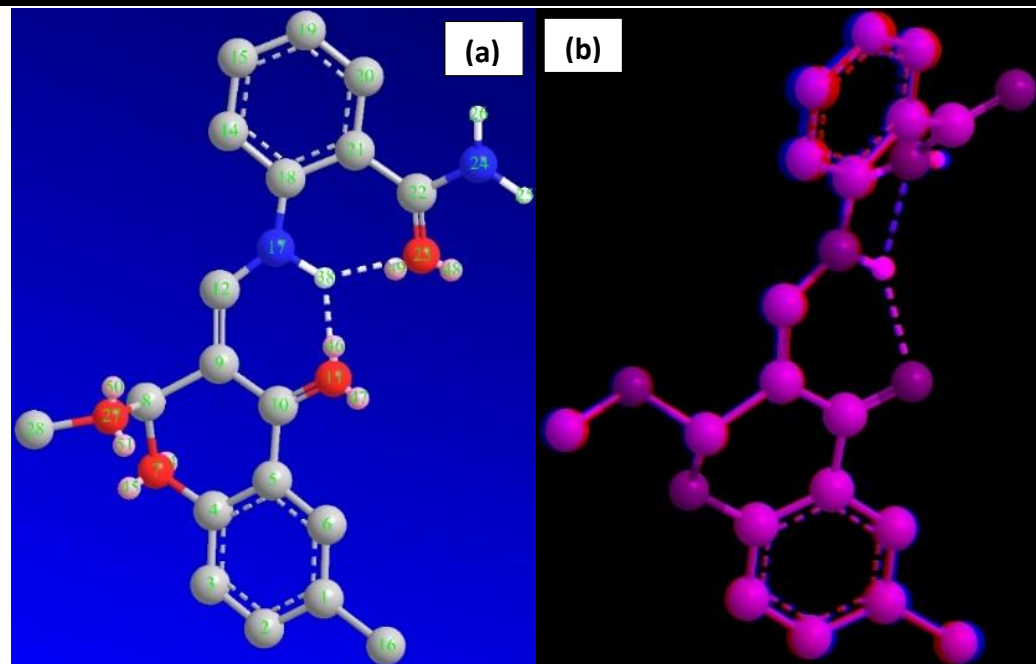


Figure 5B.19 MM2-energy-minimized structures (a) and anaglyph (b) of 3FMC-2AB-OMe

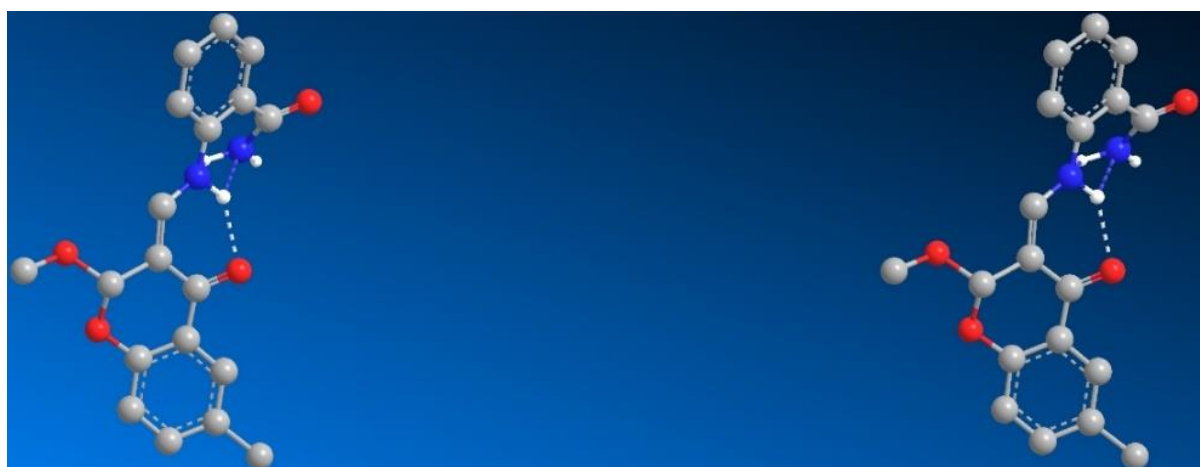


Figure 5B.20 Stereographic projection of 3FMC-2AB-OMe obtained from ChemDraw Pro

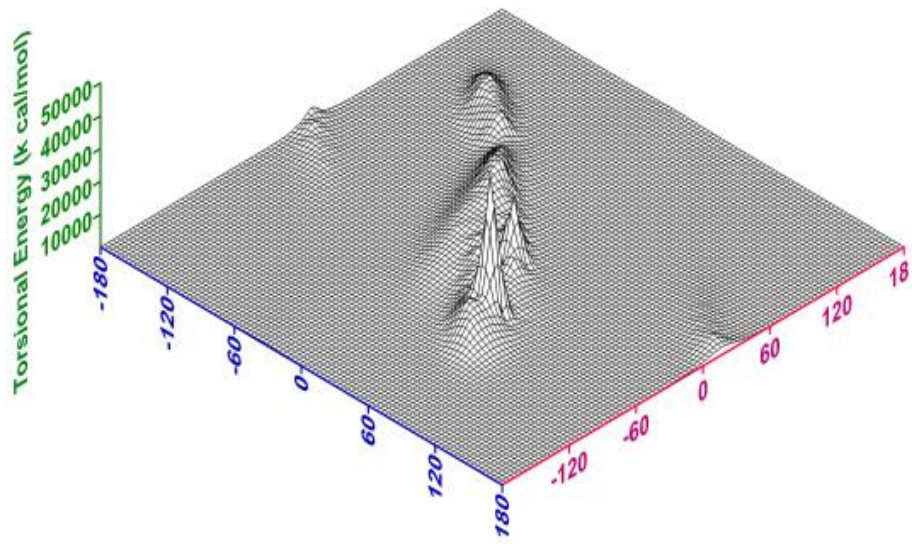


Figure 5B.21 Double dihedral torsional energy Surfer plot of **3FMC-2AB-OMe** of C9-C12 (on axis shown in blue) and C12-N17 (on axis shown in red) bonds (Refer **Figure 5B.20** for numbering of the atoms)

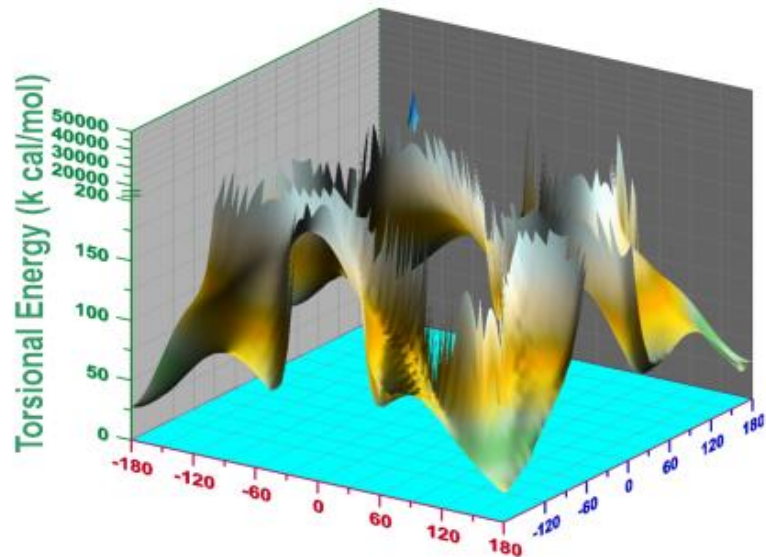


Figure 5B.22 Double dihedral torsional energy Grapher plot of **3FMC-2AB-OMe** of C9-C12 (on axis shown in blue) and C12-N17 (on axis shown in red) bonds (Refer **Figure 6B.20** for numbering of the atom

S. No	1	2	3	4	5
R	H	OMe	OEt	OiPr	OnBut
Structure					

Figure 5B.23 MM2-global-energy-minimized ball-stick model structures with atom numbering of (1)3FMC-2AB-H, (2) 3FMC-2AB-OMe, (3) 3FMC-2AB-OEt, (4) 3FMC-2AB-OiPr and (5) 3FMC-2AB-O(n-But)

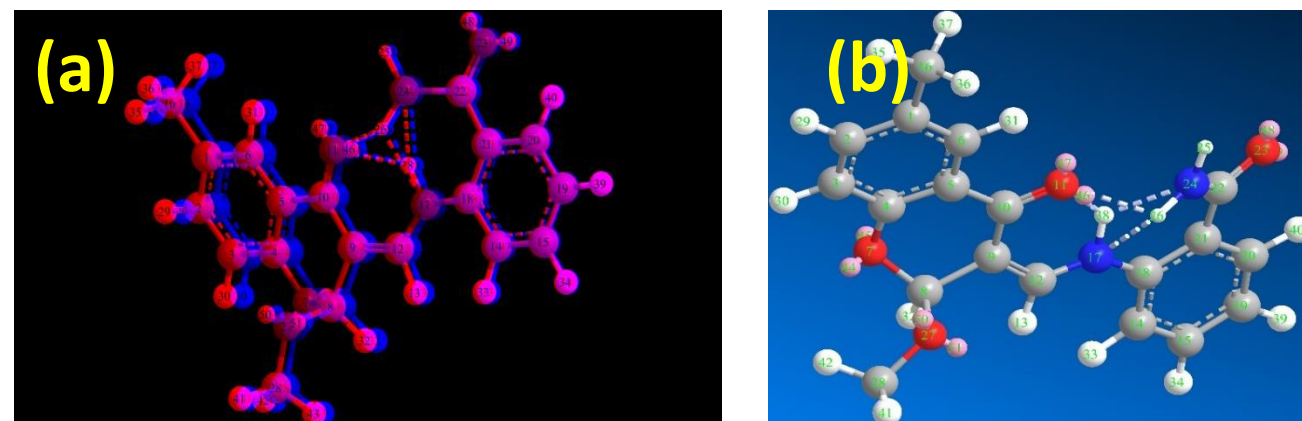
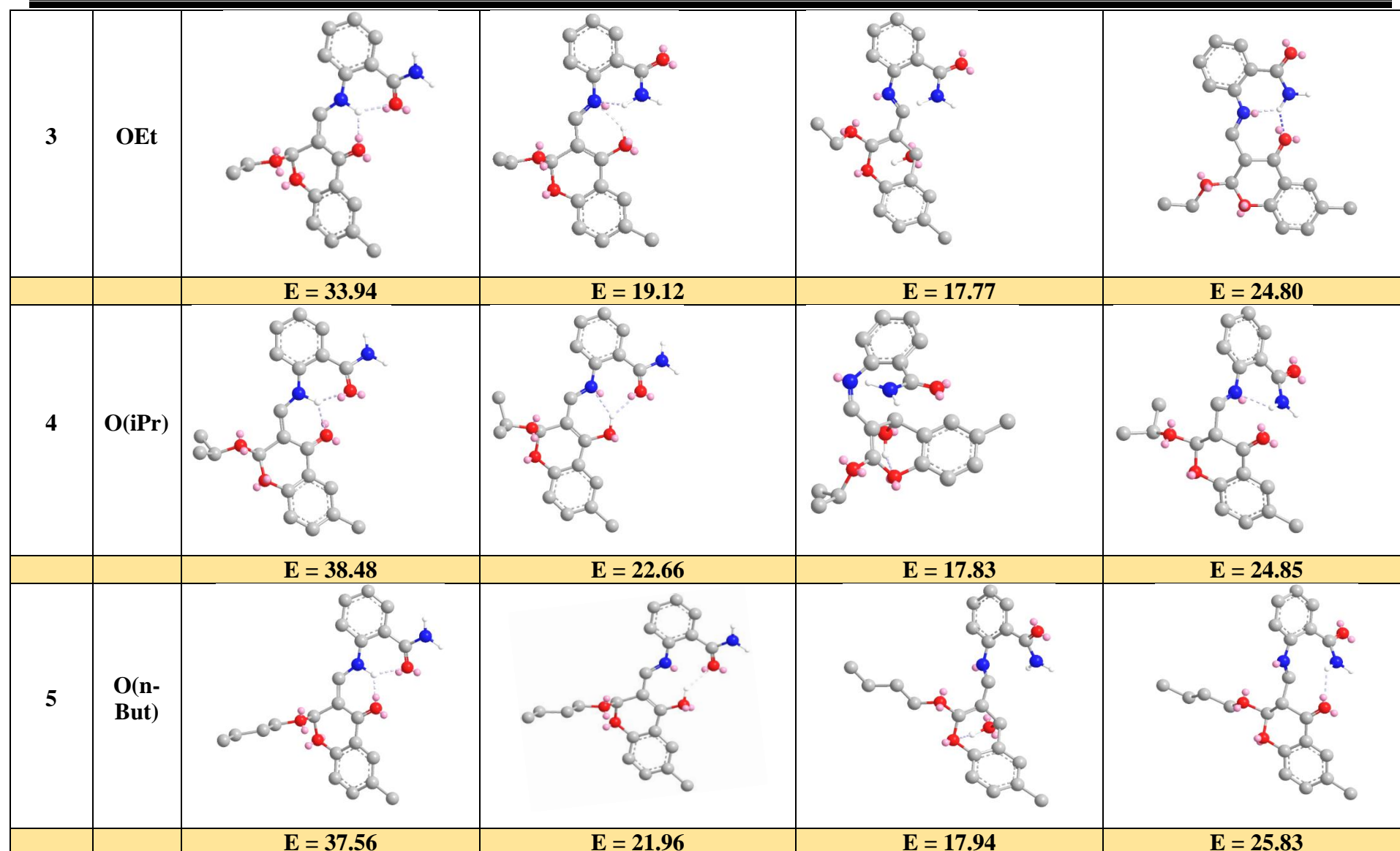


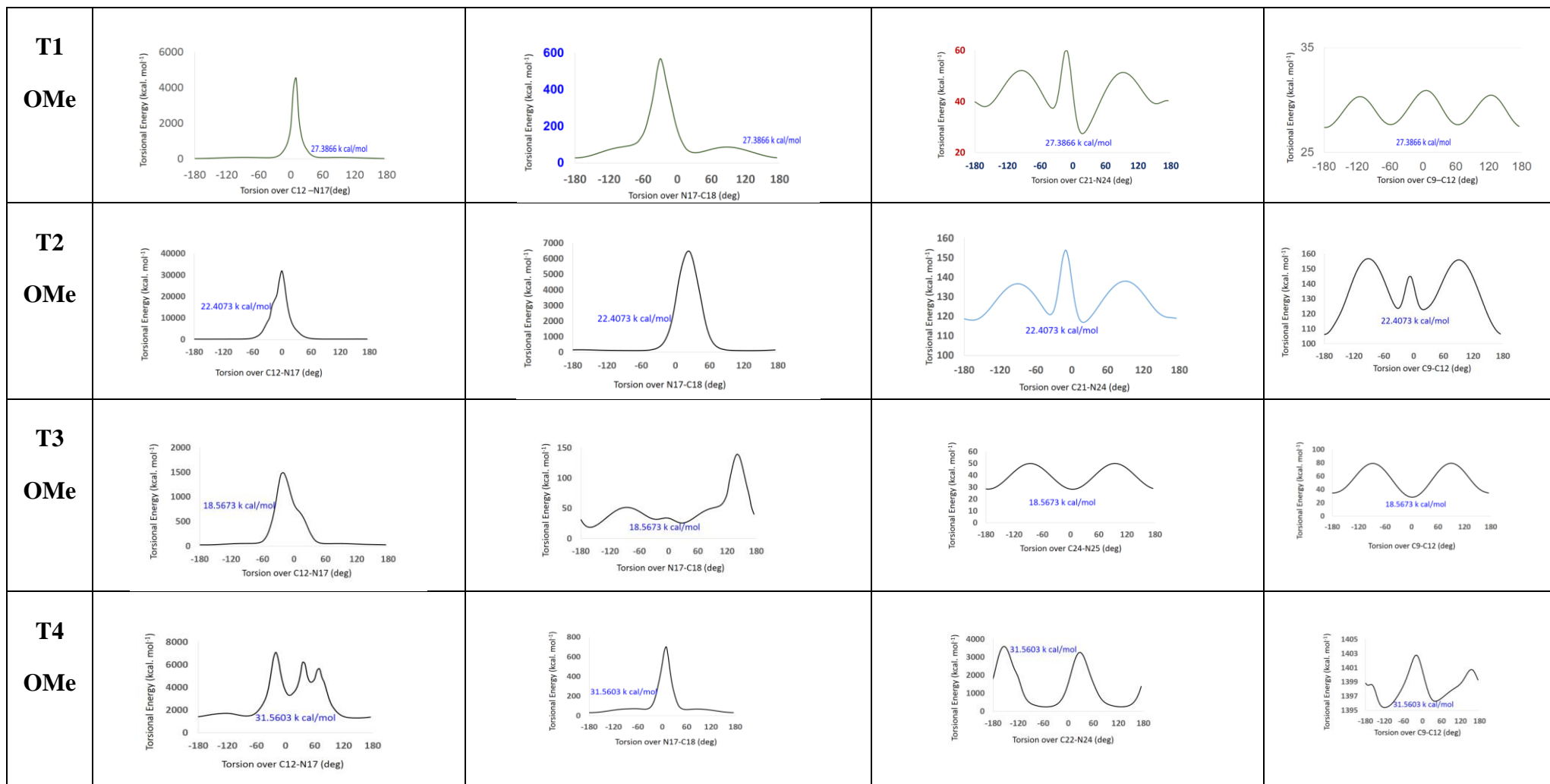
Figure 5B.24 Anaglyph and MM2-energy minimized of 3FMC-2AB-OMe Tautomer (T1)

S. No.	R	T ₁ *	T ₂	T ₃	T ₄
1	H				
		#E = 29.03	E = 14.15	E = 13.50	E = 21.53
2	OMe				
		E = 35.84	E = 16.52	E = 4.80	E = 22.51



T^* = Tautomer; $^{\#}E$ = kcal/mol

Figure 5B.25 MM2-energy-minimized ball-stick model structural tautomer and their calculated energy values in kcal/mol

**Figure 5B.26** Conformational energy plots of **3FMC-2AB-OMe** tautomer (T1-T4)

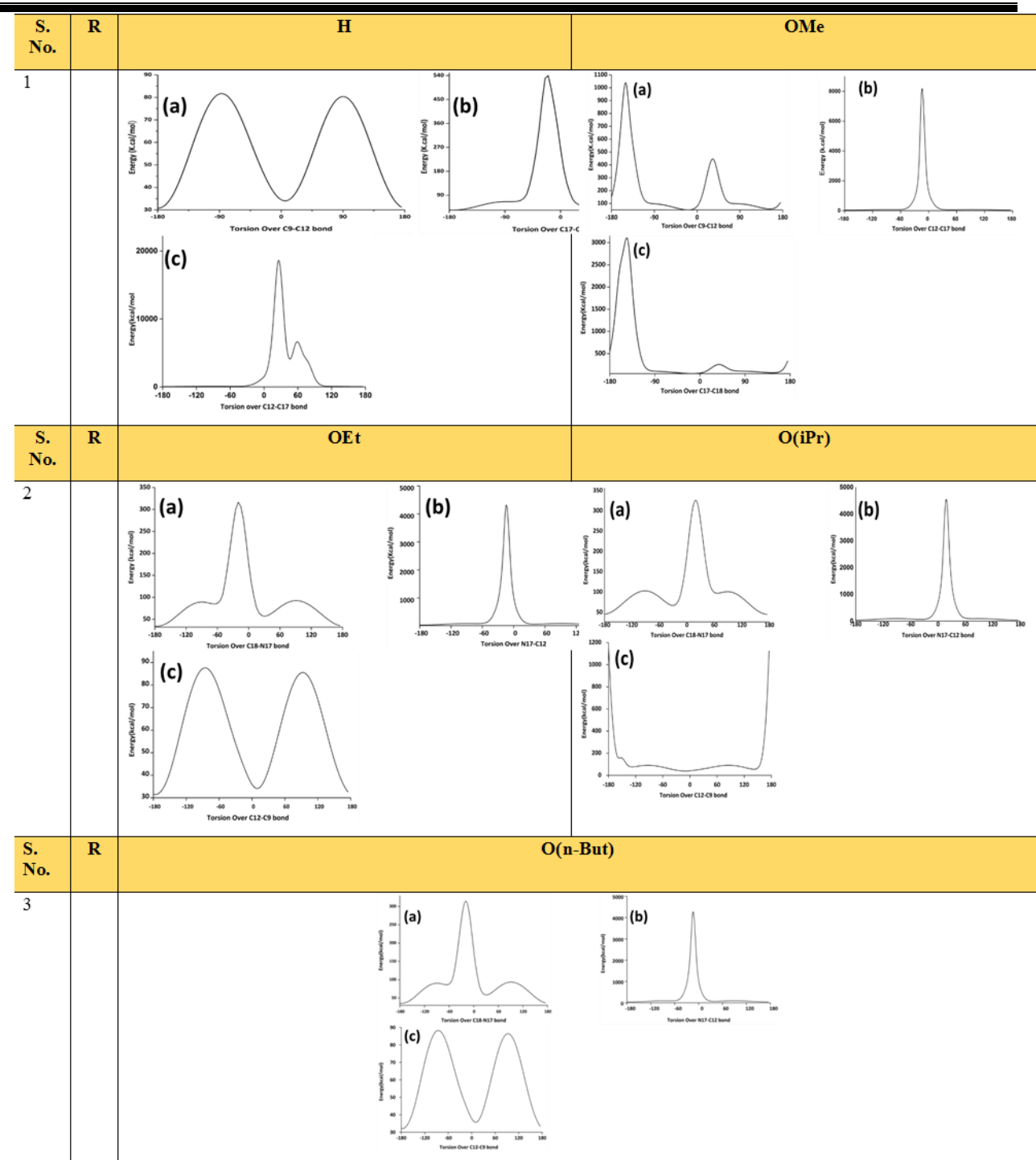


Figure 5B.27 Conformational energy plots of (1) 3FMC-2AB-H, (2) 3FMC-2AB-OMe, (3) 3FMC-2AB-OEt, (4) 3FMC-2AB-O(iPr) and (5) 3FMC-2AB-O(n-But) (Refer Figure 5B.23 for atoms numbering scheme)

PART-C**BIOLOGICAL AND MOLECULAR DOCKING STUDIES OF TATMC AND ITS COMPLEXES AND CHROMANONES 3FMC-2AB-R****SECTION-C1****5C.1 Biological Activity for TATMC and $[M(TATMC)_2X_2]$**

The biological activity of ligand and its metal complexes was screened for antibacterial, antifungal and further antioxidant activity by the DPPH assay and anti-diabetic activity by the α -amylase inhibitory assay method.

5C.1.1 Antibacterial Activity

An *in-vitro* evaluation towards antibacterial activity of **TATMC** and its metal complexes was carried out by screening them against two Gram positive bacteria, viz., *B. cereus* and *S. Aureus*, and two Gram-negative bacteria, viz., *P. aeruginosa* and *E. coli*. Their antibacterial activity is presented in **Table 5C.1** and histographically in **Figure 5C.1**. According to the Overtones concept and Tweedy's chelation theory, the antibacterial activity of metal complexes is usually better than their free ligands [14]. In our case we observed $[Ni(TATMC)_2]$ and $[Zn(TATMC)_2Cl_2]$ showing higher activity than **TATMC**.

Table 5C.1 Antibacterial activity of **TATMC** and its bivalent metal complexes

Compound	Zone of Inhibition (in mm)			
	Gram positive bacteria		Gram negative bacteria	
	<i>Bacillussubtilis</i>	<i>Bacillus cereus</i>	<i>Escherichia coli</i>	<i>Pseudomonas aeruginosa</i>
TATMC	18	15	07	10
$[Co(TATMC)_2]$	19	17	09	11
$[Ni(TATMC)_2]$	22	21	13	15
$[Cu(TATMC)_2Cl_2]$	23	19	12	11
$[Zn(TATMC)_2Cl_2]$	26	22	13	17
<i>Streptomycin (Std)</i>	27	23	14	18

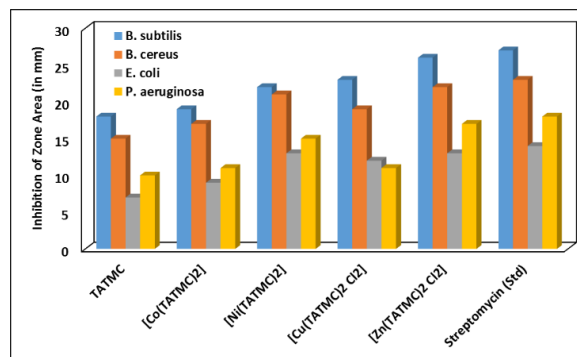


Figure 5C.1 Histographical representation of the antimicrobial activities of **TATMC** and its complexes

5C.1.2 Antioxidant Activity

Among all the free radicals, the hydroxyl radical is by far the most potent and therefore the most dangerous oxygen metabolite, and hence the elimination of this radical is one of the major aims of antioxidant administration [15]. The antioxidant activities of **TATMC**, its complexes and ascorbic acid, as the standard, were assessed on the basis of the radical scavenging effect of the stable DPPH (2,2-diphenylpicryl hydrazyl) free radical. The % of inhibition and IC_{50} values are listed in **Table 5C.2** for **TATMC** and its Co(II), Ni(II), Cu(II), and Zn(II) complexes. The activity of these compounds are found to be lower than that of the standard, ascorbic acid. From the data, it is clear that the Zn(II) complex has a closer and some promising scavenging activity whereas Cu(II) and Ni(II) complexes have some reasonable antioxidant activity. The antioxidant activity is in the order of **TATMC** > Co(II) > Ni > Cu(II) > Zn(II). The results are histographically represented in **Figure 5C.2**.

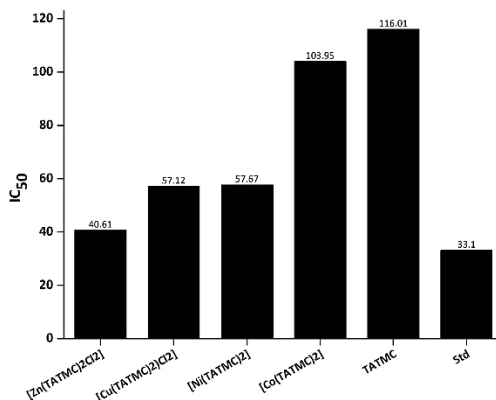


Figure 5C.2 Histogramical representation of the IC_{50} inhibition values of the DPPH radical-scavenging activity of **TATMC** and $[M(TATMC)_2X_2]$

Table 5C.2 Anti-scavenging activity inhibition values of **TATMC** and its $[M(TATMC)_2X_2]$

Compound	IC ₅₀ (μg/ml)
TATMC	116.01
[Co(TATMC)₂]	103.95
[Ni(TATMC)₂]	57.67
[Cu(TATMC)₂Cl₂]	57.12
[Zn(TATMC)₂Cl₂]	40.61
Ascorbic acid	33.10

5C.1.3 Anti-diabetic Activity by α -Amylase Inhibitory Assay Method

In-vitro α -amylase inhibitory studies reveal that **TATMC** and its complexes have promising inhibitory potential. The IC_{50} values were found to be 1.74, 3.20, 3.40 and 4.78 μ g/ml for Zn(II), Co(II), Ni(II) and Cu(II), respectively. The IC_{50} value of acarbose, at its 33.50 μ g/ml dosage has

stronger 50% inhibition of α -amylase than that of TATMC and its complexes. The results are reported in **Table 5C.3**. The inhibition is found in the order, Acarbose > TATMC > Cu(II) > Ni(II) > Co(II) > Zn(II).

Overall, the TATMC and its complexes showed moderate α -amylase inhibitory potential when compared to that of the acarbose drug.

Table-5C.3 α -Amylase anti-diabetic activity of TATMC and its complexes

Compounds	10 $\mu\text{g/ml}$	20 $\mu\text{g/ml}$	30 $\mu\text{g/ml}$	40 $\mu\text{g/ml}$	50 $\mu\text{g/ml}$	α -amylase IC ₅₀ ($\mu\text{g/ml}$)
TATMC L	12.73	48.27	45.5	60.62	65.62	8.57
[Co(TATMC) ₂]	15.03	20.72	25.02	35.5	48.39	3.20
[Ni(TATMC) ₂]	22.03	34.12	47.9	55.26	68.32	3.40
[Cu(TATMC) ₂ Cl ₂]	10.73	16.27	25.9	34.26	41.02	4.78
[Zn(TATMC) ₂ Cl ₂]	48.03	50.72	55.02	65.5	78.39	1.74
Acarbose control	78.77	82.66	82.66	90.77	98.59	33.50

5C.2 Docking Studies of TATMC and Its Complexes

Molecular docking studies of TATMC and [Co(TATMC)₂], [Ni(TATMC)₂], [Cu(TATMC)₂Cl₂], and [Zn(TATMC)₂Cl₂] with some chosen proteins reveal that the title compounds have effective interactions with the target receptor sites as shown in **Figure 5C.3** through **Figure 5C.7**. The interactions measured in terms of H-bond distances of intermolecular interactions and docking scores are tabulated in **Table 5C.4**.

Table 5C.4 Molecular docking interactions of TATMC and its complexes against the DNA- repair protein receptor (PDB ID: (2QLC)

Ligands	Receptor atoms Acceptor group	Donor Atom	Hydrogen Bonding Distance(Å)	Docking Score (kcal/mol)
TATMC	HN-GLN G-3103	O	2.23	-6.5
	HN-LEU G-101	N	2.98	
[Co(TATMC)₂]	OC-ASP C-100	HN	1.40	-7.6
[Ni(TATMC)₂]	HN-SER C-93	O	2.3	-7.7
	HN-LYS C-97	N	2.20	
[Cu(TATMC)₂Cl₂]	HN-ARG C-121	O	3.03	-7.5
[Zn(TATMC)₂Cl₂]	HN-HIS F-55	O	2.27	-7.5
	HN-ARG F-57	O	1.93	
	HN-ARG F-57	O	2.92	

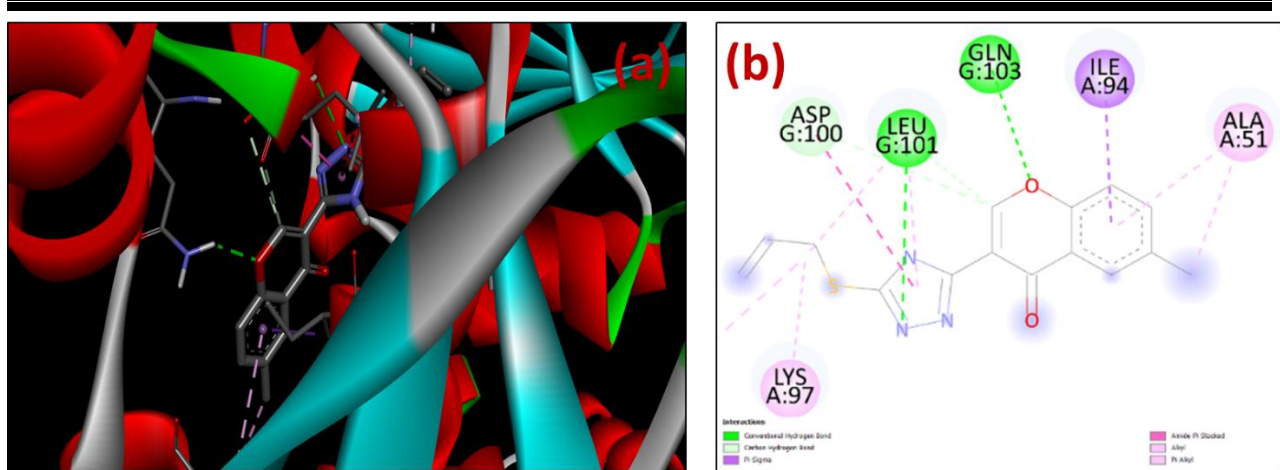


Figure 5C.3 3D (a) and 2D (b) molecular docking models illustrating interactions and intermolecular H-bond interactions between TATMC and the active site pocket residue receptors of PDB: 2QLC target

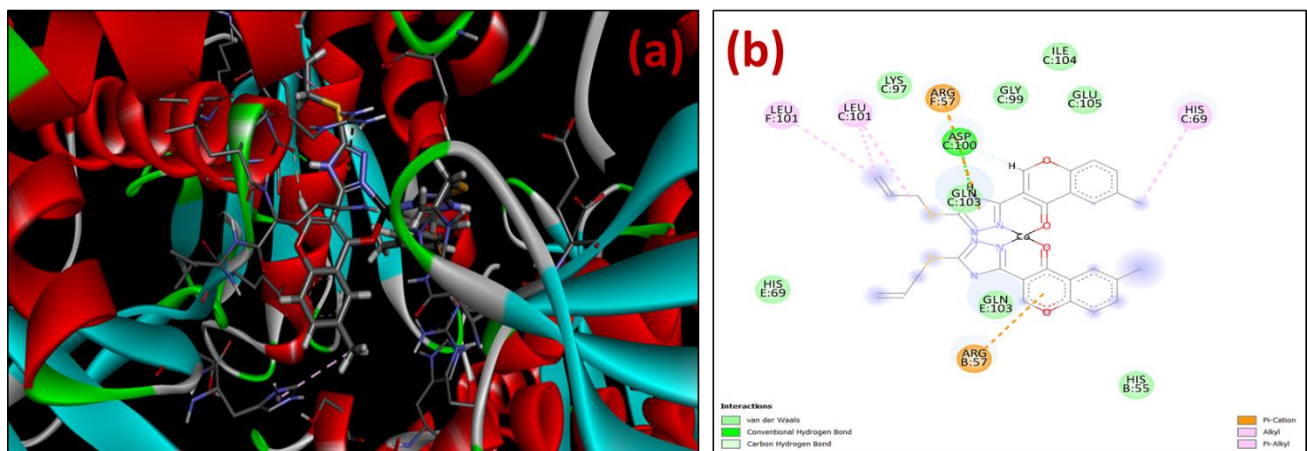


Figure 5C.4 3D (a) and 2D (b) molecular docking models illustrating interactions and intermolecular H-bond interactions between $[\text{Co}(\text{TATMC})_2]$ and the active site pocket residue receptors of PDB: 2QLC target

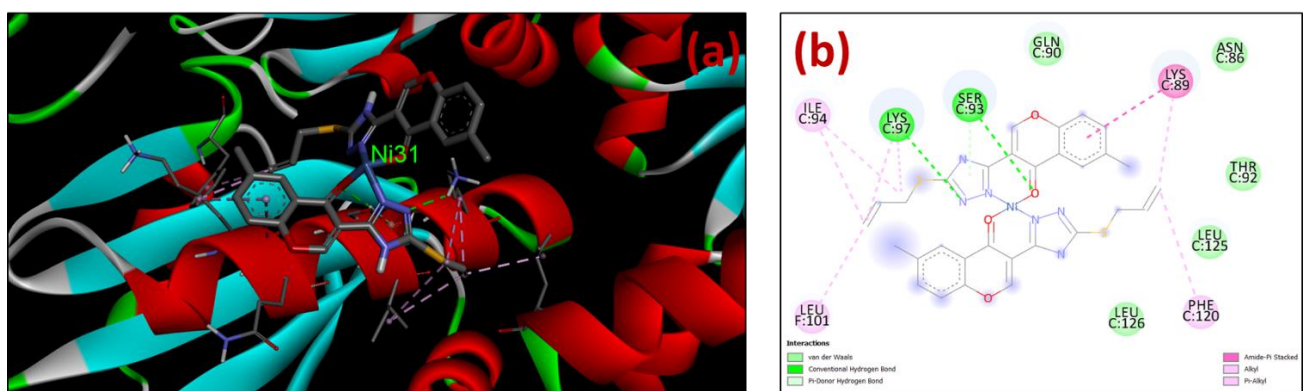


Figure 5C.5 3D (a) and 2D (b) molecular docking models illustrating interactions and intermolecular H-bond interactions between $[\text{Ni}(\text{TATMC})_2]$ and the active site pocket residue receptors of PDB: 2QLC target

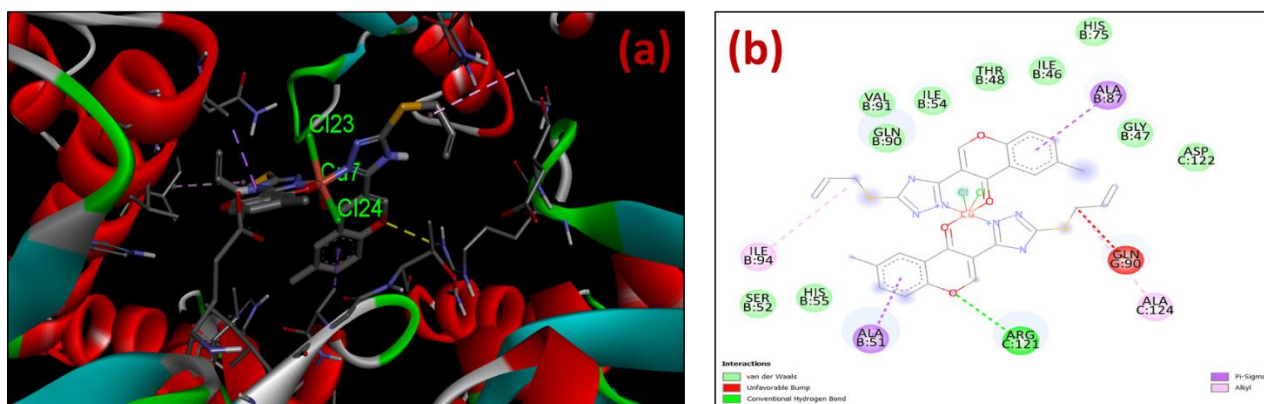


Figure 5C.6 3D (a) and 2D (b) molecular docking models illustrating interactions and intermolecular H-bond interactions between $[\text{Cu}(\text{TATMC})_2\text{Cl}_2]$ and the active site pocket residue receptors of PDB: 2QLC target

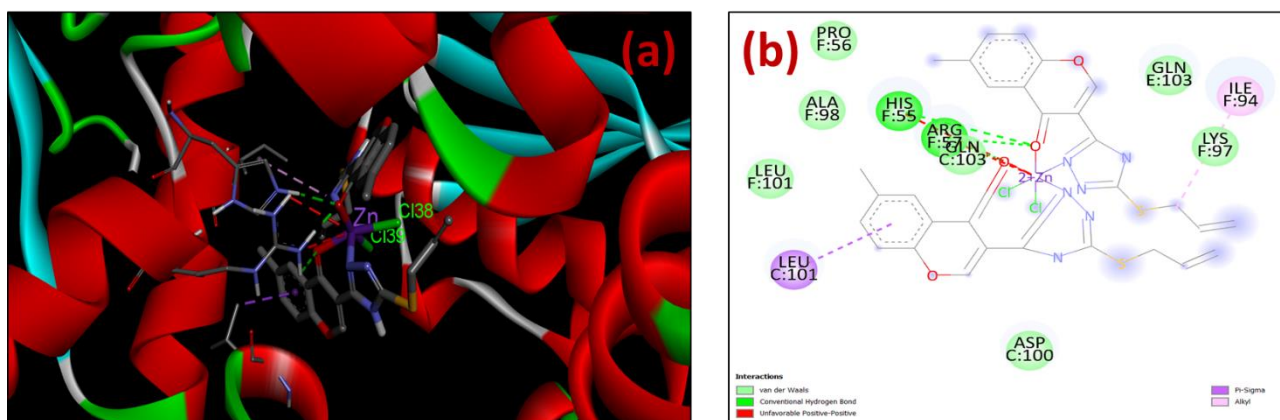


Figure 5C.7 3D (a) and 2D (b) molecular docking models illustrating interactions and intermolecular H-bond interactions between $[\text{Zn}(\text{TATMC})_2\text{Cl}_2]$ and the active site pocket residue receptors of PDB: 2QLC target

5C.3 *In-silico* Prediction of Drug Likeness and ADME Properties of TATMC

The TATMC was subjected to *in-silico* physicochemical investigations by employing the online version of Swiss ADME predictor. The compound was drawn using ChemDraw Pro and was exposed to the predictor. The results, obtained, are shown in **Figure 5C.8**. For a compound to become an effective drug candidate, it is of utmost importance to examine the ADME (absorption, distribution, metabolism, and excretion) including drug-likeness analysis and to evaluate its compliance with Lipinski's Rule of Five (RO5) [16]. According to RO5, the molecular weight of compounds should be ≤ 500 and there should be presence of hydrogen bond acceptors and donors with no rotatable bonds greater than 10. All the investigated compounds possess these permissible limits and therefore promise good drug-likeness characters. The lipophilicity parameter, as $M \log P$

lies between 0 and 5, which is within the acceptable limits for a drug to penetrate bio-membrane. **TATMC** showed the TPSA values at $\leq 140 \text{ \AA}^2$, passing the criteria of gastrointestinal absorption. The log S value of the compound lies between -4 and -6, which indicates a moderate solubility. The observed results suggest that **TATMC** possesses good attributes of drug-likeness with a bioavailability score of 0.55.

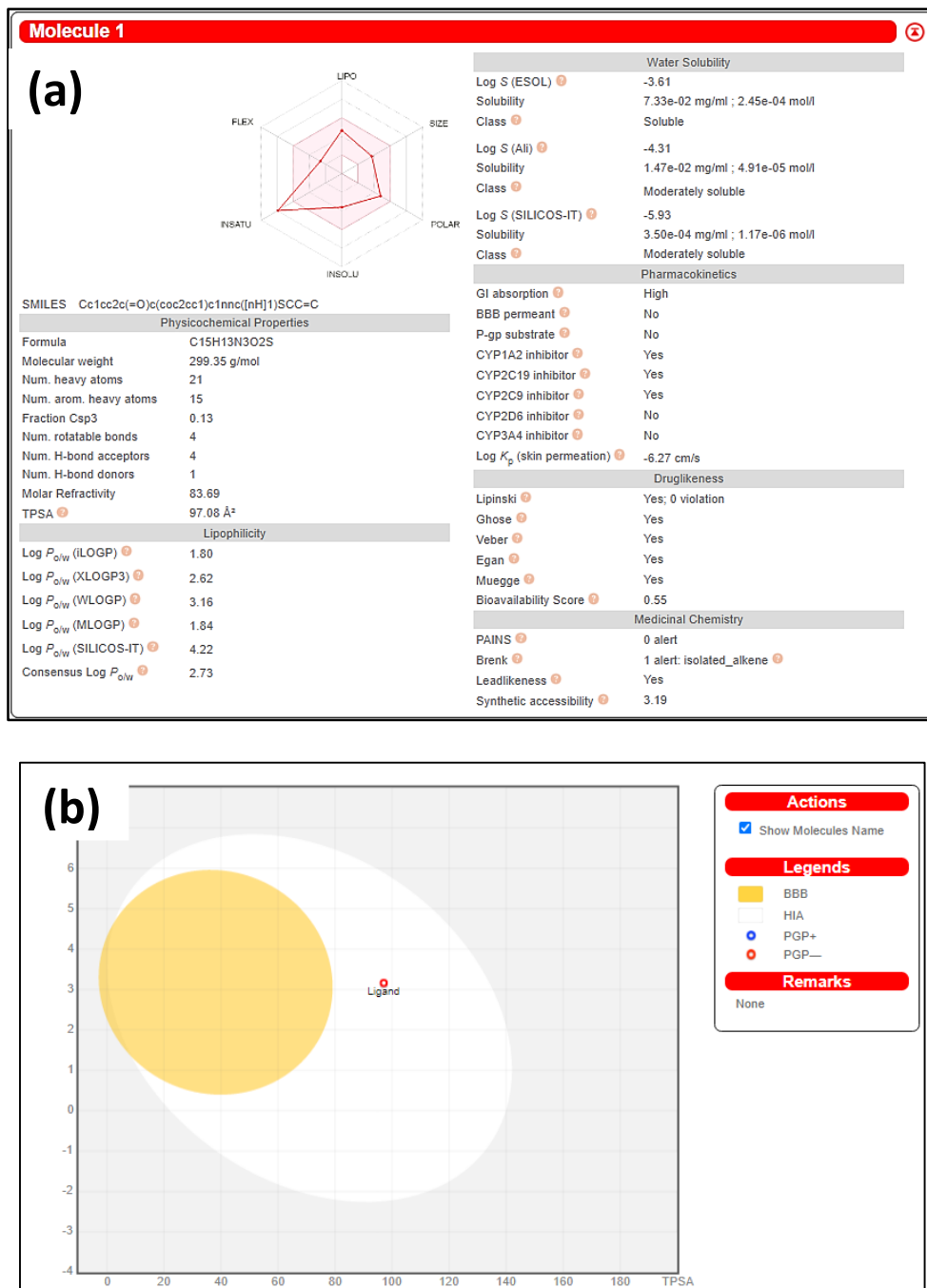


Figure 5C.8 ADME and drug-likeness parameters of **TATMC** (a), and boiled egg graph (b) demonstrating the (yellow part of the yolk area) which is estimated to inactivate the blood-brain barrier (BBB)

SECTION-C2

5C.1 Biological Studies of 3FMC-2AB-R**5C.1.1 Antimicrobial Activity of 3FMC-2AB-R**

The anti-microbial activity of chromanones, **3FMC-2AB-R (3a-e)** were screened against two gram-positive and two gram-negative bacteria with the *streptomycin* used as the standard drug. The chromanones (**3a-e**) tested moderate to lower antibacterial activity. The results are collected in **Table 5C.1**, with pathogens grown activity shown in **Figures 5C.1** and **Figure 5C.2**. The zone of inhibition (*ZOI*) activity of the chromanone, **3a-e** were found increases with increasing concentrations (200 to 400 $\mu\text{g}/\text{ml}$). the compounds, viz., **3FMC-2AB-OEt** and **3FMC-2AB-H**, exhibited very good antibacterial activity against gram positive *B. subtilis* (1.1 cm), gram negative *E. coli* (0.2 cm) and *B. subtilis* (0.9 cm), *B. cereus* (0.8 cm), gram negative (0.6 cm), and *P. aeruginosa* (0.1 cm) at 400g/ml, Other chromonone compounds, such as **3FMC-2AB-O(iPr)**, **3FMC-2AB-OMe** and **3FMC-2AB-O(n-But)**, demonstrated a moderate to lower antibacterial activity than the standard drug. The antimicrobial activity goes on increasing with the increased concentration of the compounds.

Table 5C.1 Results of antibacterial activity of **3FMC-2AB-R**

S. No.	Compound	Gram Positive Bacteria		Gram Negative Bacteria	
		<i>Bacillus subtilis</i>	<i>Bacillus cereus</i>	<i>Escherichia coli</i>	<i>Pseudomonas aeruginosa</i>
200 $\mu\text{g}/\text{ml}$					
1	3FMC-2AB-O(n-But)(3e)	NA	NA	NA	NA
2	3FMC-2AB-O(iPr)(3d)	NA	0.1	0.1	NA
3	3FMC-2AB-OMe(3b)	0.2	NA	NA	NA
4	3FMC-2AB-H(3a)	0.5	0.1	0.3	0.1
5	3FMC-2AB-OEt(3c)	0.4	0.1	0.1	NA
6	Streptomycin (standard)	0.71	0.23	0.15	NA
400 $\mu\text{g}/\text{ml}$					
1	3FMC-2AB-O(n-But)(3e)	0.2	NA	NA	NA
2	3FMC-2AB-O(iPr)(3d)	0.6	0.2	0.2	0.1
3	3FMC-2AB-OMe(3b)	0.4	NA	NA	NA
4	3FMC-2AB-H(3a)	0.9	0.8	0.6	0.1
5	3FMC-2AB-OEt(3c)	1.1	NA	0.8	0.2
6	Streptomycin (standard)	1.2	1.2	1.2	0.7



Figure 5C.1 Images of antibacterial activity of the zone of inhibition area for **3FMC-2AB-R**

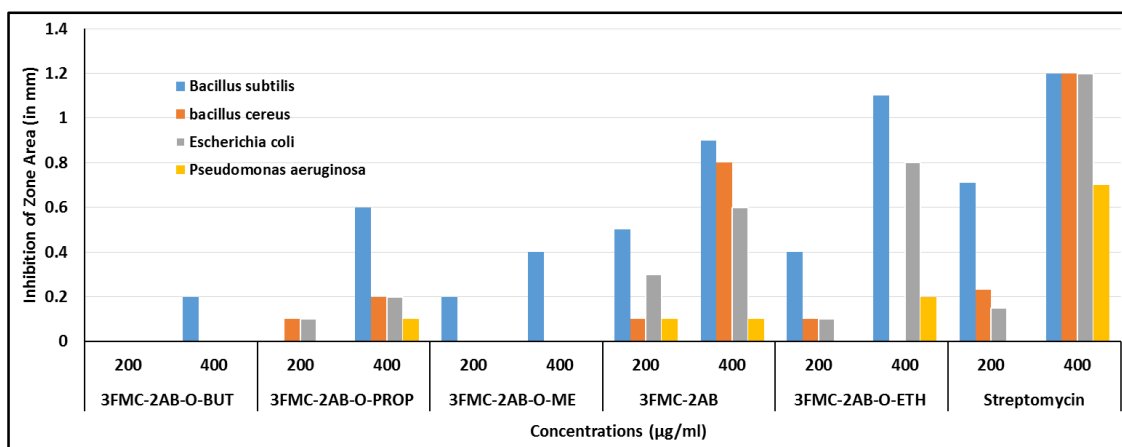


Figure 5C.2 Histogrammatical presentation of antibacterial activity of **3FMC-2AB-R**

5C.1.2 In-vitro Antifungal Activity of **3FMC-2AB-R**

In-vitro Antifungal Activity of studies of the **3FMC-2AB-R** are investigated with the help of two fungal strains, *Aspergillusniger* and *penuliumnotatum*, with ketoconazole as a standard drug. The results are placed in **Table 5C.2**. The antifungal studies of the **3FMC-2AB-H** and **3FMC-2AB-OMe** compounds are reasonably close to the standard drug for both the fungal. Further, the results reveal that all the remaining chromanones show moderate to good activity compared with standard drug.

Table 5C.2 Antifungal activity MIC values of **3FMC-2AB-R** (µg/ml)

Compound	<i>Aspergillusniger</i>	<i>Penuliumnotatum</i>
3FMC-2AB-H	4.92	6.24
3FMC-2AB-OMe	3.25	4.68
3FMC-2AB-OEt	7.29	6.18
3FMC-2AB-OiPr	4.31	6.72
3FMC-2AB-OnBut	7.35	9.11
Ketoconazole	2.67	2.78

5C.1.3 *In-vitro Antioxidant Property of 3FMC-2AB-R*

The scavenging activity has been studied for the free radical DPPH (2,2-Diphenyl-1-picrylhydrazyl. The data results in **Table 5C.3** indicates chromanone (**3d**) exhibited considerable antioxidant activity. All the compounds compared to the standard drug AA, the remaining chromanones exhibited moderate to good antioxidant activity, as shown in **Figure 5C.3**.

Table 5C.3 Anti-scavenging activity IC_{50} values of **3FMC-2AB-R**

Compound	IC_{50} ($\mu\text{g/ml}$)
3FMC-2AB-H (3a)	48.01
3FMC-2AB-OMe (3b)	50.95
3FMC-2AB-OEt (3c)	43.67
3FMC-2AB-O(iPr)(3d)	36.12
3FMC-2AB-O(nBut)(3e)	40.61
Ascorbic acid(AA)	25.36

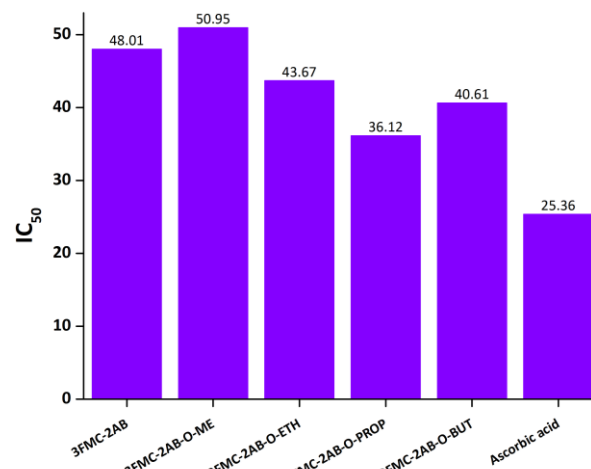


Figure 5C. 3 Histogramical representation of the IC_{50} inhibition values of the DPPH radical anti-scavenging activities of **3FMC-2AB-R** with ascorbic acid as standard drug

5C.1.4 *In vitro Alpha-Amylase Inhibitory Activity of 3FMC-2AB-R*

The *in-vitro* anti-diabetic studies of the chromanones (**3a-e**) reveal potent glucose inhibition activity. The inhibitory activity of the chromanones (**3a-e**) increased with the increasing concentration of compounds. The results are presented in **Table 5C.4**. The **3FMC-2AB-OEt**, **3FMC-2AB-OnBut** and **3FMC-2AB-OiPr** compounds exhibited potent anti-diabetic inhibitory activity which was obtained from absorbance at 505 nm of 42.55, 39.62 and 34.61% at 50 $\mu\text{g/ml}$ concentration. Among the others, **3FMC-2AB-OMe** and **3FMC-2AB-H** compounds exhibit 23.07 and 25.58 % at 50 $\mu\text{g/ml}$, respectively. The observed inhibition of α -amylase activity is due to the attack of alkoxy chains on the active sites of chromanone C2-position which interacts with the active site of α -amylase enzyme residual atoms. This lets them occupy important parts of the enzyme's active site that the more two-dimensional compounds can't reach.

In this series, the most potent compounds are ethoxy and butoxy, having long alkoxy groups attached to the C2-position in both **3FMC-2AB-OEt** and **3FMC-2AB-O(n-But)** chromanone test

concentrations. Thus, all of the chromanone compounds can be considered as possible anti-diabetic agents, though further studies may be essential to optimize.

Table 5C.4 *In vitro* α -amylase enzyme inhibitory of **3FMC-2AB-R** activity for glucose

S. No.	Test compound	% Inhibition					IC ₅₀ (μ g/ml)
		10 (μ g/ml)	20 (μ g/ml)	30 (μ g/ml)	40 (μ g/ml)	50 (μ g/ml)	
1	3FMC-2AB-OMe	7.69	13.46	17.30	21.15	23.07	36.1
2	3FMC-2AB-OEt	25.53	29.78	38.29	36.17	42.55	66.03
3	3FMC-2AB-O(iPr)	11.53	21.15	17.30	26.92	34.61	80.90
4	3FMC-2AB-O(n-But)	30.18	33.96	37.73	35.84	39.62	68.80
5	3FMC-2AB-H	11.63	25.58	20.93	23.25	25.58	115.58

5C.2 Molecular Docking Studies of 3FMC-2AB-R

All of the **3FMC-2AB-R** had excellent binding energies to the active sites of both the protein receptors, as determined by the chromanones (**3a-e**) simulation molecular docking studies. Using low binding energy, high docking score, and the quantity of H-bonding and hydrophobic interactions at the receptor site of both the compounds, viz., **3FMC-2AB-H**, **3FMC-2AB-OMe**, **3FMC-2AB-OEt**, **3FMC-2AB-O(iPr)**, and **3FMC-2AB-O(n-But)** with 2QLC protein, docking results have been identified based on the suitable intermolecular interaction binding sites, as shown in **Figure 5C.4**. The existence of electron-donating groups (methyl groups, nitrogen, and oxygen atoms), as well as the compound's electron cloud structure, may be the reason for the chromanones potency. The docking score, hydrogen bond length, and interacting atoms are shown in **Table 5C.5**. All compounds were confirmed to be buried. Moreover, molecular docking experiments verified the binding interactions with the 2QLC and 2QV4 receptors. The new series of chromanone compounds may therefore be useful in applications of pharmacological therapeutics.

Table 5C.5 Molecular docking interactions results of **3FMC-2AB-R** (3a-e) with (PDBID: 2QLC and 2QV4) receptors

Receptor	Ligand	Receptor Interaction Atoms	Ligand Interaction Atoms	H-bond Distance (Å)	Docking Score (kcal/mol)
2QLC	3FMC-2AB(3a)	SER85-OG	NH	2.59	-90.095
		ASP88-OD2	NH	2.86	
	3FMC-2AB-O(nBut)(3e)	THR45-NH	O	2.96	-87.224
		THR43-O	NH	3.00	
	3FMC-2AB-OEt(3c)	ASP10-OD2	NH	2.93	-89.659
		ARG9-NH1	O	3.01	
	3FMC-2AB-OMe(3b)	ALA8-N	O	2.98	-88.146
		ASP108-OD2	OD2	3.16	
	3FMC-2AB-O(iPr)(3d)	ALA8-NH	O	3.28	-82.150
	3FMC-2AB-H(3a)	PRO228-O	O	2.96	-80.475
2QV4	3FMC-2AB-O(nBut)(3e)	ASN250-O	NH	3.08	-81.798
	3FMC-2AB-OEt(3c)	PRO228-O	NH	2.92	-88.949
	3FMC-2AB-OMe(3b)	LYS227-O	NH	3.03	-80.501
		ASN5-ND2	O	3.10	
	3FMC-2AB-O(iPr)(3d)	TYR2-NH	O	2.85	-88.485
		LYS227-O	O	3.13	

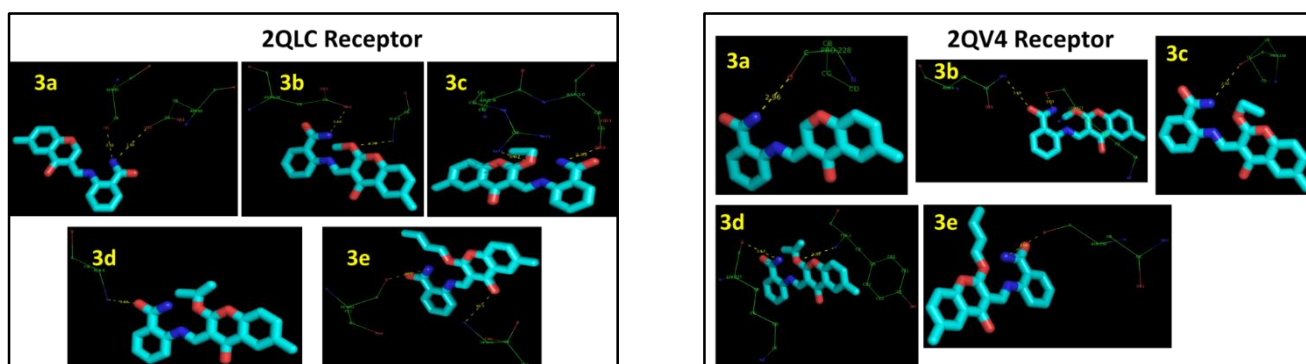


Figure 5C.4 Molecular 3D binding site poses of **3FMC-2AB-R** (3a-e) with 2QLC (left) and 2QV4 (right) DNA protein receptors

5C.3 *In-silico* Drug-Likeness Analysis of 3FMC-2AB-R

Drug likeness analysis results are reported in **Table 5C.6** showing that all **3FMC-2AB-R** compounds can easily transported in the body since their molecular weight (MW) are less than 500 g/mol. The octanol–water partition coefficient (log P), which usually measures how lipophilic a molecule is, is between -0.4 and 5.6, which is good [17]. Chromanone derivatives (**3a–e**) measured total polar surface area (TPSA \leq 160 Å²), which is a good sign that the drug molecule is bioavailable

within an acceptable range. In addition, the number of hydrogen bond acceptors (HBA < 10) and number of hydrogen bond donors (HBD < 5), are in the acceptable ranges

However, all of the chromanone derivatives pass all used rules, namely Lipinski's rule and Veber rule have desirable drug likeness criteria [17, 18].

Table 5C.6 Some calculated drug-like properties of **3FMC-2AB-R (3a-e)**

Property/rule	(3a)	(3b)	(3c)	(3d)	(3e)
MW (g/mol)	306.32	338.36	352.38	366.41	380.44
Log P	2.49	2.80	2.88	3.18	3.65
TPSA (Å ²)	85.66	90.65	90.65	90.65	90.65
nHBA	4	4	4	4	4
nHBD	1	2	2	2	2
Lipinski	Yes; 0 violation				
Veber	Yes	Yes	Yes	Yes	Yes

The bioavailability radar features are displayed in **Figure 5C.5 (a)**, and they allow for a quick assessment of a molecule's drug-likeness by taking six physicochemical factors into account: saturation, lipophilicity, polarity, size, solubility, and flexibility. The Swiss ADME online webserver was used to construct the Brain or IntestinaL EstimateD permeation predictive model (BOILED-Egg), commonly known as the Egan egg graph, which provided a clear graphical representation of the compound, **3FMC-2AB-H**, absorption in the brain and gastrointestinal system. All of the chromanones (**3a-e**), which are estimated to be absorbed a lot in the digestive system, have graph molecules in the yolk area (yellow) that are expected to pass through the blood-brain barrier is shown in **Figure 5C.5 (b)**.

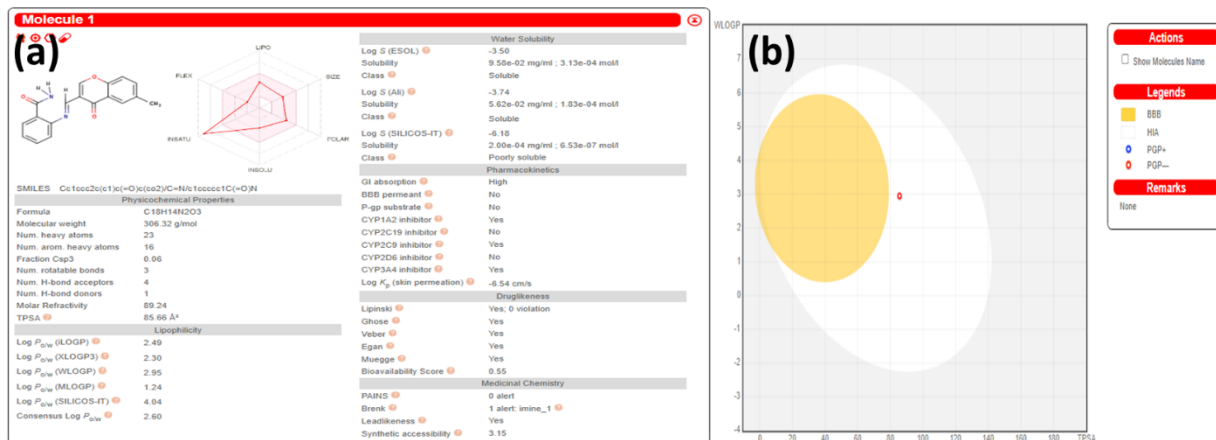


Figure 5C.5 Drug likeness property parameters of **3FMC-2AB-H (a)** and BOILED-Egg graph **(b)** demonstrating the yellow colour of boiled egg yolk represents passive permeation of the blood-brain barrier (BBB).

References

- [1] Selvamurugan, S.; Ramachandran, R.; Vijayan, P.; Manikandan, R.; Prakash, G.; Viswanathamurthi, P.; Velmurugan, K.; Nandhakumar, R.; Endo, A. Synthesis, Crystal Structure and Biological Evaluation of Ni(II) Complexes Containing 4-Chromone-N(4)-Substituted Thiosemicarbazone Ligands. *Polyhedron* **2016**, *107*, 57–67. <https://doi.org/10.1016/j.poly.2016.01.011>.
- [2] Samuel, M.; Rajasekar, R.; Jeyaraman, P.; Muthusamy, S.; Muniyandi, V.; Raman, N. DNA Interaction Perspectives of Sulphur Containing Knoevenagel Condensed Copper(II) Complexes: Molecular Docking, DFT, Anti-Biogram and Insilico Assessment. *Inorganica ChimICA Acta* **2022**, *533*, 120783. <https://doi.org/10.1016/j.ica.2021.120783>.
- [3] R, G. Inorganic Electronic Spectroscopy. *Journal of Molecular Structure* **1985**, *129* (1–2), 180–181. [https://doi.org/10.1016/0022-2860\(85\)80208-8](https://doi.org/10.1016/0022-2860(85)80208-8).
- [4] Gaber, M.; El-Baradie, K.; El-Wakiel, N.; Hafez, S. Synthesis and Characterization Studies of 3-formyl Chromone Schiff Base Complexes and Their Application as Antitumor, Antioxidant and Antimicrobial. *Applied Organometallic Chemistry* **2020**, *34* (2). <https://doi.org/10.1002/aoc.5348>
- [5] Konakanchi, R.; Pamidimalla, G. S.; Prashanth, J.; Naveen, T.; Kotha, L. R. Structural Elucidation, Theoretical Investigation, Biological Screening and Molecular Docking Studies of Metal(II) Complexes of NN Donor Ligand Derived from 4-(2-Aminopyridin-3-Methylene)Aminobenzoic Acid. *BioMetals* **2021**, *34* (3), 529–556. <https://doi.org/10.1007/s10534-021-00293-1>.
- [6] Zare, N.; Zabardasti, A.; Mohammadi, A.; Azarbani, F.; Kakanejadifard, A. Sonochemical Synthesis, Characterization, Biological Applications, and DFT Study of New Nano-Sized Manganese Complex of Azomethine Derivative of Diaminomaleonitrile. *Journal of Iranian Chemical Society* **2019**, *16* (7), 1501–1516. <https://doi.org/10.1007/s13738-019-01626-1>.
- [7] Bheemarasetti, M.; Palakuri, K.; Raj, S.; Saudagar, P.; Gandamalla, D.; Yellu, N. R.; Kotha, L. R. Novel Schiff Base Metal Complexes: Synthesis, Characterization, DNA Binding, DNA Cleavage and Molecular Docking Studies. *Journal of Iranian Chemical Society* **2018**, *15* (6), 1377–1389. <https://doi.org/10.1007/s13738-018-1338-7>.
- [8] Mayuri, B.; Kavitha, P.; Basavoju, S.; Bhargavi, G.; Reddy, K. L. Synthesis, Structural Characterisation and Biological Evolution of Chromanones. *Journal of Molecular Structure* **2017**, *1145*, 1–9. <https://doi.org/10.1016/j.molstruc.2017.05.013>.
- [9] Haribabu, J.; Srividya, S.; Mahendiran, D.; Gayathri, D.; Venkatramu, V.; Bhuvanesh, N.; Karvembu, R. Synthesis of Palladium(II) Complexes via Michael Addition: Antiproliferative Effects through ROS-Mediated Mitochondrial Apoptosis and Docking with SARS-CoV-2. *Inorganic Chemistry* **2020**, *59* (23), 17109–17122. <https://doi.org/10.1021/acs.inorgchem.0c02373>.
- [10] Satapathy, A. K.; Behera, S. K.; Yadav, A.; Mahour, L. N.; Yelamaggad, C. V.; Sandhya, K. L.; Sahoo, B. Tuning the Fluorescence Behavior of Liquid Crystal Molecules Containing Schiff-Base: Effect of Solvent Polarity. *Journal of Luminescence* **2019**, *210*, 371–375. <https://doi.org/10.1016/j.jlumin.2019.02.056>.

[11] Mayuri, B.; Kavitha, P.; Basavoju, S.; Bhargavi, G.; Reddy, K. L. Synthesis, Structural Characterisation and Biological Evolution of Chromanones. *Journal of Molecular Structure* **2017**, *1145*, 1–9. <https://doi.org/10.1016/j.molstruc.2017.05.013>.

[12] Rosu, T.; Pahontu, E.; Maxim, C.; Georgescu, R.; Stanica, N.; Almajan, G. L.; Gulea, A. Synthesis, Characterization and Antibacterial Activity of Some New Complexes of Cu(II), Ni(II), VO(II), Mn(II) with Schiff Base Derived from 4-Amino-2,3-Dimethyl-1-Phenyl-3-Pyrazolin-5-One. *Polyhedron* **2010**, *29* (2), 757–766. <https://doi.org/10.1016/j.poly.2009.10.017>.

[13] Spackman, P. R.; Turner, M. J.; McKinnon, J. J.; Wolff, S. K.; Grimwood, D. J.; Jayatilaka, D.; Spackman, M. A. CrystalExplorer: A Program for Hirshfeld Surface Analysis, Visualization and Quantitative Analysis of Molecular Crystals. *Journal of Applied Crystallography* **2021**, *54* (3), 1006–1011. <https://doi.org/10.1107/S1600576721002910>.

[14] Pangajavalli, S.; Kumar, R. R.; Ramaswamy, S. Structural, Hirshfeld, Spectroscopic, Quantum Chemical and Molecular Docking Studies of N’-(4-(4-Chlorophenyl)-1,3-Dicyano-5,6,7,8,9,10-Hexahydrobenzo[8]Annulen 2-Yl) N,N-Dimethylformimidamide as CCR2 Inhibitors. *Journal of Molecular Structure* **2021**, *1239*, 130503. <https://doi.org/10.1016/j.molstruc.2021.130503>.

[15] Şahin, S.; Dege, N. (E)-N-(3-Chlorophenyl)-1-(5-Nitro-2-(Piperidin-1-Yl)Phenyl)Methanimine: X-Ray, DFT, ADMET, Boiled-Egg Model, Druggability, Bioavailability, and Human Cyclophilin D (CypD) Inhibitory Activity. *Journal of Molecular Structure* **2022**, *1250*, 131744. <https://doi.org/10.1016/j.molstruc.2021.131744>.

[16] Kolhe, N. H.; Jadhav, S. S. Synthesis, Characterization and Biological Activity of Mixed Ligands Complexes of Quinolin-8-Ol and Substituted Chromones with Mn(II), Co(II), Ni(II) and Cu(II) Metal Ions. *Research on Chemical Intermediate* **2019**, *45* (3), 973–996. <https://doi.org/10.1007/s11164-018-3656-x>.

[17] Şahin, S.; Dege, N. (E)-N-(3-Chlorophenyl)-1-(5-Nitro-2-(Piperidin-1-Yl)Phenyl)Methanimine: X-Ray, DFT, ADMET, Boiled-Egg Model, Druggability, Bioavailability, and Human Cyclophilin D (CypD) Inhibitory Activity. *Journal of Molecular Structure* **2022**, *1250*, 131744. <https://doi.org/10.1016/j.molstruc.2021.131744>.

[18] Samuel, M.; Rajasekar, R.; Jeyaraman, P.; Muthusamy, S.; Muniyandi, V.; Raman, N. DNA Interaction Perspectives of Sulphur Containing Knoevenagel Condensed Copper(II) Complexes: Molecular Docking, DFT, Anti-Biogram and Insilico Assessment. *Inorganica Chimica Acta* **2022**, *533*, 120783. <https://doi.org/10.1016/j.ica.2021.120783>.

SUMMARY AND CONCLUSIONS

The thesis, entitled, “**Synthesis, Characterization and Single Crystal XRD, Computational and Biological Studies of Some Chromanone and Imidazole-based Azomethine Ligands and Their Bivalent Metal Complexes**”, deals with the synthesis and characterization of a few selected nitrogenous organic compounds along with their molecular structure determination by single crystal XRD and correlation of the structural parameters with those obtained by molecular modeling. Coordination compounds from some of these organic compounds have also been prepared, investigated and molecular modelled. Both, ligands and their complexes have been exposed to molecular docking on some biomolecules. They were tested for possible anti-fungal, anti-bacterial, anti-cancer and anti-oxidant *in vitro* applications.

Chapter I introduces the importance of heterocyclic organic compounds with a special emphasis on Schiff bases, chromanone derivative compounds, etc. and their metal complexes. The contemporary research on the correlation of empirical molecular structural studies by XRD and those obtained from advanced computational modeling, is highlighted with examples. The Chapter concludes with the Scope and objectives to include new candidates in this novel areas of research. In this Chapter, entitled, **Introduction**, examples, reported in literature, of data correlation between XRD and molecular modelling studies are given to highlight the remarkable success of agreement of computational data with the empirical ones.

Chapter II, entitled, ‘**Materials and Methods**’, describes the experimental procedures of the synthesis and characterization of the compounds studied. This Chapter is divided into two Parts, viz., **Part A** and **Part B** of which **Part A** deals with the synthesis of the chosen organic compounds and their metal complexes wherever feasible. **Part B** presents the details of characterization of the compounds by various wet, spectral and other instrumental methods. Introduction to current computational chemistry procedures along with the principles of some of the instrumental methods employed in these investigations are provided.

In **Chapter III**, entitled, ‘**Synthesis and Spectral, Single Crystal XRD, DFT-Computational and Biological Activity Studies of A New Schiff Base of 4-Aminoantipyrine and Investigations of Its Co(II), Ni(II), Cu(II) and Zn(II) Complexes**’, and divided into 3 Parts, **PART A** presents the details of the characterization of **4AAP-BCFI** and its metal complexes by analytical and spectroscopic studies. Single crystals could be generated only for **4AAP-BCFI**, but

not suitably with its complexes of some bivalent metal ions such as Co(II), Ni(II), Cu(II) and Zn(II). The studies indicate the formation $M(4AAP-BCFI)_2(H_2O)_2^{2+}$ complex for all where $M = Co(II)$, $Ni(II)$, $Cu(II)$ and $Zn(II)$ ions are presented. In **PART B** the crystal analysis, molecular modelling and the comparison of experimental XRD crystal data of **4AAP-BCFI** along with its metal complexes with those evaluated by computational analysis from DFT/B3LYP calculations, fully optimized semi empirical MM2 analysis are presented and discussed. There is an excellent agreement of the computationally evaluated data with the empirical data obtained by single crystal XRD data whereas in **PART C** the biological activity along with protein-molecular docking studies of ligand, **4AAP-BCFI** and its metal complexes are highlighted. The antimicrobial, antioxidant, antifungal, potent capabilities, tested for both **4AAP-BCFI** and $[M(4AAP-BCFI)_2(H_2O)_2]^{2+}$ complexes, are exhibited.

Chapter IV is titled as, ‘**Synthesis, Characterization, Crystal Structure Determination, Computational Modelling and Biological Studies of A New (2-hydroxy-5-methylphenyl)(1H-pyrazol-4-yl)methanone and Its Zn(II) and Cu(II), Ni(II), Co(II) Complexes**’. **PART A** describes a novel organic molecule, viz., (2-hydroxy-5-methylphenyl)(1H-pyrazol-4-yl)methanone (**HMPM**) and its $[M(HMPM)_4Cl_2]$ complexes characterized by various spectroscopic techniques and by single crystal XRD studies. The $[Zn(HMPM)_4Cl_2]$ crystallizes in its centrosymmetric monoclinic $P_{21/n}$ space group. The crystal structure analysis data and molecular modelling studies on the platforms of B3LYP and MM2 calculations and the data have been correlated with the XRD data. The computationally evaluated data are found to be in excellent agreement with the empirical single crystal XRD data and Hirshfeld surface analysis carried on $[Zn(HMPM)_4Cl_2]$, reveal some interesting hydrogen bond intermolecular interactions are discussed in its **PART B**. **PART C** is for the biological activity studies these new heterocyclic compounds exhibit certain level of pharmaceutical property as proven from the anti-bacterial assaying and *In-silico* drug likeness analysis.

The last **Chapter V**, entitled, ‘**Spectral and Biological Studies of a Novel Series of Chromanones and Their Metal Complexes and Correlation of Their Computational Studies with the Single Crystal XRD Molecular Structure of One Chromanone of the Series**’, is divided into 3 Parts. Due to poor solubility and other limitations, we could not generate a single crystal for any of the other $M(TATMC)_2Cl_2$ complexes and other chromanone derivatives, **3FMC-2AB-R**. **Section 1 of Part A (Section A1)** deals with the spectral, morphological studies of **TATMC** and its complexes. While **Section 2** of this Part (**Section A2**) discusses the spectral characterization of chromanone derivatives, **3FMC-2AB-R**. Single crystal XRD studies, molecular

structural determination of **TATMC** and computational chemistry of the same are discussed in **Section 2 of Part B (Section B1)**. Similarly, **Section 2 of Part B (Section B2)** covers the corresponding molecular structure conformational analysis, evaluation of structural parameters such as bond length, bond angles, torsional angles, HOMO-LUMO orbital energies, single and double dihedral analysis, etc. by molecular modeling studies of **3FMC-2AB-R**. The XRD molecular structural data of **TATMC** and **3FMC-2AB-R** obtained through single crystal XRD studies have been compared with molecular modelled structures of all the respective compounds in this Chapter. Finally, this Chapter presents briefly the biological applications of the title compounds in **PART C**.

Publications and Presentations of the Work Embodied in This Thesis

A. Publications in SCI Journals:

1. *Synthesis, DFT calculations and biological activity of a new Schiff base of 4-aminoantipyrine and its Co(II), Ni(II), Cu(II) and Zn(II) complexes and crystal structure of the Schiff base.*

Ajmeera Ramesh, R. Pawar, P. Shyam, Ramachandraiah Allikayala,
Research on Chemical Intermediates, 2021, **47**, 4673-4697, <https://doi.org/10.1007/s11164-021-04552-1>.

2. *Synthesis, characterization, crystal structure determination, computational modelling and biological studies of a new tetrakis-(2-hydroxy-5-methylphenyl)(1H-pyrazol-4-yl)methanonezinc(II) complex.*

Ajmeera Ramesh, Basavoju Srinivas, R. Pawar, Ramachandraiah Allikayala,
Journal of Molecular Structure, 2022 **1255**, 132377,
<https://doi.org/10.1016/j.molstruc.2022.132377>.

B. Presentations at National and International Conferences / Symposia:

1. **Ajmeera Ramesh** and Ramachandraiah Allikayala; *Synthesis and Characterization of Novel Schiff base Ligand N-((2-butyl-4-chloro-1H-imidazol-5-yl)methylene)-4H-1,2,4-triazol-4-amine*; National Conference of the Telangana Academy of Sciences (TSSC-2018) held at National Institute of Technology Warangal, during 22nd -24th, December 2018.
2. **AjmeeraRamesh** and Allikayala Ramachandraiah; *Synthesis, Characterization and Molecular Docking Biological Studies of the Coordination Compounds of 4AAP-BCFI with Some Bivalent Metal Ions, [M(4AAP-BCFI)₂(H₂O)₂]*; National Conference of the Telangana Academy of Sciences (TSSC-2018) held at National Institute of Technology Warangal, during 22nd -24th, December 2018.
3. **Ajmeera Ramesh** and Allikayala Ramachandraiah; *Synthesis, Characterization of Chromanones and DFT Studies*; National Conference of the Telangana Academy of Sciences (TSSC-2018) held at National Institute of Technology Warangal, during 22nd -24th, December 2018.
4. **Ajmeera Ramesh** and Allikayala Ramachandraiah; *Synthesis and Physicochemical Characterization of a Novel Thiadizole-2-Thiol Dithiocarbamate Metal Complexes*; National Conference on Emerging Trends in Instrumental Methods of Chemical Analysis (ETIMCA-2019) organized by the Department of Chemistry, National Institute of Technology Warangal during 30th -31st January, 2019.
5. **Ajmeera Ramesh** and Allikayala Ramachandraiah; *Synthesis and Spectral and Spectroelectrochemical Characterization of Schiff base Derived from Chromanone*; International Conference on Advances in Chemical Sciences and Technologies (ACST-2019) held at the Department of Chemistry, National Institute of Technology Warangal during 23rd -25th September, 2019.

Participation in Workshops / Conferences as a Delegate

1. A 10-Day Global Initiative for Academic Network (GIAN) on *Advance Materials for Sustainable Energy and Storage*, organized by the Department of Chemistry, National Institute of Technology Warangal during 23rd May – 3rd June, 2016.
2. A One-Week Faculty Development Workshop on *Teaching and Learning Chemical Spectroscopy through Hands-On Experience*, organized by the Department of Chemistry in association with the Teaching Learning Centre, National Institute of Technology Warangal during 11th-16th October, 2017.
3. An International Workshop on *Supporting Chemistry Research with modern DFT (Density Functional Theory): Software, Techniques, and Applications*, organized by the Department of Chemistry, Smt. S. S. Patel Nootan Science & Commerce College, Visnagar, Mehsana, Gujarat during 5th-16th February, 2021.
4. A Three-Day Online International Conference on *Conventional and Digital methods in Chemical Education*, organized by the Department of Chemistry, National Institute of Technology Warangal during 29th-31st July, 2021.



CURRICULUM VITAE

AJMEERA RAMESH

Contact Address

Department of Biotechnology
National Institute of Technology Warangal
Hanumakonda, 506004, Telangana

E-mail: ramesh1989@nitw.ac.in
Contact No. 9494464295

Academic Qualifications

Jan 2016 present

: Research Scholar (PhD Chemistry)

Under the supervision of **Prof. A. Ramachandraiah (HAG, Retd)** Department of Chemistry, National Institute of Technology Warangal, Telangana, India

September 2007-November 2012: Integrated MSc Chemistry

University College Kakatiya University,

Vidyaranyapuri, Hanumakonda, 506008

Division: **(First class)**

Personal Details:

- Name : Ajmeera Ramesh
- Father's Name : Mankaiah
- Mother's Name : Neela
- Date of Birth : 10-08-1989
- Gender : Male
- Marital Status : Married
- Nationality : Indian
- Languages Known : Telugu, English, Hindi

Achievements:

- Rajiv Gandhi National Fellowship to Pursue Doctoral Degree in 2015
- Permanent Job as Technician at NIT Warangal from 2016

Technical Skills:

- Experience on MS Office, ChemDraw, Surfer and Grapher, Origin, Crystal Explorer, AutoDock/Vina, etc.
- Experience on MENDELEY Platform
- Experience on retrieval of Literature from GoogleScholar, SciHub, ScienceDirect, ResearchGate

Expertise in Instrumental Techniques:

- Electrochemical Impedance Analyzer, Zahner-Elektrik (IM6e), GmbH, Germany
- Electrochemical Workstation, Sinsil CHI 619D
- UV-Visible Spectrophotometers, Analytika Jena Specord 205 and Schimadzu 1601

- UV-Visible-NIR Agilent cary 5000
- Thermo Scientific UV-Visible Spectrophotometer Evolution 600 Instrument
- Analytika F96 Pro Fluorescence Spectrophotometer
- PerkinElmer 100S FTIR Spectrophotometer
- Differential Scanning Calorimetry, Q10 TA Instruments
- JEOL FA-100, X-Band ESR Spectrometer
- Agilent 720 Series ICPOES Spectrophotometer
- BioLogic MOS-500 CD and ORD Spectrophotometer
- Many Other Minor and Semi-Major Analytical Equipment
- Laboratory Skills in Synthesis and Working Up of New Organic and Inorganic Materials
- Bio-Assaying and Bioequipment Management

Research Interest:

- Single Crystal Growth for Semiconductor Materials
- Computational and Modelling studies
- Synthesis of Organic and Inorganic Compounds
- Spectral and Electrochemical Analysis

Other Capabilities:

- Capable of carrying out both collaborative and independent research
- Motivated with strong ethics, devotion to duty and hardwork
- Strong interpersonal and communication skills along with management skills
- Expertize in writing technical documents, presentations, and drafting project reports